Cells in ecstasy

Molecular probes to map mechano-chemical patterns in walled cells

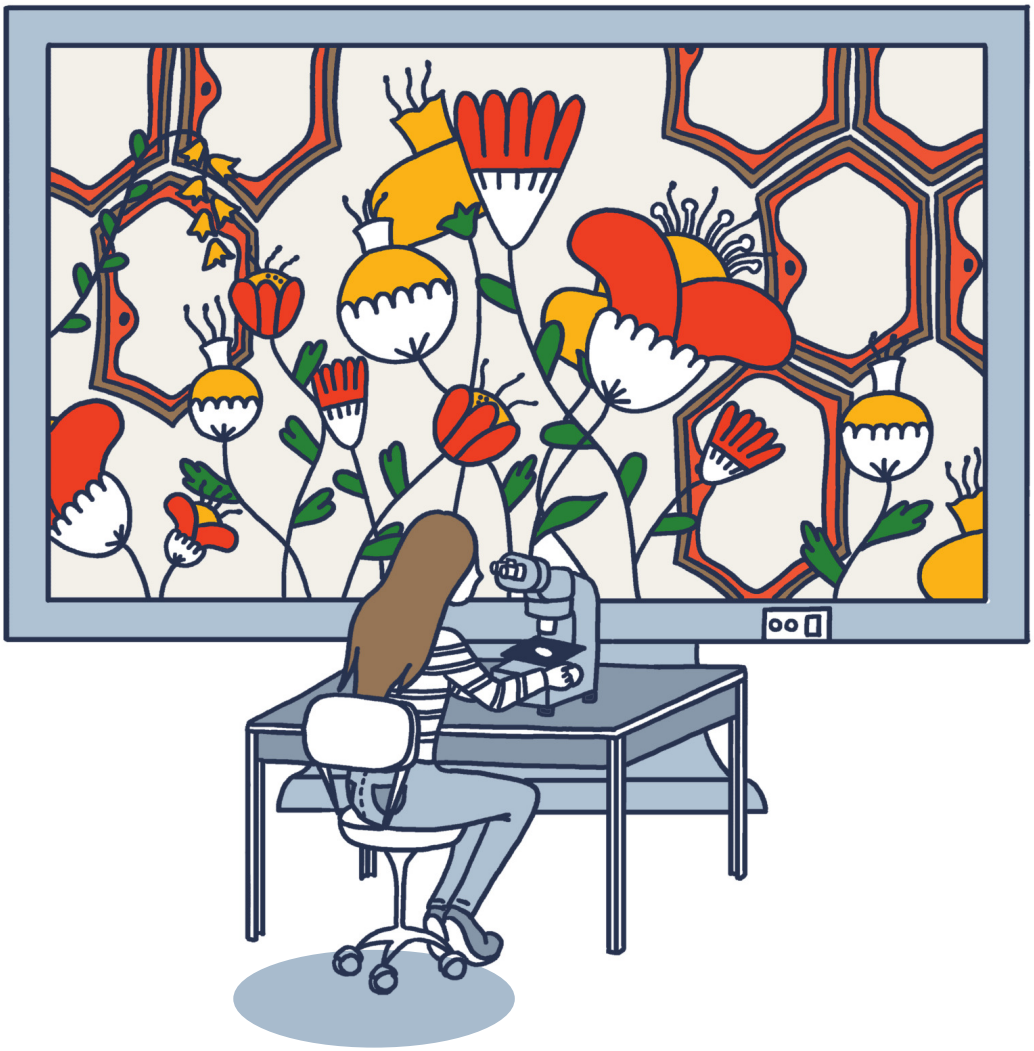

Lucile Michels

Propositions

1. When interpreting data obtained using fluorescent molecular sensors, variations in chemical polarity should be taken into account.
   (this thesis)

2. Molecular rotors are the most versatile tools to visualize physico-chemical patterns in living cells with a high spatio-temporal resolution.
   (this thesis)

3. The term 'novelty' should be redefined for interdisciplinary research to include new fields-of-application for old tools.

4. A vanity-free platform to report failed experiments would substantially reduce the waste of time and financial capital in science.

5. Doing a PhD teaches you to go from perfectionism to pragmatism.

6. When making career and life decisions, asking what you are ready to struggle for is more useful than asking what you want to achieve.

7. Living abroad teaches one to question the status quo.

Propositions belonging to the thesis entitled:
Cells in ecstasy
Molecular probes to map mechano-chemical patterns in walled cells

Lucile Michels
Wageningen, 17 december 2021

Cells in Ecstasy

Molecular probes to map mechano-chemical patterns in walled cells

Lucile Michels

Thesis committee

Promotor

Prof. Dr. Joris Sprakel
Personal chair at Physical Chemistry and Soft Matter
Wageningen University & Research

Other members

Prof. Dr. Herbert van Amerongen, Wageningen University & Research
Dr. Jessica Clough, Adolphe Merkle Institute Fribourg, Switzerland
Dr. Jose Lozano Torres, Wageningen University & Research
Prof. Dr. Cornelis Storm, Eindhoven University of Technology

This research was conducted under the auspices of
Graduate School VLAG (Advanced studies in Food Technology,
Agrobiotechnology, Nutrition and Health Sciences).

Cells in Ecstasy

Molecular probes to map mechano-chemical patterns in walled cells

Lucile Michels

Thesis
submitted in fulfillment of the requirements for the degree of doctor
at Wageningen University,
by the authority of the Rector Magnificus,
Prof. Dr. A.P.J. Mol,
in the presence of the
Thesis Committee appointed by the Academic Board,
to be defended in public
on Friday 17 December, 2021
at 4 p.m. in the Aula.

Lucile Michels
Cells in Ecstasy — Molecular probes to map mechano-chemical patterns in walled cells
242 pages

PhD thesis, Wageningen University, Wageningen, The Netherlands (2021) with references, with summary in English.

ISBN: 978-94-6395-932-2
DOI: https://doi.org/10.18174/551313

Contents

Chapter 1

Introduction

Classically, biological systems have been primarily studied from a chemistry-centred perspective explaining the processes of life as complex chemical signalling networks. In recent years, it has become clear that also mechanical forces play an important role in the regulation of biological processes. This realization has opened the way to the emerging field of mechanobiology, which aims at understanding how cells send out, interpret and internalize mechanical signals and convert these into biochemical signals that interact with the genetic machinery of the organism. Most of the efforts in this field at the interface of biology and mechanics has been focused on the animal kingdom, while the study of mechanobiological processes in plants or other walled systems (e.g. fungi and oomycetes) has received much less attention. One of the key challenges to understand how plant cells cope with mechanical stress is the detection and visualization of mechanical patterns, in-vivo and with subcellular resolution. The goal of this thesis is to develop new tools to visualize mechanical patterns in plant cells and tissues. We do so by working at the interface between the mechanochemistry of fluorescent molecular rotors and plant mechanobiology.

This thesis presents a new toolbox of target-finding molecular rotors that can be used in combination with Fluorescence Lifetime Imaging or Ratiometric Intensity Imaging to spatially-resolve microviscosity variations in plant cells. We explore how this toolbox can be used to better understand, from a mechanical point of view, fundamental cellular processes occurring during the cell life cycle. To do so we implemented the rotors both in well-defined synthetic systems (giant vesicles) as well as complex biological systems (i.e. *Arabidopsis thaliana* roots and leaves). Initially developed for plants, we show how the use of such tools

can be extended to the study of other walled systems, with a particular focus on oomycetes (i.e. *Phytophthora infestans*). In this introduction, we first provide a pertinent overview of existing experimental methods used to investigate the mechanical properties of plant cells. We then review existing molecular rotors used as mechanosensors and their implementations in synthetic or biological systems.

1.1 Experimental approaches to plant mechanobiology

In recent years it has become apparent that many aspects of cell function can be altered by mechanical stimuli; the mechanotransduction of forces into biochemical signals is of primary importance in biological systems. Cells can sense mechanical forces in their environment and translate them into intracellular signals. Those signals, initiated at the cell wall, the most rigid part of the plant cell anatomy, are transduced to the membrane and transmitted through cortical and internal cytoskeleton networks to the interior of the cell, and most often to the nucleus -thereby triggering the mechanoregulation of genetic expression patterns-[1, 2, 3]. Mechanical cues regulate or modulate a wide diversity of essential biological processes, ranging from cell differentiation[4] and polarization[5, 6], to morphogenesis and patterning[6, 7, 8, 9].

Mechanoperception in plants occurs at different length scales, going from the subcellular to the organ scale. Plants can sense gravity, touch, osmotic pressure and resistance of the cell wall. These mechanical signals regulate various developmental parameters[6, 7] such as the division orientation of cells (cells divide preferentially along the axis of maximal tension, i.e. the orientation that best resists the maximum tensile stress[10]), cytoskeletal organization[11, 12], gene expression (e.g. to allow for developmental response to touch. The most famous of these genes, whose expression is triggered a few minutes after touch, are called the TCH genes[13].), cell polarity (e.g. by inducing preferential location of the PIN1 protein at a specific site within the cell plasma membrane, depending on membrane tension[14]).

To study the influence of mechanical stimuli in plants, the general approach is to introduce a mechanical perturbation of the system (e.g. forced curvature[15],

ablation[10], inversion of the gravitational field[16]) and to observe, e.g. by time-resolved confocal microscopy, how this perturbation affects the biological response. These approaches are often supported by computer simulations, e.g. to predict stresses in a tissue after perturbation[15, 10]. However, quantitative approaches to measure mechanical properties and stress levels at subcellular scales are still restricted. In the following, we review methods employed to assess mechanical quantities at the cellular level, within four major compartments constituting a plant cell, namely the cell wall, the membranes, the cytoplasm and the vacuoles.

1.2 Investigating the mechanical modulation of cell walls

In plants, cells are interconnected through the network of their cell walls. These stiff structures, composed of a variety of carbohydrates and cell-wall binding proteins[17, 1], must be rigid to provide mechanical support to the cell and counterbalance its internal turgor pressure, yet be able to yield to accomodate cell growth and reshaping. Consequently, its mechanical properties vary significantly in space and time, and are tailored by its physico-chemical composition. From a simplified composite point of view, the cell wall is composed of stiff cellulose microfibrils embedded in a complex matrix of various compliant polymers. During its primary phase, the cell wall is flexible and plastically deformable. At this stage, the matrix contains mainly hemicelluloses, pectin, structural proteins and aromatic substances, physically or covalently crosslinked, in proportions and crosslinking degrees that can remarkably differ between species[18]. Later, as the cell wall maturates, a secondary cell wall is deposited to provide mechanical stability, supported by a more rigid matrix of hemicelluloses and lignin. Once the cell reaches its final size and shape, the primary wall is also lignified. Along the whole process, the interaction and bonding pattern between carbohydrates plays an important role in the wall mechanical properties, and is actively regulated, e.g., by cell wall degrading or modifying enzymes[1, 18, 19, 17]. As a result, cell wall composition, and therefore mechanical properties, vary depending on cell age and function[1].

As the cell wall is the stiffest part of the plant cell structure, intracellular

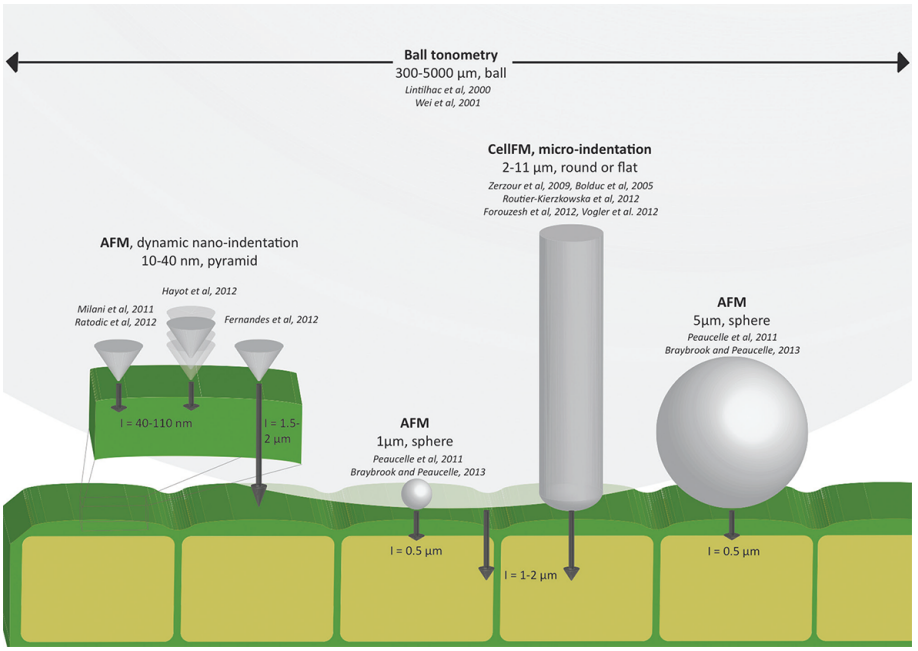

Figure 1.1: Illustration of the panorama of indentation methods applied to plant cells, reprinted with permission from reference [20]

mechanical communication will invariably commence there. This explains why many studies have focused on the mechanical modulation of cell walls within living tissues. To assess the mechanical properties of cell walls, numerous studies relied on indentation methods to probe the stiffness or apparent modulus in a spatially resolved fashion, while relating it to the local chemical composition. Figure 1.1 gives an illustration of the panorama of indentation methods applied to plant cells. Atomic Force Microscopy-based studies of mechanical properties are performed by collecting force-indentation curves at various cell-surface points. Each curve comprises the approach and retraction of the AFM cantilever from the surface, while recording its deflection as a function of travelled distance. The cantilever has a calibrated stiffness constant so that the deflection can be converted into a force, and mechanical properties such as adhesion and elasticity can be quantified. According to the indentation tip geometry, different equations can be used to fit and translate a force displacement curve into an apparent elastic

modulus. As an example, for a spherical indentation tip of radius R, the Hertzian contact model is applied[21, 22].

$$F = \frac{4}{3} R^{0.5} \frac{E}{1-\nu^2} \delta^{\frac{3}{2}} \tag{1.1}$$

where E is the apparent Young's modulus, δ is the indentation depth, and ν is the Poisson's ratio, assumed to be 0.5.

Atomic Force Microscopy has been used for instance to map the apparent elastic modulus of walls in the shoot apical meristem of *Arabidopsis thaliana*[23, 24, 21] (Fig. 1.2), to evaluate the ratio of hardness to reduced modulus of epidermal cells along *Arabidopsis thaliana* roots[25], or to recreate a stiffness distribution in the cell wall of *Arabidopsis thaliana* suspension cells in different growth phases[26].

An alternative to AFM is micro-indentation. This technique is similar to AFM, the difference resides in the size of the probing tip that allows for vertical deformations an order of magnitude larger, and therefore extends the force range accessible up to the mN range. Experiments are performed on a set-up that allows for simultaneous optical imaging of the deformed region. This technique is particularly suitable and has been employed in the study of rapidly growing cells such as pollen tubes, where the position of the indentation tip relative to the growing apex of the cell changes constantly. Geitmann et al.[27] used this technique to quantify pollen tube resistance to lateral deformation forces and analyze its visco-elasticity as a function of distance from the growing apex. They could highlight a clear correlation between the degree of pectin methyl esterification and the configuration of the actin cytoskeleton with the distribution of the physical properties on the longitudinal axis of the cell. With a finite-element based simulation approach, Bolduc et al.[28] simulated the micro-indentation of a pollen tube and manipulated geometric variables such as geometry of the cell, cell radius, thickness of the cell wall and radius of the indenting stylus, to show that these variables all play a role on the determined stiffness. Vogler et al.[29] combined micro-indentation measurements with a finite-element-based modelling approach, which allowed them to extract the Young's modulus of the cell wall, as well as turgor pressure, using data on the apparent stiffness and shrinkage of the pollen tube upon plasmolysis, respectively. By performing similar experi-

ments on onion epidermal cells, Routier-Kierzkowska et al.[30] showed that local stiffness measurements are tightly connected to the level of turgor pressure.

These indentation techniques allow for the invasive evaluation of the cell wall elasticity and strength, but face a certain number of intrinsic limitations. Mapping of the mechanical properties can be done at the surface of tissues only, as deeper cell layers are simply not accessible for indentation. Since available sensors are only capable of measuring forces parallel to the axis of the probe, every contact angle between the sample and the sensor probe greater than 0° will affect the measured forces and, thus, the apparent stiffness[30, 31] (Fig. 1.3). In addition, the influence of the size and geometry of the probe, and the influence of the indentation depth have to be considered. Exceeding a certain depth threshold, the turgor pressure might overcome the actual stiffness of the cell wall[28, 30, 20] (Fig. 1.4).

To study the mechanical modulation of cell walls within living tissues, AFM-based imaging has been one of the leading techniques, used to provide maps of apparent elastic modulus of cell walls within epidermal cell layers.

Other less common techniques involved e.g. the live cell imaging of cellulase synthase enzymes and microtubules, to study the evolution of the spatial distribution of cellulose during development[32], or Brillouin imaging to measure spatial variations in extracellular matrix stiffness[33]. However non-invasive techniques to measure local mechanical properties throughout the cell walls of epidermal but also more internal cell layers within a plant tissue are still needed. Techniques for direct observation without consequent prior data analysis would allow following processes in time and further our understanding of cell wall mechanobiology.

1.3 Lipid fluidity and microviscosity assessment at the cellular level

Just as the cell wall, the plasma membrane is a viscoelastic entity that plays a major role in mechanotransduction. The membrane possess both viscous properties, related to the diffusion rate of macromolecules and organelles, and elastic properties, which allow it to sense and respond to mechanical stresses via sensors

of e.g. membrane unfolding, tension, or changes in curvature. A well-known example of such sensors consists in mechanosensitive ion channels, which allow for the passage of ions across the membrane in response to mechanical stimuli, thereby triggering adaptive response[6].

Within a cell, the plasma membrane is physically anchored to the cell wall and cytoskeleton via the cellulose fibrils and plasma membrane proteins that interact with cell wall components[34]. This anchoring is essential, among others, for cell wall synthesis and remodelling[35, 36], and for signal transduction[37]. In particular, several classes of transmembrane receptors (i.e. receptor-like kinases) have been shown to participate indirectly in mechanoperception by detecting cell wall damage. In order to maintain cell integrity and to adjust the wall properties to accommodate the changing needs of the cell, the plasma membrane activates cytoplasmic signalling schemes and ultimately cell wall remodelling[6, 38, 37].

Plant cell membranes are chemically- and mechanically-heterogeneous lipid bilayers composed of phase separated lipid domains with embedded proteins islands[39]. The existence of particular functional domains (or rafts) that exhibit a specific molecular composition and play important roles in e.g. protein sorting or signal transduction has been highlighted and vastly discussed along the past decade. These rafts are liquid ordered domains enriched in sterol and sphingolipids, and depleted in unsaturated phospholipids[40]. This lateral variation in chemical composition along the membrane leads to a complex and heterogeneous microviscosity distribution. This heterogeneity is further amplified by differing tensions, actively transduced from the cell wall or applied by the cytoskeleton on the membrane during cellular processes[41]. The cell wall as an external component of cells is readily accessible for mechanical characterization, which is not the case for the other cellular compartments such as the plasma membrane but also e.g. the endomembranes, cytoplasm, and vacuoles. As a result, these compartments are usually characterized in terms of their local microviscosity, using either molecular diffusion approaches or more invasive microparticle tracking microrheology techniques. The existing techniques to characterize the elastic properties of these compartments (e.g. tensional forces) are however much more limited, as discussed later in this section.

Microviscosity in these complex systems reflects the local hindrance in Brow-

nian motion, experienced by e.g. a bead, a protein, or a fluorescent molecular dye, as influenced by hydrodynamic effects but also other factors such as confinement and crowding. In this context, the notion of microviscosity relates to the rate of diffusion of species, which in turn affects a multitude of cellular and subcellular processes.

To assess microviscosity in living cells, Fluorescence Recovery after Photobleaching (FRAP), Fluorescence anisotropy, or Fluorescence Correlation Spectroscopy (FCS) are commonly used molecular diffusion approaches.

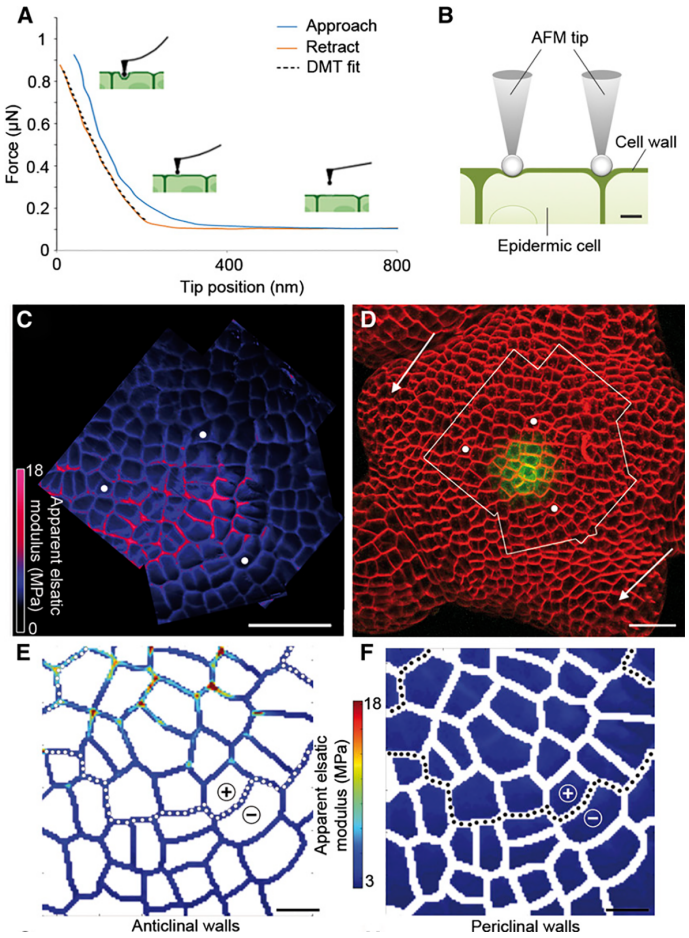

Figure 1.2: Mechanical measurements and cellular mapping of stiffness in walls from an *Arabidopsis* shoot apical meristem (SAM). A, Typical force-tip position approach (blue) and retraction (red) curves obtained on a SAM with a spherical probe tip. The retraction curve (red) is fitted using the Derjaguin-Muller-Toporov model (black dotted line) to obtain the value of the apparent elastic modulus. B, Diagrammatic representation of the AFM tip indenting an epidermal cell in the SAM, either on an outer (periclinal) wall or on walls normal to the surface (anticlinal). When indentation depth is greater than wall thickness, periclinal walls are expected to bend more and to appear softer than anticlinal walls. C and D, Analysis of stiffness in the SAM of a plant expressing GFP-tagged-CLV3 proteins. Shown is the global map of the apparent elastic modulus of a region of the SAM (C), delimited by the white outline in the surface projection of the confocal image (D), with the white dots serving as reference landmarks. The plant was stained with the FM4-64 dye to detect cell contours (in red), while GFP expression is shown in green. E and F, Quantification of stiffness maps. Maps of anticlinal (E) and periclinal (F) walls were reconstituted after segmentation of one of the AFM stiffness maps from the global map shown in C. Scale bars = 20 mm in C and D and 5 mm in E and F. Figure reprinted with permission from reference [23]

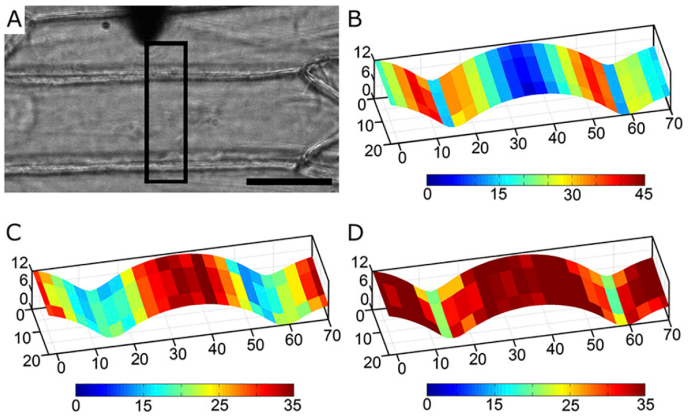

Figure 1.3: Effect of slope on the apparent stiffness. A, Microscopic view of a turgid onion epidermis during the measurements. The shadow of the indenter is visible in the top part of the photograph. The black rectangle indicates the scanned area of the tissue. Scale bar = 40 μm. B, Color map of the angle (°) formed between the cell surface and the indenter probe. C, Color map of the apparent stiffness (Nm^{-1}) measured during the scan. D, Color map of the corrected stiffness (Nm^{-1}) computed using the measured stiffness, the surface slope, and the bending stiffness of the indenter probe. Figure reprinted with permission from reference [30]

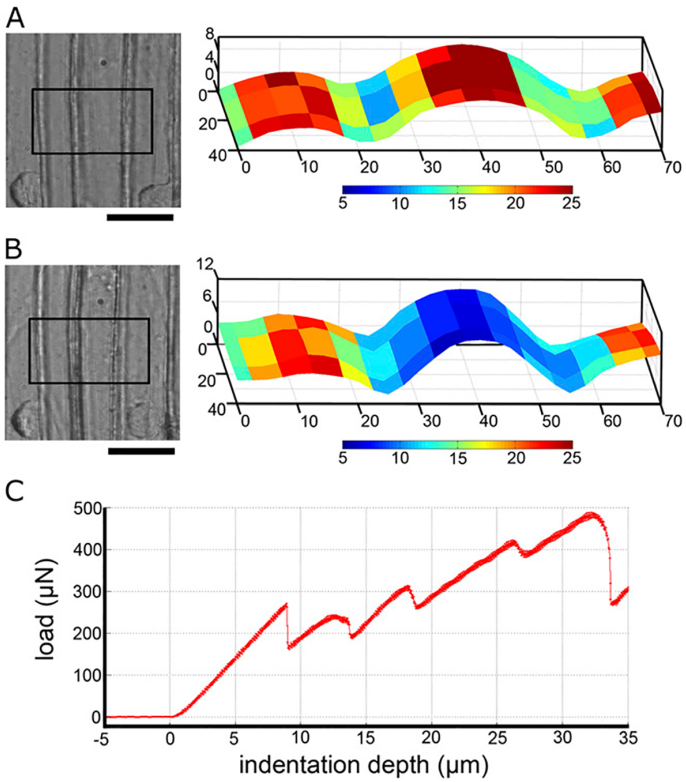

Figure 1.4: Puncture of the cell wall and effect of the release of turgor pressure on apparent stiffness. A, Light microscopy image and heat maps of the measured stiffness for the scanned region before puncture. B, Light microscopy image and stiffness map of the same region after puncturing the middle cell. The site of puncture is out of the image frame. Bars = 40 μm. C, Force-displacement signal during cell wall perforation. The first noticeable rupture occurs at around 9 μm indentation depth. Locally releasing turgor pressure by puncturing the top wall produced similar stiffness values as for plasmolysed cells after correcting for geometry. The color scale indicates apparent stiffness in Nm^{-1}. Figure reprinted with permission from reference [30]

Table 1.1: Comparative table of the different main approaches used to investigate cellular and subcellular mechanical properties, both in animal and plant cells.

Experimental approach	*Lateral resolution*	*Time resolution (i.e. time of one measurement)*	*Mechanical property*	*Cellular compartment studied*
Indentation methods e.g. Atomic Force Microscopy (AFM)	10 nm – 1 μm	1 – 10 min	Elastic modulus	Cell wall[24, 23, 21]
Fluorescence Recovery After Photobleaching (FRAP)	3 – 10 μm	1s – a few min for a single spatial coordinate	Translational diffusion coefficient "Translational" microviscosity	Plasma membrane[42] Endomembranes[43] Cytoplasm[44, 45]
Fluorescence anisotropy	200 nm – 1 μm	Tens of seconds for a single spatial coordinate 300-450s for an image	Fluorescence anisotropy Rotational correlation time "Rotational" microviscosity	Plasma membrane[46, 47] Cytoplasm[48]
Fluorescence Correlation Spectroscopy (FCS)	30 nm (STED-FCS) – 500 nm	10 s – 10 min for a single spatial coordinate	Translational diffusion coefficient "Translational" microviscosity Convection velocity Chemical reaction rate	Plasma membrane[49, 50, 51] Cytoplasm[52]
Particle Tracking Microrheology (PTM)	5 – tens of nm	10 s – 2 min for a single or a few discrete spatial coordinates	Complex shear modulus Translational diffusion coefficient "Translational" microviscosity	Cytoplasm[53, 54]
Fluorescence Lifetime Imaging Microscopy (FLIM) with molecular rotors	200 nm – 1 μm	180 - 450 s for an image	Fluorescence lifetime "Rotational" microviscosity	Plasma membrane[55] Endomembranes[56]
Ratiometric imaging	200 nm – 1 μm	A few seconds for an image	"Rotational" microviscosity	Plasma membrane
Single-molecule methods	200 nm – 1 μm	100 ms – a few seconds for an image	Cell-substrate adhesion forces	n.a.[57, 58, 59, 60]

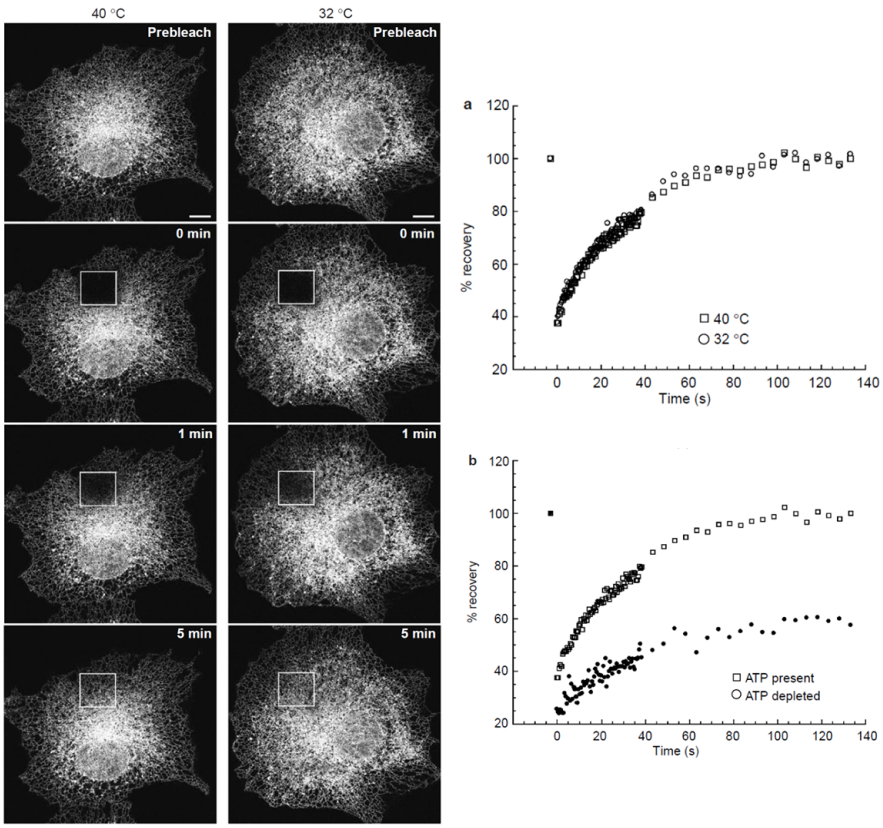

Figure 1.5: FRAP analysis of the diffusion of GFP-tagged vesicular stomatitis virus G (VSVG) protein within the endoplasmic reticulum membrane of COS cells. Cells were incubated at 40°C or 32°C in the presence of brefeldin A for 24h. Images were obtained before photobleaching and at the indicated time points after. The photobleached area is outlined by a box. Scale bars = 10 μm. The VSVG protein is misfolded at 40°C and correctly folded at 32°C. This data shows that both forms of protein are highly mobile in endoplasmic reticulum membranes. a, Evolution of fluorescence intensities (normalized to prebleach values) from FRAP analyses, plotted against time for VSVG–GFP in the endoplasmic reticulum, at 40°C or 32°C, in the presence of brefeldin A. b, Evolution of fluorescence intensities for VSVG–GFP in the endoplasmic reticulum, at 40°C, with or without ATP depletion. Figure reprinted with permission from reference [43]

FRAP relies on the rapid and irreversible photobleaching of fluorescently labelled molecules within a region of interest (ROI) using a laser pulse tuned to an

appropriate wavelength. Following the light pulse, the recovery of fluorescence intensity, mediated by diffusion of unbleached molecules into the ROI, is monitored to assess the diffusion rate of fluorescent species. By fitting the recovery curve with a mathematical model suitable in terms of system geometry and ROI size and shape[61], the mobile fraction of fluorophores and their diffusion coefficient can be determined.

FRAP has been extensively used in biological systems to study the diffusion dynamics of proteins in membranes. Consistent examples are the study of protein[62] and lipid[42] lateral diffusion in the plasma membrane of animal cells. Klein et al.[42] emphasized that internalization of the fluorescent probe, or non-specific staining, can easily corrupt the computed diffusion coefficient, as not only intra-membrane diffusion, but also diffusion of dye present in the vicinity of the membrane, will contribute to the overall fluorescence recovery.

This technique has also been employed to study the diffusional mobility of membrane components within endomembranes[43, 63] as well as to monitor events inherent to cell division and signalling, such as nuclear membrane dynamics during mitosis[64, 65]. An example of FRAP analysis within the endoplasmic reticulum membrane of COS cells is given in Figure 1.5. The determination of diffusion coefficients requires assumptions to be made so as to choose the appropriate mathematical model to fit the fluorescence recovery curve. In membranes, a 1D[63] or 2D[42] diffusion model is commonly used. In the case of more complex, tortuous membranes, this can lead to an underestimation of the diffusion coefficient.

FRAP has provided insight into cytoplasmic diffusion dynamics within diverse types of animal cells[44, 66, 67], and more recently Kingsley et al.[45] used FRAP to probe the cytoplasmic viscosity within tip-growing plant cells of *Physcomitrella* patens. By combining experimental and simulated FRAP, they highlighted the non-negligible sensitivity of FRAP curve fitting analysis to cell geometry, comparing the cytoplasmic diffusion coefficient in the same cell but at two different locations, namely the tip and shank of the cell.

Even though FRAP is a valuable technique for studying diffusion dynamics, it requires care when translating recovery dynamics into diffusion coefficients, or microviscosities. Moreover, the high laser intensities used can alter cellular

responses (e.g. by locally heating the cell). FRAP stays limited in its resolution, as a reduction of the radius of the bleached spot increases the error associated with the measurement. As a consequence, this technique cannot provide sufficient insight into the mechanical microdomains constituting the membrane, as the measurement is an average over a ROI larger than the typical domain size.

In a fluorescence anisotropy experiment, a fluorophore is excited by a polarized laser beam. The fluorescent emission thereby generated is recorded through a polarizer which allows to collect both vertically and horizontally polarized light separately. From those quantities, the anisotropy can be computed. In the case of time-resolved fluorescence anisotropy measurements, an anisotropy decay can be plotted. By fitting the decay curve with an exponential function, a rotational diffusion coefficient is deducted[68, 69]. Best et al.[70] determined the diffusion coefficient of small fluorophores in synthetic dimyristoylphosphatidylcholine bilayers. They concluded that to describe membrane fluidity three viscosities need to be considered; one viscosity for motions connected with positional displacements of lipid molecules (e.g. translation and rotation of proteins and small molecules such as lipids), another viscosity for motions which are coupled to orientational fluctuations of lipid molecules (e.g. wobbling of small molecules), and a third viscosity for motions which are not hindered by lipid molecules (e.g. the rotation of small molecules).

Fluorescence anisotropy measurements have been performed in live cell membranes to measure membrane fluidity[47] and lipid order[71], but also in other cellular compartments, e.g. to measure the cytoplasmic viscosity of fibroblasts[48] the one of B cells[68], or the vacuolar viscosity of yeast cells[72]. These measurements provide insight into fluorophore rotational mobility, but spatial variations of anisotropy in systems as complex as living cells are in general difficult to interpret accurately without performing other types of experiments. To circumvent this limitation, fluorescence anisotropy measurements are usually combined with other techniques to gather more information on diffusion processes. For example, Swaminathan et al.[44] used FRAP combined with fluorescence anisotropy measurements with a GFP protein to measure cytoplasmic diffusion in CHO cells. They showed that solute translational mobility in the cytoplasm is determined primarily by the crowding density. In several studies,

fluorescence anisotropy rotational correlation time imaging has also been combined with Fluorescence Lifetime Imaging Microscopy (FLIM)[68, 46, 73], as it can provide valuable complementary information on the viscosity of the probe environment, or allow to distinguish viscosity variations from binding effects.

Another technique to monitor cellular viscosity and translational diffusion is FCS. FCS measures the spatio-temporal correlation of individual fluorophores with themselves in a femtoliter observation volume. It is therefore especially useful for characterising small dynamic systems. By fitting the correlation decay with a suitable model depending on the situation[74], one can compute the average diffusion time, the convection velocity, or the chemical reaction rate constants of molecules through the studied volume. FCS has mainly been used in the study of lipid fluidity and membrane viscosity, to monitor the diffusion of membrane microdomain markers[49, 50], which provided evidence for the existence of microdomains in the plasma membrane. Other applications of FCS include the study of microdomain formation[75, 76, 77], membrane-associated proteins diffusion and segregation[78, 79] or protein-molecule interactions[80, 81]. A few studies used FCS to probe other cellular compartments. For instance, Berland et al.[52] showed that two-photon FCS can be used to measure the cytoplasmic microviscosity of mouse fibroblast cells, and Wachsmuth et al.[82] investigated the diffusion characteristics of GFP mutants in the nuclei of AT1 and COS7 cells. While useful to probe translational diffusion at discrete locations in cells, FCS remains a complex technique that involves long measurements times. When probing slow membrane dynamics for instance, a loss of focus in time can lead to enlargement of the detection area, and membrane motions can lead to distortions of the correlation curves. Moreover this technique requires low fluorophore concentrations and is sensitive to photobleaching[83].

Finally, mechanical and more invasive techniques, such as particle-tracking microrheology (PTM), have been used to characterize the cytoplasm of live animal cells in discrete locations of the cell[84, 85, 53, 86, 87]. An example is given in Figure 1.6. The motion of 10^{-1}-100 μm exogenous particles, freely diffusing or actively dragged under the action of an external magnetic field, is monitored optically and provides information on local densities and configurations of the cytoplasm and cytoskeleton. The dynamics of particle motion are usually de-

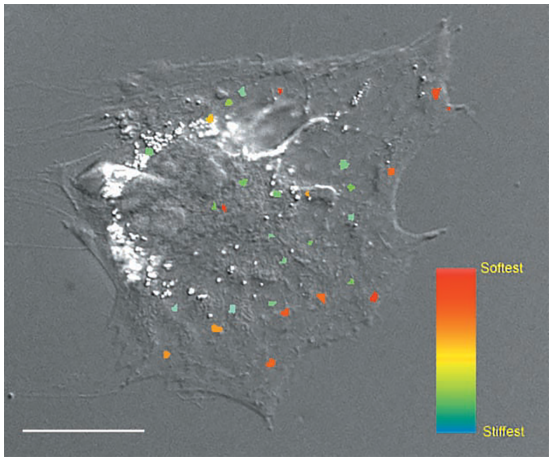

Figure 1.6: Multiple-particle microrheology mapping of a living cell. A differential interference contrast micrograph was superimposed to a fluorescence micrograph of the trajectories of microinjected microspheres. The trajectories, which were recorded for 20 s, were transformed into local compliances, which were normalized by the maximum compliance and color coded between red (most compliant microenvironment within the cell) to blue (least compliant microenvironment). For the measurement 0.1 μm-diameter carboxylated microspheres. Scale bar, 30 μm. Figure reprinted with permission from reference [53]

scribed by the time-dependent mean-square-displacement, calculated from the three-dimensional trajectories of the particles' centroids. In the active approach, or in the passive approach applied to systems assumed to be at equilibrium, the mean-square-displacement provides a direct measurement of the diffusion coefficient and complex shear modulus of the medium. However, results in cells from studies using single-particle versions of the two approaches yield shear moduli differing by orders of magnitude and exhibiting qualitatively different frequency dependencies[88, 89, 90]. These results are further limited by ambiguities associated with tracer boundary conditions, medium heterogeneity, and the applicability of the Fluctuation Dissipation theorem[87].

A non-invasive particle tracking method, replacing exogenous beads with endogenous subcellular markers (e.g. lipid-storage granules) has been used to investigate the viscoelastic properties in the cytoplasm of frog oocytes[91]. However, extra care has to be taken when translating mean square displacements into

diffusion coefficients; the particles must be spherical and rigid-like beads to satisfy Stokes' law, and the surface chemistry as well as exact size of the particles should be known. Even though this technique requires low collection times (e.g. 10-20 s to measure the frequency-dependent viscoelastic moduli over two decades in frequency), it does not allow to resolve a microviscosity pattern at the pixel size resolution. All these techniques can provide insight into cellular processes but methods for direct local observations at high resolution are still needed.

In parallel to the diffusion-related viscous properties of the plasma membrane, investigating its elastic properties turns out to be challenging in plant cells. Numerous studies conducted on animal cells investigated membrane tension using micropipette aspiration[92, 93]. This technique is however not applicable to plant cells where the membrane is protected by a stiff cell wall. In that context, non-invasive fluorescence imaging techniques, such as FLIM, appear as a logical solution. For example, Colom et al.[94] developped a planarizable fluorescent probe, FliptR, to monitor changes in membrane tension. Upon increased tension, FliptR planarizes and its fluorescence lifetime increases, giving an easy readout for spatio-temporal variations in membrane tension.

In the next section we focus on molecular rotors in combination with imaging techniques such as FLIM or ratiometric imaging. We show why this approach is a promising alternative to follow cellular processes in time, with high spatial resolution.

1.4 Molecular rotors applied to cell mechanobiology

One of the great advances from the field of mechanochemistry in the past decade, providing a basis for progress in mechanobiology, is the development of molecular probes in which mechanical stress elicits a detectable optical signal. Such optical mechanoprobes can aid in the visualization of mechanical patterns with molecular precision, without necessitating external perturbation of the organism or biological structure. Molecular mechanoprobes come in many different flavors and operate on the basis of different mechanisms, such as bond rupture sensors (e.g. spiropyran[95, 96, 97], dioxetane[98, 99]), molecular elastic springs (e.g. conjugated polymers[100], DNA-unzipping force sensors[57, 59]), or mo-

lecular rotors, in which a molecular rotation couples to the mechanics of its surroundings. Molecular rotors constitute 'passive' probes, in the sense that they do not require active stress generation, while the other examples are 'active' probes that only function under the action of actively generated stresses. In the previous sections we described existing techniques that have been employed to probe the mechanical properties at the cellular level, as well as their drawbacks. In this section we introduce molecular rotors as choice candidates to map microviscosity patterns at the cellular and subcellular levels. This constitute the starting point of this thesis.

Molecular rotors are small fluorophores whose fluorescence emission intensity vary in response to changes in the microviscosity of their direct environment. This change in emission occurs through the competition between the two main energy decay paths of the molecules; a radiative decay of the excited state, and an intramolecular rotation that changes the nature of the electronically excited state responsible for photoemission. The majority of molecular rotors exhibit a Twisted Intramolecular Charge Transfer (TICT) mechanism[56, 101]. TICT is an electron transfer process that occurs upon photoexcitation in molecules that usually consist of a donor and acceptor part linked by a single bond. For these molecules, TICT state formation takes place by photoinduced charge transfer from the donor to the acceptor unit with subsequent intramolecular rotation. This new adopted conformation is lower in energy, and decay from this charge transfer state to the ground state leads to a decreased emission intensity, and to a decreased fluorescence lifetime. As the rate of rotation is dependent on the local free volume available, those molecules can be used to probe microviscosity; the intramolecular rotation will become more hindered as the solvent viscosity increases (i.e. as the molecular free volume decreases), which will result in an increased quantum yield and fluorescence lifetime. It is important to highlight that the charge separation associated with TICT formation is accompanied by an increased dipole moment, which can lead to a more or less pronounced polarity sensitivity of fluorescence[101, 102]. A more polar solvent stabilizes the TICT state further, and thus favours relaxation from that state, resulting in a lower quantum yield as well as a lower fluorescence lifetime.

The quantum yield Φ and fluorescence lifetime τ of fluorescent molecular

rotors are defined by Equation (1.2)

$$\Phi = \frac{k_r}{k_r + k_{nr}} = k_r \tau \tag{1.2}$$

where k_r and k_{nr} are the radiative and non-radiative decay rate constants respectively. They can be expressed as a function of viscosity through the equations first derived by Förster and Hoffman[103];

$$\Phi = z\eta^{\alpha} \tag{1.3}$$

$$\tau = \frac{z\eta^{\alpha}}{k_r} \tag{1.4}$$

$$log\tau = log\frac{z}{k_r} + \alpha log\eta \tag{1.5}$$

where z and α are constants, and η is the viscosity.

Equation (1.5) highlights a direct linear relation between the fluorescence lifetime and the decimal logarithm of the viscosity, which can be used to determine viscosity from experimentally determined lifetimes. However this equation is valid in a limited range of intermediate viscosities. Indeed, at low viscosities the quantum yield becomes solvent-independent, and at high viscosities the quantum yield plateaus as the radiative relaxation of the excited state predominates over non-radiative processes. The optimal range of viscosity sensitivity varies according to the nature of the molecular rotor and the mechanism responsible for its viscosity-sensitive response. The advantage of using fluorescence lifetime over quantum yield to determine microviscosity (Equation (1.5)) resides in the independence of the fluorescence lifetime over variations in fluorophore concentration. On the other hand, fluorophore concentration has a major effect on fluorescence intensity. Thus, when measuring fluorescence intensity throughout a heterogeneous sample, it becomes impossible to decouple changes in concentration to actual changes in quantum yield.

Time-correlated single-photon counting (TCSPC)-FLIM is commonly used to achieve spatially resolved imaging of fluorescence lifetimes in biological samples. In order to recreate a 2D map of fluorescence lifetimes at pixel resolution, a sample incubated with the molecular rotor is repeatedly scanned by a high-

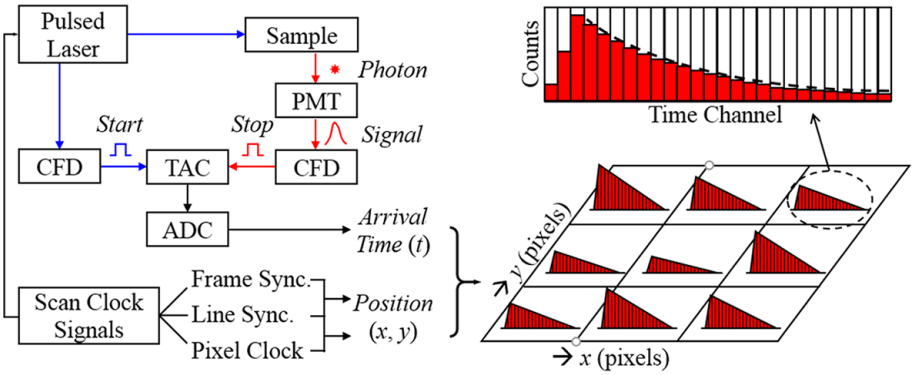

Figure 1.7: Principle of TCSPC-FLIM. CFD: constant fraction discriminator; TAC: time-to-amplitude converter; ADC: analog-to-digital converter; Sync.: synchronization. A photon distribution n(x, y, t) is obtained and converted into FLIM image with data analysis, by fitting the fluorescence decay in each pixel with an exponential function. Figure reprinted with permission from reference [104]

repetition rate pulsed laser beam, and a detector detects single photons of the fluorescence signal emitted by the sample. Figure 1.7 illustrates the principle of a TCSPC-FLIM measurement to recreate a fluorescence-lifetime-based image. Each photon is characterized by its time in the laser pulse period and the coordinates of the laser spot in the scanning area in the moment of its detection. The recording process builds up a photon distribution over these parameters. The result is given by an array of pixels, each containing a fluorescence decay curve in a large number of time channels. Each curve can be fitted with an exponential function so as to determine the characteristic intensity decay time, i.e. the fluorescence lifetime [104, 56].

The success of a FLIM measurement relies on the availability of suitable molecular rotors that exhibit high sensitivity to viscosity variations (large α, Equation (1.5)), as well as high quantum yields to allow for fast signal accumulation. Figure 1.8 shows examples of molecular rotors. The photophysical properties of molecular rotors based on the 1,4-dimethylaminobenzonitrile (DMABN) design have been investigated extensively[107, 108, 109]. DMABN is characterized by an excitation wavelength centred on 300 nm, and a dual fluorescence emission ranging from 340 to 460 nm. The low wavelength range of these dyes significantly

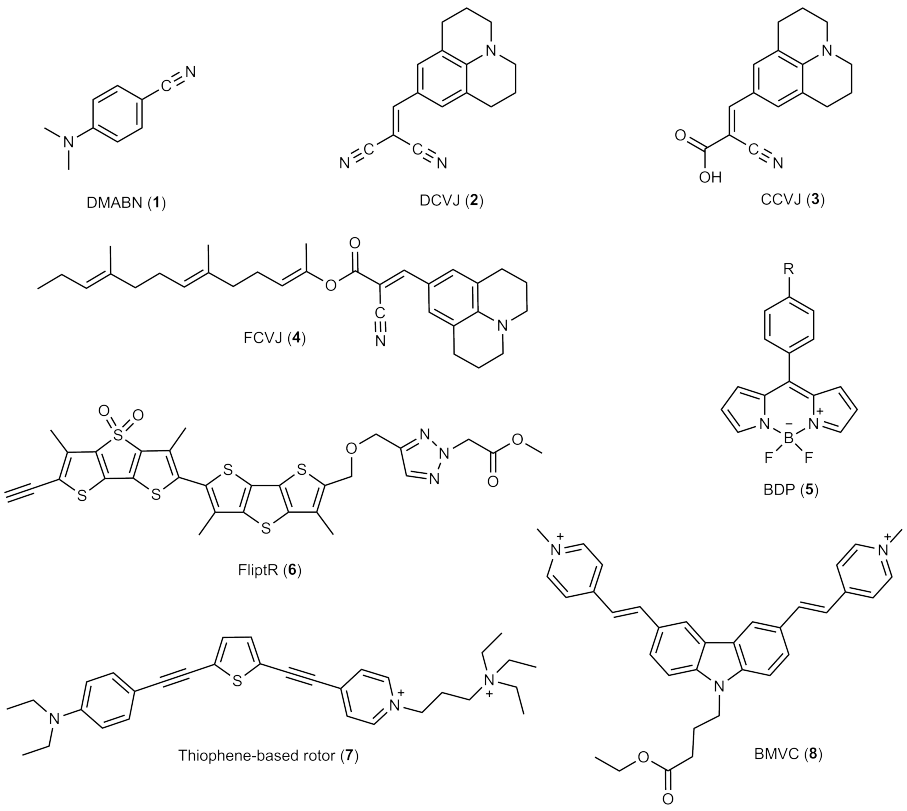

Figure 1.8: Structures of commonly used TICT molecular rotors: p-dimethylaminobenzonitrile (DMABN) (1), 9-(2,2-dicyanovinyl)julolidine (DCVJ) (2), 9-(2-carboxy-2-cyanovinyl)julolidine (CCVJ) (3), (farnesyl-(2-carboxy-2-cyanovinyl)-julolidine (FCVJ) (4). Structures of more recent rotor designs: 4,4'-difluoro-4-bora-3a,4a-diaza-s-indacene (BODiPY) based rotors (5), FliptR[94] (6), a thiophene-based rotor[105] (7) and ethyl-4-[3,6-bis(1-methyl-4-vinylpyridium iodine)-9H-carbazol-9-yl)] butanoate (BMVC)[106] (8)

limit their application in biological medium. More importantly, their fluorescence properties have been shown to vary significantly depending on solvent polarity, making it impossible to differentiate between viscosity and polarity effects[102, 108].

Other rotors have been developed to circumvent these limitations. In particular, julolidine-based dyes such as 9-(2,2-dicyanovinyl)julolidine (DCVJ), 9-(2-

carboxy-2-cyanovinyl)julolidine (CCVJ), or (farnesyl-(2-carboxy-2-cyanovinyl)-julolidine (FCVJ) have been employed to investigate the increase of membrane fluidity in endothelial cells upon fluid shear stress[110, 111, 112]. These rotors are less sensitive to polarity compared to the DMABN analogues, and their excitation and emission wavelength range are compatible with imaging in cells[101, 102]. However their short excited state lifetime (i.e. 10-100 ps) does not fall in the accessible detection range of TCSPC-FLIM. Therefore the use of these probes is restricted to intensity imaging, and local variations in probe concentration have to be accounted for.

More recently, rotors based on the 4,4'-difluoro-4-bora-3a,4a-diaza-s-indacene (BODIPY) unit have emerged as FLIM-compatible microviscosity probes for biological systems; these probes can be excited with a standard 488 nm or 514 nm laser line, and usually emit in the green region with long fluorescence lifetimes (typically ranging from 500 ps to a few ns). The high sensitivity of their quantum yield and fluorescence lifetime upon viscosity variations highlights them as potential candidates to probe microviscosity in cells[73]. Moreover, they are intrinsically less sensitive to polarity than other molecular rotors as they do not follow an ICT type of mechanism. Indeed, in the case of BODIPY-based rotors, the non-radiative decay pathway is not activated by a charge transfer but by a structural distorsion of the dipyrrin unit, accompanied by a rotation of the phenyl unit into the plane of the dipyrrin core[113, 114]. As a result the change of dipolar moment is significantly smaller and the polarity sensitivity weaker.

BODIPY-based rotors have been used in combination with FLIM to measure microviscosity in the plasma membrane[55], endomembranes[73], or mitochondrial membrane[115] of cultured cells, as well as in vivo, in the connecting tissues of subcutaneous tumors in mice[116].

Other molecular rotor designs have been developed, essentially to probe membrane fluidity and lipid order. Colom et al.[94] developed a planarizable fluorescent probe made of two dithienothiophene units connected through a single covalent bond, FliptR, to monitor changes in membrane tension by changing its fluorescent lifetime as a function of the twist angle between these two units. Dent et al.[105] studied a thiophene-based molecular rotor to probe microviscosity in the plasma membrane of diverse live animal cells, supposed to parti-

tion equally in ordered and disordered lipid domains and allow full membrane mapping. Zou et al.[106] designed a molecular rotor composed of two positively charged 1-methyl-4-vinylpyridium components to image microviscosity variation in mitochondria during mitophagic elimination. When a perturbed mitochondria fuses with a lysosome to form an autolysosome during the mitophagy process, the rotation of the rotor anchored to the mitochondrial membrane gets hindered, resulting in an increased fluorescence lifetime.

Even though FLIM offers the possibility to image without correcting for the spatial variations in dye concentration, TCSPC is a relatively slow acquisition process. Enough photon counts need to be collected in each pixel in order to obtain a well resolved fluorescence intensity decay to fit for lifetime determination. Those photons are collected at a rate far below the repetition rate of the excitation laser, to prevent detector saturation and fluorescence signal pile-up. As a result, the acquisition of a complete Fluorescence Lifetime map takes one to several minutes, which limits the processes that can be monitored in time.

In that context, ratiometric molecular rotors could allow for a much faster measurement with a simple confocal microscope setup, while suppressing the dye concentration dependency. A few examples can be found in literature; Luby-Phelps et al.[120] used the indocyanine dyes Cy3 and Cy5, covalently attached to separate carrier macromolecules, as a dye pair to probe cytoplasmic microviscosity in CV1 and PtK1 cells; Cy3 acts as a molecular rotor with viscosity-dependent nonradiative deactivation channel, and the relatively rigid Cy5 acts as reference fluorophore. Kuimova et al.[119] developed a porphyrin-dimer-based molecular rotor that play the dual role of microviscosity probe and photosentisizer, to image viscosity variations during photoinduced cell death in the endocytotic vesicles of CHO and HeLa cells (Fig. 1.9, (1)).

BODIPY-based ratiometric probes have been synthesized by covalently binding a BODIPY-based rotor to a reference dye (e.g. coumarin[117], fluorene[118], Fig. 1.9 (2)&(3)) whose quantum yield does not vary with microviscosity. In their study, Xochitiotzi-Flores et al.[118] extended the conjugation length between the rotor and the reference fluorene unit to inhibit the ICT process and have little to no polarity dependence. Indeed, fluorene being an electron donor, and the BODIPY core an electron acceptor, connecting those units together directly through

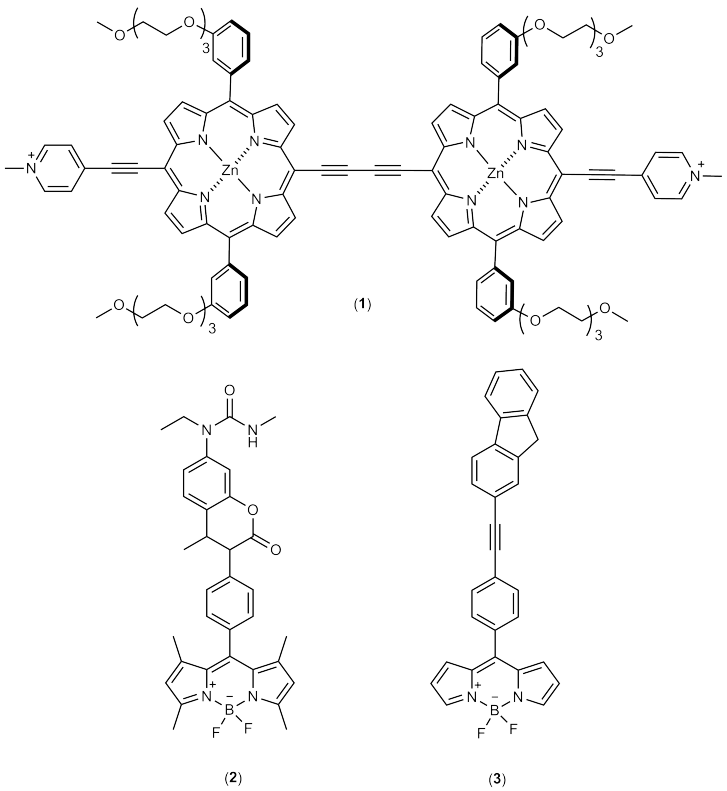

Figure 1.9: Examples of viscosity-sensitive ratiometric probes: (1)[117], (2)[118] and (3)[119].

the phenyl ring (π-conjugated linker) could allow for charge transfer. Yang et al.[117] obtained negligible to no dependence upon polarity when connecting a BODIPY-based rotor to a coumarin unit via a single covalent bond.

All these investigations have mainly focused on the study of membrane fluidity in animal cells, leaving other cellular compartment unexplored. Our interest is to develop a toolbox of molecular rotors applied to plant cells, or more generally to walled cells, to map microviscosity not only within the membranes, but throughout the whole cell, across compartments of very different physicochemical compositions.

1.5 Outline

The content of this thesis is divided as follows; in **Chapter 2**, we provide a technical overview of the recipes used throughout this thesis for the synthesis of fluorescent molecular probes. Concise recipes are provided, along with design and synthesis considerations for BODIPY-based molecular rotors.

In **Chapter 3** we introduce a set of molecular rotors designed to target the four main compartments in plant cells (i.e. vacuole, cytoplasm, membrane and cell wall). Our results show that we can easily implement those rotors in *Arabidopsis* root and leaf so as to map microviscosity patterns throughout the cells with a good spatio-temporal resolution.

In **Chapter 4** we challenge the notion of 'microviscosity' and we discuss the potential factors controlling the rotation rate of BODIPY-based molecular rotors in plant cells. We conclude that fluorescence lifetime mapping with those rotors gives information on the relative confinements and crowding density within cells, but that care should be taken when wanting to translate lifetime into absolute microviscosity values.

Chapter 5 illustrates the use of the cell-wall targeting molecular rotor in combination with a plasma membrane chemical polarity probe, to study the structural effects of mechanical and chemical stress on a model plant pathogen, *Phytophthora infestans*, during invasion.

References

[1] *Mechanical Integration of Plant Cells and Plants*. Signalling and Communication in Plants. Springer-Verlag Berlin Heidelberg, 2011.

[2] Donald E. Ingber. Tensegrity-based mechanosensing from macro to micro. *Progress in Biophysics and Molecular Biology*, 97:163–179, 2008.

[3] Ning Wang, Jessica D. Tytell, and Donald E. Ingber. Mechanotransduction at a distance: mechanically coupling the extracellular matrix with the nucleus. *Nat. Rev. Mol. Cell Biol.*, 10:75–82, 2009.

[4] Magalie Uyttewaal, Agata Burian, Karen Alim, Benoît Landrein, Dorota Borowska-Wykret, Annick Dedieu, Alexis Peaucelle, Michal Ludynia, Jan Traas, Arezki Boudaoud, Dorota Kwiatkowska, and Olivier Hamant. Mechanical stress acts via katanin to amplify differences in growth rate between adjacent cells in arabidopsis. *Cell*, 149:439–451, 2012.

[5] Behruz Bozorg, Pawel Krupinski, and Henrik Jönsson. Stress and strain provide positional

and directional cues in development. *PLOS Computational Biology*, 10:e1003410–e1003410, 2014.

[6] Olivier Hamant and Elizabeth S. Haswell. Life behind the wall: sensing mechanical cues in plants. *BMC Biology*, 15, 2017.

[7] Arun Sampathkumar, An Yan, Pawel Krupinski, and Elliot M. Meyerowitz. Physical forces regulate plant development and morphogenesis. *Curr. Biology*, 24:R475–R483, 2014.

[8] Carl-Philipp Heisenberg and Yohanns Bellaïche. Forces in tissue morphogenesis and patterning. *Cell*, 153:948–962, 2013.

[9] Ewa K. Paluch, Celeste M. Nelson, Nicolas Biais, Ben Fabry, Jens Moeller, Beth L. Pruitt, Carina Wollnik, Galina Kudryasheva, Florian Rehfeldt, and Walter Federle. Mechanotransduction: use the force(s). *BMC Biology*, 13, 2015.

[10] Marion Louveaux, Jean-Daniel Julien, Vincent Mirabet, Arezki Boudaoud, and Olivier Hamant. Cell division plane orientation based on tensile stress in arabidopsis thaliana. *Proc. Natl. Acad. Sci.*, 113:e4294–e4303, 2016.

[11] Olivier Hamant, Marcus G. Heisler, Henrik Jönsson, Pawel Krupinski, Magalie Uyttewaal, Plamen Bokov, Francis Corson, Patrik Sahlin, Arezki Boudaoud, Elliot M. Meyerowitz, Yves Couder, and Jan Traas. Developmental patterning by mechanical signals in arabidopsis. *Science*, 322:1650–1655, 2008.

[12] P.B. Green and A. King. A mechanism for the origin of specifically oriented textures in development with special reference to nitella wall texture. *Australian Journal of Biological Sciences*, 19:421 – 438, 1966.

[13] Janet Braam. In touch: plant responses to mechanical stimuli. *New Phytologist*, 165:373–389, 2005.

[14] Naomi Nakayama, Richard S. Smith, Therese Mandel, Sarah Robinson, Seisuke Kimura, Arezki Boudaoud, and Cris Kuhlemeier. Mechanical regulation of auxin-mediated growth. *Curr. Biology*, 22:1468–1476, 2012.

[15] Marta Laskowski, Verônica A. Grieneisen, Hugo Hofhuis, Colette A. ten Hove, Paulien Hogeweg, Athanasius F. M. Marée, and Ben Scheres. Root system architecture from coupling cell shape to auxin transport. *PLoS Biol.*, 6:e307, 2008.

[16] Frank B. Salisbury and Raymond M. Wheeler. Interpreting plant responses to clinostating. *Plant Physiol.*, 67:677–685, 1981.

[17] Daniel J. Cosgrove. Growth of the plant cell wall. *Nat. Rev. Mol. Cell Biol.*, 6:850–861, 2005.

[18] Nicholas C. Carpita. Structure and biogenesis of the cell wall of grasses. *Annual Review of Plant Physiology and Plant Molecular Biology*, 47:445–476, 1996.

[19] Nicholas C. Carpita and David M. Gibeaut. Structural models of primary cell walls in flowering plants: consistency of molecular structure with the physical properties of the walls during growth. *The Plant Journal*, 3:1–30, 1993.

[20] Pascale Milani, Siobhan A. Braybrook, and Arezki Boudaoud. Shrinking the hammer: micromechanical approaches to morphogenesis. *Journal of Experimental Botany*, 64:4651–4662, 2013.

[21] Alexis Peaucelle, Siobhan A. Braybrook, Laurent Le Guillou, Emeric Bron, Cris Kuhlemeier,

and Herman Höfte. Pectin-induced changes in cell wall mechanics underlie organ initiation in arabidopsis. *Curr. Biology*, 21:R840–R841, 2011.

[22] David C. Lin, Emilios K. Dimitriadis, and Ferenc Horkay. Robust strategies for automated afm force curve analysis–i. non-adhesive indentation of soft, inhomogeneous materials. *J. Biomech. Eng.*, 129:430–440, 2007.

[23] Pascale Milani, Vincent Mirabet, Coralie Cellier, Frédérique Rozier, Olivier Hamant, Pradeep Das, and Arezki Boudaoud. Matching patterns of gene expression to mechanical stiffness at cell resolution through quantitative tandem epifluorescence and nanoindentation. *Plant Physiology*, 165:1399–1408, 2014.

[24] Pascale Milani, Maryam Gholamirad, Jan Traas, Alain Arnéodo, Arezki Boudaoud, Françoise Argoul, and Olivier Hamant. In vivo analysis of local wall stiffness at the shoot apical meristem in arabidopsis using atomic force microscopy. *The Plant Journal*, 67:1116–1123, 2011.

[25] Anwesha N. Fernandes, Xinyong Chen, Colin A. Scotchford, James Walker, Darren M. Wells, Clive J. Roberts, and Nicola M. Everitt. Mechanical properties of epidermal cells of whole living roots of arabidopsis thaliana: An atomic force microscopy study. *Phys. Rev. E*, 85:021916, 2012.

[26] Ksenija Radotic, Charles Roduit, Jasna Simonovic, Patricia Hornitschek, Christian Fankhauser, Dragosav Mutavdzic, Gabor Steinbach, Giovanni Dietler, and Sandor Kasas. Atomic force microscopy stiffness tomography on living arabidopsis thaliana cells reveals the mechanical properties of surface and deep cell-wall layers during growth. *Biophys. J.*, 103:386–394, 2012.

[27] Anja Geitmann and Elodie Parre. The local cytomechanical properties of growing pollen tubes correspond to the axial distribution of structural cellular elements. *Sexual Plant Reproduction*, 17:9–16, 2004.

[28] Jean-François Bolduc, Laurent J. Lewis, Carl-Éric Aubin, and Anja Geitmann. Finite-element analysis of geometrical factors in micro-indentation of pollen tubes. *Biomechanics and Modeling in Mechanobiology*, 5:227–236, 2006.

[29] Hannes Vogler, Christian Draeger, Alain Weber, Dimitris Felekis, Christof Eichenberger, Anne-Lise Routier-Kierzkowska, Aurelien Boisson-Dernier, Christoph Ringli, Bradley J. Nelson, Richard S. Smith, and Ueli Grossniklaus. The pollen tube: a soft shell with a hard core. *The Plant Journal*, 73:617–627, 2013.

[30] Anne-Lise Routier-Kierzkowska, Alain Weber, Petra Kochova, Dimitris Felekis, Bradley J. Nelson, Cris Kuhlemeier, and Richard S. Smith. Cellular force microscopy for in vivo measurements of plant tissue mechanics. *Plant Physiology*, 158:1514–1522, 2012.

[31] Hannes Vogler, Dimitrios Felekis, Bradley J. Nelson, and Ueli Grossniklaus. Measuring the mechanical properties of plant cell walls. *Plants*, 4:167–182, 2015.

[32] Charlotte Kirchhelle, Daniel Garcia-Gonzalez, Niloufer G. Irani, Antoine Jérusalem, and Ian Moore. Two mechanisms regulate directional cell growth in arabidopsis lateral roots. *Elife.*, 8:e47988, 2019.

[33] Kareem Elsayad, Stephanie Werner, Marçal Gallemi, Jixiang Kong, Edmundo R.

Sánchez Guajardo, Lijuan Zhang, Yvon Jaillais, Thomas Greb, and Youssef Belkhadir. Mapping the subcellular mechanical properties of live cells in tissues with fluorescence emission-brillouin imaging. *Sci. Signal*, 9:rs5, 2016.

[34] František Baluška, Jozef Šamaj, Przemyslaw Wojtaszek, Dieter Volkmann, and Diedrik Menzel. Cytoskeleton-plasma membrane-cell wall continuum in plants. emerging links revisited. *Plant Physiol.*, 133:482–491, 2003.

[35] Julien Alassimone, Sadaf Naseer, and Niko Geldner. A developmental framework for endodermal differentiation and polarity. *Proc. Natl. Acad. Sci.*, 107:5214–5219, 2010.

[36] Daniele Roppolo and Niko Geldner. Membrane and walls: who is master, who is servant? *Curr. Opin. Plant Biol.*, 15:608–617, 2012.

[37] Sebastian Wolf, Kian Hématy, and Herman Höfte. Growth control and cell wall signaling in plants. *Annu. Rev. Plant Biol.*, 63:381–407, 2012.

[38] Blaire J. Steinwand and Joseph J. Kieber. The role of receptor-like kinases in regulating cell wall function. *Plant Physiol.*, 153:479–484, 2010.

[39] Björn F. Lillemeier, Janet R. Pfeiffer, Zurab Surviladze, Bridget S. Wilson, and Mark M. Davis. Plasma membrane-associated proteins are clustered into islands attached to the cytoskeleton. *Proc. Natl. Acad. Sci.*, 103:18992–18997, 2006.

[40] Linda J. Pike. Rafts defined: a report on the keystone symposium on lipid rafts and cell function. *J. Lipid Res.*, 47:1597–1598, 2006.

[41] Nils C. Gauthier, Thomas A. Masters, and Michael P. Sheetz. Mechanical feedback between membrane tension and dynamics. *Trends Cell Biol.*, 22:527–535, 2012.

[42] Christophe Klein, Thierry Pillot, Jean Chambaz, and Beatrice Drouet. Determination of plasma membrane fluidity with a fluorescent analogue of sphingomyelin by frap measurement using a standard confocal microscope. *Brain Res. Brain Res. Protoc.*, 11:46–51, 2003.

[43] Sarah Nehls, Erik L. Snapp, Nelson B. Cole, Kristien J.M. Zaal, Anne K. Kenworthy, Theresa H. Roberts, Jan Ellenberg, John F. Presley, Eric Siggia, and Jennifer Lippincott-Schwartz. Dynamics and retention of misfolded proteins in native er membranes. *Nat. Cell Biol.*, 2:288–295, 2000.

[44] R. Swaminathan, Cathy P. Hoang, and A. S. Verkman. Photobleaching recovery and anisotropy decay of green fluorescent protein gfp-s65t in solution and cells: cytoplasmic viscosity probed by green fluorescent protein translational and rotational diffusion. *Biophys. J.*, 72:1900–1907, 1997.

[45] James L. Kingsley, Jeffrey P. Bibeau, Zhilu Chen, Xinming Huang, Luis Vidali, and Erkan Tuzel. Probing cytoplasmic viscosity in the confined geometry of tip-growing plant cells via frap. *bioRxiv preprint*, 2016.

[46] James A. Levitt, Penny E. Morton, Gilbert O. Fruhwirth, George Santis, Pei-Hua Chung, Maddy Parsons, and Klaus Suhling. Simultaneous frap, flim and faim for measurements of protein mobility and interaction in living cells. *Biomed. Opt. Express*, 6:3842–3854, 2015.

[47] Jean-Georges Kuhry, Guy Duportail, Christian Bronner, and Gilbert Laustriat. Plasma membrane fluidity measurements on whole living cells by fluorescence anisotropy of trimethylammoniumdiphenylhexatriene. *Biochim. Biophys Acta.*, 845:60–67, 1985.

[48] Kiyohide Fushimi and A. S. Verkman. Low viscosity in the aqueous domain of cell cytoplasm measured by picosecond polarization microfluorimetry. *J. Cell Biol.*, 112:719–725, 1991.

[49] Christian Eggeling, Christian Ringemann, Rebecca Medda, Günter Schwarzmann, Konrad Sandhoff, Svetlana Polyakova, Vladimir N. Belov, Birka Hein, Claas von Middendorff, Andreas Schönle, and Stefan W. Hell. Direct observation of the nanoscale dynamics of membrane lipids in a living cell. *Nature*, 457:1159–1162, 2009.

[50] Veronika Mueller, Christian Ringemann, Alf Honigmann, Günter Schwarzmann, Rebecca Medda, Marcel Leutenegger, Svetlana Polyakova, Vladimir N. Belov, Stefan W. Hell, and Christian Eggeling. Sted nanoscopy reveals molecular details of cholesterol- and cytoskeleton-modulated lipid interactions in living cells. *Biophys. J.*, 101:1651–1660, 2011.

[51] Jonas Ries, Salvatore Chiantia, and Petra Schwille. Accurate determination of membrane dynamics with line-scan fcs. *Biophys. J.*, 96:1999–2008, 2009.

[52] Keith M. Berland, Peter T. C. So, and Enrico Gratton. Two-photon fluorescence correlation spectroscopy: method and application to the intracellular environment. *Biophys. J.*, 68:694–701, 1995.

[53] Yiider Tseng, Thomas P. Kole, and Denis Wirtz. Micromechanical mapping of live cells by multiple-particle-tracking microrheology. *Biophys. J.*, 83:3162–3176, 2002.

[54] Thierry Savin and Patrick S. Doyle. Static and dynamic errors in particle tracking microrheology. *Biophys. J.*, 88:623–638, 2005.

[55] Ismael López-Duarte, Thanh Truc Vu, M. Angeles Izquierdo, James A. Bull, and Marina K. Kuimova. A molecular rotor for measuring viscosity in plasma membranes of live cells. *Chem. Commun.*, 50:5282–5284, 2014.

[56] Marina K. Kuimova. Mapping viscosity in cells using molecular rotors. *Phys. Chem. Chem. Phys.*, 14:12671–12686, 2012.

[57] Yun Zhang, Chenghao Ge, Cheng Zhu, and Khalid Salaita. Dna-based digital tension probes reveal integrin forces during early cell adhesion. *Nat. Comm.*, 5, 2014.

[58] Yang Liu, Kevin Yehl, Yoshie Narui, and Khalid Salaita. Tension sensing nanoparticles for mechano-imaging at the living/nonliving interface. *J. Am. Chem. Soc.*, 135:5320–5323, 2013.

[59] Palash K. Dutta, Yun Zhang, Aaron T. Blanchard, Chenghao Ge, Muaz Rushdi, Kristin Weiss, Cheng Zhu, Yonggang Ke, and Khalid Salaita. Programmable multivalent dna-origami tension probes for reporting cellular traction forces. *Nano Lett.*, 18:4803–4811, 2018.

[60] Melis Goktas and Kerstin G. Blank. Molecular force sensors: From fundamental concepts toward applications in cell biology. *Adv. Mater. Interfaces*, 4:1600441, 2017.

[61] Jennifer Lippincott-Schwartz, Erik Snapp, and Anne Kenworthy. Studying protein dynamics in living cells. *Nat. Rev. Mol. Cell Biol.*, 2:444–456, 2001.

[62] Manfred Frick, Katja Schmidt, and Benjamin J. Nichols. Modulation of lateral diffusion in the plasma membrane by protein density. *Curr. Biology*, 17:462–467, 2007.

[63] Nelson B. Cole, Carolyn L. Smith, Noah Sciaky, Mark Terasaki, Michael Edidin, and Jennifer Lippincott-Schwartz. Diffusional mobility of golgi proteins in membranes of living cells. *Science*, 273:797–801, 1996.

[64] Jan Ellenberg, Eric D. Siggia, Jorge E. Moreira, Carolyn L. Smith, John F. Presley, Howard J.

Worman, and Jennifer Lippincott-Schwartz. Nuclear membrane dynamics and reassembly in living cells: targeting of an inner nuclear membrane protein in interphase and mitosis. *J. Cell Biol.*, 138:1193–1206, 1997.

[65] Miroslav Dundr, Tom Misteli, and Mark O.J. Olson. The dynamics of postmitotic reassembly of the nucleolus. *J. Cell. Biol.*, 150:433–446, 2000.

[66] Katherine Luby-Phelps, Frederick Lanni, and D. Lansing Taylor. Behavior of a fluorescent analogue of calmodulin in living 3t3 cells. *J. Cell Biol.*, 101:1245–1256, 1985.

[67] Peter Hinow, Carl E. Rogers, Christopher E. Barbieri, Jennifer A. Pietenpol, Anne K. Kenworthy, and Emmanuele DiBenedetto. The dna binding activity of p53 displays reaction-diffusion kinetics. *Biophys. J.*, 91:330–342, 2006.

[68] Klaus Suhling, Jan Siegel, Peter M. P. Lanigan, Sandrine Lévêque-Fort, Stephen E. D. Webb, David Phillips, Daniel M. Davis, and Paul M. W. French. Time-resolved fluorescence anisotropy imaging applied to live cells. *Opt. Lett.*, 29:584–586, 2004.

[69] Albert J. Cross and Graham R. Fleming. Analysis of time-resolved fluorescence anisotropy decays. *Biophys. J.*, pages 45–56, 1984.

[70] L. Best, E. John, and F. Jähnig. Order and fluidity of lipid membranes as determined by fluorescence anisotropy decay. *Eur. Biophys. J*, 15:87–102, 1987.

[71] Arun Gidwani, David Holowka, and Barbara Baird. Fluorescence anisotropy measurements of lipid order in plasma membranes and lipid rafts from rbl-2h3 mast cells. *Biochemistry*, 40:12422–12429, 2001.

[72] Evgeny O. Puchkov. Single yeast cell vacuolar milieu viscosity assessment by fluorescence polarization microscopy with computer image analysis. *Yeast*, 29:185–190, 2012.

[73] Marina K. Kuimova, Gokhan Yahioglu, James A. Levitt, and Klaus Suhling. Molecular rotor measures viscosity of live cells via fluorescence lifetime imaging. *J. Am. Chem. Soc.*, 130:6672–6673, 2008.

[74] Elliot L. Elson. Fluorescence correlation spectroscopy: Past, present, future. *Biophys. J.*, 101:2855–2870, 2011.

[75] Hai-Tao He and Didier Marguet. Detecting nanodomains in living cell membrane by fluorescence correlation spectroscopy. *Annu. Rev. Phys. Chem.*, 62:417–436, 2011.

[76] Rémi Lasserre, Xiao-Jun Guo, Fabien Conchonaud, Yannick Hamon, Omar Hawchar, Anne-Marie Bernard, Saïdi M'Homa Soudja, Pierre-François Lenne, Hervé Rigneault, Daniel Olive, Georges Bismuth, Jacques A. Nunès, Bernard Payrastre, Didier Marguet, and Hai-Tao He. Raft nanodomains contribute to akt/pkb plasma membrane recruitment and activation. *Nat. Chem. Biol.*, 4:538–547, 2008.

[77] Cyrille Billaudeau, Sébastien Mailfert, Tomasz Trombik, Nicolas Bertaux, Vincent Rouger, Yannick Hamon, Hai-Tao He, and Didier Marguet. Probing the plasma membrane organization in living cells by spot variation fluorescence correlation spectroscopy. *Methods in Enzymology*, 519:277–302, 2013.

[78] Björn F. Lillemeier, Manuel A. Mörtelmaier, Martin B. Forstner, Johannes B. Huppa, Jay T. Groves, and Mark M Davis. Tcr and lat are expressed on separate protein islands on t cell membranes and concatenate during activation. *Nat. Immuno.*, 11:90–96, 2010.

[79] Tong Hao, Zheng Zeng, Bin Wang, Yichen Zhang, Yichen Liu, Xuyun Geng, and Jinsheng Sun. The protein-protein interaction network of eyestalk, y-organ and hepatopancreas in chinese mitten crab eriocheir sinensis. *BMC Syst. Biol.*, 8, 2014.

[80] Pierre-François Lenne, Laure Wawrezinieck, Fabien Conchonaud, Olivier Wurtz, Annie Boned, Xiao-Jun Guo, Hervé Rigneault, Hai-Tao He, and Didier Marguet. Dynamic molecular confinement in the plasma membrane by microdomains and the cytoskeleton meshwork. *The EMBO Journal*, 25:3245–3256, 2006.

[81] Marcel Leutenegger, Christian Ringemann, Theo Lasser, Stefan W. Hell, and Christian Eggeling. Fluorescence correlation spectroscopy with a total internal reflection fluorescence sted microscope (tirf-sted-fcs). *Opt. Express*, 20:5243–5263, 2012.

[82] Malte Wachsmuth, Waldemar Waldeck, and Jörg Langowski. Anomalous diffusion of fluorescent probes inside living cell nuclei investigated by spatially-resolved fluorescence correlation spectroscopy. *J. Mol. Biol.*, 298:677–689, 2000.

[83] Jonas Ries and Petra Schwille. Fluorescence correlation spectroscopy. *BioEssays*, 34:361–368, 2012.

[84] Peter Scherp and Karl H. Hasenstein. Anisotropic viscosity of the chara (characeae) rhizoid cytoplasm. *Am. J. Bot.*, 94:1930–1934, 2007.

[85] Denis Wirtz. Particle-tracking microrheology of living cells: principles and applications. *Annu. Rev. Biophys.*, 38:301–326, 2009.

[86] Brenton D. Hoffman, Gladys Massiera, Kathleen M. van Citters, and John C. Crocker. The consensus mechanics of cultured mammalian cells. *Proc. Natl. Acad. Sci.*, 103:10259–10264, 2006.

[87] A. W. C. Lau, B. D. Hoffman, A. Davies, J. C. Crocker, and T. C. Lubensky. Microrheology, stress fluctuations, and active behavior of living cells. *Phys. Rev. Lett.*, 91:198101, 2003.

[88] Avi Caspi, Rony Granek, and Michael Elbaum. Diffusion and directed motion in cellular transport. *Phys. Rev. E Stat. Nonlin. Soft Matter Phys.*, 66:011916, 2002.

[89] G. Holzwarth, Keith Bonin, and David B. Hill. Forces required of kinesin during processive transport through cytoplasm. *Biophys. J.*, 82:1784–1790, 2002.

[90] Ben Fabry, Geoffrey N. Maksym, James P. Butler, Michael Glogauer, Daniel Navajas, and Jeffrey J. Fredberg. Scaling the microrheology of living cells. *Phys. Rev. Lett.*, 87:148102, 2001.

[91] Lara Selvaggi, Marinella Salemme, Carmen Vaccaro, Giuseppe Pesce, Giulia Rusciano, Antonio Sasso, Chiara Campanella, and Rosa Carotenuto. Multiple-particle-tracking to investigate viscoelastic properties in living cells. *Methods*, 51:20–26, 2010.

[92] Robert M. Hochmuth. Micropipette aspiration of living cells. *Journal of Biomechanics*, 33:15–22, 2000.

[93] Alba Diz-Munoz, Daniel A. Fletcher, and Orion D. Weiner. Use the force: membrane tension as an organizer of cell shape and motility. *Trends in Cell Biology*, 23:47–53, 2012.

[94] Adai Colom, Emmanuel Derivery, Saeideh Soleimanpour, Caterina Tomba, Marta Dal Molin, Naomi Sakai, Marcos González-Gaitán, Stefan Matile, and Aurélien Roux. A fluorescent membrane tension probe. *Nat. Chem.*, 10:1118–1125, 2018.

[95] Douglas A. Davis, Andrew Hamilton, Jinglei Yang, Lee D. Cremar, Dara van Gough, Stephanie L. Potisek, Mitchell T. Ong, Paul V. Braun, Todd J. Martínez, Scott R. White, Jeffrey S. Moore, and Nancy R. Sottos. Force-induced activation of covalent bonds in mechanoresponsive polymeric materials. *Nature*, 459:68–72, 2009.

[96] Gregory R. Gossweiler, Tatiana B. Kouznetsova, and Stephen L. Craig. Force-rate characterization of two spiropyran-based molecular force probes. *J. Am. Chem. Soc.*, 137:6148–6151, 2015.

[97] Brett A. Beiermann, Douglas A. Davis, Sharlotte L. B. Kramer, Jeffrey S. Moore, Nancy R. Sottosab, and Scott R. White. Environmental effects on mechanochemical activation of spiropyran in linear pmma. *J. Mater. Chem.*, 21:8443–8447, 2011.

[98] Yulan Chen, A. J. H. Spiering, S. Karthikeyan, Gerrit W. M. Peters, E. W. Meijer, and Rint P. Sijbesma. Mechanically induced chemiluminescence from polymers incorporating a 1,2-dioxetane unit in the main chain. *Nat. Chem.*, 4:559–562, 2012.

[99] Yulan Chen and Rint P. Sijbesma. Dioxetanes as mechanoluminescent probes in thermoplastic elastomers. *Macromolecules*, 47:3797–3805, 2014.

[100] Ties van de Laar, Hent Schuurman, Pieter van der Scheer, Jan Maarten van Doorn, Jasper van der Gucht, and Joris Sprakel. Light from within: Sensing weak strains and femtonewton forces in single molecules. *Chem.*, 4:269–284, 2018.

[101] Mark A. Haidekker, Matthew Nipper, Adnan Mustafic, Darcy Lichlyter, Marianna Dakanali, and Emmanuel A. Theodorakis. *Dyes with segmental mobility: molecular rotors*. Advanced Fluorescence Reporters in Chemistry and Biology I. 2010.

[102] Mark A. Haidekker, Thomas P. Brady, Darcy Lichlyter, and Emmanuel A. Theodorakis. Effects of solvent polarity and solvent viscosity on the fluorescent properties of molecular rotors and related probes. *Bioorg. Chem.*, 33:415–425, 2005.

[103] Th. Förster and G. Hoffmann. Die viskositätsabhängigkeit der fluoreszenzquantenausbeuten einiger farbstoffsysteme. *Zeitschrift für Physikalische Chemie*, 75:63–76, 1971.

[104] Xiongbo Liu, Danying Lin, Wolfgang Becker, Jingjing Niu, Bin Yu, Liwei Liu, and Junle Qu. Fast fluorescence lifetime imaging techniques: A review on challenge and development. *Journal of Innovative Optical Health Sciences*, 12:1930003, 2019.

[105] Michael R. Dent, Ismael López-Duarte, Callum J. Dickson, Phoom Chairatana, Harry L. Anderson, Ian R. Gould, Douglas Wylie, Aurimas Vyšniauskas, Nicholas J. Brooks, and Marina K. Kuimova. Imaging plasma membrane phase behaviour in live cells using a thiophene-based molecular rotor. *Chem. Commun.*, 52:13269–13272, 2016.

[106] Zhen Zou, Qi Yan, Sixin Ai, Peng Qi, Hua Yang, Yufei Zhang, Zhihe Qing, Lihua Zhang, Feng Feng, and Ronghua Yang. Real-time visualizing mitophagy-specific viscosity dynamic by mitochondria-anchored molecular rotor. *Anal. Chem.*, 91:8574–8581, 2019.

[107] Hyung J. Kim and James T. Hynes. Excited state intramolecular charge transfer rates of p-dirnethylaminobenzonitrile (dmabn) in solution: a two-dimensional dynamics perspective. *Journal of Photochemistry and Phorobiology A: Chemistry*, 105:337–343, 1997.

[108] Tesfay Atsbeha, Ahmed M. Mohammed, and Mesfin Redi-Abshiro. Excitation wavelength dependence of dual fluorescence of dmabn in polar solvents. *J. Fluoresc.*, 20:1241–1248,

2010.

[109] Andreas Köhn and Christof Hättig. On the nature of the low-lying singlet states of 4-(dimethyl-amino)benzonitrile. *J. Am. Chem. Soc.*, 126:7399–7410, 2004.

[110] Mark A. Haidekker, Nicolas L'Heureux, and John A. Frangos. Fluid shear stress increases membrane fluidity in endothelial cells: a study with dcvj fluorescence. *Am. J. Physiol. Heart Circ. Physiol.*, 278:H1401–H1406, 2000.

[111] Mark A. Haidekker, Taotao Ling, Michael Anglo, Hazel Y. Stevens, John A. Frangos, and Emmanuel A. Theodorakis. New fluorescent probes for the measurement of cell membrane viscosity. *Chem. Biol.*, 8:123–131, 2001.

[112] Matthew E. Nipper, Sheereen Majd, Michael Mayer, James C.-M. Lee, Emmanuel A. Theodorakis, and Mark A. Haidekker. Characterization of changes in the viscosity of lipid membranes with the molecular rotor fcvj. *Biochimica et Biophysica Acta*, 1778:1148–1153, 2008.

[113] Mohammed A. H. Alamiry, Andrew C. Benniston, Graeme Copley, Kristopher J. Elliott, Anthony Harriman, Beverly Stewart, and Yong-Gang Zhi. A molecular rotor based on an unhindered boron dipyrromethene (bodipy) dye. *Chem. Mater.*, 20:4024–4032, 2008.

[114] Tomislav Suhina, Saeed Amirjalayer, Sander Woutersen, Daniel Bonn, and Albert M. Brouwer. Ultrafast dynamics and solvent-dependent deactivation kinetics of bodipy molecular rotors. *Phys. Chem. Chem. Phys.*, 19:19998–20007, 2017.

[115] Ida Emilie Steinmark, Arjuna L. James, Pei-Hua Chung, Penny E. Morton, Maddy Parsons, Cécile A. Dreiss, Christian D. Lorenz, Gokhan Yahioglu, and Klaus Suhling. Targeted fluorescence lifetime probes reveal responsive organelle viscosity and membrane fluidity. *PLoS ONE*, 14:e0211165, 2019.

[116] Lyubov E. Shimolina, Maria Angeles Izquierdo, Ismael López-Duarte, James A. Bull, Marina V. Shirmanova, Larisa G. Klapshina, Elena V. Zagaynova, and Marina K. Kuimova. Imaging tumor microscopic viscosity in vivo using molecular rotors. *Sci. Rep.*, 7:41097, 2017.

[117] Zhigang Yang, Yanxia He, Jae-Hong Lee, Nayoung Park, Myungkoo Suh, Weon-Sik Chae, Jianfang Cao, Xiaojun Peng, Hyosung Jung, Chulhun Kang, and Jong Seung Kim. A self-calibrating bipartite viscosity sensor for mitochondria. *J. Am. Chem. Soc.*, 135:9181–9185, 2013.

[118] Elba Xochitiotzi-Flores, Arturo Jiménez-Sánchez, Héctor García-Ortega, Nuria Sánchez-Puig, Margarita Romero-Ávila, Rosa Santilland, and Norberto Farfán. Optical properties of two fluorene derived bodipy molecular rotors as fluorescent ratiometric viscosity probes. *New J. Chem.*, 40:4500–4512, 2016.

[119] Marina K. Kuimova, Stanley W. Botchway, Anthony W. Parker, Milan Balaz, Hazel A. Collins, Harry L. Anderson, Klaus Suhling, and Peter R. Ogilby. Imaging intracellular viscosity of a single cell during photoinduced cell death. *Nat. Chem.*, 1:69–73, 2009.

[120] Katherine Luby-Phelps, Swati Mujumdar, Ratnakar B. Mujumdar, Lauren A. Ernst, William Galbraith, and Alan S. Waggoner. A novel fluorescence ratiometric method confirms the low solvent viscosity of the cytoplasm. *Biophys. J.*, 65:236–242, 1993.

Chapter 2

Chapter 2

Synthesis of the molecular fluorescent probes

2.1 Introduction

Research on force assessment at the molecular level in synthetic materials has yielded a large collection of mechanoprobes to study macroscopic deformation, failure and healing phenomena[1]. Yet, the implementation of such tools to investigate cells and tissues mechanobiology is an open frontier, especially in organisms possessing walled cells (plants, oomycetes, fungi). In the context of walled cell mechanobiology, being able to report mechanical patterns actively generated in vivo is a challenge of primary importance. To achieve this goal, one needs to design and synthesize molecular sensors that meet a number of criteria; i) the sensor should be soluble in water, to allow for cell incubation. Water-solubility becomes unnecessary in the case of plasma membrane staining, but the dye should still be able to partition in water to some extent; ii) the sensor needs to stain the designated sub-cellular target with high specificity; iii) it should be suitable for live-cell imaging, and as such be non-cytotoxic, small enough to penetrate the cell -without requiring permeabilization or fixation chemicals-, and excitable at wavelengths that do not trigger cell autofluorescence; iv) the probe should have a suitable dynamic range in its response, to enable clear analysis of small differences in properties.

In this thesis we synthesized and implemented molecular fluorescent probes in plant and oomycete systems, so as to investigate mechano-chemical properties in the different cellular compartments (i.e. cell wall, plasma membrane, cytoplasm, vacuole). To enable modifications of the molecular structures in order to address different cellular compartments and/or to tune the emission wavelength of the probes, synthetic protocols need to be modified and optimized accordingly. For example, to target the cell wall, one could imagine a molecular sensor containing positively charged moieties able to establish electrostatic interactions with the negatively charged units of the wall carbohydrate network, but not too amphiphilic and linear, to avoid intercalation between the plasma membrane phospholipids. To target the plasma membrane, an amphiphilic dye containing an aliphatic tail and a low positive net charge might be more suitable. To target the cytoplasm, the probe should be able to penetrate the cell without sticking to the charged wall and/or phospholipids, but bulky enough to diffuse only very slowly inside the vacuoles. In contrast, a small negatively charged dye will readily diffuse inside the vacuoles.

In this Chapter we will detail the synthesis protocols used to synthesize the various fluorescent probes used in this study. We first developed a set of BODIPY-based mechanoprobes to map microviscosity patterns in cells, with an initial focus on plant cells, broadened later on to other non-animal cells (e.g. oomycetes). As a follow-up, to increase the accessibility of this method in mapping mechanical gradients, we worked on the development of ratiometric analogs composed of the same microviscosity-sensitive BODIPY-based molecular rotor, covalently bound to a coumarin reference unit. Additionally, we synthesized a ratiometric probe developed by Kucherak et al.[2] (NR12S), initially designed to report chemical polarity in the plasma membrane of mammalian cells. Using this probe allowed us to highlight changes in membrane structure and composition during the growth and invasion process of oomycete cells, along with imaging the cell wall microviscosity using our initial cell wall targeting molecular rotor. Figure 2.1 gives an overview of all the probes synthesized.

In the following sections, we describe the synthesis and chemical characterization of these probes in more details.

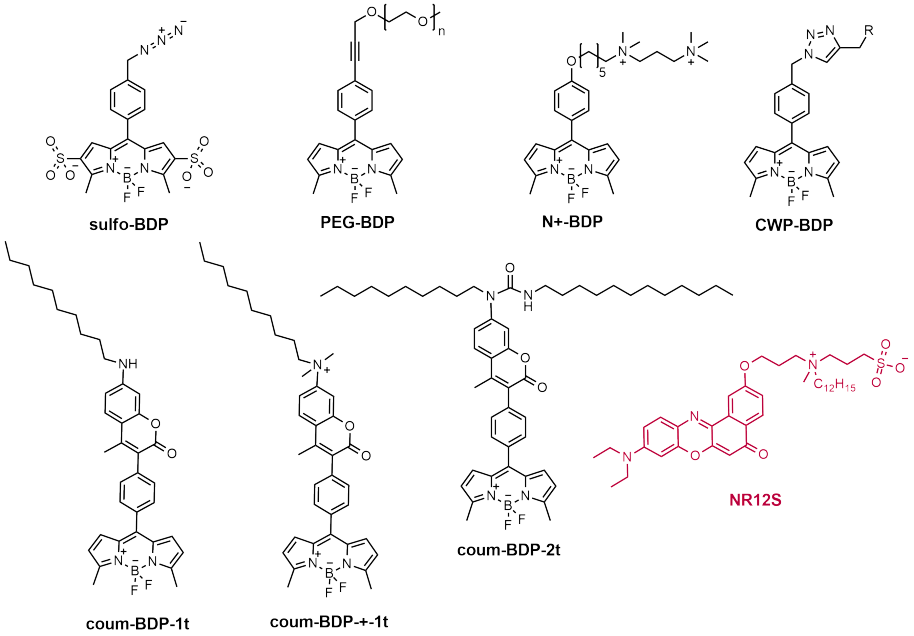

Figure 2.1: Overview of the fluorescent probes synthesized in this study to map microviscosity (black) and chemical polarity (red) patterns

2.2 Synthetic procedures

All chemicals were purchased from Sigma-Aldrich, TCI Chemicals or Fischer Scientific and used as received unless indicated otherwise. 2-Methylpyrrole was purchased from Oxchem Corporation. All oxygen-sensitive reactions were performed under nitrogen atmosphere (by sparging reaction mixtures with gaseous nitrogen) and slightly negative pressure. Column chromatography was performed on silica gel of 40–63 μm particle size. Where the reaction solvent or eluent consisted of mixture of solvents, the ratios are reported by volume. ^{1}H and ^{13}C spectra were recorded on a Bruker Avance III 400MHz spectrometer. Mass spectra (MS) were recorded using ElectroSpray Ionization (ESI) on a Thermo Scientific Exactive mass spectrometer. All the NMR and MS spectra can be found in the Appendix of this Chapter (Figures 2.11-2.66).

2.2.1 Microviscosity probes

In a typical Boron-dipyrromethene (BODIPY) rotor synthesis from a pyrrole derivative and an aromatic aldehyde, the aldehyde is dissolved in dichloromethane in presence of an excess pyrrole, at room temperature, to form a dipyrromethane intermediate. This step is catalyzed by trifluoroacetic acid (TFA). The intermediate is then oxidized with 2,3-dichloro-5,6-dicyano-1,4-benzoquinone (DDQ) and consecutively complexed with boron to give the final mechanophore. When forming the BODIPY-rotor, one can use a benzaldehyde functionalized with a reactive group in para position (commonly Br or I), to allow for post-functionalization without hindering the rotation between the BODIPY core and the benzaldehyde unit -as substitution in ortho does-; this is the approach we used to synthesize e.g. our cytoplasm targeting rotor (PEG-BDP) or our cell-wall binding rotor (CWP-BDP). Another possibility is to use pre-modified benzaldehyde derivatives, when more complex functional groups need to be inserted, to avoid deterioration of the rotor under the required reaction conditions; this is the approach we used to introduce the coumarin reference unit when synthesizing the BODIPY ratiometric analogs.

BODIPY-based molecular rotors for Fluorescence Lifetime Imaging Microscopy (FLIM)

10-(4-(Bromomethyl)phenyl)-5,5-difluoro-3,7-dimethyl-5H-dipyrrolo [1,2-c:2',1'-f] [1,3,2] diazaborinin-4-ium-5-uide (1)

Freshly distilled 2-methylpyrrole (421 μL, 5 mmol) and 4-(bromomethyl)-benzaldehyde (500 mg, 2.5 mmol) were added to anhydrous dichloromethane (130 mL) and the mixture was degassed by sparging with nitrogen for 30 min before addition of TFA (100 μL, 1.3 mmol). The mixture was stirred for 2h at room temperature. 2,3-dichloro-5,6-dicyano-1,4-benzoquinone (570 mg, 2.5 mmol) was added and the mixture degassed by sparging with nitrogen for 10 min. The mixture was stirred further for 20 min. Diisopropylethylamine (3.06 mL, 17.6 mmol) was added, followed by the addition of boron trifluoride diethyl etherate (3.1 mL, 25.1 mmol). The reaction was stirred at room temperature for 24h. The solvent was evaporated at 40°C under reduced pressure to give a dark purple residue that was purified by column chromatography on silica gel (dichlorometh-

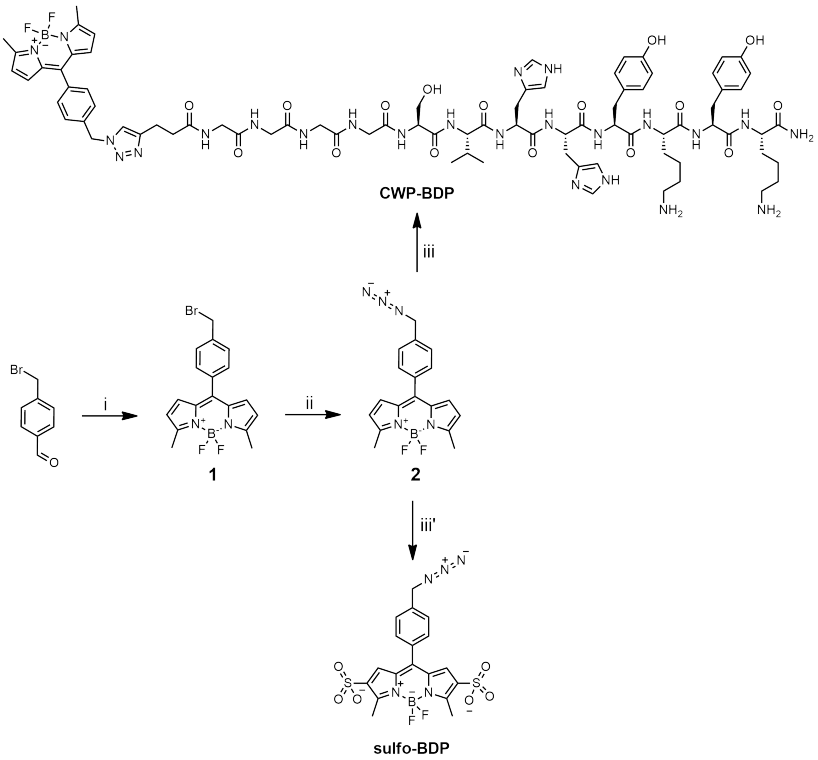

Figure 2.2: Synthesis pathway of sulfo-BDP and CWP-BDP

ane) to give **1** as an orange solid (130 mg, 13% yield). ^{1}H NMR (400 MHz, $CDCl_3$) δ 7.48 (m, 4H), 6.71 (d, 2H), 6.28 (d, 2H), 4.56 (s, 2H), 2.65 (s, 6H). ^{13}C NMR (101 MHz, $CDCl_3$) δ 157.85, 141.61, 139.67, 134.18, 130.80, 130.30, 128.86, 119.56, 32.48, 14.94. HRMS (ESI) calcd for $C_{18}H_{16}BBrF_2N_2$ $[M-H]^-$, 387.0527; found, 387.0486.

10-(4-(Azidomethyl)phenyl)-5,5-difluoro-3,7-dimethyl-5H-dipyrrolo [1,2-c:2',1'-f] [1,3,2] diazaborinin-4-ium-5-uide (2)

Sodium azide (80 mg, 1.2 mmol) was dissolved in Milli Q water (200 μL) and the solution was added dropwise to DMF (5 mL). **1** (100 mg, 0.26 mmol) was added and the mixture was degassed by sparging with nitrogen for 15 min. The reaction was stirred at room temperature overnight, and then diluted with di-

chloromethane. The organic solution was washed five times with Milli Q water, dried over magnesium sulfate, filtered, and the solvent was removed at 40°C under reduced pressure. The residue was purified by column chromatography on silica gel (petroleum ether:dichloromethane=1:1) to yield **2** as an orange solid (64 mg, 71% yield). ^{1}H NMR (400 MHz, $CDCl_3$) δ 7.51 (m, 2H), 7.44 (m, 2H), 6.69 (d, 2H), 6.28 (d, 2H), 4.46 (s, 2H), 2.65 (s, 6H). ^{13}C NMR (101 MHz, $CDCl_3$) δ 157.84, 141.71, 137.46, 134.44, 134.08, 130.82, 130.29, 127.83, 119.55, 99.98, 54.37, 14.93. HRMS (ESI) calcd for $C_{18}H_{16}BF_2N_5$ $[M-H]^-$, 350.1427; found, 350.1395.

CWP-BDP (3)

To obtain a cell-wall binding molecular rotor, we functionalized the dye with a peptide known to mimic the pectin binding domain of Extensin proteins[3]. The resulting molecule can then target and bind specifically to the pectin network of plant cell walls. The peptide (SVHHYKYK)[3] derivative was prepared using standard Fmoc/tBu-based protocols on a Rink amid resin by means of an automated peptide synthesizer. Specifically, the sequence was extended on the N-terminus with four G residues and 4-pentynoic acid in order to separate the cell wall binding peptide from the BODIPY rotor. After acidic cleavage and side-chain deprotection of the resin-bound peptide, the crude alkyne-peptide derivative was subjected to copper-catalyzed alkyne-azide cycloaddition (CuAAC) conjugation to the azide-functionalized BODIPY rotor. For this, **2** (4.2 mg; 12 μmol) was mixed with a calculated excess of the expected amount of peptide obtained from the resin (i.e. 24.6 mg, 18 μmol) in DMF:water=1:1 (2 mL). $CuSO_4$ (20 mg, 90 μmol) and sodium ascorbate (35 mg, 180 μmol) were added. The reaction was performed overnight at room temperature. The crude mixture was subjected to preparative reversed phase-HPLC using a prep-LC-MS system (Alltima, C18, 5μ, 250mm x 22mm; gradient: 0–5 min @A, in 5–25 min to B, 25–30 min @B, in 30–35 min to A, 35–40 min @A [buffer A: 95% MilliQ, 5% MeCN, 0.1% TFA; buffer B: 95% MeCN, 5% MilliQ, 0.1% TFA], tR = 15.46 min). The purified fraction was freeze-dried to get **3** (3.3mg, 16% yield). HRMS (ESI) calcd for $C_{81}H_{105}BF_2N_{24}O_{16}$ $[M+3H]^{3+}$, 573.9473; found, 573.9475 and $[M+2H]^{2+}$, 860.4174; found, 860.4167.

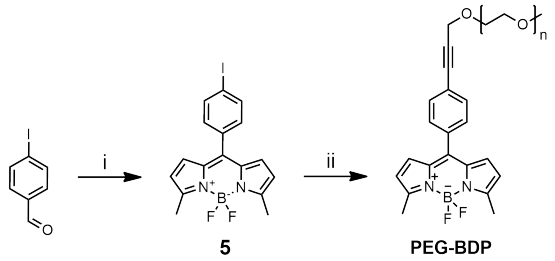

Figure 2.3: Synthesis pathway of PEG-BDP

Sulfo-BDP (4)

2 (45 mg, 0.13 mmol) and sulfur trioxide pyridine complex (408 mg, 2.5 mmol) were dissolved in DMF (6 mL). The mixture was degassed by sparging with nitrogen for 15 min. The mixture was stirred at 60°C for 24h. The solution was diluted with Milli Q water, and the aqueous phase extracted twice with chloroform. The aqueous phase was filtered with a 0.2 μm pore diameter filter, and the water evaporated under reduced pressure. The residue was run over a silica gel column (dichloromethane:methanol=9:1 to dichloromethane:methanol=8:2) to get **4** as an orange solid (66 mg). At this stage the product still contains 3 equivalents of pyridine for one equivalent of sulfo-BDP. This can be explained by a strong electrostatic interaction established between the sulfonate groups decorating the molecular rotor and the pyridinium ions introduced by the sulfur trioxide pyridine complex (that seem to play the role of counterions). In addition, sulfo-BDP carrying two negative charges, it is not possible to run the product over long silica gel columns to ensure full separation, as it would result in more silica contamination when flushing the column with dichloromethane:methanol=8:2. ^{1}H NMR (400 MHz, D_2O) δ 7.38 (m, 4H), 6.97 (s, 2H), 4.38 (s, 2H), 2.72 (s, 1H), 2.62 (s, 6H). ^{13}C NMR (101 MHz, D_2O) δ 155.73, 146.34, 139.20, 134.77, 131.71, 131.42, 129.97, 128.41, 127.30, 53.59, 38.79, 13.00. HRMS (ESI) calcd for $C_{18}H_{14}BF_2N_5O_6S_{22}$ $[M-H]^+$, 510.0572; found, 510.0529.

5,5-Difluoro-10-(4-iodophenyl)-3,7-dimethyl-5H-dipyrrolo [1,2-c:2',1'-f] [1,3,2] diazaborinin-4-ium-5-uide (5)

Freshly distilled 2-methylpyrrole (743 μL, 8.5 mmol) and 4-iodobenzalde-

hyde (990 mg, 4.3 mmol) were added in anhydrous dichloromethane (180 mL) and the mixture was degassed by sparging with nitrogen for 30 min before addition of TFA (180 μL, 2.3 mmol). The mixture was stirred for 2h. 2,3-dichloro-5,6-dicyano-1,4-benzoquinone (969 mg, 4.3 mmol) was added and the mixture degassed by sparging with nitrogen for 10 min. The mixture was stirred further for 20 min. Diisopropylethylamine (5.19 mL, 30 mmol) was added, followed by the addition of boron trifluoride diethyl etherate (5.26 mL, 43 mmol). The reaction was stirred at room temperature for 24h. The solvent was evaporated at 40°C under reduced pressure to give a dark purple residue that was purified by column chromatography on silica gel (dichloromethane) to give **5** as an orange solid (355 mg, 20% yield). ^{1}H NMR (400 MHz, $CDCl_3$) δ 7.82 (m, 2H), 7.23 (m, 2H), 6.68 (d, 2H), 6.28 (d, 2H), 2.65 (s, 6H). ^{13}C NMR (101 MHz, $CDCl_3$) δ 158.06, 141.02, 137.46, 134.17, 133.56, 131.89, 130.12, 119.70, 96.35, 14.95. HRMS (ESI) calcd for $C_{17}H_{14}BF_2IN_2$ $[M-H]^-$, 421.0227; found, 421.0187.

Alkyne-PEG (6)

Alkyne-PEG was synthesized as reported previously[4] from poly(ethylene glycol) methyl ether 550 g/mol. Sodium hydride (303 mg of 60wt% suspension in mineral oil, 4.5 mmol) was dissolved in anhydrous THF (50 mL). The mixture was degassed by sparging nitrogen for 10 min and equilibrated at 0°C in an ice bath. PEG-OH 550 g/mol (2.5g, 4.5 mmol) was added and the reaction was stirred at 0°C for 30 min. Propargyl bromide (759.4 μL of 80wt% solution in toluene, 7 mmol) was added, the mixture was warmed up to room temperature, degassed by applying five successive vacuum/nitrogen cycles, and stirred overnight. The solvent was removed at 40°C under reduced pressure and the residue dissolved in dichloromethane. The solution was washed twice with brine and dried over magnesium sulfate. The solvent was removed to get **6** as a viscous oil (2.5g, 92% yield). ^{1}H NMR (400 MHz, $CDCl_3$) δ 4.16 (d, 2H), 3.60 (m, 50H), 3.33 (s, 3H). ^{13}C NMR (101 MHz, $CDCl_3$) δ 79.62, 74.57, 71.89, 70.53, 70.37, 70.28, 69.06, 58.99, 58.35.

PEG-BDP (7)

6 (109 mg, 0.18 mmol) was dissolved in anhydrous THF (7 mL) and the mix-

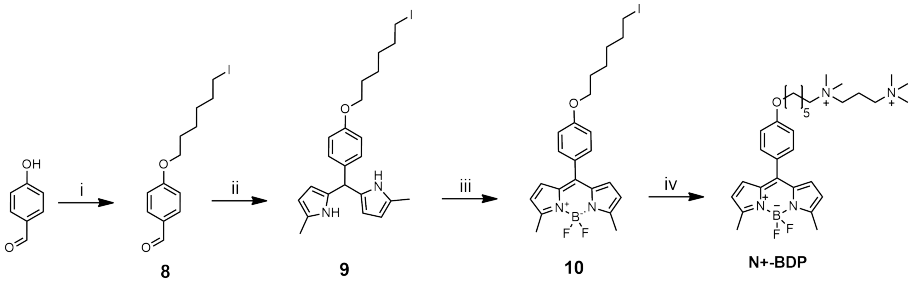

Figure 2.4: Synthesis pathway of N+-BDP

ture was degassed by sparging with nitrogen for 15 min. I-BDP (60 mg, 0.14 mmol), copper iodide (2 mg, 0.01 mmol) and bis(triphenylphosphine)palladium (II) dichloride (2.3 mg, 3.3 μ mol) were added, followed by the addition of diisopropylethylamine (4 mL, 23 mmol). The mixture was stirred at 70°C overnight. The solvent was removed at 40°C under reduced pressure. The residue was dissolved in dichloromethane and the organic solution washed with 1M HCl, saturated NaHCO3 and brine. The organic phase was dried over magnesium sulfate, filtered and the solvent removed at 40°C under reduced pressure. The residue was purified by running through a neutral alumina plug with dichloromethane as an eluent to flush the impurities, and 5 v% methanol in dichloromethane to collect the product. The solvent was evaporated at 40°C under reduced pressure and the residue dried for 4 days in a vacuum oven at 40°C to give **7** as a red oil (108 mg, 86% yield). ^{1}H NMR (400 MHz, $CDCl_3$) δ 7.53 (m, 2H), 7.45 (m, 2H), 6.69 (d, 2H), 6.26 (d, 2H), 4.46 (s, 2H), 3.64 (m, 52H), 3.37 (s, 3H), 2.64 (s, 6H). ^{13}C NMR (101 MHz, $CDCl_3$) δ 157.87, 141.48, 134.25, 134.07, 131.50, 130.31, 124.53, 119.59, 87.33, 85.44, 71.93, 70.66, 69.32, 59.03, 14.93.

Compounds 8-11 were synthesized as reported previously[5], replacing pyrrole by 2-methylpyrrole.

4-((6-Iodohexyl)oxy)benzaldehyde (8)

Hydroxybenzaldehyde (1g, 8.2 mmol) and potassium carbonate (3.45g, 25 mmol) were dissolved in anhydrous DMF (15 mL). Diiodohexane was added (5.8

mL, 35 mmol) and the mixture was stirred at 70°C for 5h. The mixture was cooled down, diluted with dichloromethane and washed thrice with Milli Q water. The organic phase was dried over magnesium sulfate, filtered, and the solvent was removed at 40°C under reduced pressure. The residue was purified by column chromatography on silica gel (petroleum ether:ethyl acetate =7:1) to give **8** as a colorless oil (1.18g, 43% yield). ^{1}H NMR (400 MHz, $CDCl_3$) δ 9.90 (s, 1H), 7.84 (m, 2H), 7.02 (m, 2H), 4.06 (t, 2H), 3.23 (t, 2H), 1.85 (m, 4H), 1.51 (m, 4H). ^{13}C NMR (101 MHz, $CDCl_3$) δ 190.79, 164.13, 131.99, 129.82, 114.74, 68.14, 33.30, 30.18, 28.87, 24.99, 6.89.

5,5'-((4-((6-Iodohexyl)oxy)phenyl)methylene)bis(2-methyl-1H-pyrrole) (9)

8 (1g, 3 mmol) and freshly distilled 4-methylpyrrole (13 mL, 150 mmol) were mixed and degassed by sparging with nitrogen for 20 min. TFA (50 μL, 0.65 mmol) was added and the mixture was stirred at room temperature for 2h. The mixture was diluted with dichloromethane and washed with Milli Q water, 0.5M $NaHCO_3$ and Milli Q water. The organic phase was dried over magnesium sulfate, filtered, and the solvent and excess 4-methylpyrrole were removed at 60°C under reduced pressure. The residue was purified by column chromatography on silica gel (dichloromethane:petroleum ether = 2:1) to give a green viscous oil (1.03 g, 65% yield). ^{1}H NMR (400 MHz, $CDCl_3$) δ 7.61 (s, 2H), 7.14 (d, 2H), 6.85 (d, 2H), 5.80 (s, 2H), 5.76 (s, 2H), 3.95 (t, 2H), 3.21 (t, 2H), 2.21 (s, 6H), 1.87 (m, 4H), 1.50 (m, 4H). ^{13}C NMR (101 MHz, $CDCl_3$) δ 157.90, 134.44, 131.64, 129.36, 127.07, 114.46, 107.06, 105.82, 67.75, 43.31, 33.41, 30.27, 29.12, 25.12, 13.09, 7.01.

5,5-Difluoro-10-(4-((6-iodohexyl)oxy)phenyl)-3,7-dimethyl-5H-dipyrrolo [1,2-c:2',1'-f] [1,3,2] diazaborinin-4-ium-5-uide (10)

9 (0.926 g, 1.9 mmol) was dissolved in anhydrous dichloromethane (50 mL) and 2,3-dichloro-5,6-dicyano-1,4-benzoquinone (441 mg, 1.9 mmol) was added. The reaction was stirred at room temperature for 1h. Triethylamine (590 mg, 5.8 mmol) was added, followed by the addition of boron trifluoride diethyl etherate (0.6 mL, 4.8 mmol). The reaction was performed at room temperature overnight. The organic phase was washed with Milli Q water, 0.5M NH_4Cl and Milli Q water, dried over magnesium sulfate, filtered and the solvent was removed at 40°C

under reduced pressure. The residue was purified by column chromatography on silica gel (dichloromethane) to get **10** (590 mg, 58% yield) as a red-orange sticky solid. ^{1}H NMR (400 MHz, $CDCl_3$) δ 7.33 (m, 2H), 6.90 (m, 2H), 6.65 (d, 2H), 6.18 (d, 2H), 3.94 (t, 2H), 3.13 (t, 2H), 2.55 (s, 6H), 1.77 (m, 4H), 1.43 (m, 4H). ^{13}C NMR (101 MHz, $CDCl_3$) δ 160.78, 156.92, 142.67, 134.48, 132.03, 130.24, 126.42, 119.11, 114.19, 67.94, 33.36, 30.23, 29.00, 25.08, 14.87, 6.92. HRMS (ESI) calcd for $C_{23}H_{26}BF_2IN_2O$ $[M-H]^-$, 521.1127; found, 521.1078.

N+-BDP (11)

10 (200 mg, 0.4 mmol) was dissolved in THF (20 mL) and tetramethylpropanediamine (7.5 mL) was added. The mixture was stirred at room temperature overnight. The solvent and excess diamine were evaporated at 50°C under reduced pressure. The residue was washed thrice with diethyl ether, and dried before the addition of DMF (5 mL) and iodomethane (2 mL, 31 mmol). The reaction was performed at room temperature overnight. The solvent and excess iodomethane were removed at 50°C under reduced pressure and the residue was purified by column chromatography on silica gel (methanol). The methanol was evaporated at 40°C under reduced pressure and the residue run though a Dowex (1X8, 100-200 mesh) ion exchange resin (chloride form) plug (Milli Q water). The product was freeze-dried to get **11** as a red sticky solid (145 mg, 59% yield). ^{1}H NMR (400 MHz, MeOD) δ 7.35 (d, 2H), 6.98 (d, 2H), 6.68 (d, 2H), 6.25 (d, 2H), 4.00 (t, 2H), 3.35 (m, 6H), 3.14 (s, 9H), 3.09 (s, 6H), 2.48 (s, 6H), 2.27 (m, 2H), 1.79 (m, 4H), 1.55 (m, 2H), 1.42 (m, 2H). ^{13}C NMR (101 MHz, MeOD) δ 161.10, 156.68, 142.87, 134.20, 131.89, 130.04, 126.01, 118.89, 114.03, 67.63, 64.89, 62.47, 60.18, 52.64, 50.04, 28.68, 25.72, 25.39, 22.22, 17.31, 13.45. HRMS (ESI) calcd for $C_{31}H_{47}BF_2N_4O^{2+}$ $[M]^{2+}$, 270.19; found, 270.1898.

The syntheses of compounds **12**, **13** and **14**, schematized on Figures 2.5 and 2.6, were performed following reference [6]. These dyes were not used to measure free volumes, but to investigate the effect of adding substituents directly on the BODIPY core, either with direct π-conjugation to the aromatic structure, or by substitution of the fluor atoms.

5,5-difluoro-2,8-diiodo-10-(4-iodophenyl)-3,7-dimethyl-5H-dipyrrolo[1,2-

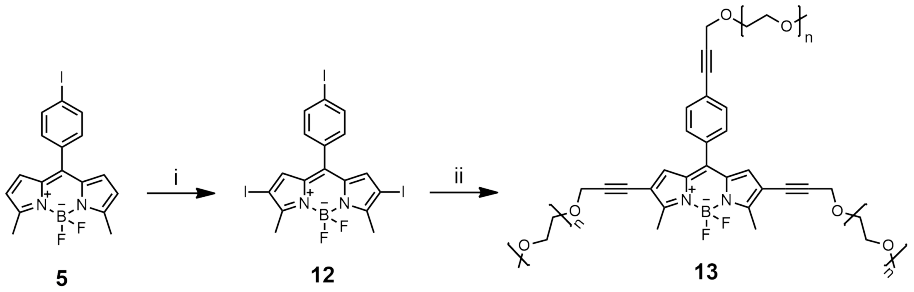

Figure 2.5: Synthesis pathway of **13**

c:2',1'-f][1,3,2]diazaborinin-4-ium-5-uide (12)

5 (89.5 mg, 0.2 mmol) was dissolved in dimethylformamide (DMF) (2.5 mL). Iodine (145 mg, 1.1 mmol) was added. After complete dissolution, a solution of iodic acid (74.6 mg, 0.4 mmol) dissolved in the minimum amount of MQ water was added dropwise. Upon adding the water, the BODIPY rotor precipitated partially. Extra DMF (3 mL) was added to redissolve the BODIPY dye without precipitating the iodic acid. The mixture was stirred at 70°C for 3h. The solvent was evaporated at 70°C under reduced pressure. The residue was dissolved in dichloromethane to perform a two-phase extraction with water. The organic phase was dried over magnesium sulfate, the solvent evaporated under reduced pressure, and the product further dried at 40°C in a vacuum oven for four days. The product was purified by column chromatography on silica gel (dichloromethane) to yield **12** (27 mg, 19% yield). The resulting dye has a maximum fluorescent emission shifted from 535 nm to 575 nm. ^{1}H NMR (400 MHz, CDCl3) δ 7.88-6.93 (6H), 2.66-1.27 (6H). HRMS (ESI) calcd for $C_{17}H_{12}BF_2I_3N_2$ $[M-H]^-$, 672.81; found, 672.8120.

3PEG-BDP via Sonogashira coupling (13)

12 (17mg, 25 μmol), Copper iodide (0.7 mg, 3.6 μmol) and $PdCl_2(PPh_3)_2$ (0.9 mg, 1.3 μmol) were dissolved and suspended in anhydrous tetrahydrofuran (1 mL). A solution of **6** (56 mg, 93 μmol) in THF (1.5 mL) was added. The solution was purged with nitrogen gas for 10 min. Nitrogen-purged diisopropylethylamine (660 μL, 3.8 mmol) was added to the reaction mixture, and the flask was

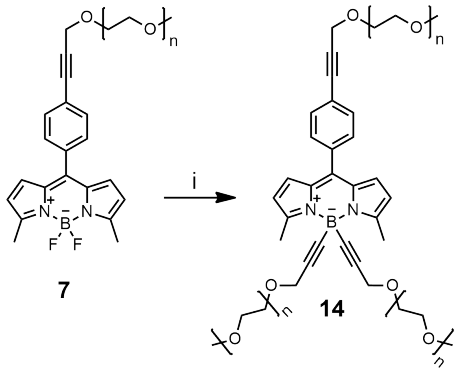

Figure 2.6: Synthesis pathway of **14**

further deoxygenated by performing five N_2/vacuum cycles, ending by a slight vacuum. The reaction was performed at 70°C overnight. The solution turned from pink red to violet in a few minutes. At the end of the reaction, the solvent was removed and the crude product purified by column chromatography on alumina (dichloromethane:hexane:methanol=6:3:0.5) to yield **13** as a violet product (35 mg). The NMR of this product shows extra PEG contamination, and peaks from the protons of the BODIPY unit are in comparison very small and difficult to integrate. The resulting product has the same fluorescence characteristics as its precursor but goes from non water-soluble to extremely water-soluble, which suggests a successful reaction.

3PEG-BDP via substitution of the fluor atoms (14)

6 (33.8 mg, 55.8 μmol) was dissolved in anhydrous THF (0.5 mL), and deoxygenated by sparging with nitrogen. Ethylmagnesium bromide 1M solution in THF (100 μL, 0.1 mmol) was added. The mixture was deoxygenated by performing four N_2/vacuum cycles, and stirred for 2h at 60°C. The solution became darker as the reaction progressed. The mixture was then transferred to a nitrogen-purged flask containing **7** (20 mg, 22.6 μmol), and was left to react at 60°C overnight. The solvent was then evaporated, MQ water was added, and then dichloromethane to perform a two-phase extraction. The organic phase was dried over magnesium sulfate, and the solvent evaporated. The residue was dis-

solved in MQ water and dialyzed against MQ for 3 days in a 0.1-0.5 kDa MWCO Cellulose Ester dialysis bag, before being freeze-dried to yield **14** (13.3 mg). The NMR of this product shows extra PEG contamination, and peaks from the protons of the BODIPY unit are in comparison very small. Even if neither the NMR nor mass spectrometry allowed to confirm the structure of the resulting product (due to PEG contamination and the heavy mass of the molecule, that prevents its ionization), the clear color change and the improved water solubility after reaction suggest that at least one substitution event occurred. This is enough for us to study the impact of such a modification on the rotor properties.

Coumarin-BODIPY probes for ratiometric imaging

The imaging of micromechanical patterns using the rotor toolbox relies on advanced FLIM imaging equipment, and has a relatively low temporal resolution, making it difficult to follow fast (i.e. occuring in less than 10 min) cellular processes. To make our toolbox more widely accessible and improve on its temporal resolution, a ratiometric probe whose response signal can be recorded using simpler fluorescence imaging tools would present an advantage. In this context, we synthesized three ratiometric probes based on a mechanochromic BODIPY rotor unit covalently bound to a coumarin reference unit. Their structures and synthesis pathways are illustrated in Figure 2.7. The protocols used for their synthesis were inspired by references [7, 8, 5].

3-(Decylamino)-phenol (15)

3-Aminophenol (10 g, 91.6 mmol), iododecane (21.5 mL, 100.7 mmol), and potassium carbonate (13 g, 94.1 mmol) were dissolved in anhydrous dimethylformamide (50 mL). The mixture was refluxed at 60°C for 3h. The solution was filtered to remove the excess of base, the solvent evaporated, and the resulting residue dissolved in dichloromethane. This solution was washed three times with MQ water and dried over magnesium sulfate The solvent was evaporated and the crude product purified by column chromatography on silica gel (hexane:ethyl acetate = 5:1), to yield **15** (11.8 g, 51.7% yield) as a white/brownish waxy solid. ^{1}H NMR (400 MHz, $CDCl_3$) δ 7.03 (s, 1H), 6.21 (d, 1H), 6.18 (d, 1H), 6.14 (s, 1H), 3.08 (t, 2H), 1.62 (m, 2H), 1.27 (m, 14H), 0.91 (t, 3H). ^{13}C NMR (101 MHz, $CDCl_3$)

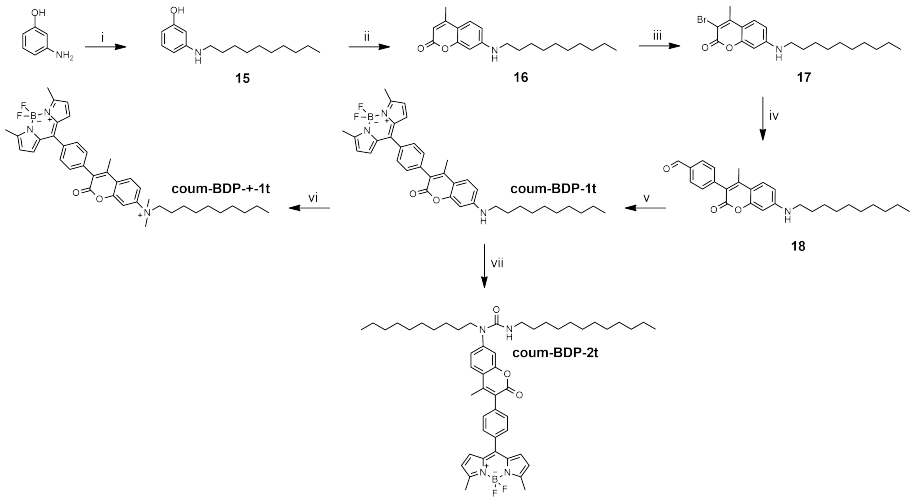

Figure 2.7: Synthesis pathway of the coumarin-BODIPY ratiometric probes; coum-BDP-1t, coum-BDP-+-1t, and coum-BDP-2t

δ 156.73, 150.13, 130.15, 105.97, 104.17, 99.55, 44.04, 31.91, 29.62, 29.58, 29.51, 29.46, 29.34.

7-(Decylamino)-4-methyl-2H-chromen-2-one (16)

15 (10.96 g, 10.96 mmol), ethyl acetoacetate (6.3 g, 48.4 mmol) and anhydrous zinc chloride (3 g, 22.0 mmol) were dissolved in ethanol (50 mL). The mixture was refluxed at 85°C for 24h. The flask was cooled to room temperature and the solvent evaporated at 40°C under reduced pressure. A solution of MQ water (320 mL) and 37% hydrochloric acid (3.6 mL) was added to the residue. The mixture was then extracted with dichloromethane. The organic phase was washed successively with a solution of sodium hydroxide (0.2 M) and brine, before being dried with magnesium sulfate. The solvent was evaporated and the crude product washed three times with hexane:ethyl acetate = 5:1 (3x100 mL). A recrystallization in ethanol (100 mL) was performed to yield **16** (5.1 g, 36.8% yield) as a yellow solid. The product precipitated out of ethanol upon cooling rather than crystallizing. ^{1}H NMR (400 MHz, $CDCl_3$) δ 7.35 (d, 1H), 6.51 (d, 1H), 6.44 (s, 1H), 5.97 (s, 1H), 4.27 (m, 1H), 3.18 (m, 2H), 1.64 (m, 2H), 1.27 (m, 14H), 0.90 (t, 3H). ^{13}C

NMR (101 MHz, $CDCl_3$) δ 162.07, 156.04, 153.02, 151.70, 125.45, 110.33, 125.45, 110.26, 109.20, 97.88, 43.51, 31.88, 29.56, 29.54, 29.38, 29.30, 29.18, 27.06, 22.67, 18.51, 14.11.

3-Bromo-7-(decylamino)-4-methyl-2H-chromen-2-one (17)

16 (5.09 g, 16.1 mmol) was dissolved in anhydrous dimethylformamide (70 mL). N-bromosuccinimide (2.9 g, 16.3 mmol) was added slowly, within 1 min. The mixture was stirred at room temperature overnight. It was then poured into brine, resulting in the precipitation of a yellow solid. Ethyl acetate was added to extract the aqueous phase (a relatively big volume of ethyl acetate was needed, as the solubility of the product is low in this solvent), and the resulting organic phase was washed with brine. The solvent was evaporated, and the residue dissolved in dichloromethane, and dried over magnesium sulfate. The solvent was evaporated, and the crude product purified by column chromatography on silica gel (dichloromethane:ethyl acetate = 20:1) to yield **17** (6 g, 94% yield) as a yellow solid. ^{1}H NMR (400 MHz, $CDCl_3$) δ 7.39 (d, 1H), 6.53 (d, 1H), 6.42 (s, 1H), 4.32 (m, 1H), 3.18 (m, 2H), 2.53 (s, 3H), 1.63 (m, 2H), 1.42-1.27 (m, 14H), 0.90 (t, 3H). ^{13}C NMR (101 MHz, $CDCl_3$) δ 158.02, 154.44, 151.78, 151.61, 125.99, 110.91, 110.16, 106.32, 97.48, 43.49, 31.88, 29.56, 29.54, 29.37, 29.30, 29.13, 27.05, 22.68, 19.25, 14.12.

4-(7-(Decylamino)-4-methyl-2-oxo-2H-chromen-3-yl)benzaldehyde (18)

In a microwave vial, **17** (1 g, 2.5 mmol), formylphenylboronic acid (570 mg, 3.8 mmol) and $Pd(PPh_3)_4$ (146.5 mg, 0.13 mmol) were added. The flask was degassed under vacuum for 30min. In the meantime a solution of dimethoxymethane (30 mL), MQ water (4 mL) and potassium carbonate (1.05 g, 7.6 mmol) was prepared and de-oxygenated by bubbling with nitrogen gas for 10 min. This solution was added to the sealed microwave vial containing the solids using a syringe, and the mixture was de-oxygenated by bubbling nitrogen and performing nitrogen/vacuum cycles, ending by a slight vacuum. The mixture was left to react at 100°C overnight, progressively becoming orange. The solvent was evaporated, and the crude product purified by column chromatography on silica gel (chloroform:ethyl acetate=20:1) to yield **18** (840 mg, 79% yield) as a yellow/orange solid.

^{1}H NMR (400 MHz, $CDCl_3$) δ 10.05 (s, 1H), 7.96 (d, 2H), 7.50 (d, 2H), 7.44 (d, 1H), 6.55 (d, 1H), 6.48 (s, 1H), 4.31 (m, 1H), 3.20 (m, 2H), 2.24 (s, 3H), 1.64 (m, 2H), 1.42-1.27 (m, 14H), 0.90 (t, 3H). ^{13}C NMR (101 MHz, $CDCl_3$) δ 191.94, 161.37, 155.29, 151.77, 149.05, 141.91, 135.52, 131.44, 129.62, 126.19, 120.25, 110.66, 110.43, 97.62, 43.53, 31.89, 29.57, 29.54, 29.39, 29.31, 29.17, 27.06, 22.68, 16.47, 14.12.

Coum-BDP-1t (19)

In a well dried 250 mL round-bottom flask, distilled methylpyrrole (200 μL, 2.38 mmol) and **18** (500 mg, 1.2 mmol) were dissolved in anhydrous dichloromethane (150 mL). The mixture was de-oxygenated by bubbling nitrogen gas for 30min. Trifluoroacetic acid (100 uL) was added. The flask was de-oxygenated by performing nitrogen gas/vacuum cycles, and put under slight vacuum. The reaction was performed at room temperature for 3h. After that, 2,3-dichloro-5,6-dicyano-1,4-benzoquinone (559 mg, 2.46 mmol) in anhydrous dichloromethane (30 mL) was added. The reaction mixture was purged once more with nitrogen gas for 10min, and left to react for 1h in total. Triethylamine (8 mL, 57.0 mmol), pre-purged with nitrogen gas was added, and a minute later, pre-purged boron trifluoride etherate (8 mL, 64.8 mmol). The flask was de-oxygenated by performing nitrogen gas/vacuum cycles, and put under slight vacuum. The reaction was performed at room temperature overnight. The solution was then washed with MQ water, dried over magnesium sulfate, and the solvent was evaporated. The crude product was purified by column chromatography on silica gel (hexane:ethyl acetate = 2:1) to yield **coum-BDP-1t** (75 mg, 10.3% yield) as a bright orange/red solid. ^{1}H NMR (400 MHz, $CDCl_3$) δ 7.58 (d, 2H), 7.47 (m, 3H), 6.83 (s, 2H), 6.57-6.29 (d,s,d, 4H), 4.29 (s, 1H), 3.21 (m, 2H), 2.67 (s, 6H), 2.30 (s, 3H), 1.69 (m, 2H), 1.43-1.29 (m, 14H), 0.90 (t, 3H). ^{13}C NMR (101 MHz, $CDCl_3$) δ 161.69, 157.56, 155.22, 151.64, 148.95, 142.32, 137.27, 134.48, 133.37, 130.59, 130.54, 130.31, 126.18, 120.46, 119.41, 110.65, 97.63, 43.55. HRMS (ESI) calcd for $C_{37}H_{42}BF_2N_3O_2$ $[2M+Na]^+$, 1241.6492; found, 1241.6557.

Coum-BDP-2t (20)

Coumarin-BDP-1t (40 mg, 65.6 μmol) was dissolved in anhydrous dichloro-

methane (26 mL). The solution was cooled in an ice bath, and triphosgene (39 mg, 0.13 mmol) was slowly added, at ice bath. The reaction was performed at room temperature for 1h. The solvent was evaporated, the flask put in an ice bath. Anhydrous dichloromethane (34 mL), N,N-diisopropylethylamine (36 μL, 0.2 mmol), and dodecylamine (26 mg, 0.14 mmol) in dichloromethane (10 mL) were added. The mixture was then stirred at room temperature overnight. The solvent and excess of N,N-Diisopropylethylamine were evaporated, and the crude product was purified using column chromatography on silica gel (hexane:ethyl acetate = 4:1) to yield 12 mg of what the NMR showed to be an acyl chloride derivative, not yet substituted with a dodecyl tail. The product was dissolved in anhydrous tetrahydrofuran (300 mL). Potassium phosphate tribasic (5 mg, 23.5 μmol) and dodecylamine (4 mg, 21.6 μmol) were added. The flask was put under a nitrogen atmosphere, and the reaction was performed at room temperature overnight. The solvent was evaporated and the crude product run over a short silica plug (hexane:ethyl acetate = 4:1), and then over a longer silica column (hexane:ethyl acetate = 1:1) to remove the excess of dodecylamine and yield **coum-BDP-2t** (5.6 mg, 12.7% yield) still containing 0.9 equivalent of free dodecylamine. To improve this step, the first step of the reaction (acyl chloride formation) should be performed as described, without adding the dodecylamine yet. The latter should have only been added during the second step. ^{1}H NMR (400 MHz, $CDCl_3$) δ 7.76 (d, 1H), 7.63 (d, 2H), 7.46 (d, 2H), 6.82 (s, 2H), 6.31 (d, 2H), 4.38 (m, 1H), 3.77 (m, 2H), 3.23 (m, 2H), 2.68 (s, 6H), 2.41 (s, 3H), 1.54-1.25 (m, m, 29H), 0.90 (t, 6H). ^{13}C NMR (101 MHz, $CDCl_3$) δ 160.32, 157.87, 156.25, 153.52, 147.53, 145.82, 135.95, 134.19, 130.46, 130.08, 126.46, 126.25, 123.66, 119.54, 118.76, 115.38, 49.47, 41.03, 40.72, 31.92, 31.89, 30.22, 30.15, 29.66, 29.64, 29.60, 29.57, 29.54, 29.37, 29.35, 29.29, 28.78, 26.92, 26.80, 22.68, 16.86, 14.95. HRMS (ESI) calcd for $C_{50}H_{67}BF_2N_4O_3$ $[M+Na]^+$, 843.5141; found, 843.1592.

Coum-BDP-+-1t (21)

In a microwave vial, **coumarin-BDP-1t** (20 mg, 32.8 μmol) was dissolved in anhydrous dimethylformamide (0.5 mL). Methyl iodide (320 μL, 5 mmol) was added in excess. The reaction was performed at 40°C for 48h. The mixture was diluted with dichloromethane, washed with MQ water, and dried over magnesium

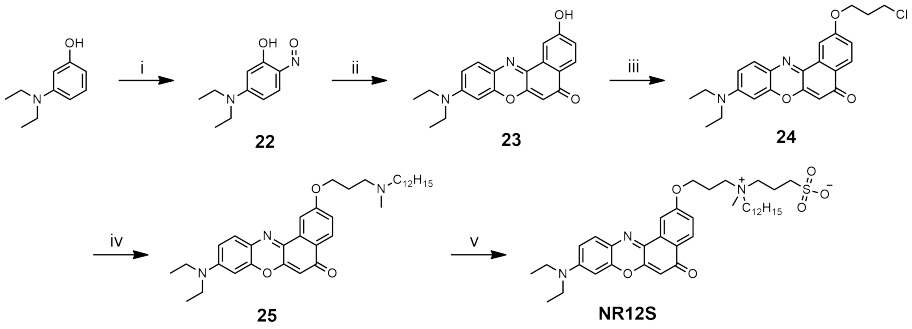

Figure 2.8: Synthesis pathway of NR12S

sulfate. The solvent was then evaporated and the crude product run over a short silica plug (hexane:ethyl acetate = 4:1) to remove the uncharged product. The quaternized product was flushed out of the column with methanol. The product was run through a Dowex plug with methanol, and the solvent evaporated to give **coum-BDP-+-1t** (12 mg, which would correspond to 57% yield). The product still contains a small amount of silica, visible as tiny spherical particles. Any protocol mentioning flushing of a polar compound out of a silica column using 10% methanol or more is most likely to obtain a product that contains residual silica. HRMS (ESI) calcd for $C_{39}H_{47}BF_2N_3O_2^+$ $[M]^+$, 638.3700; found, 638.3708.

2.2.2 Chemical polarity probe - NR12S

The group of A. Klymchenko, in Strasbourg, has developed a set of solvatochromic probes to visualize variations in plasma membrane microenvironment. A subsection of them, based on a Nile Red unit, is sensitive to changes in membrane hydration and surface charge, transmembrane potential, or lipid order. NR12S is one of them; due to its high sensitivity to membrane hydration, it has allowed visualization of lipid domains in model membranes, and monitoring of the lipid order in mammalian cell membranes using ratiometric imaging. Its synthesis takes place in five steps, depicted in Figure 2.8, and described further in this section. They follow the protocols described in reference [2].

5-(Diethylamino)-2-nitrosophenol (22)

M-diethylaminophenol (6 g, 36 mmol) was grinded in a mortar and dissolved in 37% HCl (40 mL). While stirring, the mixture was cooled to 0°C using an ice bath. To the cold solution, a solution of sodium nitrite (2.5 g in 20 mL MQ water) was added dropwise over 40 min, while keeping the temperature between 0-5°C. Once the addition was complete, the reaction mixture was stirred at 0-5°C for 3h. The crude HCl salt was collected by filtration and dried in a vacuum oven overnight. The product was then dissolved in the minimum amount of ethanol, at 100°C, cooled down to 40°C, and diethyl ether was slowly added until the apparition of a solid precipitate. The mixture was then cooled down to room temperature and stored at -20°C overnight for recrystallization to take place. The recrystallized solid was filtered, and dried overnight at 40°C in a vacuum oven, to yield **22** (1.46 g, 21% yield). The yield was much lower than in the reference paper (reported to be 70%), due to an attempt to wash the recrystallized solid with MQ water, which also dissolves the wanted product. ^{1}H NMR (400 MHz, MeOD) δ 7.73 (d, 1H), 7.22 (d, 1H), 6.41 (s, 1H), 3.99 (m, 4H), 1.48 (t, 6H). ^{13}C NMR (101 MHz, MeOD) δ 165.82, 162.64, 144.48, 123.41, 119.59, 13.24, 11.71.

9-(Diethylamino)-2-hydroxy-5H-benzo[a]phen oxazin-5-one (23)

22 (1 g, 5 mmol) and 1,6-dihydroxynaphtalene (0.85 g, 5 mmol) were refluxed (150°C) for 4h in anhydrous DMF (15 mL). This step should have been done under nitrogen atmosphere, which was not specified in the reference paper. The solvent was evaporated under nitrogen flow, and the crude product purified by Silica column chromatography with ethyl acetate:2-propanol=5:2 as eluent to yield **23** (166 mg, 9.6% yield) as a purple solid with green reflections. ^{1}H NMR (400 MHz, DMSO-d6) δ 10.40 (s, 1H), 7.96 (d, 1H), 7.87 (s, 1H), 7.57 (d, 1H), 7.09 (d, 1H), 6.79 (d, 1H), 6.76 (s, 1H), 6.13 (s, 1H), 3.5 (m, 4H), 1.17 (t, 6H). ^{13}C NMR (101 MHz, DMSO-d6) δ 182.83, 161.87, 152.86, 151.94, 147.67, 139.98, 135.02, 132.08, 128.73, 125.12, 119.62, 111.16, 109.38, 105.35, 97.30, 63.29, 45.69, 26.77, 13.77.

2-(3-Chloropropoxy)-9-(diethylamino)-5H-benzo[a]phenoxazin-5-one (24)

23 (110 mg, 0.3 mmol) was dissolved in anhydrous DMF (1.5 mL) and deoxygenated by bubbling nitrogen for 5 min. The mixture was cooled down to

0-5°C using an ice bath. Potassium carbonate (239 mg, 1.7 mmol) and 1-bromo-3-chloropropane (548 mg, 3 mmol) were added. The reaction flask was sealed and de-oxygenated under nitrogen. The reaction was performed for 4h30 at 70°C. The solvent was then evaporated under nitrogen flow. The resulting crude product was triturated with water, filtered, rinsed once with water, triturated with heptane, and rinsed once with heptane. The filtered compound was dried at 40°C in a vacuum oven overnight to yield **24** (120 mg, 89% yield) as a dark violet solid. ^{1}H NMR (400 MHz, $CDCl_3$) δ 8.26 (d, 1H), 8.09 (s, 1H), 7.63 (d, 1H), 7.20 (d, 1H), 6.69 (d, 1H), 6.66 (s, 1H), 6.31 (s, 1H), 4.37 (t, 2H), 3.83 (t, 2H), 3.51 (m, 4H), 2.37 (m, 2H), 1.31 (t, 6H). ^{13}C NMR (101 MHz, $CDCl_3$) δ 183.24, 161.38, 152.11, 150.79, 146.91, 139.99, 134.11, 131.09, 127.83, 125.88, 124.72, 118.25, 109.54, 106.65, 105.34, 96.34, 64.67, 45.08, 41.44, 32.24, 12.62.

9-(Diethylamino)-2-[3-(dodecylmethylamino)propoxy]-5H-benzo[a]phenoxazin-5-one (25)

24 (100 mg, 0.2 mmol) and n-dodecylmethylamine (194 mg, 0.97 mmol) were dissolved in 2-butanone (2 mL). The mixture was de-oxygenated by bubbling nitrogen for 5 min. Potassium carbonate (84 mg, 0.6 mmol) and potassium iodide (43 mg, 0.26 mmol) were added. The mixture was further de-oxygenated by bubbling nitrogen and the flask was sealed and put under nitrogen atmosphere. It might be needed to adjust the volume of 2-butanone, so as to dissolve all the reactants and have a volume suitable for nitrogen bubbling, without drying out the mixture and get a solid deposit along the flask walls. The reaction was performed under reflux at 85°C for 48h. The solvent was evaporated and the crude product purified by silica column chromatography using dichloromethane:methanol=95:5 as eluent, to yield **25** (70 mg, 50%) as a dark violet solid. ^{1}H NMR (400 MHz, $CDCl_3$) δ 8.23 (d, 1H), 8.06 (s, 1H), 7.63 (d, 1H), 7.17 (d, 1H), 6.69 (d, 1H), 6.66 (s, 1H), 6.31 (s, 1H), 4.29 (t, 2H), 3.51 (m, 4H), 2.98 (m, 2H), 2.75 (m, 2H), 2.57 (s, 3H), 1.71 (m, 2H), 1.34 (m, 24H), 0.86 (t, 3H). ^{13}C NMR (101 MHz, $CDCl_3$) δ 131.13, 127.84, 118.20, 109.59, 106.53, 105.30, 96.32, 54.02, 45.09, 31.90, 29.61, 29.55, 29.51, 29.33, 27.17, 22.68, 14.11, 12.62.

N-[3-[[9-(Diethylamino)-5-oxo-5H-benzo[a]phenoxazin-2-yl]oxy]propyl]-

N-methyl-N-(3-sulfopropyl)-1-dodecanaminium (NR12S)

In a well dried, degassed flask, **25** (20 mg, 34.8 μmol) was dissolved in anhydrous acetonitrile (3 mL). The mixture was de-oxygenated by bubbling nitrogen for 5 min. 1,3-propanesultone (50 μL, 57.3 μmol) was added, and the flask was sealed and put under nitrogen atmosphere. The reaction was performed at 80°C for 48h. The solvent was then evaporated and the crude product purified by silica column chromatography (short, 10 cm long, 5cm wide) using dichloromethane:methanol=85:15 as eluent, to yield **NR12S** (20 mg, 82% yield) as a dark violet solid. The product still contains a small amount of impurity, probably unreacted sultone that was added in slight excess. ^{1}H NMR (400 MHz, $CDCl_3$) δ 8.05 (d, 1H), 7.68 (s, 1H), 7.34 (d, 1H), 7.09 (d, 1H), 6.44 (d, 1H), 6.17 (s, 1H), 6.00 (s, 1H), 4.12 (s, 2H), 3.68-3.54 (m, 4H), 3.36-3.16 (m, 7H), 2.99-2.92 (m, 2H), 2.42 (m, 6H), 1.29-1.16 (m, 24H), 0.84 (m, 3H). HRMS (ESI) calcd for $C_{39}H_{57}N_3O_6S$ $[M+H]^+$: 696.40; found, 696.4039.

2.3 Discussion

2.3.1 Tips and tricks on synthesizing BODIPY-based molecular rotors

The yield of the BODIPY-rotor synthesis is very low (typically between 10 and 20%). To increase this yield, distillation of the pyrrole prior to the reaction is necessary, so as to use the reactants as clean and pure as possible. Indeed, even under recommended storage conditions (under inert gas, between 2-8°C), pyrrole polymerizes in time, and undergoes oxidation in the presence of small amounts of oxygen. The more substituents on the pyrrole, the more stable the pyrrole becomes; the α position of the pyrrole ring being the most sensitive to electrophilic substitution, using 2-methylpyrrole instead of normal pyrrole already helps to reduce side reactions of pyrrole substitution or pyrrole dimerization and polymerization. During the synthesis, it is important to work under an oxygen-deprived atmosphere. This is done by purging the reaction mixture with nitrogen gas. As the reaction is not heated, it becomes possible to do the reaction in a sealed flask, under nitrogen and a slightly reduced pressure -to do so, one can apply a slight vacuum before leaving the reaction to perform over an extended period of time-.

Purifying the dipyrromethane intermediate during the BODIPY-rotor synthesis seems to help increase the yield, as seen when comparing the synthesis of (10) to the synthesis of e.g. (1) and (5). In the first case, a purification by column chromatography on silica gel is done after reaction with trifluoroacetic acid and before oxidation with DDQ and ring closure. This allows for a combined yield (step (9) and (10)) of about 36%, i.e. about 10% higher than when the rotor is formed in a one-pot-synthesis. This purification might however not be possible with less stable intermediates.

For the purification of the newly synthesized rotor, it is best to avoid a two-phase extraction step, as during mixing of the organic and aqueous phases, an emulsion is formed and becomes highly stabilized by particles of the insoluble side products. As a result, very little to no decantation happens within hours. It is best to purify the crude product using column chromatography directly. When doing silica column chromatography, a long column is needed to separate all the subproducts. As an example, a column of 5 cm diameter minimum, and about 50-60 cm length was needed with the silica gel used in this study (40-63μm particle size, 60A pore diameter) to ensure full separation in one go. Indeed, apart from having several side products formed, the ring closure step with boron trifluoride etherate generates a black solid, soluble in acetone but not in the needed eluents (commonly dichloromethane or an ethylacetate:hexane mixture), that entraps the products, causing wide migration bands. Moreover, the solid itself tends to saturate the top of the column and to migrate along. To shorten the column, a possibility would have been to use a smaller particle size silica. For purification of the rotor by column chromatography after functionalization with polar groups (e.g. sulfonate, quaternary ammonium), a better option than using silica gel could be to use alumina. In our purification procedures, we could always get the charged product to migrate out of the column by flushing with an eluent containing at least 15% methanol, but this flushing step results into some extent of silica contamination which is hard to quantify. Preventing too strong electrostatic interaction of aminated compounds with the stationary phase by adding a small amount of base (e.g. triethylamine) or sodium iodide to the eluent could also have facilitated migration of the product without requiring the use of methanol.

2.3.2 BODIPY rotor functionalization

Functionalization is desirable to target different subcellular compartments, to increase water-solubility, or to tune the rotor emission to different wavelengths (in order to image microviscosity in different cellular compartments simultaneously). Functionalization can be done on the phenyl ring or on the BODIPY core of the dye, before or after rotor formation. Many reactions have been reported[9, 10], but only few of them are compatible with keeping the rotor properties and microviscosity sensitivity.

To keep the rotor properties, substitution of the phenyl ring should be done in para (or meta) position, but not in ortho position, as it sterically hinders the rotation of the two units with respect to each other, and therefore suppresses the sensitivity to microviscosity. When wanting to substitute the phenyl ring with very bulky groups (e.g. a long poly(ethylene glycol) chain of a hundred repeat units), substitution should be done after rotor formation. In fact, the presence of very bulky groups prevents closure of the BODIPY ring; the resulting product is blue-fluorescent, has a very low quantum yield, and its fluorescence response to viscosity variations is not monotonic. Functionalization with bulky groups in para of the phenyl ring after rotor synthesis does not hinder the rotation, and these rotors have been used to functionalize e.g. long polymer chains and solid substrates[11].

To add functional groups to the BODIPY core, it is possible to either use pyrrole derivatives or to modify the BODIPY core after formation. The latter approach is more risky as it modifies directly the electronic structure of the emitting unit, which might quench the fluorescence, and/or suppress the rotor effect. Again, the functionalization should not be made on the carbon the closest to the phenyl unit (1,7) as it would sterically hinder the rotation. Functionalization can then be done in 2,3,5 or 6 position, or on the Boron atoms. When substituting the BODIPY core with two short poly(ethylene glycol) chains (11 repeat units), in 2 and 6 via a Sonogashira coupling[6] (Figure 2.9), the BODIPY emission maximum gets shifted from 520 nm to 590 nm, and the rotor effect is significantly reduced, with a fluorescence lifetime that varies from 3.3 ns in water to 3.9 ns in 50% PEG10k solution. When performing the substitution on the Boron atoms via Fluorine substitution using a Grignard reagent[6], the rotor effect remains; the

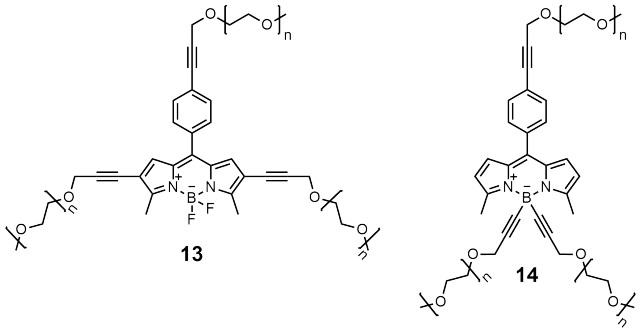

Figure 2.9: BODIPY-based dyes substituted on their emissive core with poly(ethylene glycol) chains (n=11).

probe lifetime varies from 2.7 ns in water to 4.5 ns in 50% PEG10k solution. In the first case the π-conjugation got extended by the presence of an alkyne group, which could lower the energy of the local emitting excited state, and increase the energy barrier that has to be overcome for rotation between the two subunits. In addition, Vu et al.[12], who attached phenanthrene and naphtalene units on carbon 3 and 5 of the BODIPY core to shift the rotor emission to the red by increasing the conjugation length, show that the molecules are no longer responsive to changes in microviscosity. Instead, they respond exclusively to variations in temperature.

These observations suggest that functionalization of the BODIPY core should be done without direct π-conjugation to the substituents, but that the bulkiness of the substituents, in the case of polymer chains that remain relatively short, is not necessarily an issue. This outcome has implications for the tuning of the dyes' emission wavelengths. In order to shift the fluorescence emission to higher wavelengths, one should rely on the mechanism of Förster Resonance Energy Transfer (FRET) rather then on the extension of the conjugation length, and try a substitution on the BODIPY core with a FRET acceptor, keeping the distance between the two units fixed but without direct π-conjugation.

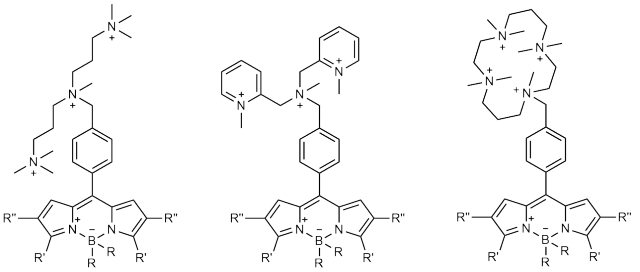

Figure 2.10: New designs for the cell wall-targeting BODIPY rotor. R can be either a fluor atom or a bigger hydrophilic moiety attached by e.g. reaction with a Grignard reagent. R' can be a methyl or an amide group. R" can be a proton or a sulfonate group.

2.4 Outlook

To go further into the optimization of this toolbox of mechanoprobes, we note the benefits of making a new version of the cell wall binding rotor. CWP-BDP targets and reports free volume variations in the cell wall as expected, but its synthesis has a particularly low yield (1.5% combined yield), which makes it time-consuming and expensive. The targeting peptide used to achieve wall binding is a limiting factor, and developing a new probe with properties inspired from CWP-BDP, but without requiring peptide synthesis and attachment would present an advantage. The pectin-binding peptide used in this project has a net charge comprised between +2 (pH 7) and +4 (pH 5) in the range of pH commonly used for plant and oomycete cell studies. From its amino-acid-based composition, it contains numerous amide groups, and carbon atoms arranged in a non-linear fashion. In parallel, we notice that propidium iodide, dye used to label demethoxylated pectins in *Arabidopsis thaliana* cell walls[13], has a chemical structure composed of two positive net charges surrounded by either short but sterically hindering alkyl groups, or by the aromatic rings themselves. The emitting core is also decorated with two amine groups, thereby reducing the amphiphilic character of the molecule. Calcofluor white, which is also a frequently used cell wall stain, features both non-quaternized secondary amine groups and two sulfonate groups. From these examples of cell wall targeting dyes, we can imagine new designs for the molecular rotor. Some design options are represented in Figure

2.10 and are currently being explored in our lab.

2.5 Appendix - Chemical analysis

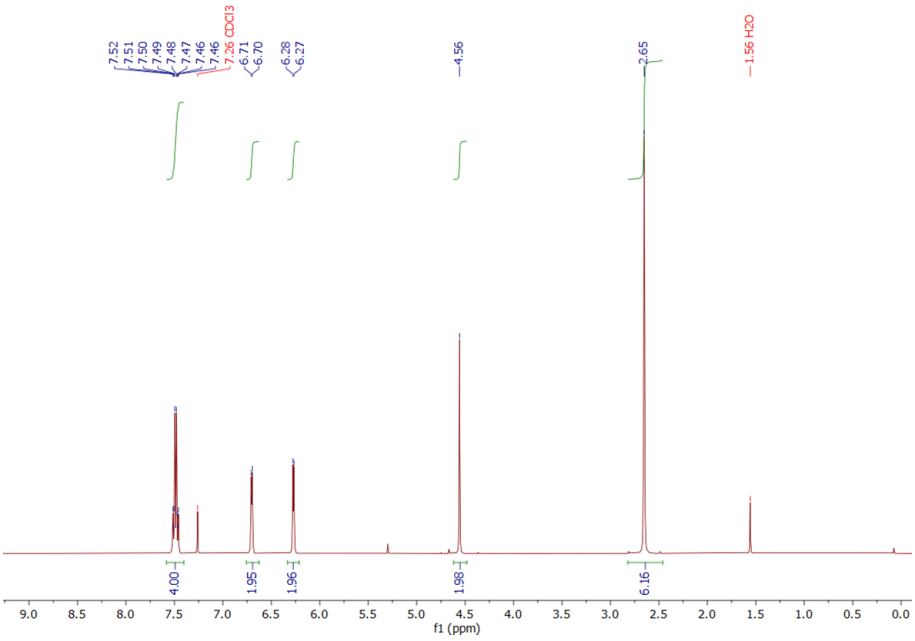

Figure 2.11: ^{1}H NMR spectrum of **1**

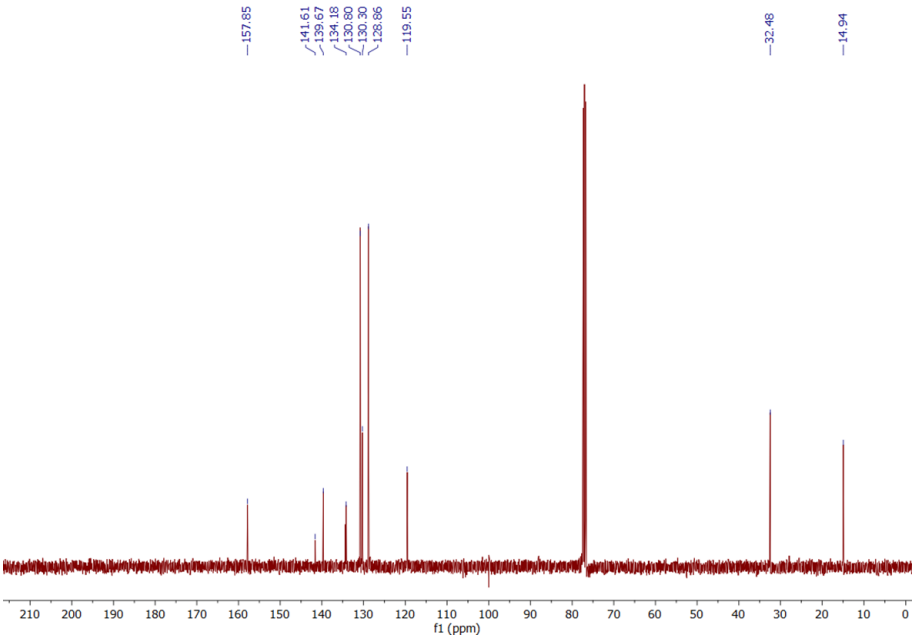

Figure 2.12: ^{13}C NMR spectrum of **1**

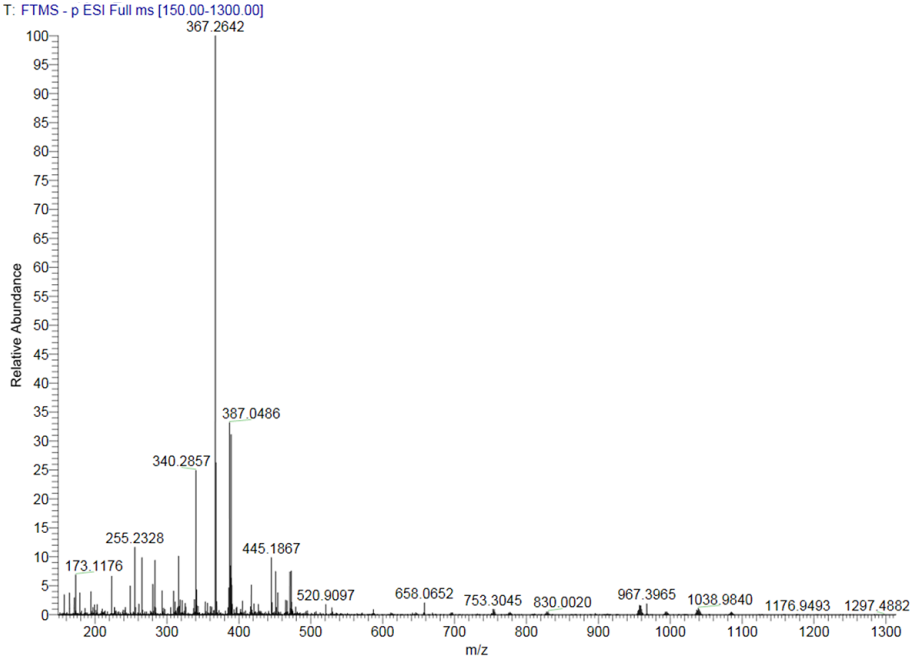

Figure 2.13: HRMS (ESI) spectrum of **1**

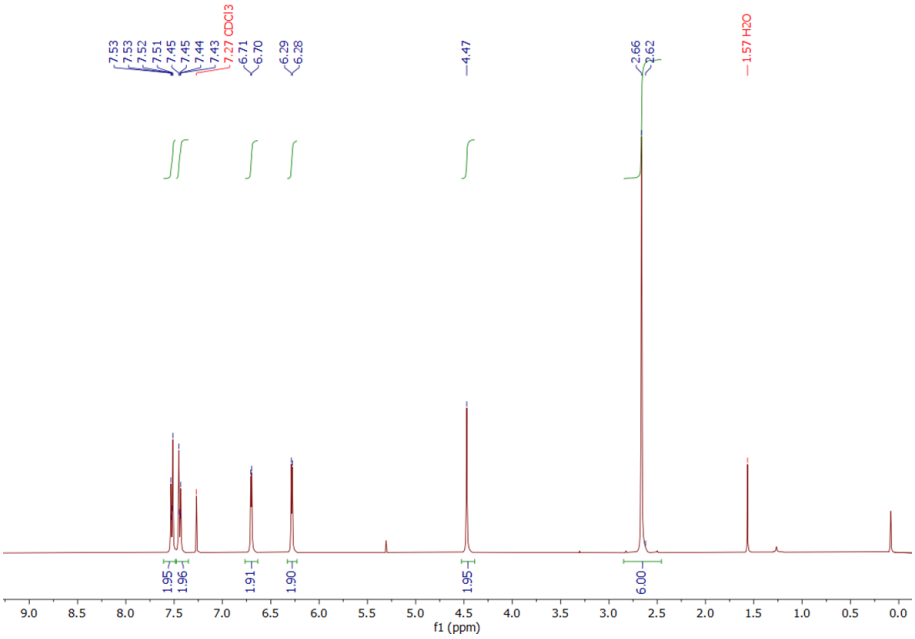

Figure 2.14: ^{1}H NMR spectrum of **2**

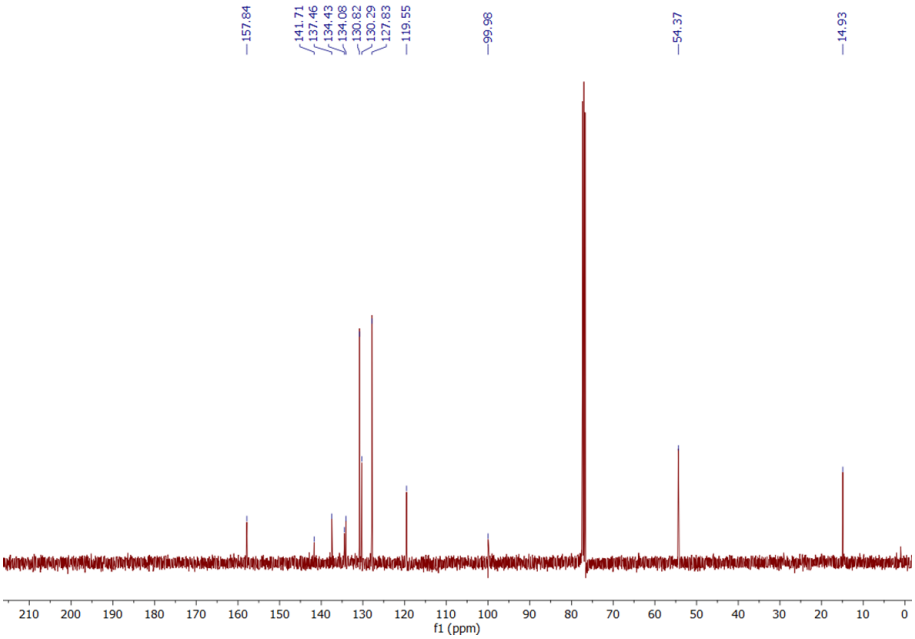

Figure 2.15: ^{13}C NMR spectrum of **2**

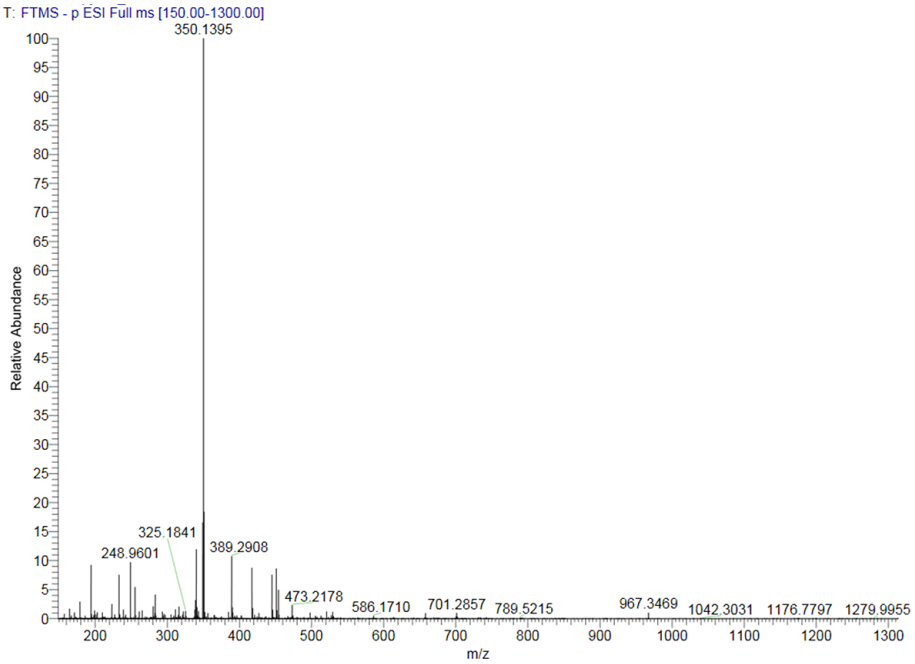

Figure 2.16: HRMS (ESI) spectrum of **2**

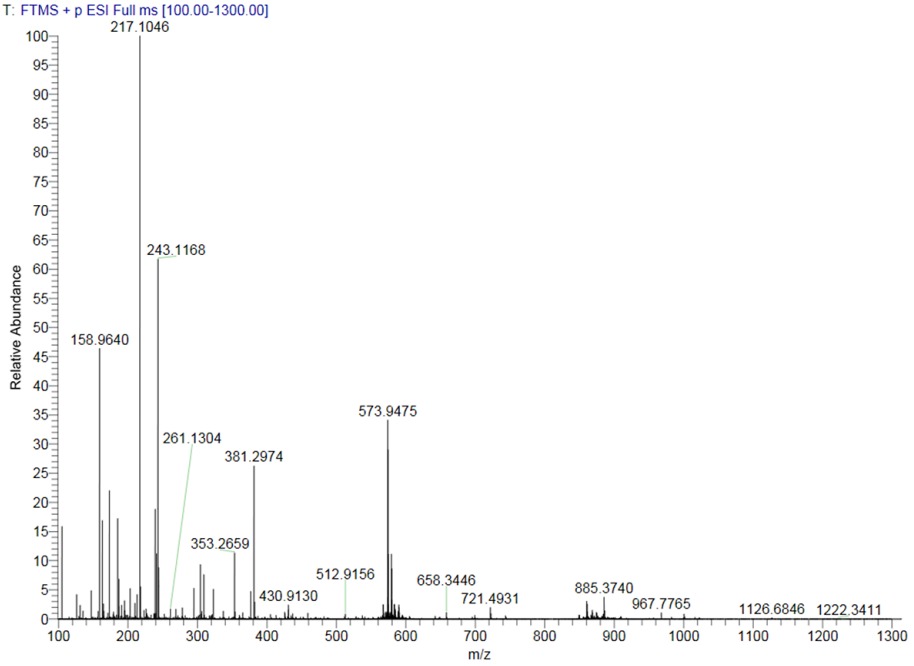

Figure 2.17: HRMS (ESI) spectrum of CWP-BDP

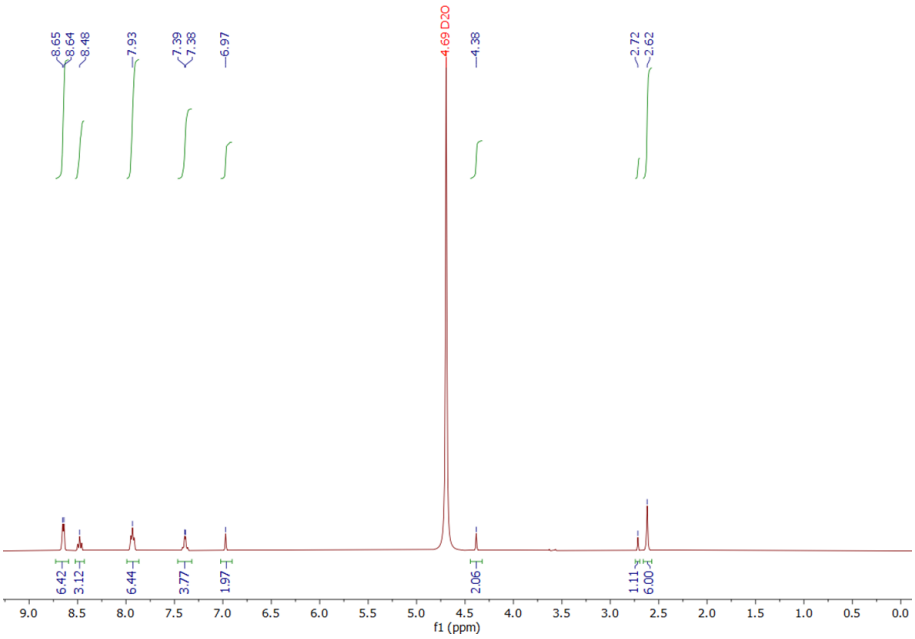

Figure 2.18: ^{1}H NMR spectrum of sulfo-BDP

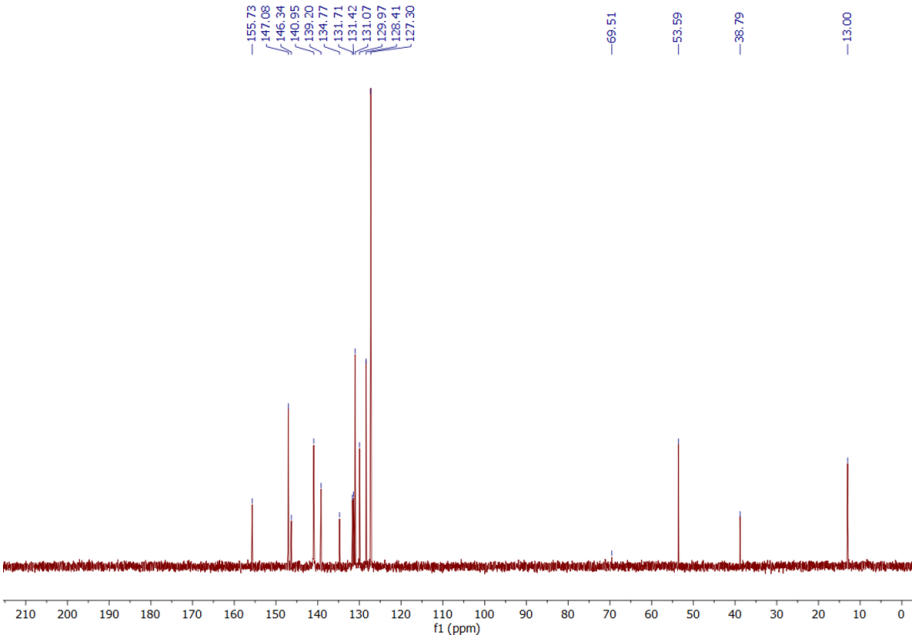

Figure 2.19: ^{13}C NMR spectrum of sulfo-BDP

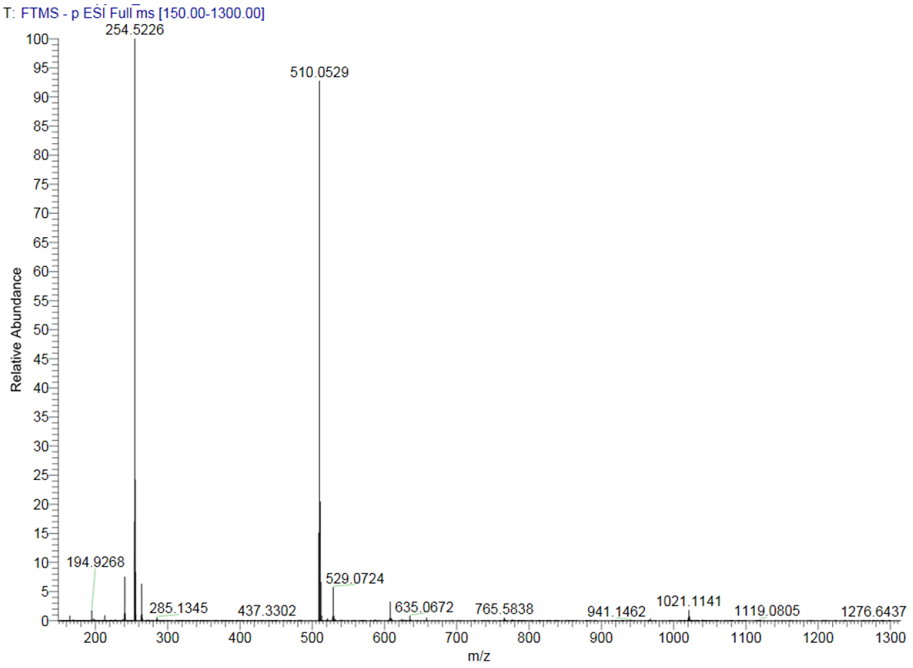

Figure 2.20: HRMS (ESI) spectrum of sulfo-BDP

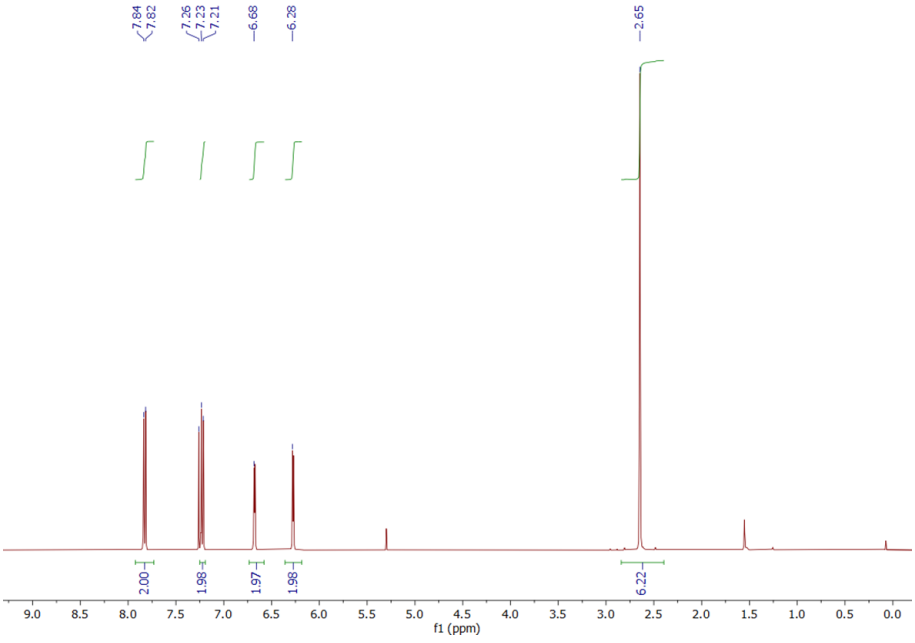

Figure 2.21: ^{1}H NMR spectrum of **5**

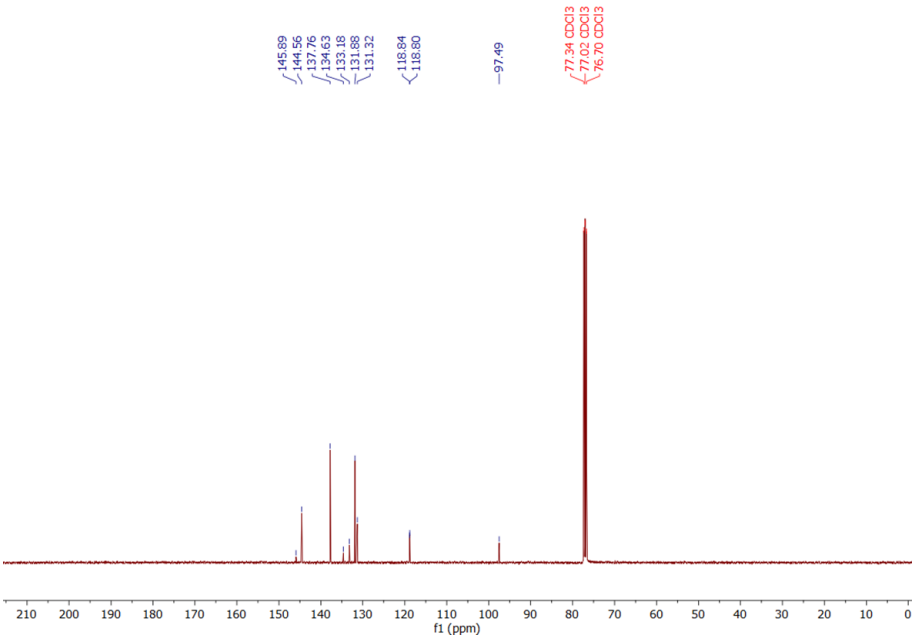

Figure 2.22: ^{13}C NMR spectrum of **5**

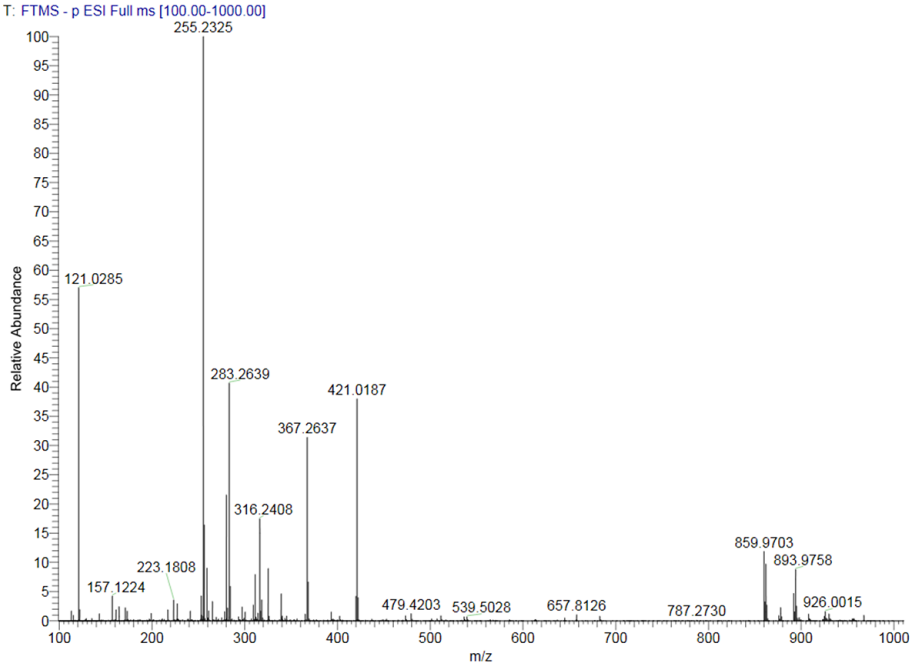

Figure 2.23: HRMS (ESI) spectrum of **5**

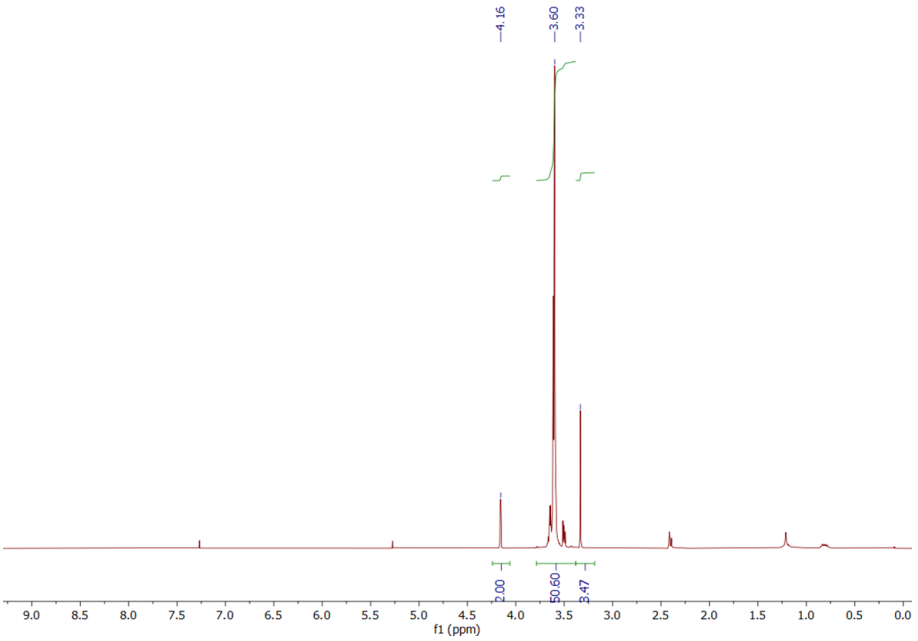

Figure 2.24: ^{1}H NMR spectrum of **6**

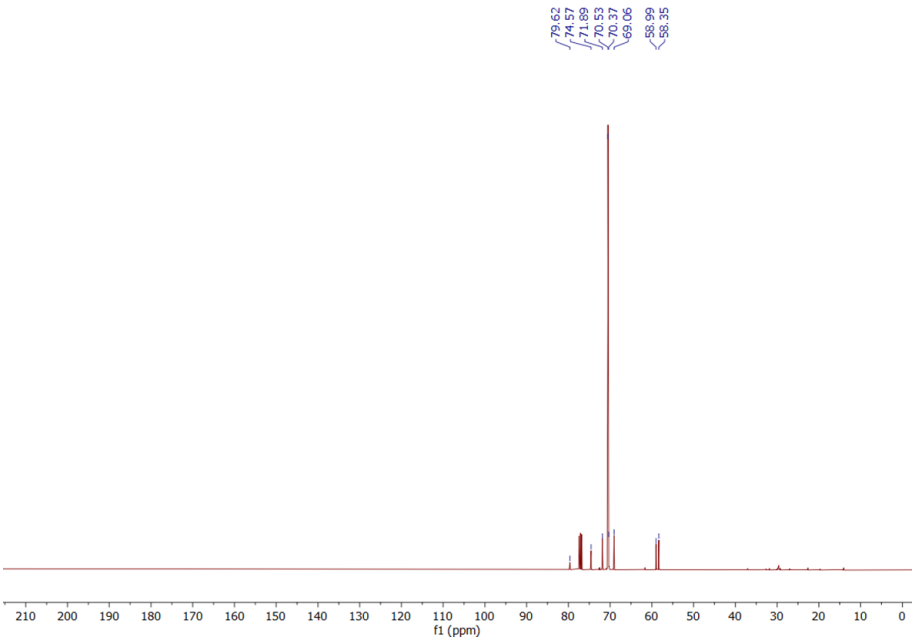

Figure 2.25: ^{13}C NMR spectrum of **6**

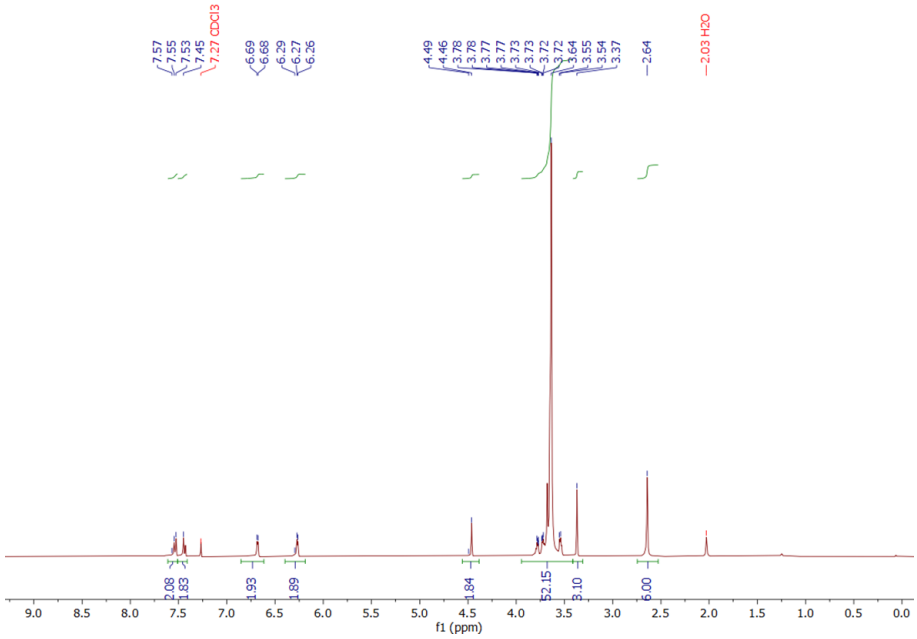

Figure 2.26: ^{1}H NMR spectrum of PEG-BDP

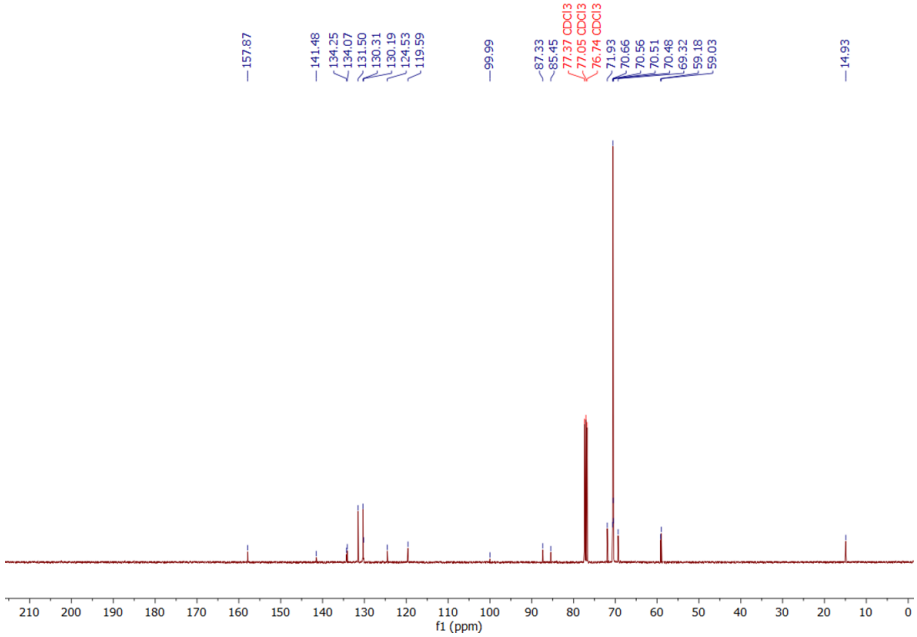

Figure 2.27: ^{13}C NMR spectrum of PEG-BDP

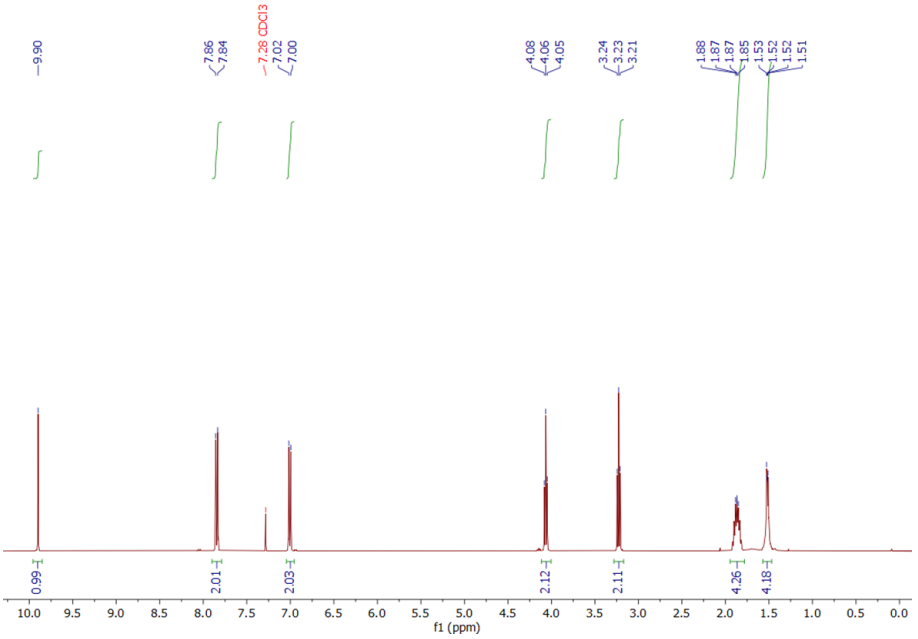

Figure 2.28: ^{1}H NMR spectrum of **8**

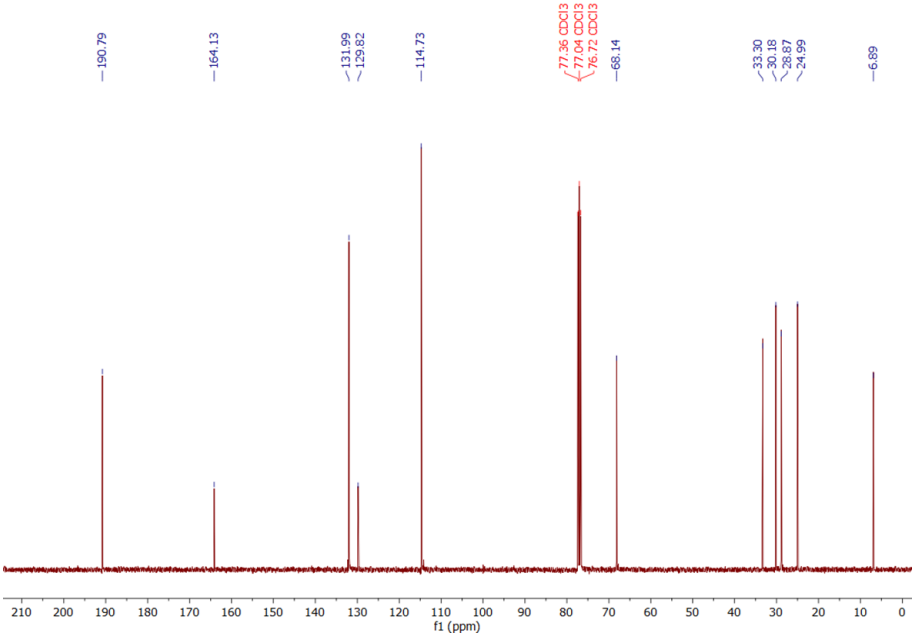

Figure 2.29: ^{13}C NMR spectrum of **8**

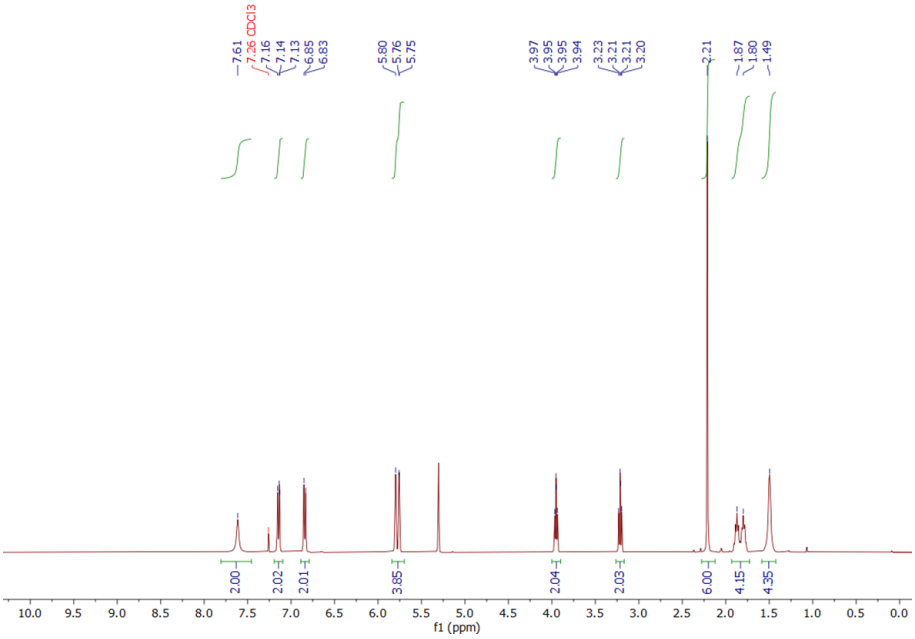

Figure 2.30: ^{1}H NMR spectrum of **9**

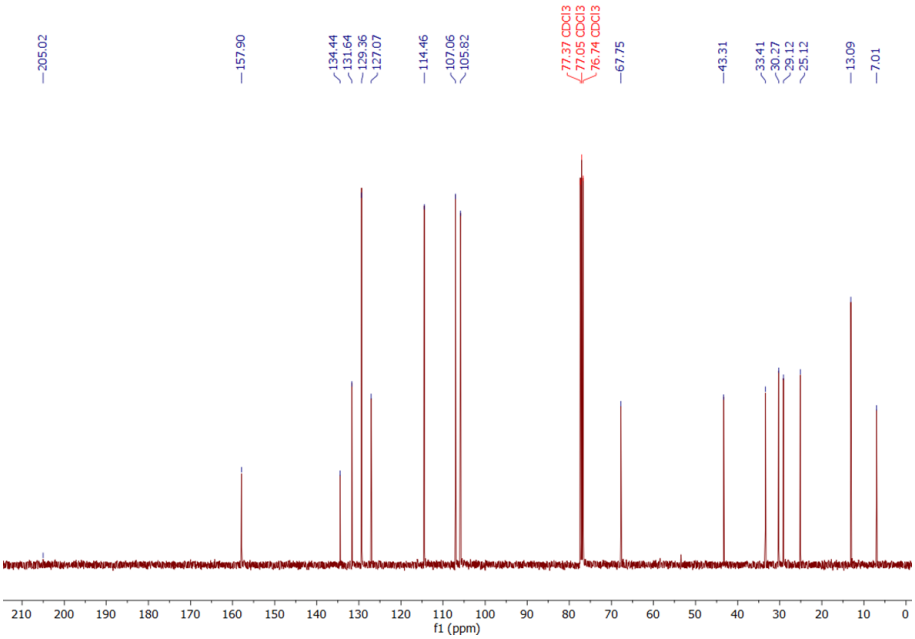

Figure 2.31: ^{13}C NMR spectrum of **9**

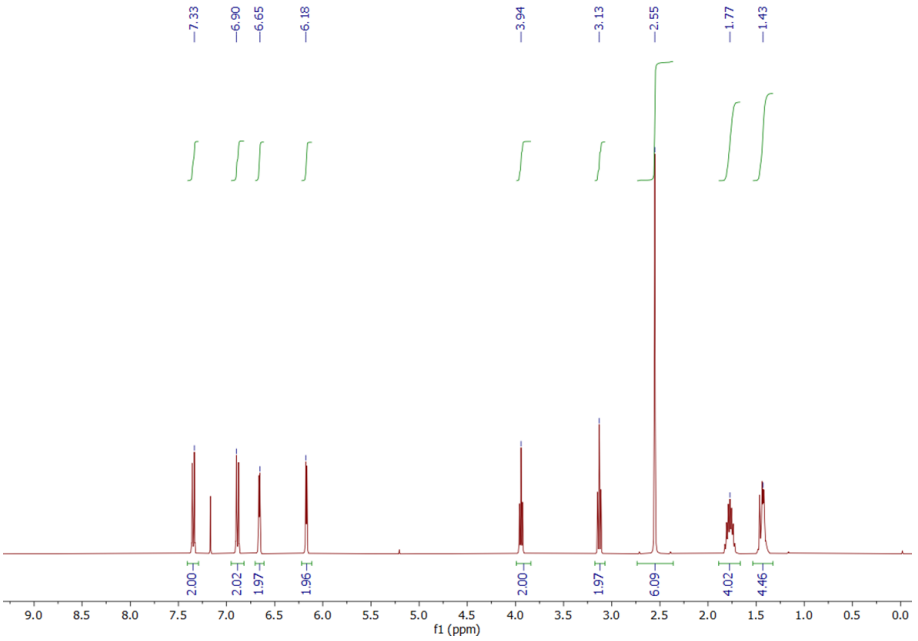

Figure 2.32: ^{1}H NMR spectrum of **10**

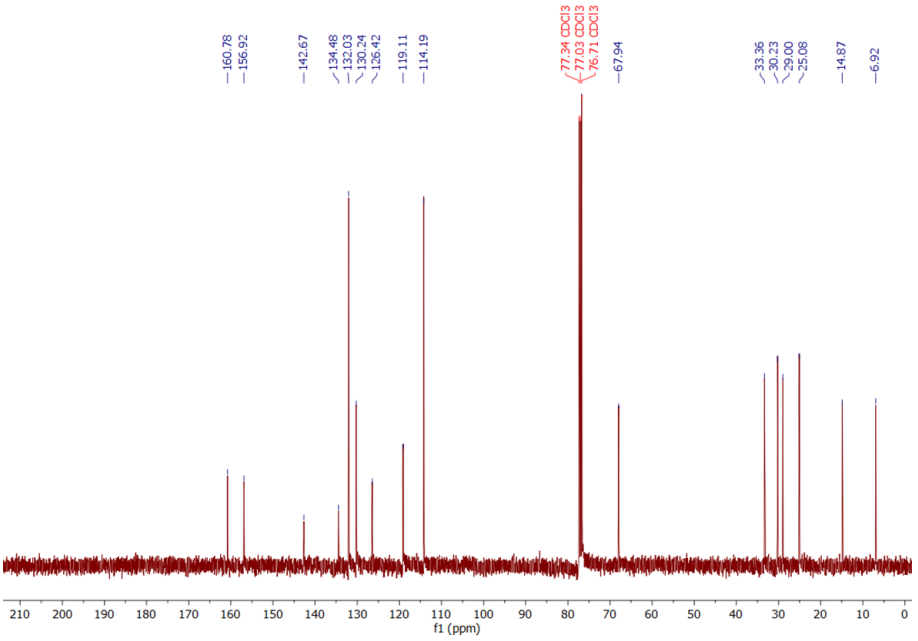

Figure 2.33: ^{13}C NMR spectrum of **10**

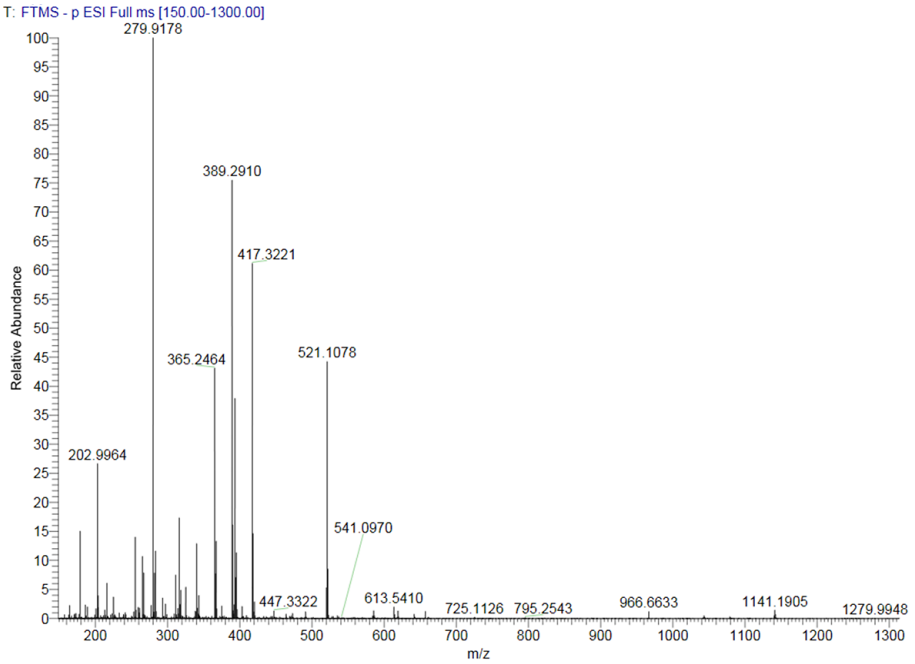

Figure 2.34: HRMS (ESI) spectrum of **10**

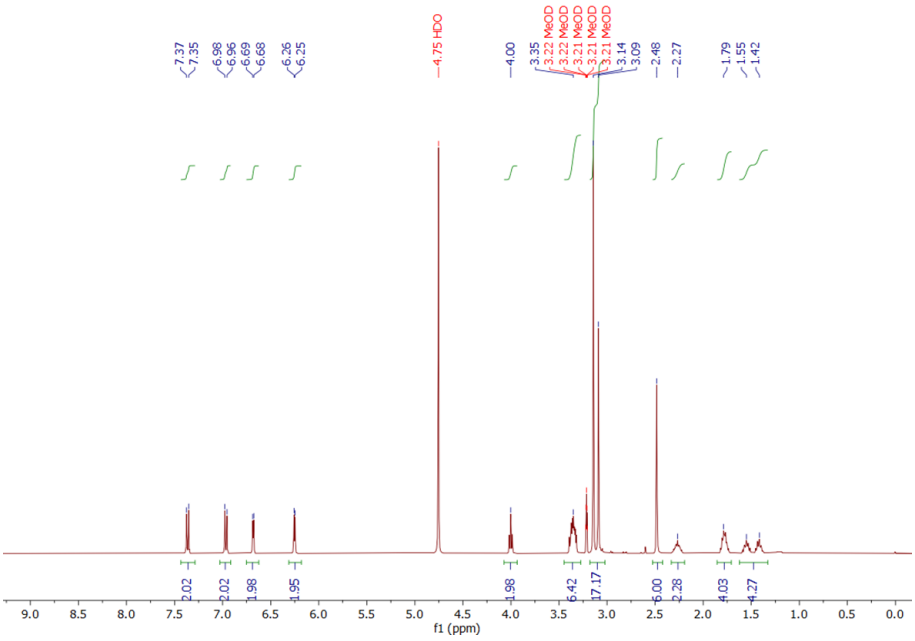

Figure 2.35: ^{1}H NMR spectrum of N+-BDP

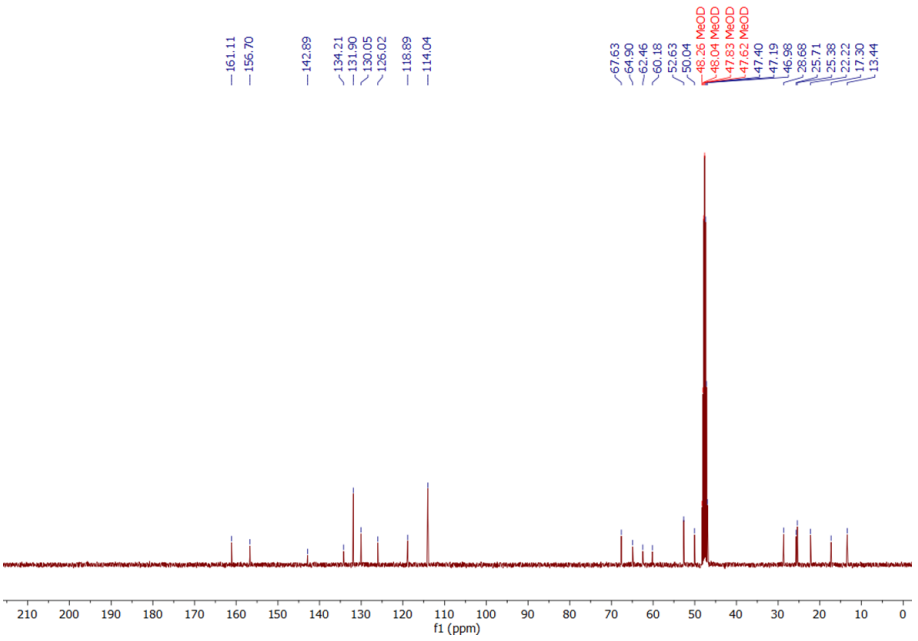

Figure 2.36: ^{13}C NMR spectrum of N+-BDP

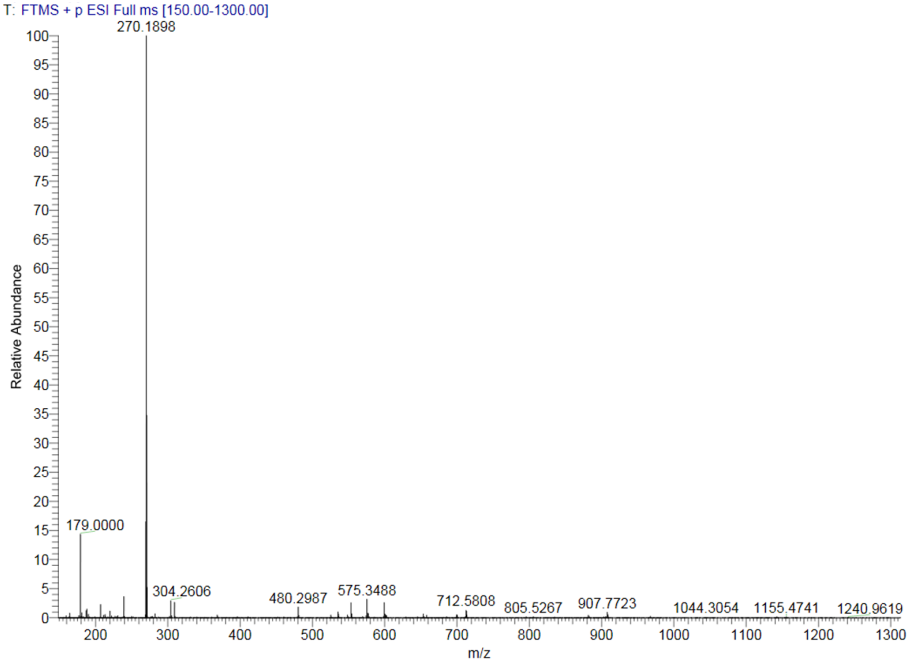

Figure 2.37: HRMS (ESI) spectrum of N+-BDP

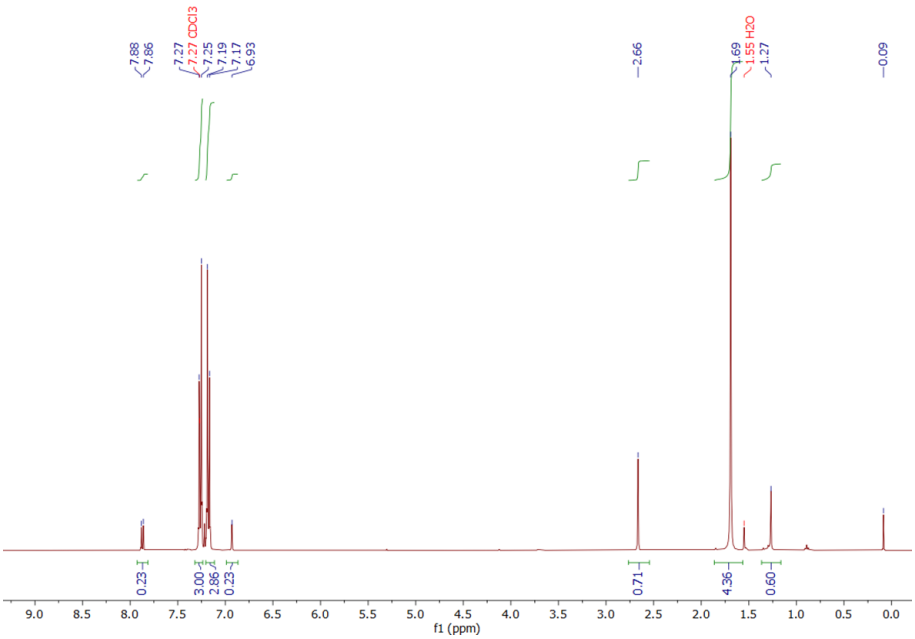

Figure 2.38: ^{1}H NMR spectrum of **12**

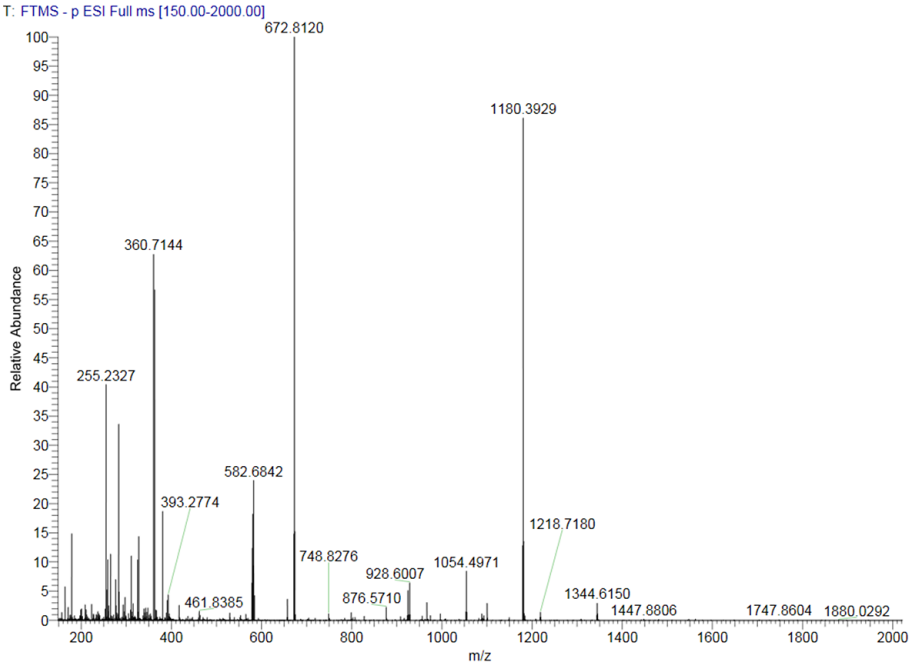

Figure 2.39: HRMS (ESI) spectrum of **12**

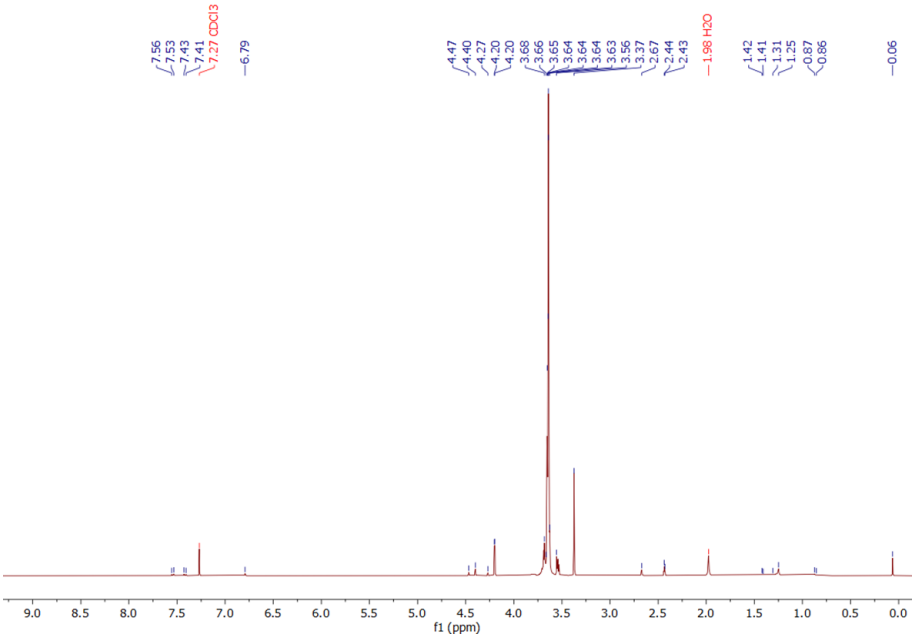

Figure 2.40: ^{1}H NMR spectrum of **14**

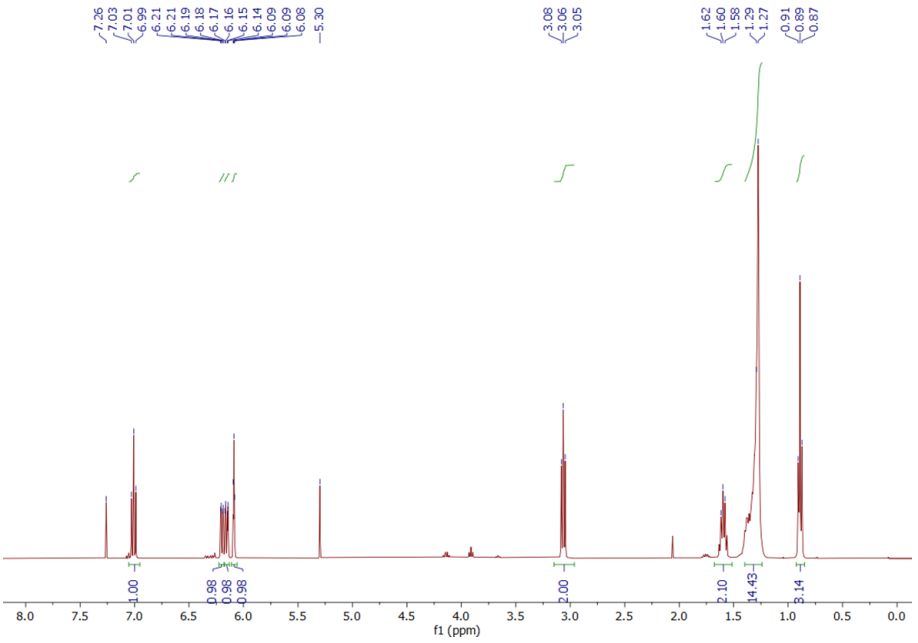

Figure 2.41: ^{1}H NMR spectrum of **15**

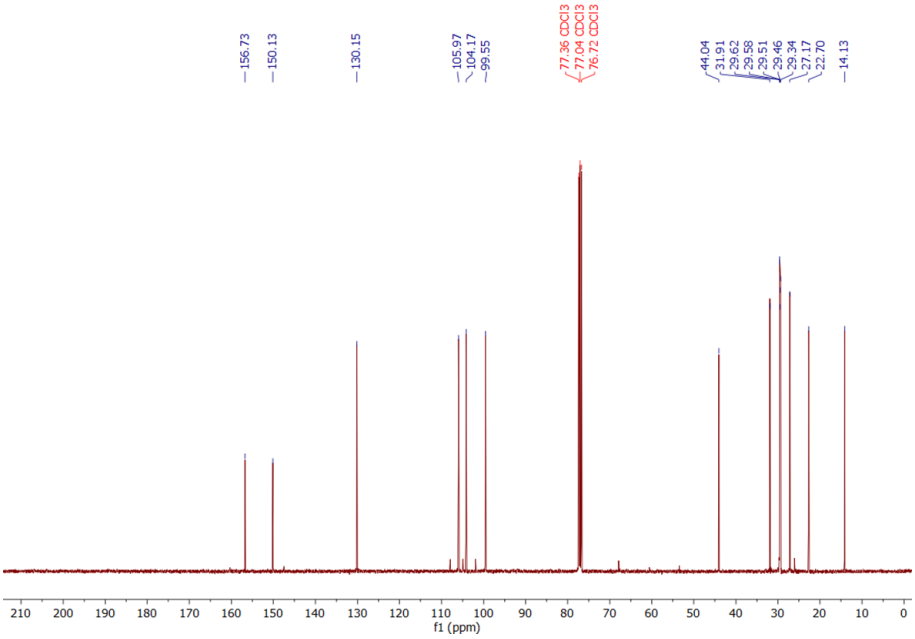

Figure 2.42: ^{13}C NMR spectrum of **15**

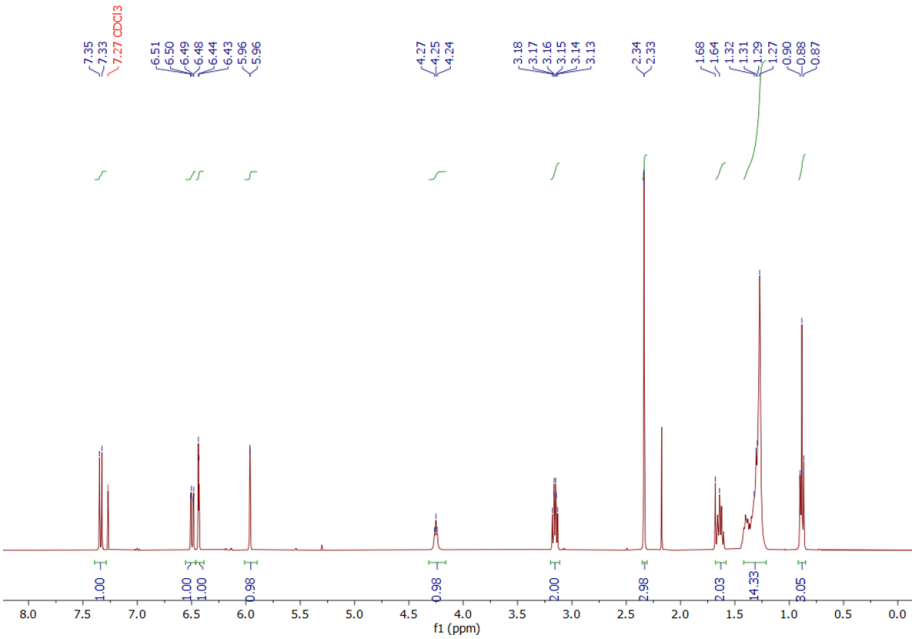

Figure 2.43: ^{1}H NMR spectrum of **16**

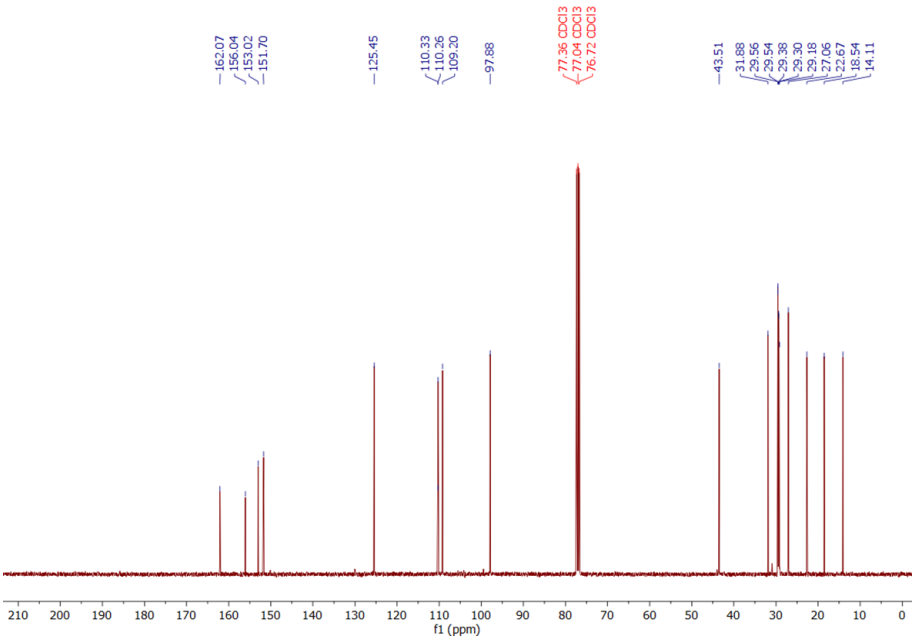

Figure 2.44: ^{13}C NMR spectrum of **16**

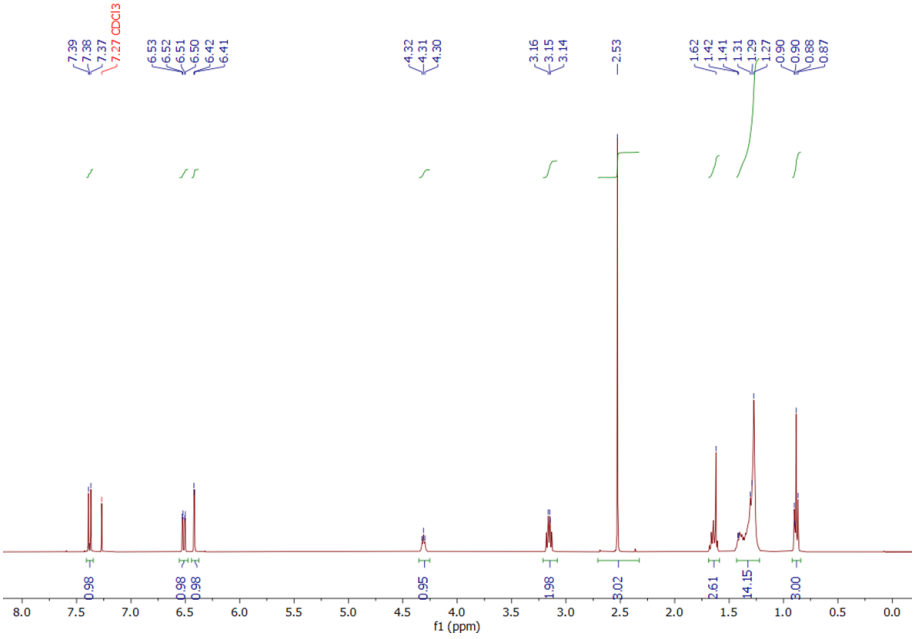

Figure 2.45: ^{1}H NMR spectrum of **17**

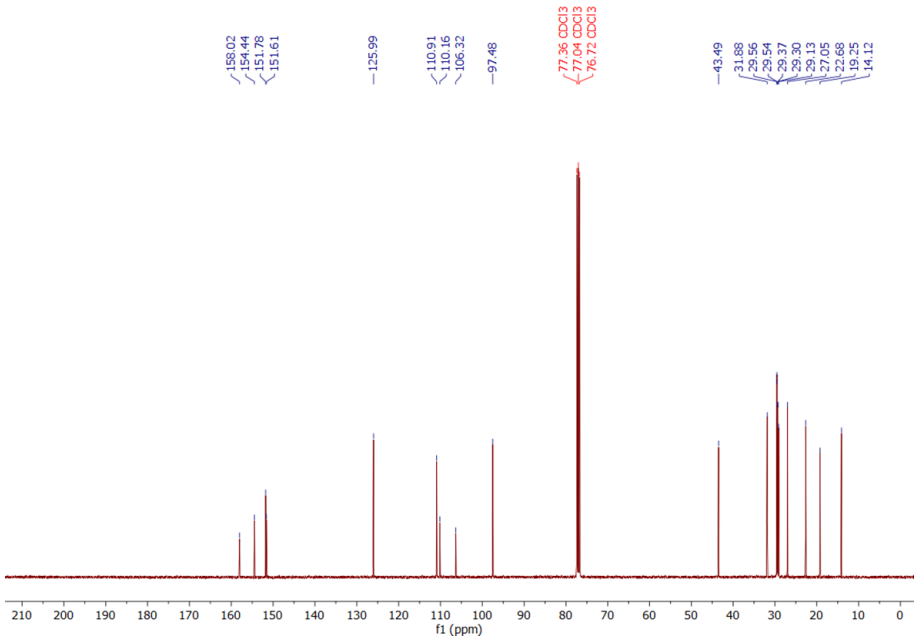

Figure 2.46: ^{13}C NMR spectrum of **17**

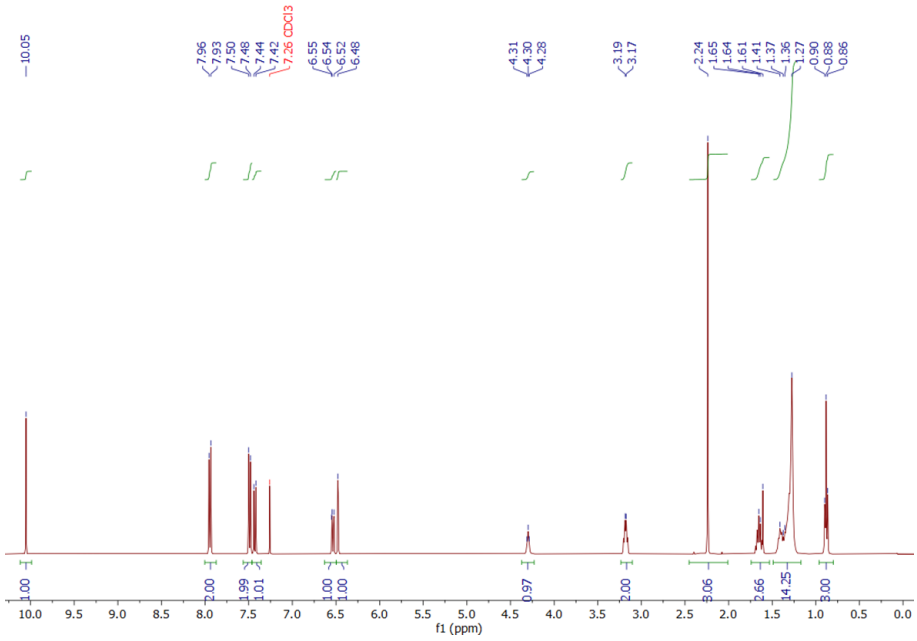

Figure 2.47: ^{1}H NMR spectrum of **18**

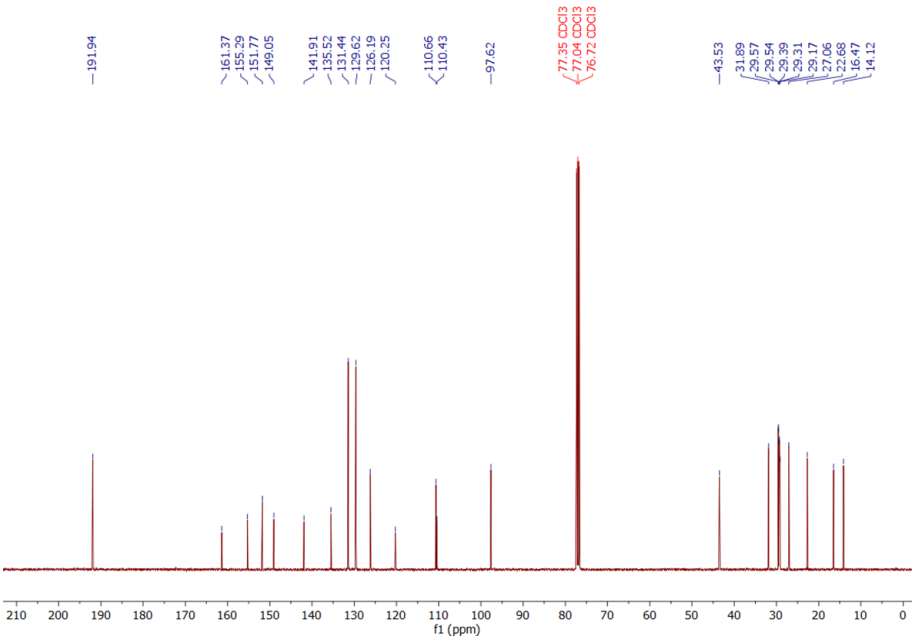

Figure 2.48: ^{13}C NMR spectrum of **18**

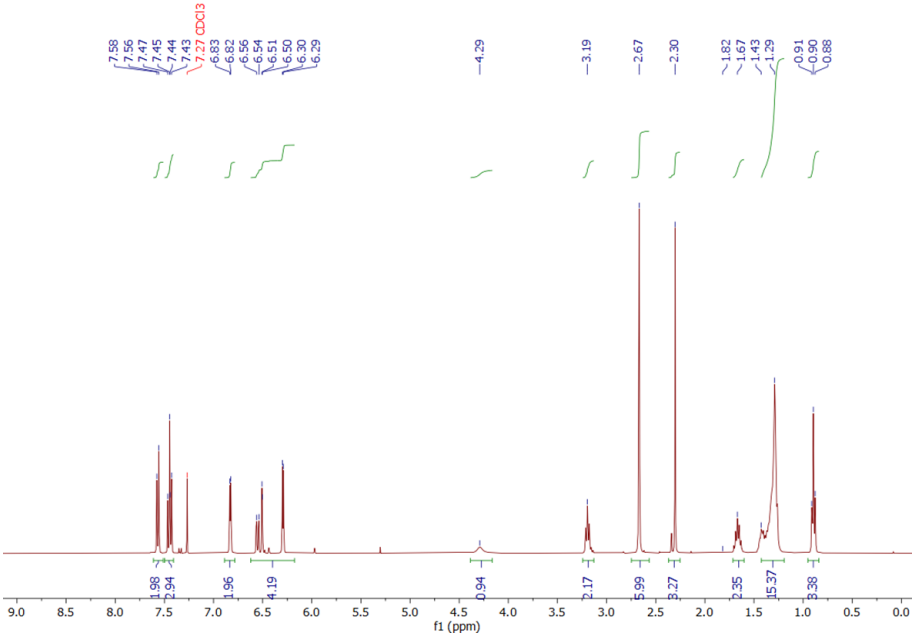

Figure 2.49: ^{1}H NMR spectrum of **coum-BDP-1t**

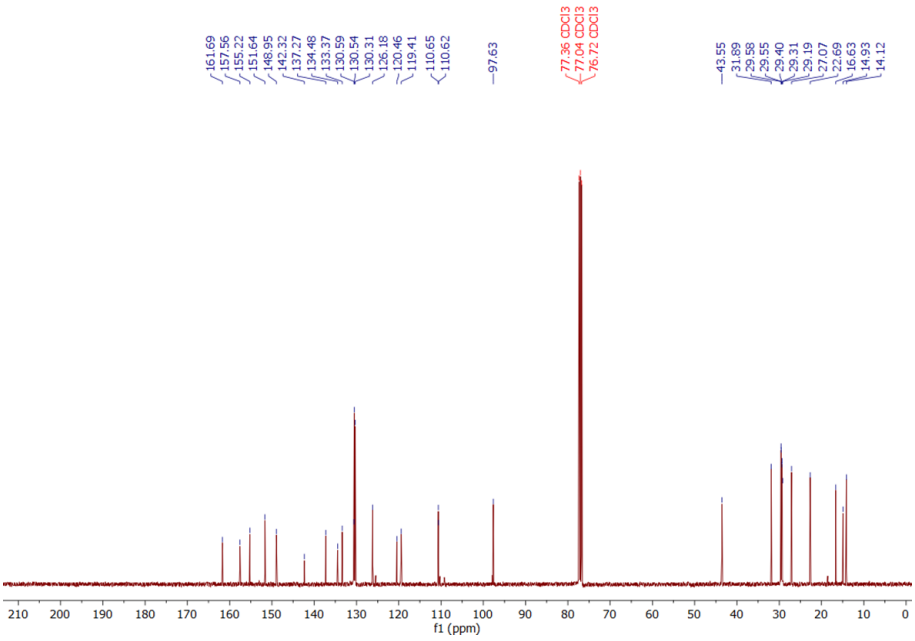

Figure 2.50: ^{13}C NMR spectrum of **coum-BDP-1t**

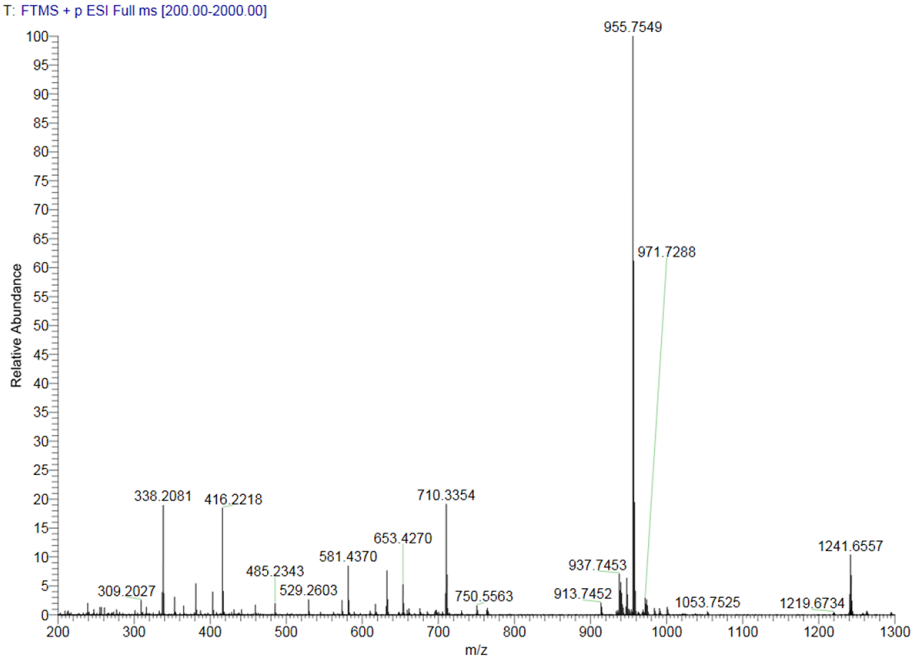

Figure 2.51: HRMS (ESI) spectrum of **coum-BDP-1t**

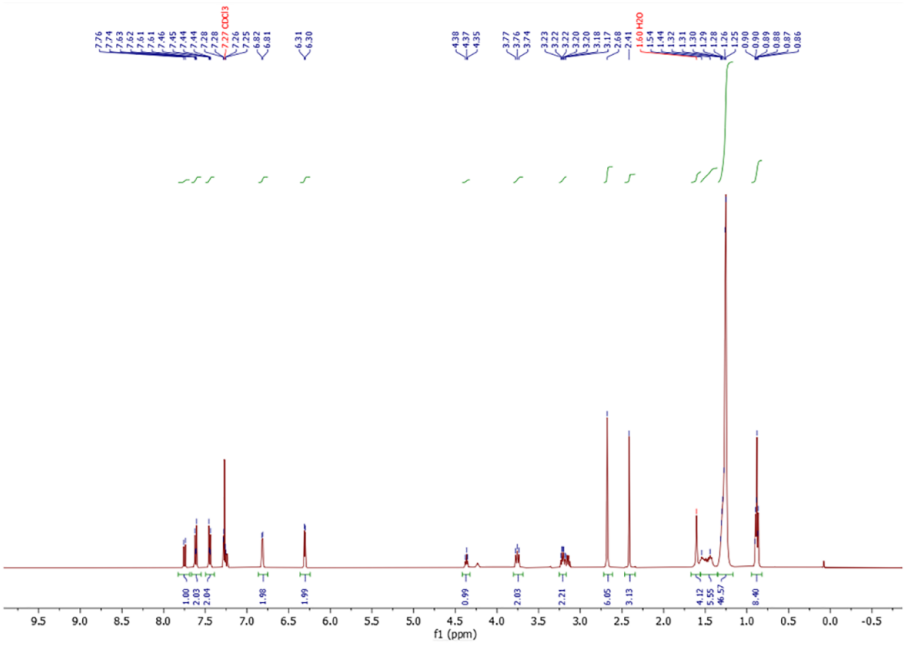

Figure 2.52: ^{1}H NMR spectrum of **coum-BDP-2t**

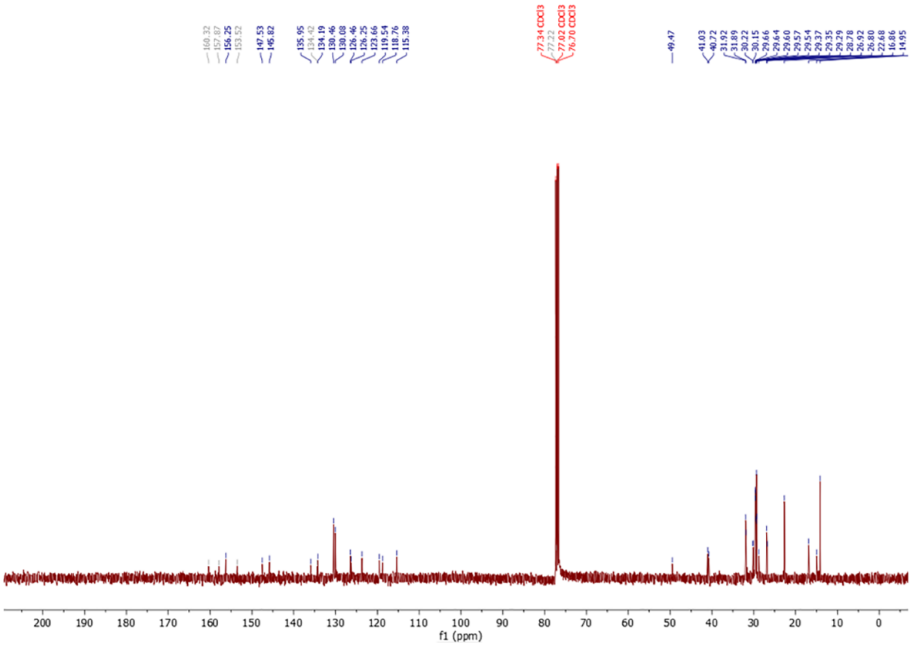

Figure 2.53: ^{13}C NMR spectrum of **coum-BDP-2t**

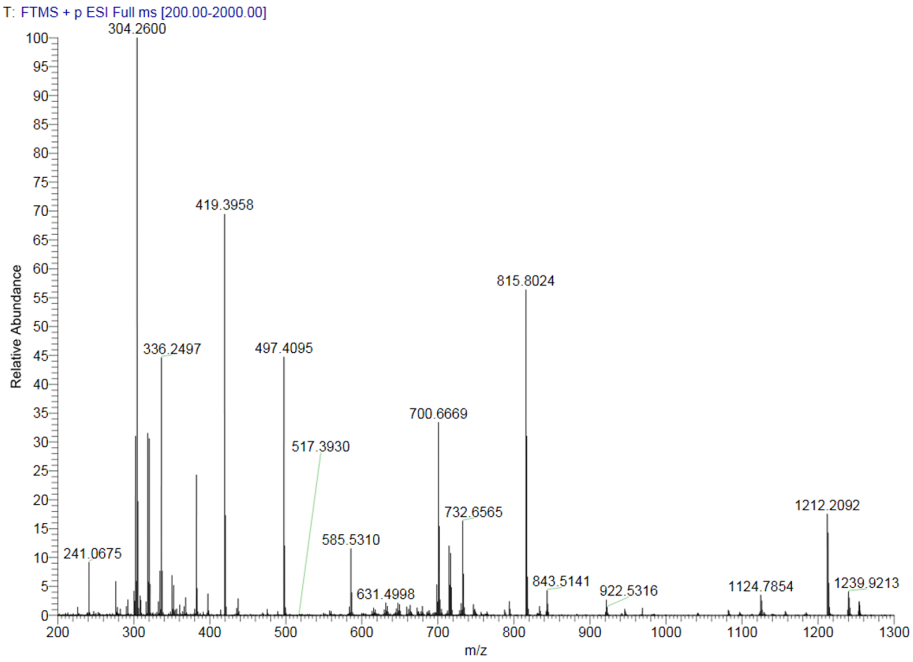

Figure 2.54: HRMS (ESI) spectrum of **coum-BDP-2t**

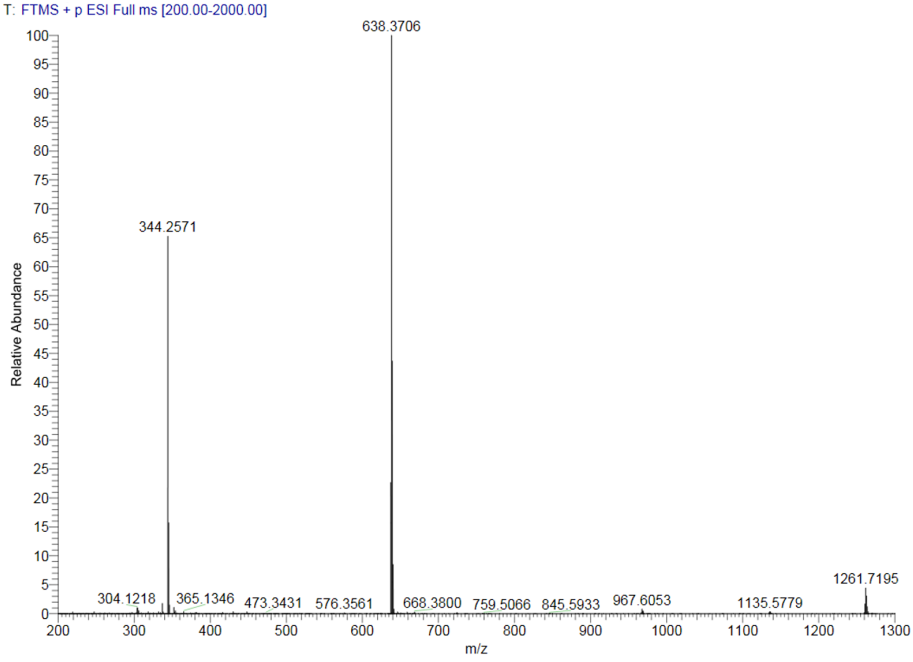

Figure 2.55: HRMS (ESI) spectrum of **coum-BDP-+-1t**

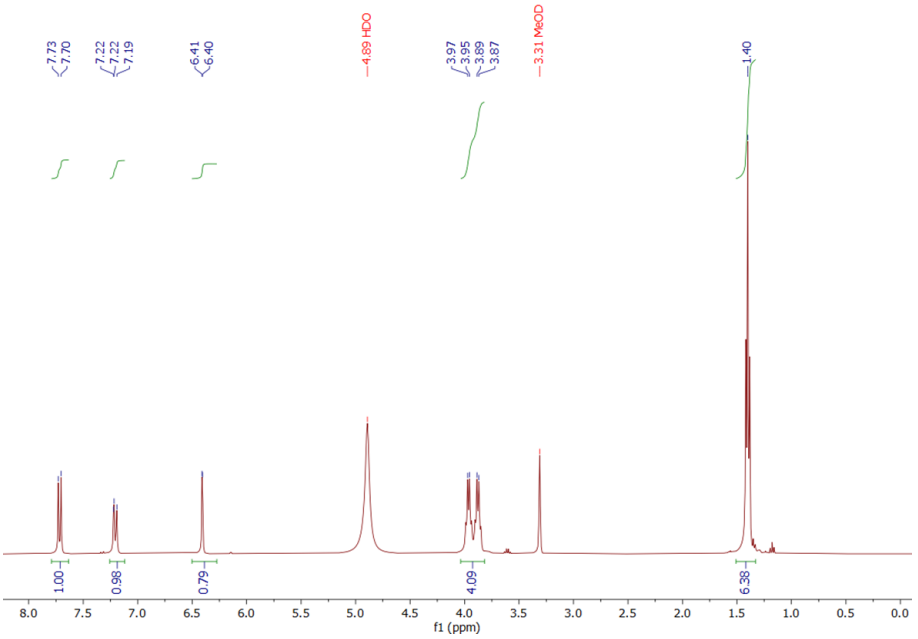

Figure 2.56: ^{1}H NMR spectrum of **22**

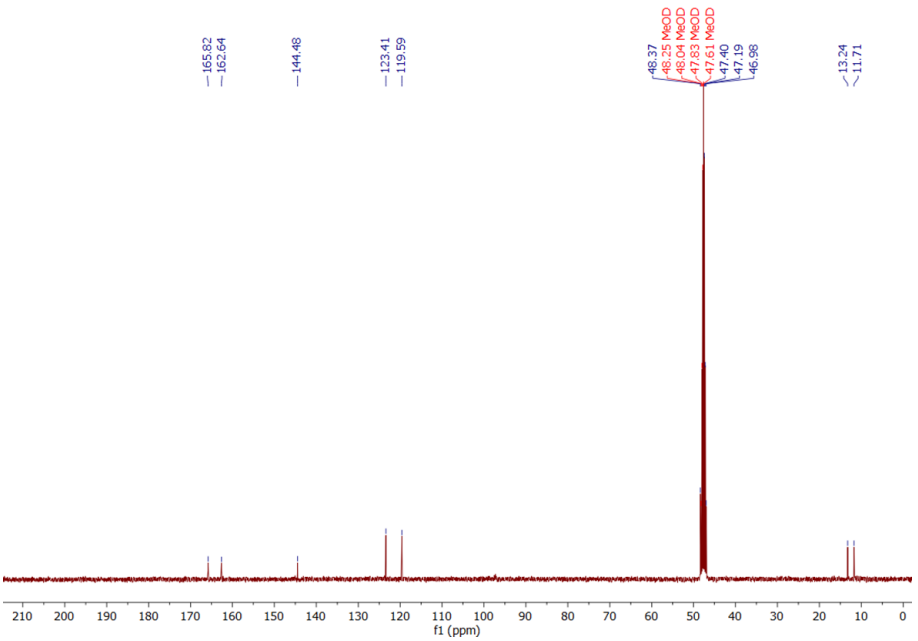

Figure 2.57: ^{13}C NMR spectrum of **22**

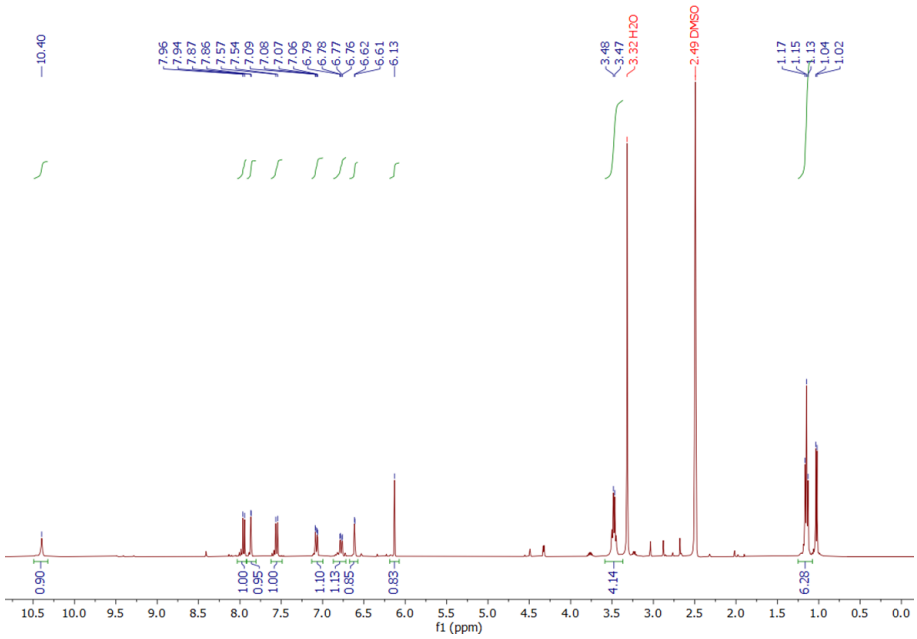

Figure 2.58: ^{1}H NMR spectrum of **23**

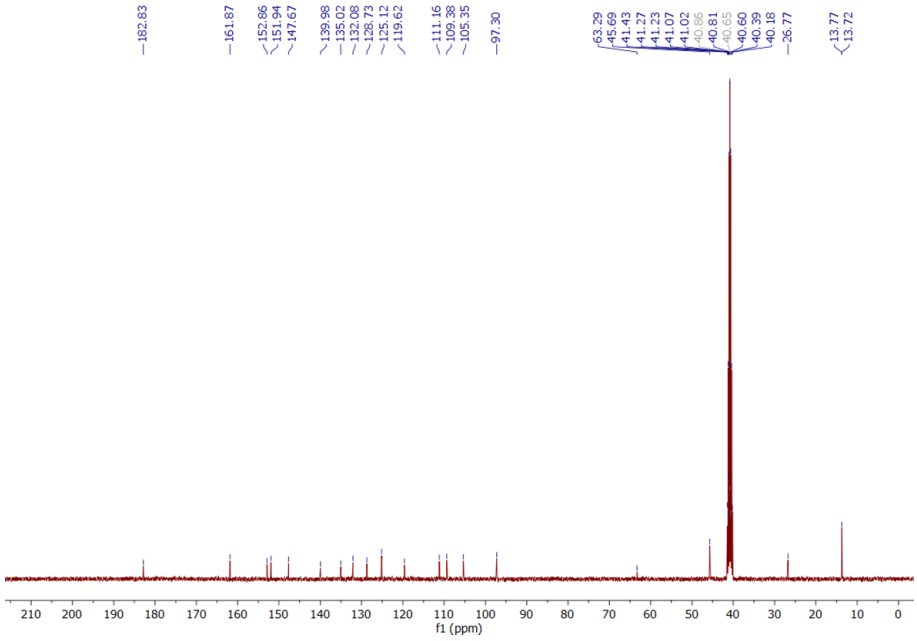

Figure 2.59: ^{13}C NMR spectrum of **23**

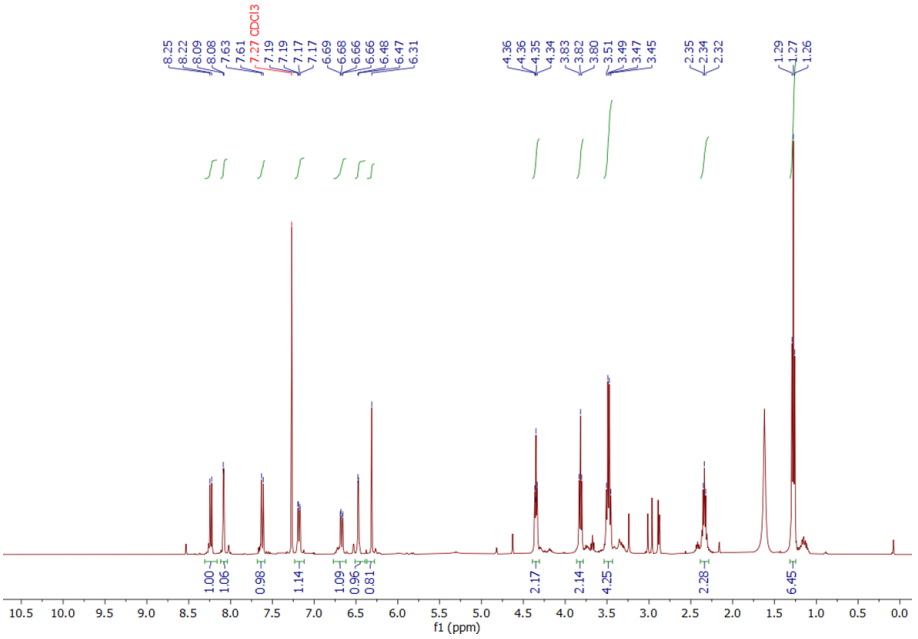

Figure 2.60: ^{1}H NMR spectrum of **24**

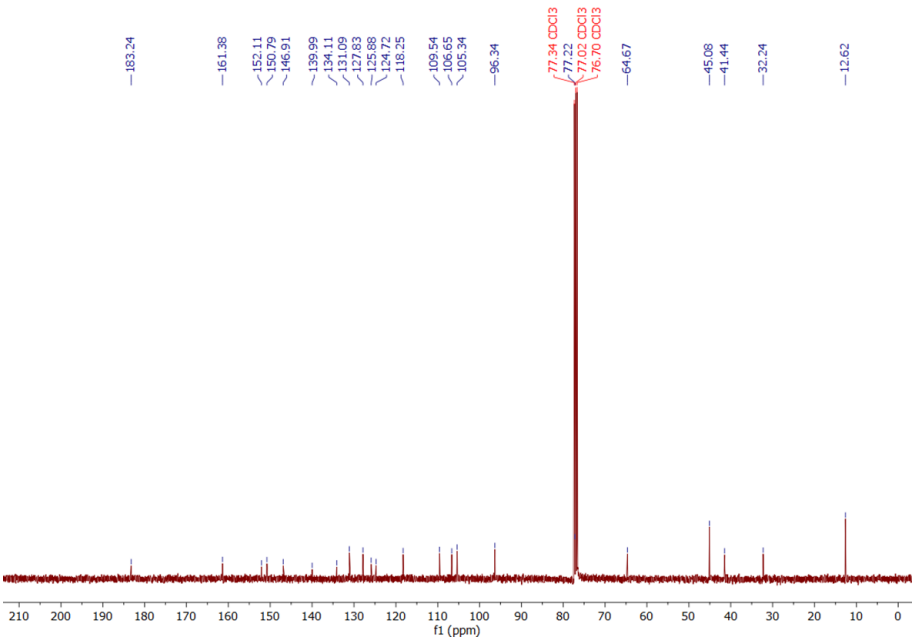

Figure 2.61: ^{13}C NMR spectrum of **24**

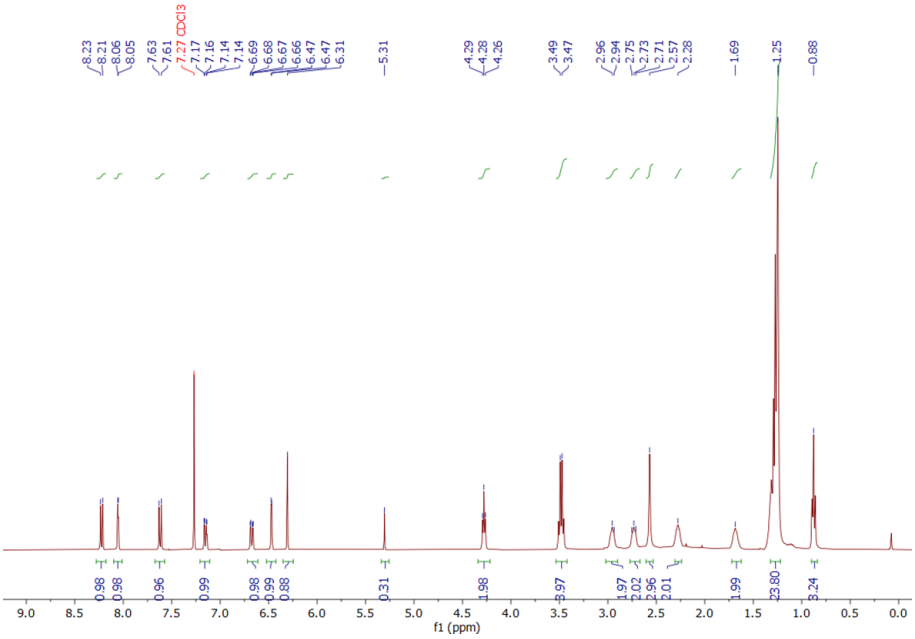

Figure 2.62: ^{1}H NMR spectrum of **25**

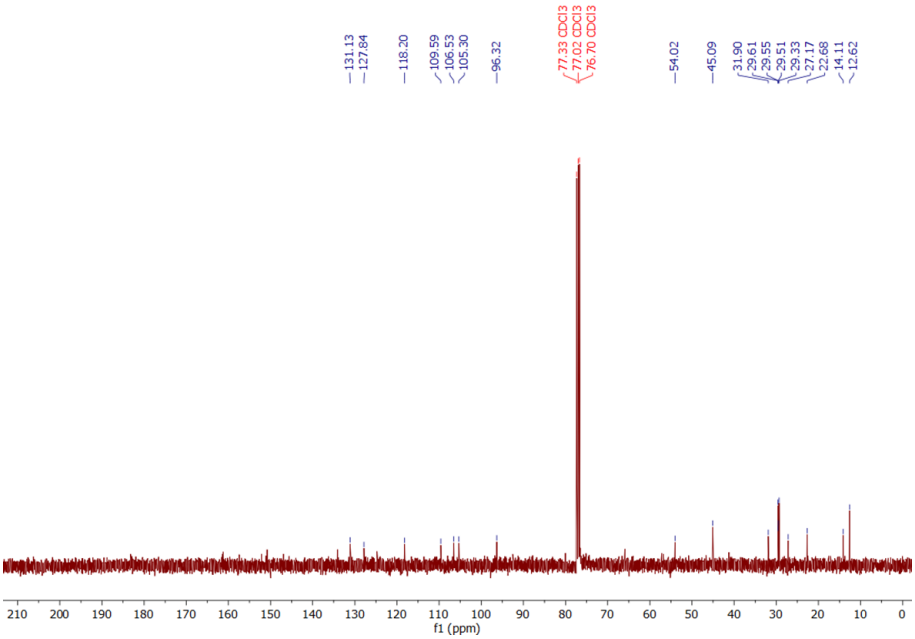

Figure 2.63: ^{13}C NMR spectrum of **25**

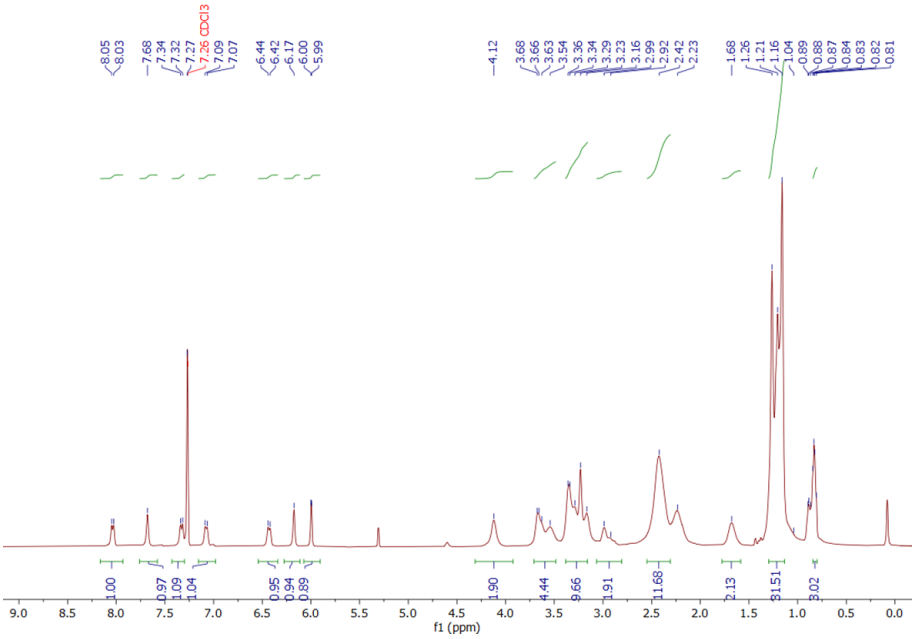

Figure 2.64: ^{1}H NMR spectrum of **NR12S**

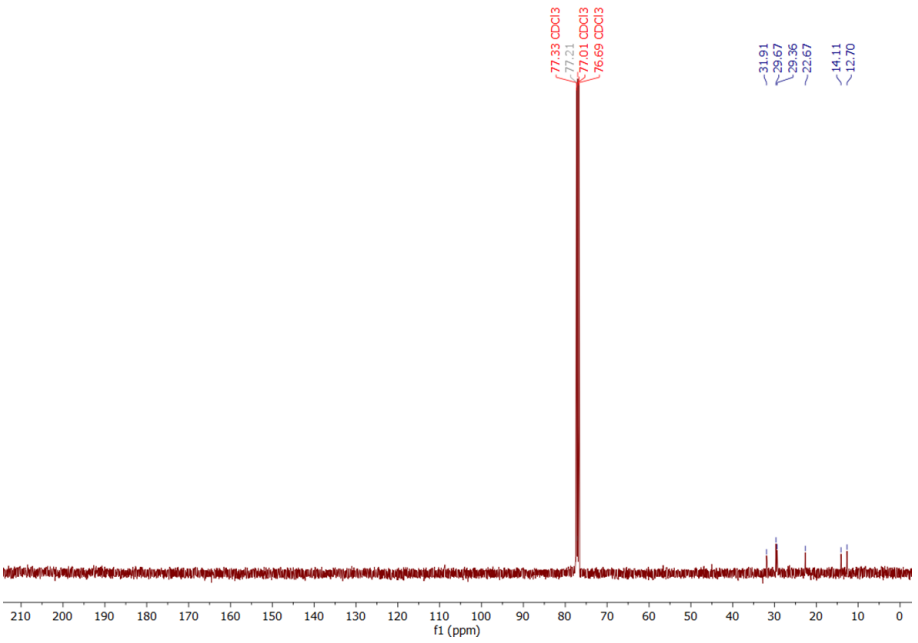

Figure 2.65: ^{13}C NMR spectrum of **NR12S**

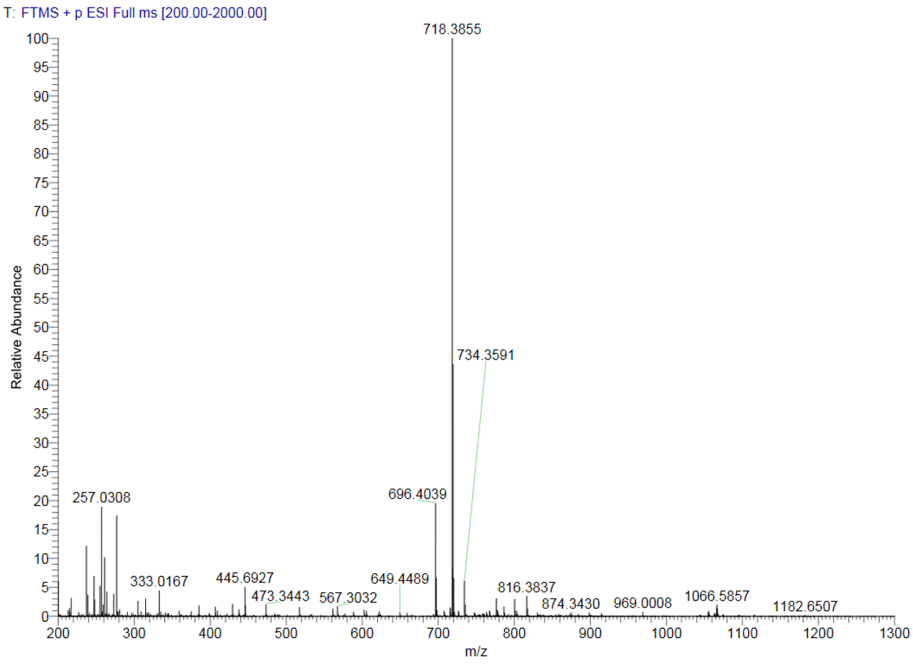

Figure 2.66: HRMS (ESI) spectrum of **NR12S**

References

[1] Yinjun Chen, Gaëlle Mellot, Diederik van Luijk, Costantino Creton, and Rint P. Sijbesma. Mechanochemical tools for polymer materials. *Chem. Soc. Rev.*, 50:4100–4140, 2021.

[2] Oleksandr A. Kucherak, Sule Oncul, Zeinab Darwich, Dmytro A. Yushchenko, Youri Arntz, Pascal Didier, Yves Mély, and Andrey S. Klymchenko. Switchable nile red-based probe for cholesterol and lipid order at the outer leaflet of biomembranes. *J. Am. Chem. Soc.*, 132(13):4907–4916, 2010.

[3] A. J. MacDougall. The effect of peptide-pectin interactions on the gelation behaviour of a plant cell wall pectin. *Carbohydr. Res.*, 335:115–126, 2001.

[4] B.A. Scates. Polyethylene glycol-based homologated ligands for nicotinic acetylcholine receptors. *Bioorg. Med. Chem.*, 16:10295–10300, 2008.

[5] Ismael López-Duarte, Thanh Truc Vu, M. Angeles Izquierdo, James A. Bull, and Marina K. Kuimova. A molecular rotor for measuring viscosity in plasma membranes of live cells. *Chem. Commun.*, 50:5282–5284, 2014.

[6] Shilei Zhu, Jingtuo Zhang, Giri Vegesna, Fen-Tair Luo, Sarah Green, and Haiying Liu. Highly water-soluble neutral bodipy dyes with controllable fluorescence quantum yields. *Org. Lett.*, 13(3):438–441, 2011.

[7] Li Zhang, Xiao-jun Wang, Jing Wang, Nelu Grinberg, Dhileep Kumar Krishnamurthy, and Chris H. Senanayake. An improved method of amide synthesis using acyl chlorides. *Tetrahedron Letters*, 50(24):2964–2966, 2009.

[8] Zhigang Yang, Yanxia He, Jae-Hong Lee, Nayoung Park, Myungkoo Suh, Weon-Sik Chae, Jianfang Cao, Xiaojun Peng, Hyosung Jung, Chulhun Kang, and Jong Seung Kim. A self-calibrating bipartite viscosity sensor for mitochondria. *J. Am. Chem. Soc.*, 135(24):9181–9185, 2013.

[9] Aurore Loudet and Kevin Burgess. Bodipy dyes and their derivatives: Syntheses and spectroscopic properties. *Chem. Rev.*, 107:48914932, 2007.

[10] Noël Boens, Bram Verbelen, María J. Ortiz, Lijuan Jiao, and Wim Dehaen. Synthesis of bodipy dyes through postfunctionalization of the boron dipyrromethene core. *Coordination Chemistry Reviews*, 399:213024, 2019.

[11] Aurimas Vyšniauskas, Ismael Lopez-Duarte, Alex J. Thompson, James A. Bull, and Marina K. Kuimova. Surface functionalisation with viscosity-sensitive bodipy molecular rotor. *Methods Appl. Fluoresc.*, 6:034001, 2018.

[12] Thanh Truc Vu, Rachel Méallet-Renault, Gilles Clavier, Boris A. Trofimov, and Marina K. Kuimova. Tuning bodipy molecular rotors into the red: sensitivity to viscosity vs. temperature. *J. Mater. Chem. C*, 4:2828–2833, 2016.

[13] Caleb M. Rounds, Eric Lubeck, Peter K. Hepler, and Lawrence J. Winship. Propidium iodide competes with ca2+ to label pectin in pollen tubes and arabidopsis root hairs. *Plant Physiology*, 157:175–187, 2011.

Chapter 3

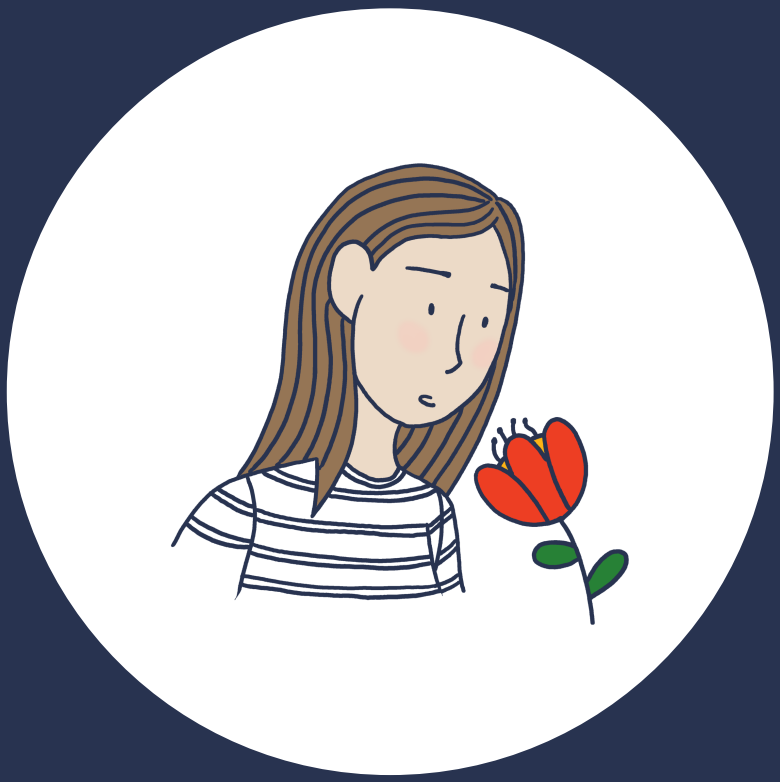

Chapter 3

Complete microviscosity maps of living plant cells and tissues with a toolbox of targeting mechanoprobes

Mechanical patterns control a variety of biological processes in plants. The microviscosity of cellular structures effects the diffusion rate of molecules and organelles, thereby affecting processes such as metabolism and signalling. Spatial variations in local viscosity are also generated during fundamental events in the cell life cycle. While crucial to a complete understanding of plant mechanobiology, resolving subcellular microviscosity patterns in plants has remained an unsolved challenge. We present an imaging microviscosimetry toolbox of molecular rotors that yield complete microviscosity maps of cells and tissues, specifically targeting the cytosol, vacuole, plasma membrane, and wall of plant cells. These BODIPY-based molecular rotors are rigidochromic by means of coupling the rate of an intramolecular rotation, which depends on the mechanics of their direct surroundings, with their fluorescence lifetime. This enables the optical mapping of fluidity and porosity patterns in targeted cellular compartments. We show how apparent viscosity relates to cell function in the root, how the growth of cellular protrusions induces local tension, and how the cell wall is adapted to perform actuation surrounding leaf pores. These results pave the way to the non-invasive micromechanical mapping of complex tissues.

This chapter was published as:

Lucile Michels, Vera Gorelova, Yosapol Harnvanichvech, Jan Willem Borst, Bauke Albada, Dolf Weijers and Joris Sprakel *Complete microviscosity maps of living plant cells and tissues with a toolbox of targeting mechanoprobes*, Proc. Natl. Acad. Sci., 117:18110-18118, (2020)

3.1 Introduction

The function and development of organisms are generally described by gene expression and interactions between proteins and signalling molecules. Although this chemistry-centred view on the processes of life has provided tremendous insight in the inner workings of living systems, it is becoming clear that mechanical forces also play a profound role in biological systems. There are no generalized concepts yet that explain how molecular interactions intertwine with mechanical forces across the kingdoms of life. Therefore, at present, mechanical and chemical influences on living systems are mostly disconnected. Single-molecule methods have generated deep insights into the mechanical response of individual molecules or molecular assemblies. Nevertheless, mapping mechanical patterns *in vivo*, from the subcellular scale up to that of multicellular tissues, remains a daunting challenge. One mechanical property of particular importance is the microviscosity of sub-cellular structures and spaces. Microviscosity determines the diffusion rates of all molecules and organelles within a cell, thereby impacting cellular metabolism[1] and processes such as signalling and enzymatic reactions[2, 3]. Spatial gradients in local viscosity can also be actively generated by cells during important stages of the life cycle, such as polarization, division or differentiation[4, 5, 6, 7, 8, 9]. In plants, cells are mechanically confined by and connected through a network of cell walls. Due to their high rigidity, cell walls are central in plant mechanobiology. These walls must be rigid to provide strength, yet yield readily to accommodate growth[10]. The mechanical modulation of cell walls within living tissues has been previously explored via live cell imaging of cellulase synthase enzymes and microtubules, to assess evolution of the spatial distribution and amount of cellulose during development[11]. Additionally, atomic force microscopy (AFM)-based imaging has been used to provide complete maps of apparent elastic modulus of cell walls[12], while Brillouin imaging was employed to measure spatial variations in extracellular matrix stiffness[13]. However, methods for direct observations at high resolution are still needed. Existing methods to probe viscosity in living cells, such as fluorescence recovery after photobleaching[14, 15, 16] (FRAP) or particle-tracking microrheology[17, 18], can provide valuable insight into these phenomena but do not enable observations to be made with sufficient spatial and temporal res-

olution to create viscosity maps of entire tissues with sub-cellular resolution.

Here we describe a set of four rigidochromic molecular rotors as microviscosity probes that target the cytosol, vacuole, plasma membrane and cell walls in plant cells and tissues. Combined with fluorescence lifetime imaging, these sensors are used to create complete microviscosity maps of individual cells or multicellular plant tissues. We employ this approach to show how apparent viscosity correlates to cell identity and function in growing roots. Moreover, we use the probes to visualize changes in cell wall flexibility during the formation of root hairs, and during the actuation of stomata.

3.2 Results

Molecular rotors are fluorescent probes that undergo an internal rotation upon photoexcitation. Conversion to this twisted state enables intramolecular charge transfer, and opens a pathway of non-radiative decay for the excited state. The rate at which this rotation occurs is determined by the direct environment in which the molecular rotor is situated; molecular rotors are rigidochromic, with a fluorescence lifetime and intensity that depends on the rotational constraints imposed by their surroundings. As a result, the fluorescence lifetime provides with a direct measurement of the probe rotation rate, and is completely independent of the probe concentration. This rate is determined by several factors, such as hydrodynamic drag (viscosity), probe confinement, solvent polarity[19, 20] and binding. The term microviscosity refers to the apparent viscosity a simple liquid should have to give the same rotation rate. Even though it is difficult to strictly disentangle the respective effects of these factors in all cases, we can interpret the observed fluorescence lifetime patterns by taking into account the nature of the different cell compartments. For instance, lifetime fluctuations observed within the plasma membrane will not have the same implications as similar fluctuations observed in the cell wall. In the plasma membrane, a change in lifetime will reflect changes in free volume, which can be interpreted as alterations in the lipid spacing. By contrast, in the cell wall it will most likely reflect changes in the network mesh size. In the cytoplasm, the rotation rate of the probe will be mainly affected by the local crowding density, but in the

non-crowded and more homogeneous environment of the vacuole, the rotor will act as a simple viscosity probe. Rigidochromic dyes have found use as microviscosity probes in polymeric materials[21], as pressure sensors in frictional contacts[22, 23] and as flow sensors in microfluidics[24]. Due to their hydrophobic structure, their use in biology has so far been limited to studies of plasma membranes in mammalian cells[25, 26, 27]. To enable broad, universal use of these sensors, we use phenyl-substituted boron-dipyrromethene (Ph-BODIPY) molecular rotors of which the substitutions on the phenyl ring facilitate selective targeting of the different parts of the plant cell. Addition of anionic sulfonate groups (sulfo-BDP, Fig. 3.1a) should facilitate diffusion across the wall and plasma membrane, and indeed results in localization into the aqueous vacuole. Functionalization of the Ph-BODIPY with a neutral poly(ethylene glycol) (PEG) chain substituent (PEG-BDP, Fig. 3.1b) enables passage of wall and plasma membranes but restricts entry to the vacuole, resulting in cytoplasm localization. To target the plasma membrane, we modified the phenyl ring with an aliphatic tail that carries two permanent cationic charges[26] (N+-BDP, Fig. 3.1c). Finally, binding to the cell wall was achieved through modification of the rotor with a peptide that mimics the pectin-binding domain of Extensin proteins[28] (CWP-BDP, Fig. 3.1d). Each probe was used for plant cell staining at a concentration of 10 μM.

The localization in these different compartments is exemplified by staining suspension-cultured cells of *Arabidopsis thaliana*, as shown in Fig. 3.1e-h and in the Supporting Information section, Fig. 3.6. We confirm the high selectivity of localization in the walls and plasma membranes in root tissues of *Arabidopsis* by means of colocalization analysis using established counterstains (See Supporting Information section, Fig. 3.7-3.10). We show that the selectivity is retained for N+-BDP when varying the probe concentration and incubation time (See Supporting Information section, Fig. 3.9-3.10). Using water-glycerol mixtures, we studied the response of the rotors to changes in viscosity. We find that the modified rotors exhibit a continuous increase in fluorescence lifetime with decreasing solution viscosity, and thus retain their rigidochromic properties (See Supporting Information section, Fig. 3.11). Importantly, we observed that the different targeting functionalities of the probes have limited effect on the fluorescence lifetime, except in the case of PEG-BDP, whose viscosity response deviates from the

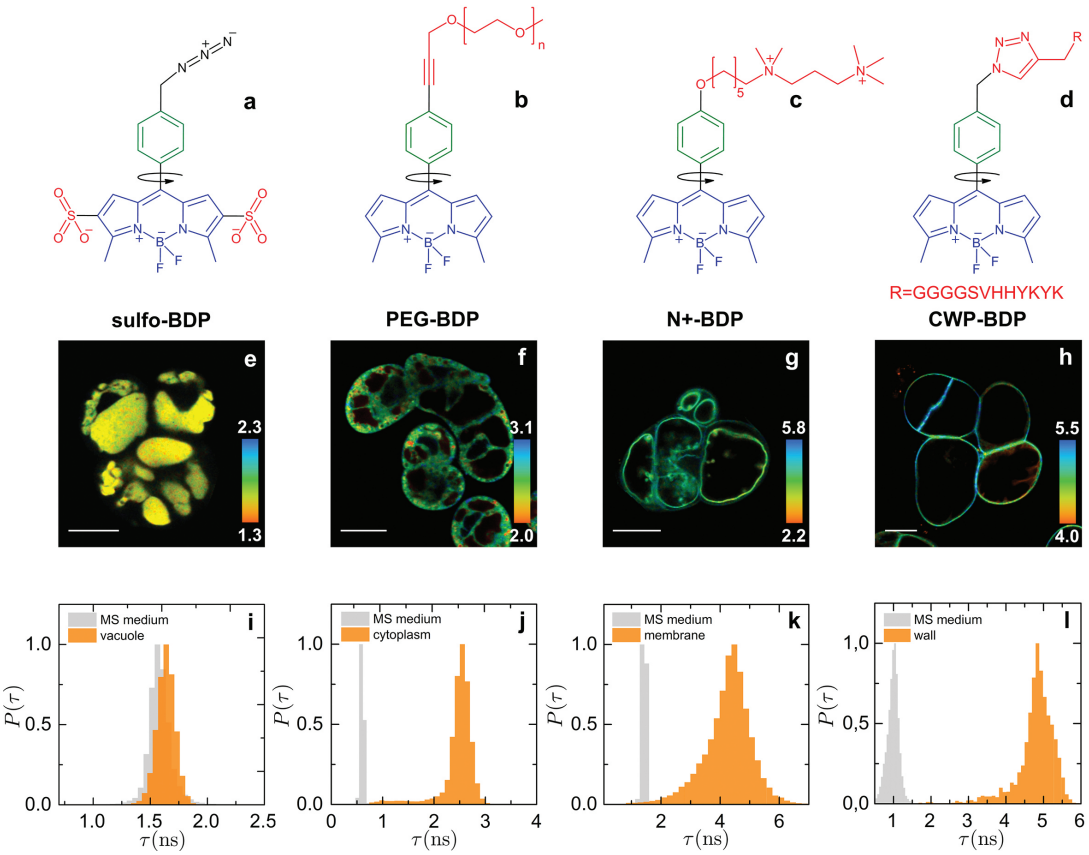

Figure 3.1: Chemical structures of the four rotors (a-d) that target (from left to right) the vacuole, cytosol, plasma membrane, and cell wall, with (e-h) representative FLIM images of rotor-stained *Arabidopsis* suspension-cultured cells (scale bar = 20 μm. The color scale translates the fluorescence lifetime values expressed in ns.) and corresponding fluorescence lifetime probability distributions (i-l); control measurements of fluorescence lifetime distributions are shown in grey.

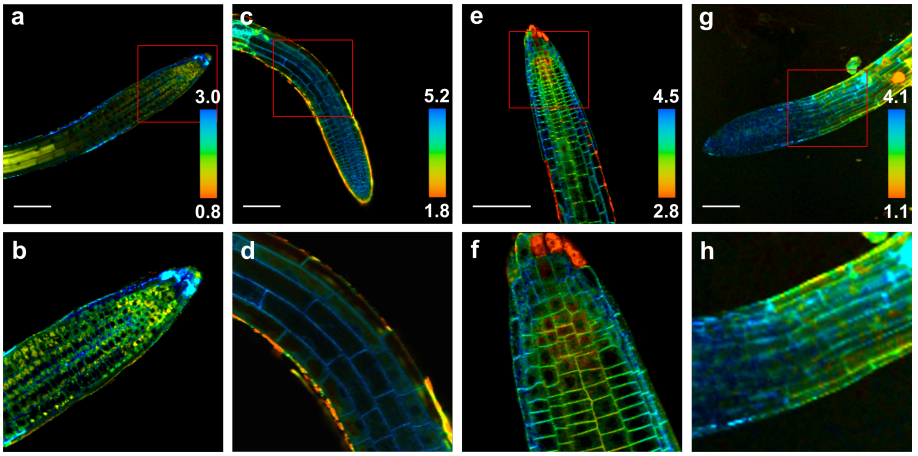

Figure 3.2: Fluorescence lifetime microviscosity maps of *Arabidopsis* roots showing the vacuoles (sulfo-BDP, a-b), cytosol (PEG-BDP, c-d; note that the dye penetrates poorly in the meristem region), plasma membranes (N+-BDP, e-f) and cell walls (CWP-BDP, g-h), in all images scale bar = 100 μm.

one of the other probes. One possible explanation for this divergence relates to the bigger volume occupied by the PEG tail compared to the other functional groups. The PEG chain could modify the environment locally probed by the rotor.

The fluorescence lifetime imaging microscopy (FLIM) microviscosity images also provide with quantitative information, which we extract as lifetime probability distributions P(t). As a control, we determine the width of the lifetime distribution in pure culture medium, which gives a measure for the statistical uncertainty in our experiments. For example, the lifetime distribution in the vacuole (Fig. 3.1i), with sulfo-BDP, exhibits a monomodal distribution centred at 1.6 ± 0.1 ns. This is almost identical to that of the culture medium and reflects the aqueous and non-crowded nature of the vacuolar environment, with a viscosity almost identical to that of pure medium. By contrast, all other cell compartments exhibit both a significant increase in lifetime and width of the distribution, as compared to medium alone (Fig. 3.1j-l). This reflects the much higher confinement and spatial inhomogeneity within the different cellular sub-structures.

Contrary to the non-crowded vacuoles, the cytoplasm consists of an aqueous

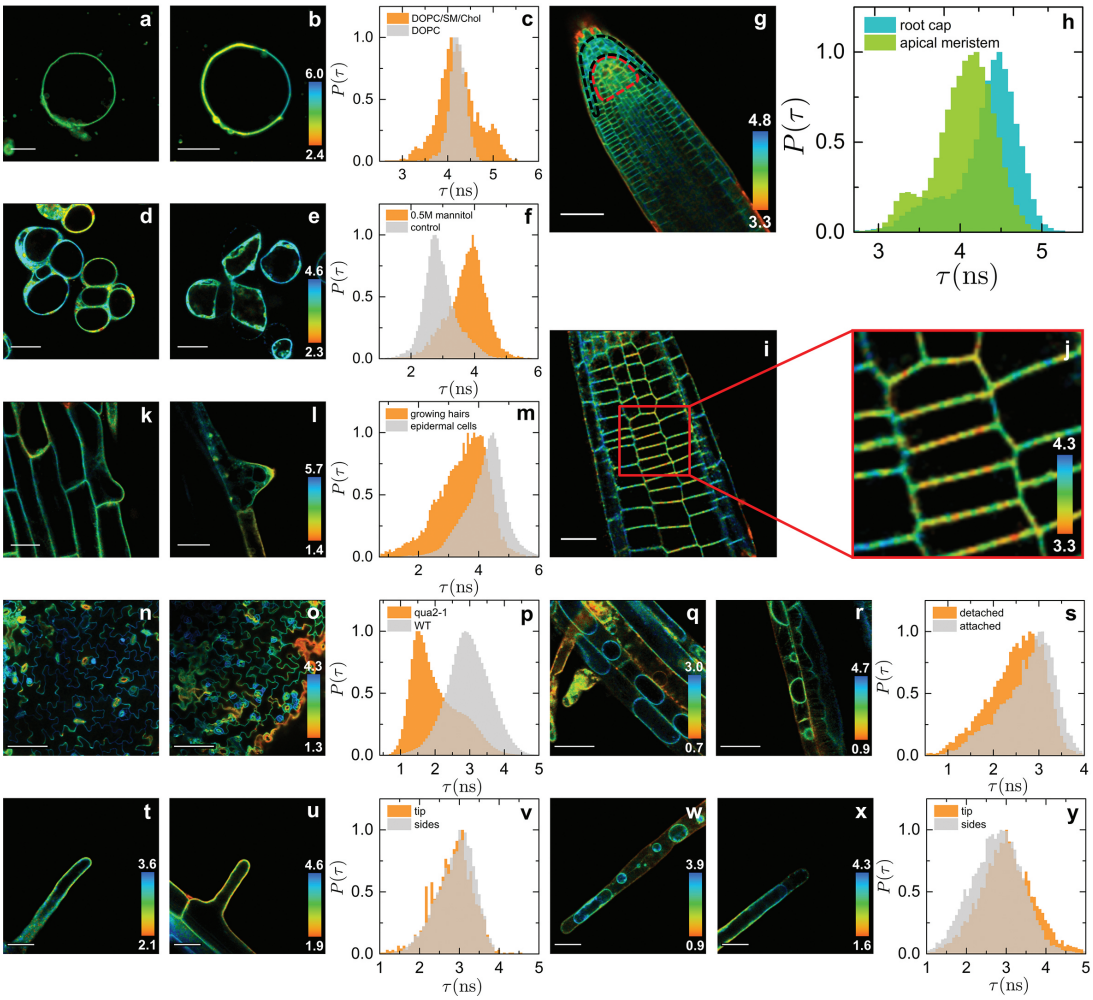

Figure 3.3: Plasma membrane composition and tension imaging with N+-BDP. FLIM images of homogeneous DOPC Giant Unilamellar Vesicles (GUV) (a) and demixed DOPC/Sphingomyelin/cholesterol GUVs (b) (scale bars = 10 μm) and corresponding lifetime distributions (c). FLIM images of *Arabidopsis* suspension-cultured cells before (d) and after (e) osmotic shock (scale bar = 20 μm) and corresponding distributions (N = 30) (f). Microviscosity maps of plasma membranes in the *Arabidopsis* root tip (g, scale bar = 50 μm) and corresponding distributions (h) in the meristem (red dotted line) and in the root cap (black dotted line). Microviscosity maps of the root tip cortical cells (i, scale bar = 20 μm, j, close-up view). FLIM images of growing root hairs in the maturation zone (k and l, scale bar = 20 μm) and corresponding distributions (m) in regular epidermal cells (N = 36) and in growing root hairs (N = 18). FLIM images of cotyledon pavement cells in wild type (n) and *qua2-1* mutant (o) (scale bars = 100 μm), and corresponding distributions (p) obtained for wild type (N > 230) and *qua2-1* mutant (N > 230) pavement cells. FLIM images of root epidermal cells after plasmolysis (q and r, scale bar = 50 μm) and corresponding distributions (s) in sections of the plasma membrane that detached vs sections that are still attached to the wall (N = 23). FLIM images of root hairs before plasmolysis (t-u, scale bar = 20 μm) and corresponding distributions (v) in the tip vs the sides of the hairs (N = 5). FLIM images of root hairs after plasmolysis (w-x, scale bar = 20 μm) and corresponding distributions (y) in the tip vs the sides of the hairs (N = 9).

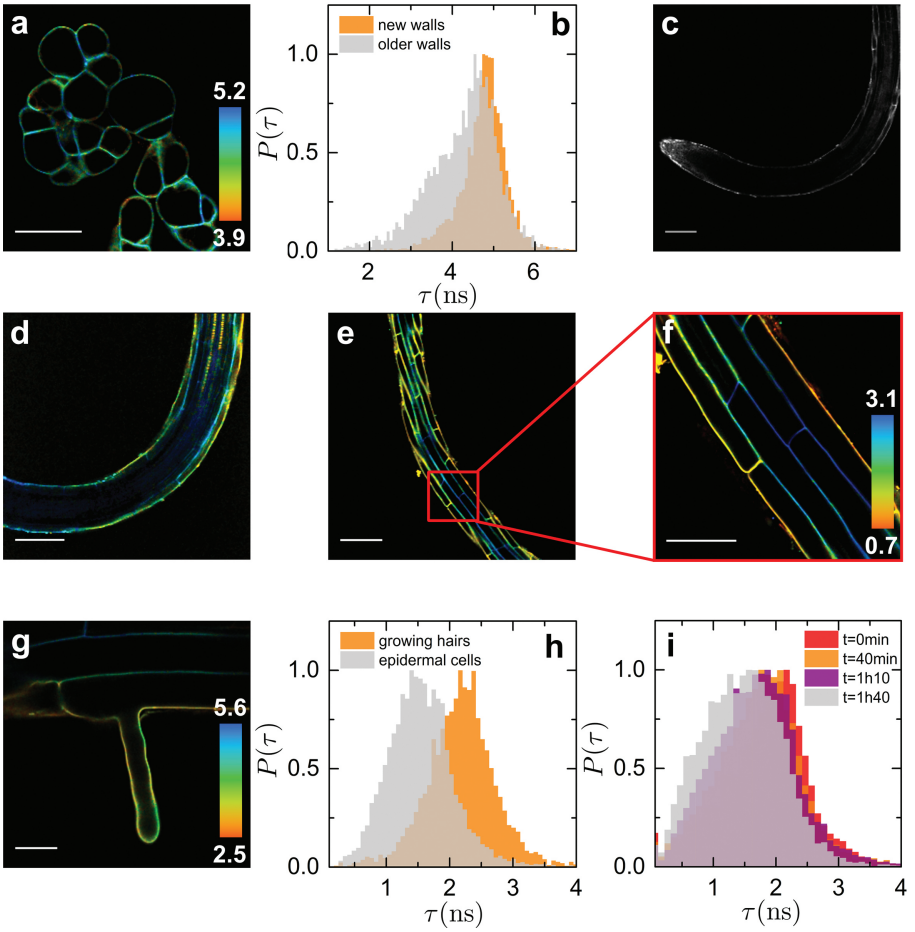

Figure 3.4: Cell wall mesh size with CWP-BDP. FLIM image of *Arabidopsis* suspension-cultured cells (a, scale bar = 100 μm) and corresponding lifetime distributions (b) in newly formed and mature walls for cells (N = 30). Confocal image in the *Arabidopsis* root apex (c, scale bar = 100 μm). Microviscosity maps of epidermal cells in the elongation (d) and the maturation zone (e, scale bar = 100 μm, f, scale bar = 50 μm), which exhibit transverse variations in wall mesh size and compliance. FLIM images in growing root hairs (g) (scale bar = 20 μm) and corresponding lifetime distributions (h) in regular epidermal cells and in growing root hairs for epidermal cells (N = 20) and root hairs (N = 10). Temporal evolution of the lifetime distribution in a growing root hair (i).

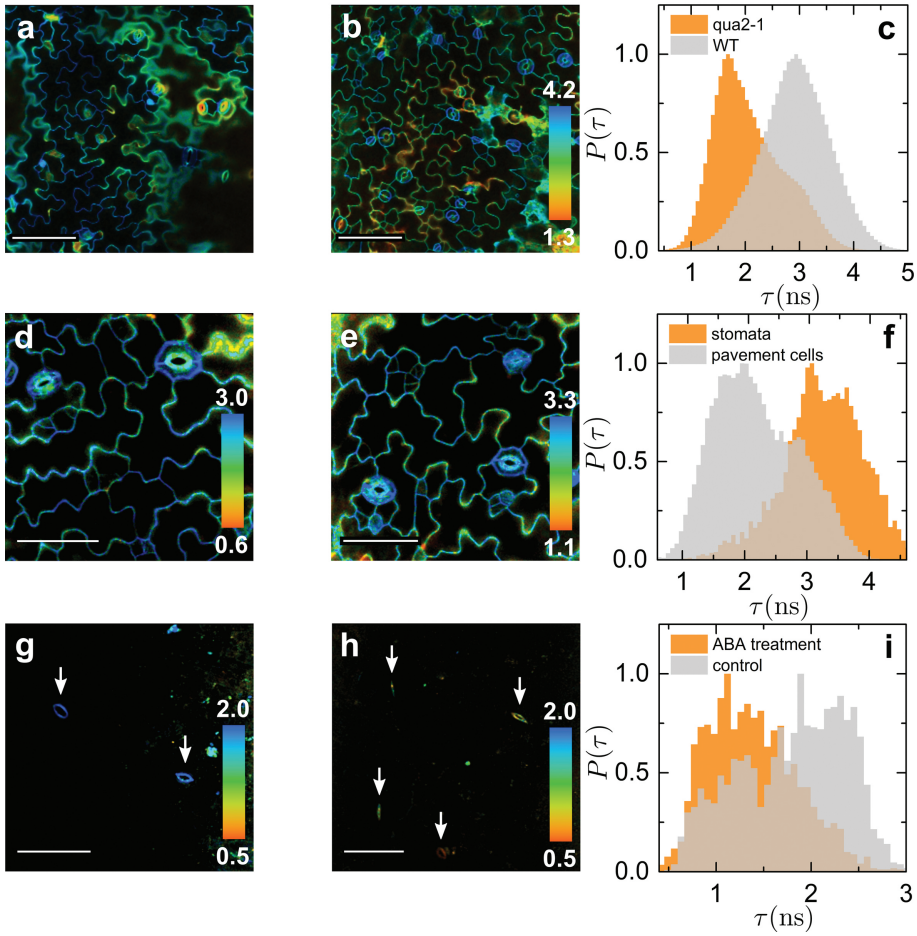

Figure 3.5: Cell wall mesh size with CWP-BDP. FLIM images of cotyledon pavement cells in a wild type *Arabidopsis* seedling (a) versus a *qua2-1* mutant seedling (b) (scale bars = 100 μm) and corresponding lifetime distributions obtained within wild type (N > 230) and *qua2-1* (N > 230) pavement cell walls (c). Zoomed in FLIM images of wild type cotyledon epidermal layer with stomata (d and e, scale bar = 50 μm) and corresponding lifetime distributions (f) for stomata (N = 11) in comparison with pavement cells (N = 15). FLIM images of cotyledon guard cells before (g) and after abscisic acid (ABA) treatment (h) (scale bar = 50 μm), and corresponding lifetime distributions (i) obtained for non-treated (N = 13) and ABA-treated cells (N = 18).

solution crowded with a wide variety of bio(macro)molecules. Indeed, for suspension-cultured *Arabidopsis* cells the PEG-BDP probe reveals an average lifetime of 2.6 ± 0.2 ns in the cytoplasm (Fig. 3.1j). Interestingly, the distribution is very wide; comparison to the control data shows that this broadening is well above the noise level of the measurements, and thus reflects the spatial inhomogeneity of the crowded cytosolic solution. Apparently, the cytoplasm undergoes large density fluctuations. The plasma membrane and tonoplast (Fig. 3.1k) also exhibit a broad distribution that reflects spatial inhomogeneities, as we will discuss in more detail below, with a characteristic average lifetime of 4.4 ± 0.6 ns. Finally, the broad lifetime distribution obtained with the wall targeting rotor (Fig. 3.1l) reveals a strongly inhomogeneous microenvironment for the walls in cultured cells. Moreover, different wall types exhibit striking differences in their observed apparent viscosity. This will be discussed in more detail in the following.

After this calibration using suspension-cultured cells and cell clusters, we applied our method to 4-day-old *Arabidopsis* roots (Fig. 3.2a-h, See Supporting Information section, Fig. 3.12-3.13). Qualitatively, the localization was equal to that in the suspension culture, we only needed to optimize the incubation times based on permeation kinetics assays (See Supporting Information section, Fig. 3.14-3.17). For the N+-BDP plasma membrane probe, the incubation time does not significantly affect the localization specificity in *Arabidopsis* roots, as can be seen in the Supporting Information section, Fig. 3.10. The high quantum yield of the rotors allows for the use of low laser intensities, i.e. less than 10 μW after the objective, resulting in low autofluorescence (See Supporting Information section, Fig. 3.18) and a high signal to noise ratio. Moreover, the staining is persistent over at least 5h (See Supporting Information section, Fig. 3.19), indicating limited or no metabolic turn-over of the dye. To within resolution, the vacuoles (Fig. 3.2a-b) do not show any significant spatial gradients in viscosity along the root, consistent with homogeneous aqueous solutions. The other rotors, as for the suspension cells, reveal strong spatial inhomogeneities in the microviscosity of the tissue (Fig. 3.2c-h). We note that internalization of the PEG-decorated cytosolic probe is weak in the root tip (Fig. 3.2c-d), probably because it may adhere to the protective cuticle. During cell division and differentiation, strong changes are

expected to occur primarily to the apparent viscosity of the plasma membranes and walls. For example, growth and changes in cell geometry induce localized tension on the plasma membranes[29, 30, 31], and require loosening of the cell walls to accommodate these processes[10, 32, 33]. We thus focused essentially on the plasma membranes and cell walls.

The positively charged plasma membrane-targeting rotor N+-BDP is designed to insert between the negatively charged phospholipids. Changes in lipid packing order and density change the volume available for the rotational motion of the probe and thus induce a change in their fluorescence lifetime. As our plasma membrane probe will sense both lipid phase transition as well as changes in local membrane tension, it becomes difficult to disentangle those two effects in a static FLIM experiment. We developed a model system to highlight the probe sensitivity to changes in lipid packing. Specifically, we introduced our plasma membrane probe into giant unilamellar vesicles (GUVs) composed of sphingomyelin (SM), 1,2-dioleoyl-sn-glycero-3-phosphocholine (DOPC), and cholesterol (0.56:0.24:0.20) in order to study lipid phase transition. This lipid composition leads to phase separation between a gel-like ordered (Lo) phase, rich in SM and cholesterol, and a liquid-like phase (Ld) that is enriched in DOPC. This phase separation shows similarities to the formation of lipid microdomains in biological membranes by chemical incompatibility of different lipids[34, 35, 36]. A homogeneous GUV of only DOPC shows a narrow monomodal lifetime distribution with lifetimes of 4.2 ± 0.1 ns (Fig. 3.3a,c). In the mixed GUV the formation of distinct mechanical domains can be observed (Fig. 3.3b,c, See Supporting Information section, Fig. 3.20), with lifetimes of 4.2 ± 0.4 ns in the Ld phase, which is almost identical to that measured in a pure DOPC membrane, and 5.0 ± 0.3 ns in the Lo phase. Clearly, our probe senses the stronger mechanical restriction for rotations in the tightly-packed and solid-like SM-rich Lo phase. Importantly, the same rotor reveals mechanical stress on biological membranes that are exposed to external stimuli. Specifically, exposing suspension cells in their growth medium to hyperosmotic shock results in compression of the plasma membrane and concomitant reduction of the rotational motion (Fig. 3.3d-e). As a consequence, lifetime distributions show a distinct shift to higher lifetimes (Fig. 3.3f).

When used in multicellular tissue, clear differences in microviscosity between

the root cap and the meristem emerge, as seen both in the FLIM images and corresponding lifetime distributions (Fig. 3.3g-h). The meristem is the tissue in plants where division of undifferentiated cells takes place. As result of this continuous division and initial growth of the cells in the meristem, the cell plasma membranes are under constant tension. This tension, by contrast to compression that was discussed above, increases the spacing between the lipids[37], and thus leads to a distinct reduction in the plasma membrane rotor lifetime: 4.4 ± 0.1 ns in the relaxed plasma membranes of the root cap cells and 4.2 ± 0.2 ns in the proximal (youngest part of the) root meristem. A close-up of the plasma membranes of young epidermal cells in the meristem (Fig. 3.3i-j) reveals distinct lipid microdomains within a single bilayer. Since their size are in agreement with previous findings[38], we assume that these islands where the rotor has a longer lifetime are formed by lipid compositions with higher packing density. The fact that we also observe these domains in the plasma membrane of the outermost cell layer and in suspension-cultured cells (See Supporting Information section, Fig. 3.21), strongly suggests that they are not plasmodesmata.

A striking example of how cellular processes control tension in the plasma membrane is found in the growth of root hairs. These are cellular protrusions that form in the differentiation zone of the root and that increase the root surface area to enhance nutrient uptake. Root hairs are commonly used as a model to study cell growth at the single cell level as they grow as fast as 1 μm/min or more, without losing their integrity. The distinct bulging of the trichoblast cells at the initial stage of hair growth can be seen in Fig. 3.3k-l. As could be expected, the lifetime is lower in the plasma membrane at the tip of the hair as compared to that of a non-growing epidermal cell plasma membrane (Fig. 3.3m), shifting from 3.6 ± 0.8 ns in the hair tip to 4.3 ± 0.6 ns in non-hair epidermal cell (atrichoblast). This shift corresponds to the increased tension in the hair tip where growth occurs and curvature of the plasma membrane is largest. A plasmolysis experiment performed on root hairs (Fig. 3.3t-y, See Supporting Information section, Fig. 3.22) corroborated the probe responsiveness to changes in membrane tension within *Arabidopsis* root tissues. Upon hyperosmotic shock, the fluorescence lifetime within hair tip plasma membranes increases noticeably, and becomes higher than within the side plasma membranes (Fig. 3.3y). This

change follows the drop in tension occurring upon plasmolysis, as the plasma membrane retracts and detaches from the cell wall. The same trend is observed in plasmolysed atrichoblast cells (Fig. 3.3q-s, See Supporting Information section, Fig. 3.23). After having shown the level of insight that our molecular rotors provide in the dynamics of such a compact, dynamic, and fluidic cell component as the plasma membrane, we were keen to find out which light the rotors could shed on the developmental stages of the more rigid but still dynamic cell wall that is less densely packed with molecules than the plasma membrane. For this, we equipped the azide-functionalized Ph-BODIPY rotor with a pectin-binding peptide using copper-catalysed alkyne-azide cycloadditon (CuAAC) reaction[39].

The cell wall-targeting molecular rotor binds to pectin polymers in the walls through a recognition peptide, with an amino acid sequence derived from wall binding Extensin proteins[28]. Initially, a young cell has a thin and flexible primary wall that is rich in callose and contains highly methyl-esterified pectin polymers. As the cell grows, the wall is progressively consolidated by cellulose, and callose is degraded. While entering the elongation phase, the cell wall is loosened by specialized proteins, e.g. Expansins, resulting in increasing mesh size and flexibility to enable growth driven by turgor pressure. The cell wall is then stiffened by cross-linking of wall extensins. Meanwhile, the pectins are selectively de-esterified, which allow them to form a gel-like matrix around the cellulose-xyloglucan network via Ca^{2+} linkages. Those dynamic changes stabilize the cell wall and result in a rigid structure with larger meshes[10, 40, 41]. In mesostructured materials, such as the polymeric network of the cell wall, molecular rotors probe the local free volume rather than the viscosity of the solvent in the meshes[42]. The rotation of the molecule to its twisted state sets up a hydrodynamic field of the fluid; the strength of the coupling of this field to the surrounding network determines the rotation rate. Thus, the rotor is expected to experience distinct fluorescence lifetime changes during cell wall remodelling, decreasing the lifetime as the cell wall increases its mesh size. This is exactly what we observe in suspension-cultured cells (Fig. 3.4a-b). Newly formed cell-connecting walls exhibit substantially higher fluorescence lifetimes, as compared to mature walls which feature larger meshes in which the rotor can rotate more freely. Thus, this rotor enables insights into the mechanical restructuring of cell walls, upon go-

ing from flexible and compliant walls (high lifetime) to more rigid and stiff ones (low lifetime). The cell wall-binding rotor shows weak internalization into the root apex perhaps due to the poor interaction of the rotor with the highly esterified pectins[43](Fig. 3.4c). However, in the elongation (Fig. 3.4d) and differentiation zones (Fig. 3.4e-f, See Supporting Information section, Fig. 3.24) the rotor is well internalized in the epidermal layer, and reveals a distinct reduction in the fluorescence lifetime in more mature tissue. This confirms the process of loosening the wall to accommodate volumetric expansion during elongation. The root epidermis in the differentiation zone (Fig. 3.4f) shows an increase in the fluorescence lifetime along the transverse direction, going from the outside in. This change in wall mesh structure could be related to changes in permeability, with the outer epidermal cells being the most permeable to facilitate the uptake of water and nutrients[44]. To validate the use of the CWP-BDP probe in visualising mechanical defects in biological setting, we compared its fluorescence lifetime in the walls of wild type cotyledon pavement cells to that of pectin-impaired *qua2-1* (*quasimodo*) mutants (Fig. 3.5a-c, See Supporting Information section, Fig. 3.25). Previous studies demonstrated that the cell walls of calli in *qua* mutants show increased porosity, reflected by an increased release of cell wall material in the growth medium[45] and an increased water proton mobility within wall pores, as measured by nuclear magnetic resonance (NMR) spectroscopy[46]. With our cell-wall-specific probe we observe the same trend for the walls of pavement cells: the clear diminution in lifetime in mutants, that reflects an increased wall mesh size (Fig. 3.5c). Interestingly, this decrease in fluorescence lifetime within cell walls is accompanied by a decrease in lifetime within plasma membranes reported by N+-BDP (Fig. 3.3n-p, See Supporting Information section, Fig. 3.26). We thereby highlight a decreased plasma membrane tension coupled to the increased wall porosity. No such trend was evidenced when comparing walls of wild type and *qua2-1* mutant roots (See Supporting Information section, Fig. 3.27). This observation is to be expected, given that cell adhesion defects are most pronounced in the shoots than in the roots of the mutant.

The mechanical maturation of walls is also seen in actively growing root hairs (Fig. 3.4g-i). Lifetimes within the tip of root hairs are significantly higher as compared to epidermal walls that show no root hair growth (Fig. 3.4h). In the

hair tip, building blocks are secreted by exocytosis to build a new wall[47, 48]. This new wall must remain compliant to accommodate further growth, and is thus composed of a primary wall enriched in a dense network of flexible pectin chains[32, 49]. In addition, these root hairs must be sufficiently strong to penetrate the surrounding soil and allow water and nutrient uptake. By monitoring a young hair growth over time (Fig. 3.4i), we observe a progressive decrease in lifetime along the hair, which reflects the same wall maturation process observed in the root itself. Finally, we remark that spatial modulation of cell wall mechanics is not only relevant during the growth of cells or cellular protrusions, but is also key to enable the active actuation of structures in the plant. Microscopic and macroscopic motion requires the walls to be sufficiently compliant. An example of actuating organs are the stomata, pores found at the underside of the leaf that can be actively opened and closed to toggle gas exchange with the environment[50, 51, 52]. Imaging with our cell wall-targeting rotor reveals a distinct zone of compliant wall tissue (Fig. 3.5d-f, See Supporting Information section, Fig. 3.28), with a high lifetime reflecting dense pectin-rich matter (Fig. 3.5f), in the guard cells surrounding individual stoma[53]. This is corroborated by the fact the fluorescence intensity is substantially higher in these areas, which indicates a higher pectin content and/or a lower pectin methylation status. Pectin de-esterification has been previously correlated to wall softening in *Arabidopsis* meristem and hypocotyl[54, 55, 56]. Triggering stomatal closure using an abscisic acid (ABA) treatment results in lower fluorescence lifetimes (Fig. 3.5g-i, See Supporting Information section, Fig. 3.29) likely due to the induced decrease in turgor pressure. Clearly, cell wall compliance is actively regulated to match the biological function at the site of interest; our toolbox enables a direct quantification of these effects even in complex living tissues during biological function.

3.3 Discussion

We show how a set of rigidochromic molecular rotors, featuring the same mechanoresponsive core, but chemically-modified to target different parts of the plant cell, can be harnessed to create complete mechanical maps of complex plant tissues. Using our tailor-made probes we have shown how the mechanics

of plasma membranes and cell walls are adaptively modulated to accommodate growth or actuation. The ability to create complete time-dependent microviscosity maps of multicellular tissues, with sub-cellular resolution and targeting of the key structures in the cell, opens up new ways to understand the role of mechanics in the regulation of biological processes. Moreover, in combination with markers highlighting plant membrane microdomains (that remain to be identified), the plasma membrane tension probe might prove useful to study how those domains contribute to the adjustment of the plasma membrane mechanical properties. Many challenges remain in the field of plant mechanobiology, to which our approach could provide new and valuable insights, including the role of mechanical stress in cell polarization and differentiation, and the adaptation of local mechanics during important stages in the life cycle of the cell such as oriented division during morphogenesis. Moreover, our toolbox is not restricted to use in plants, but can be readily adapted for microviscosity mapping in multicellular tissues of other organisms, or used to probe mechanobiological phenomena in microorganisms. To bring a more quantitative assessment, more systematic studies are needed to calibrate the rotors. For instance, work on model lipid membranes to dissect the effect of membrane tension, or on synthetic polymer networks to investigate the effect of mesh confinement would allow for quantitation of actual tensions and free volumes.

3.4 Materials and Methods

A comprehensive overview of the synthetic protocols and chemical characterization, as well as all experimental details, including culture of the biological specimens, imaging and analysis, and statistical details for all experiments, are provided in **Chapter 2** and the Supplementary Information respectively.

Molecular rotors: Molecular rotors were prepared by trifluoroacetic acid (TFA)-mediated condensation of 2-methylpyrrole and appropriately functionalized benzaldehydes, followed by ring closure to form the BODIPY core using boron trifluoride diethyl etherate. These basic building blocks were modified to yield the desired chemical functionality, and subsequently purified by column chromatography. Detailed procedures, yields, ^{1}H-NMR spectra, ^{13}C-NMR spec-

tra and mass spectrometry data are reported in **Chapter 2**. The wall targeting peptide, inspired by the pectin-binding domain of extensin proteins[28], was prepared by Fmoc-based solid-phase peptide synthesis and attached to an azide-function rotor probe using a copper-catalyzed azide-alkyne cycloaddition[39]. The peptide-functional rotor was purified using preparative reversed-phase high performance liquid chromatography (HPLC). The absorption and fluorescence emission spectra of the four rotors were recorded in Milli Q water (See Supporting Information section, Fig. 3.30-3.33), so as to determine the excitation and emission wavelengths to use for imaging.

Lifetime calibration and imaging: Viscosity-lifetime calibration curves were established by dissolving 10 μM of rotor dyes in water-glycerol mixtures of known viscosity. Lifetimes were recorded by time-correlated single-photon counting (TCSPC) experiments performed on an Edinburgh FS5 spectrometer, equipped with a 100 ps pulsed laser at 475 nm. In all cases, a single-exponential decay was observed in the time-resolved fluorescence measurements, from which the characteristic fluorescence lifetime was obtained. FLIM imaging experiments were performed on a Leica TCS SP8 inverted confocal microscope coupled to a Becker & Hickl TCSPC lifetime module (SPC830). Samples were excited with a 488 or 514 nm pulsed laser source (pulse duration < 1 ps) and fluorescence was captured through a 63x water immersion objective (suspension cultured cells) or a 20x water immersion objective (roots and cotyledons). Acquisition time was fixed at 120 s for each 256x256 pixel image. FLIM images were processed using the SPCImage 7.1 software to fit the fluorescence decay curves in each pixel with a 2-component exponential decay. Images are reported in a false-colour scale that represent the mean fluorescence lifetime for each pixel, expressed in nanoseconds.

Suspension cultured cells: *Arabidopsis thaliana* PSB-D cells were maintained in suspension culture in a Murashige & Skoog minimal organics (MSMO) medium at 25 °C, in the dark under continuous agitation. Culture medium was replaced once a week. For imaging experiments, cells were first washed by centrifugation with fresh MSMO medium prior to incubation for 5h in MSMO medium containing 10 μM of the rotor dye. Cells were then washed again against fresh MSMO medium and directly used for imaging. Osmotic shock experiments

where performed by replacing the MSMO medium with MSMO medium containing 0.5M mannitol as the osmotic agent and the cells observed 5 min after application of the hyperosmotic shock.

Multicellular tissues: *Arabidopsis thaliana* wild type or *qua2-1* (*quasimodo*) mutant Col-0 seeds were surface-sterilized in a bleach:ethanol solution for 8 min. They were subsequently washed twice in 70% ethanol and once in 100% ethanol. Sterilized seeds were plated on 0.5x Murashige & Skoog (MS) growth plates and vernalized at 4 °C for 24h. They were grown vertically under long-day conditions (16h light, 8h dark) at 22 °C for 4 days. The 4-day old seedlings were then transferred to 0.5x MS medium containing 10 μM of the rotor dye and incubated in constant light at 22 °C for 120, 90, 15 and 20 minutes for sulfo-BDP, PEG-BDP, N+-BDP and CWP-BDP, respectively. The seedlings where then washed for 30s with fresh 0.5x MS medium and transferred onto a glass slide for FLIM imaging of the roots or cotyledons. Osmotic shock experiments where performed by replacing the 0.5x MS medium with 0.5x MS medium containing 0.5M mannitol as the osmotic agent and the seedlings observed within 7 to 15 mins after application of the hyperosmotic shock.

To compare the mechanical properties of the plasma membrane and the cell wall within wild type versus *qua2-1* mutant plants, 5-day-old *Arabidopsis* seedlings were incubated in 0.5x MS containing 10 μM N+-BDP or 10 μM CWP-BDP for 15 min. FLIM imaging of roots epithelial and cotyledon pavement cells was then performed as described above.

GUV preparation: All lipid compounds were purchased from Avanti Polar Lipids and used as is. Giant unilamellar vesicles were prepared using the method of Moscho et al.[57]. In short: stock solutions of the lipids and cholesterol in chloroform were added to methanol placed in a roundbottom flask. An aqueous solution of 100 mM sucrose, containing N+-BDP in a molar ratio of 1:33 dye:lipids, was carefully added along the wall of the flask. The organic solvents were gently evaporated in a rotary evaporator at 40 °C and 40 rpm while gradually reducing the pressure. This resulted in the spontaneous formation of rotor-dye-labelled GUVs. The vesicles were then immobilized in a 0.5 w/v% agarose gel for imaging[58].

Colocalization analysis: To confirm the selective localization of plasma

membrane and cell wall probes, *Arabidopsis* seedlings, grown as described above, were incubated in medium containing both the rotor dyes at 10 μM and the counterstains propidium iodide[63] (PI) (cell wall, 10 mg/L) or 1,1'-Dioctadecyl-3,3,3',3'-Tetramethylindotricarbocyanine Iodide[64] (DiI-C18) (plasma membrane, 5 mg/L) for 5 minutes. The seedlings were then washed three times in fresh 0.5x MSMO medium and placed on a coverslip for imaging.

The plasma membrane staining specificity of N+-BDP was demonstrated via a colocalization analysis with a Pleckstrin homology (PH) domain specific for PI(4,5)P2, a type of plasma membrane lipid, using *pUBQ10::mCherry-1xPH(PLC)* seedlings[59].

To further study the impact of N+-BDP concentration and incubation time on the staining specificity, colocalization concentration series (1 μM, 5 μM, 10 μM and 20 μM) and time series at 10 μM were recorded. In those series, N-(3-Triethylammoniumpropyl)-4-(6-(4-(Diethylamino) Phenyl) Hexatrienyl) Pyridinium Dibromide (FM4-64)[60] was used as counterstain to mark the plasma membrane. Internalization of FM4-64 in endomembranes was avoided by pre-treating the seedlings with Brefeldin A.

3.5 Supporting Information

3.5.1 Spectroscopic characterization

Steady-state spectroscopy

UV-Visible absorption spectra were recorded in 1 cm path quartz cuvettes on a Shimadzu UV-2600 Spectrophotometer. Fluorescence emission and excitation measurements were performed in 10 mm path quartz cuvettes on an Agilent Technologies Cary Eclipse Fluorescence Spectrophotometer with a Xenon Lamp. The dye concentrations were adjusted to keep a maximum absorbance below 0.1 to avoid reabsorption effects.

Fluorescence Lifetime measurements – Rotor Calibration

We studied the molecular rotor response to viscosity variations by measuring fluorescence lifetimes in Milli Q water-glycerol mixtures of varied composition

(0, 30, 50, 60, 75, 80, 85, 90, 91, 93, 96, 98 and 99% glycerol) at a fixed temperature of 20°C. The viscosity of those solutions was determined in a previous study[62]. The dye concentration was set to 10 μM to prevent reabsorption effects. Fluorescence decays were recorded on an Edinburgh FS5 Spectrofluorometer with a 475 ± 10 nm pulsed diode laser. Measurements were performed in 10 mm path quartz cuvettes and photons were collected at 535 ± 2 nm (PEG-BDP), 525 ± 2 nm (sulfo-BDP) and 520 ± 2 nm (N+-BDP). The acquisition time window was set to 50 ns with 4096 collection channels and the photon collection was done until reaching a total of 10,000 counts. In order to fit the fluorescence decays the instrument response function was determined by measuring the scattering intensity of diluted Ludox solution. The decays were fitted with a single-component exponential to create the calibration curves of fluorescence lifetime vs viscosity for each molecular rotor.

3.5.2 Imaging procedures

GUV preparation

Brain SM and DOPC stock solutions in chloroform were purchased from Avanti Polar Lipids. Cholesterol was purchased from VWR All lipids were used without further purification. Giant Unilamellar Vesicles were formulated as described previously[57]. In a 50 mL round-bottomed flask Brain SM (1.12 mM, 81.9 μL of 10 g/L stock solution in chloroform), DOPC (0.48 mM, 15.1 μL of 25 g/L stock solution in chloroform) and cholesterol (0.4 mM, 15.5 μL of 10 g/L stock solution in chloroform) were mixed in chloroform (888 μL). Methanol (150 μL) was added. 100 mM sucrose solution in Milli Q water (7 mL) containing N+-BDP dye at a 3:100 dye-to-lipid molar ratio was carefully added along the wall of the flask. The organic solvent was gently evaporated at 40°C, 40 rpm, slowly reducing the pressure in order to observe two distinct boiling events. The pressure was decreased till reaching 150 mbar and the evaporation was further performed for 2 min to get about 6 mL of GUV suspension. The vesicles were immobilized in a 0.5w/v% agarose gel for imaging, as reported previously[58].

Cell incubation and Fluorescence lifetime imaging

Arabidopsis PSB-D cell suspension culture was maintained in MSMO [4.4 g/L Murashige and Skoog salts, 3% (wt/vol) sucrose, 0.5 mg/L NAA, 0.05 mg/L kinetin] medium at 25°C, in the dark, 130 rpm shaking. The culture was passaged once a week. For imaging cells were washed with fresh MSMO medium and incubated in MSMO medium supplemented with 10 μM of dye for 5 h. The cells were subsequently washed once with fresh MSMO medium and observed in imaging chambers as described below.

Arabidopsis thaliana Col-0 wild type or *qua2-1* (*quasimodo*) mutant seeds were surface-sterilized in a bleach:ethanol=20:75 solution for 8 min. They were subsequently washed twice in 70% ethanol and once in 100% ethanol. Dried sterilized seeds were plated on 0.5x MS [2.15 g/L Murashige and Skoog salts, 0.01% (wt/vol) MES, 1% (wt/vol) sucrose, 0.8% (wt/vol) Daishin agar]. Seeds were vernalized at 4 °C for 24h and grown vertically in long-day conditions (16h light, 8h dark) at 22 °C for 4 to 5 days. Grown *Arabidopsis* seedlings were transferred from 0.5 xMS agar plates to 0.5x MS containing 10 μM of dye, and incubated in constant light at 22°C for 2h, 1h30, 15 min or 20 min (for sulfo-BDP, PEG-BDP, N+-BDP and CWP-BDP respectively). The seedlings were washed for 30s with fresh 0.5x MS and transferred onto a glass slide for root or cotyledon imaging.

FLIM images of 256×256 pixels were recorded using a Leica TCS SP8 inverted scanning confocal microscope coupled with a Becker-Hickl SPC830 time-correlated single photon counting (TCSPC) module. The sample was excited at either 488 or 514 nm by a pulsed white light laser with a repetition rate of 40 MHz. Imaging was performed with a 63× 1.2 NA water immersion objective on cells from suspension and with a 20× 0.7 NA water immersion objective on root tissues. A line scanning speed of 400 Hz was used and the emission was collected using a spectral window of 20 nm bandwidth centered on 535 ± 10 nm (PEG-BDP), 525 ± 10 nm (sulfo-BDP) and 520 ± 10 nm (N+-BDP, CWP-BDP) onto a Leica HyD SMD hybrid photodetector. The acquisition time was set to 120 s for each image. After image acquisition SPCImage 7.1 software (Becker & Hickl) was used to fit the fluorescence decay curves in each pixel. A two-component exponential decay was used to obtain the best fit ($\chi^2 < 1.3$) and determine the average fluorescence lifetimes. A false colour scale was used to report lifetime values and

yield the fluorescence lifetime maps.

Control images of autofluorescence intensity and lifetime were taken on unstained specimens with the same imaging conditions and the highest laser intensity used, i.e. less than 10 μW after objective. The number of photons collected by pixel in the root was too low to allow for lifetime determination.

Viability testing on *Arabidopsis* seedlings

The viability of *Arabidopsis* seedlings after staining with the rotors was assessed by looking at root growth. After incubation with each rotor, N=10 roots were transferred back to their 0.5x MS agar culture plates and cultured in the same conditions as prior to incubation. 100% of the replicates continued to grow after staining.

Colocalization analysis

For colocalization analysis seedlings were stained with the molecular rotors as described in the previous section, and with 10 mg/L propidium iodide[63] (PI) or 5 mg/L 1,1'-Dioctadecyl-3,3,3',3'-Tetramethylindotricarbocyanine Iodide[64] (DiI-C18) in 0.5x MS for 5 min to highlight the cell-wall and plasma membrane respectively. The seedlings were washed thrice for 15s in fresh 0.5x MS before imaging. A hyperosmotic treatment in fresh 0.5x MS supplemented with 0.5M mannitol was performed to distinguish plasma membrane from wall staining. Seedlings were imaged within 15 min after immersion in the mannitol-rich medium.

The plasma membrane-specificity of N+-BDP was studied by colocalization with a Pleckstrin homology (PH) domain that is specific for PI(4,5)P2, a plasma membrane lipid, using 4-day-old *pUBQ10::mCherry-1xPH(PLC)* seedlings[59].

To further confirm the plasma membrane specificity of N+-BDP, a colocalization analysis was performed with N-(3-Triethylammoniumpropyl)-4-(6-(4-(Diethylamino) Phenyl) Hexatrienyl) Pyridinium Dibromide (FM4-64)[60], a styryl plasma membrane-specific dye. Apart from binding to the plasma membrane, FM4-64 also marks endosomes, which appear as a dotted pattern in the cytoplasm. To abolish membrane trafficking and to get FM4-64 signal only in the plasma membrane, seedlings were pre-treated with 20 μM Brefeldin A (B6542,

Sigma), an inhibitor of membrane trafficking, in liquid 0.5x MS for 30 min in the dark at room temperature. After the pre-treatment with Brefeldin A, FM4-64 was added to the final concentration of 20 μM and seedlings were incubated for another 20 min in the same conditions. N+-BDP was then added to the final concentration of 10 μM, seedlings were rinsed in 0.5x MS for 30 seconds and mounted in fresh 0.5x MS. Fluorescence of N+-BDP and FM4-64 was detected using laser excitation at 514 nm and 561 nm and emission at 510-530 nm and 700-750 nm, respectively. A hyperosmotic treatment in fresh 0.5x MS supplemented with 0.5M mannitol was performed to distinguish plasma membrane from wall staining.

To test the effect of different concentrations of N+-BDP on its plasma membrane specificity, a co-localization analysis of N+-BDP and FM4-64 signals was performed in 4-day-old seedlings treated with either 1 μM, 5 μM, 10 μM or 20 μM of N+-BDP using the procedure described above. To study the impact of N+-BDP incubation time on the staining specificity, colocalization time series were recorded at 10 μM dye concentration with FM4-64 as membrane counterstain.

Osmotic treatment of cell suspension cultures

The cell suspension was centrifuged and the MSMO medium replaced by fresh MSMO supplemented with 0.5M mannitol. The cells were imaged after 5 min equilibration.

Osmotic treatment of root hairs

To explore the N+-BDP response to changes in plasma membrane tension in planta, 5-day-old *Arabidopsis* seedlings were stained with 10 μM N+-BDP for 15 min and mounted in fresh 0.5x MS supplemented with 0.5 M mannitol. Imaging was performed within 7 min after mounting.

Fluorescence lifetime pattern comparison within wild type versus *qua2-1* seedlings

To compare the mechanical properties of the plasma membrane and the cell wall within wild type versus *qua2-1* mutant plants, 5-day-old *Arabidopsis* seedlings

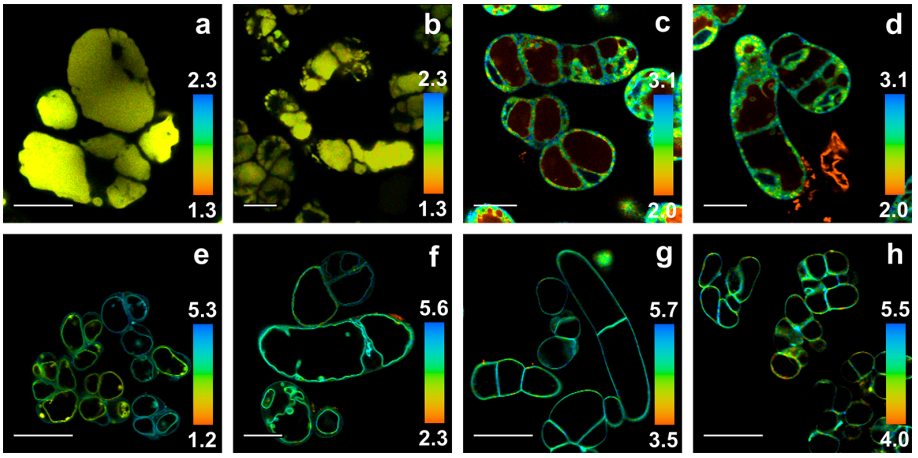

Figure 3.6: Rotor dyes in *Arabidopsis* suspension-cultured cells. FLIM images of *Arabidopsis* suspension-cultured cells stained with sulfo-BDP (a-b, scale bar = 50 μm), PEG-BDP (c-d, scale bar = 20 μm), N+-BDP (e, scale bar = 50 μm, f, scale bar = 20 μm), CWP-BDP (g-h, scale bar = 50 μm). sulfo-BDP accumulates in the relatively homogeneous vacuoles. PEG-BDP accumulates in the cytoplasm, highlighting a high crowding density. N+-BDP stains the plasma membrane, showing inter- and intracellular variations in lipid composition and/or membrane tension. CWP-BDP stains the cell wall, highlighting clear differences in mesh size between newly formed walls (high lifetimes) and older peripheral walls (lower lifetimes).

were incubated in 0.5x MS containing 10 μM N+-BDP or 10 μM CWP-BDP for 15 min. FLIM imaging of roots epithelial and cotyledon pavement cells was performed as described above.

Abscisic acid (ABA) treatment on cotyledons

To induce stomatal closure, 4-day-old seedlings were treated with 10 μM ABA for 2h, in conditions reported previously[65]. As a control, seedlings were incubated in the same conditions but without ABA.

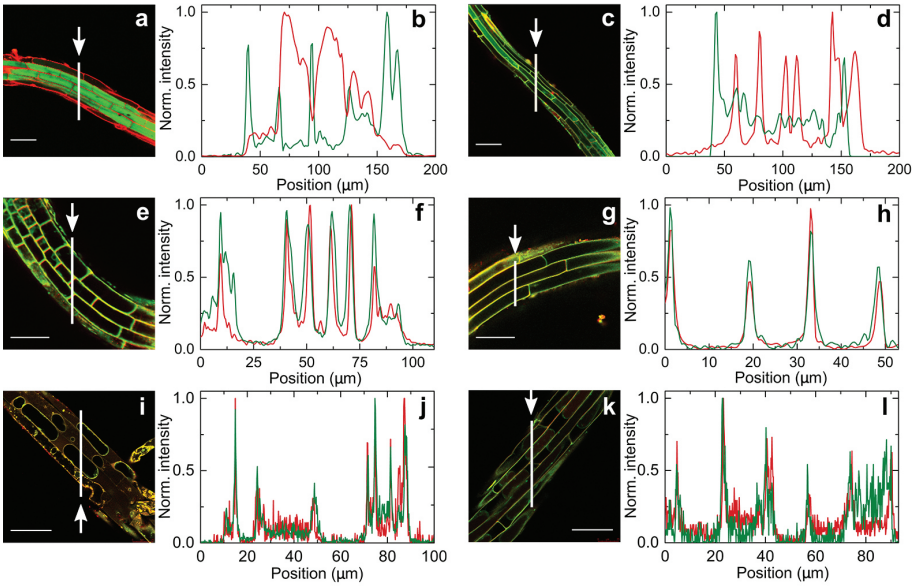

Figure 3.7: Colocalization analysis of the four rotors in roots of 4-day-old *Arabidopsis* seedlings. Superimposed confocal images of sulfo-BDP signal and Propidium Iodide (PI) (cell wall stain)[63] (a), PEG-BDP and PI signals (c), N+-BDP signal and 1,1'-Dioctadecyl-3,3,3',3'-Tetramethylindotricarbocyanine Iodide (DiI-C18) (membrane stain)8 signal (e), CWP-BDP and PI signals (g) in the maturation zone of *Arabidopsis* roots. Superimposed confocal images of N+-BDP and DiI-C18 signals (i), CWP-BDP and PI signals (k) in the maturation zone of *Arabidopsis* roots after hyperosmotic shock in 0.5M mannitol-supplemented 0.5x MS medium. (a,c,e,g: scale bar = 100 μm, i,k: scale bar = 50 μm). Corresponding intensity profiles (b,d,f,h,j,l; rotor in green, DiI or PI in red) plotted along the drawn white line indicated by an arrow. The profiles obtained with N+-BDP and DiI-C18 show a good superposition even after plasmolysis, suggesting that N+-BDP targets the membranes with a high specificity. Similarly, the profiles obtained with CWP-BDP show a good superposition with the ones obtained with PI after plasmolysis, suggesting that CWP-BDP targets the cell wall with a high specificity. Sulfo-BDP shows a signal exclusion with PI. PEG-BDP exhibits a partial colocalization with PI, which highlights its lack of specificity towards the cytoplasm.

Table 3.1: Number of samples and observations

Experiments	Figures	Sample numbers
Cell suspension imaging	Figure 3.1e-l Figure 3.4a-b Figure 3.6 Figure 3.21	Sulfo-BDP (n>110 cells from 3 cell batches), PEG-BDP (n>220 cells from 4 cell batches), N+-BDP (n>200 cells from 4 cell batches), CWP-BDP (n>40 cells from 2 cell batches) were observed to confirm the patterns.
Root imaging	Figure 3.2 Figure 3.3g-j Figure 3.4c-f Figures 3.12-3.13 Figure 3.24	Sulfo-BDP (n=5 roots), PEG-BDP (n=8 roots), N+-BDP (n=18 roots), CWP-BDP (n=10 roots) were observed to confirm the patterns.
Colocalization analysis in roots	Figure 3.7	Sulfo-BDP (n=2 roots), PEG-BDP (n=2 roots), N+-BDP (n=2 roots), CWP-BDP (n=2 roots) were observed to confirm the patterns.
Colocalization analysis of N+-BDP in roots	Figures 3.8-3.10	Colocalization in \textit{pUBQ10::mCherry-1xPH(PLC)} seedlings (n= 5 seedlings) and colocalization with FM4-64 (n= 5 seedlings) were observed to confirm the patterns.
GUV imaging	Figure 3.3 a-c Figure 3.20	N+-BDP: n=16 SM:DOPC:Chol GUV and n=9 DOPC GUV were observed to confirm the patterns.
Osmotic treatment on suspension cells	Figure 3.3d-f	N+-BDP: n>50 cells and n>110 cells from the same batch were observed for statistics before and after hyperosmotic treatment respectively.
Root hair imaging	Figure 3.3k-m,t-v Figure 3.4g-h	n=18 hairs from 8 roots (N+-BDP) and n=10 hairs from 4 roots (CWP-BDP) were imaged for statistics in the hair tip membrane and wall respectively. n>40 and n>30 non-hair epidermal cells were imaged for statistics in non-hair cells membrane and wall respectively.
Root hair maturation imaging	Figure 3.4i	CWP-BDP: The growth and maturation of n=9 hairs from 4 roots was followed over 1h40 to confirm the observed fluorescence lifetime evolution trend.
Osmotic treatment on root hairs	Figure 3.3w-y Figure 3.22	N+-BDP : n=8 plasmolysed hairs from at least 10 roots and n=5 control hairs from at least 10 roots were imaged for statistics in the hair membrane.
Osmotic treatment on root epidermal cells	Figure 3.3q-s Figure 3.23	N+-BDP : n=23 plasmolysed cells were imaged for statistics in the membrane.
Root imaging in wild type and \textit{qua2-1} mutant seedlings	Figure 3.27	CWP-BDP : n= 12 roots were imaged to confirm the patterns.
Pavement cells imaging in wild type and \textit{qua2-1} mutant seedlings	Figure 3.3n-p Figure 3.5a-c Figures 3.25-3.26	N+-BDP (n >230 cells from at least 10 seedlings), CWP-BDP (n >230 cells from at least 10 seedlings)
Stomata imaging	Figure 3.5d-f Figure 3.28	CWP-BDP: n>30 stomata and n>40 mesophyll cells on the cotyledons of 2 seedlings were imaged for statistics in stomatal cells wall and mesophyll cells wall respectively.
Stomatal closing and guard cell imaging	Figure 3.5g-i Figure 3.29	CWP-BDP: n>20 closed stomata (after ABA treatment) and n>15 open stomata on the cotyledons of 2 seedlings each were imaged for statistics in closed and open guard cell walls respectively.
Dye uptake kinetics	Figures 3.14-3.17	PEG-BDP (n=2 roots), N+-BDP (n=2 roots), CWP-BDP (n=2 roots) were observed.
Dye persistence	Figure 3.19	n=2 roots per time for each rotor
Autofluorescence control	Figure 3.18	n>50 suspension cells, n>3 roots, n>10 guard cells were observed.

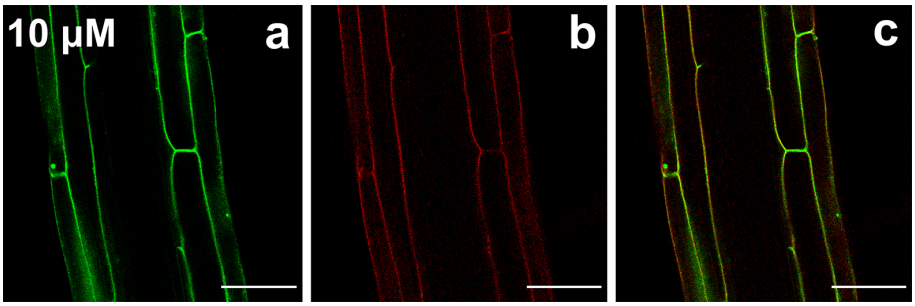

Figure 3.8: Colocalization analysis of N+-BDP with PI(4,5)P2 reporter in the plasma membrane. Confocal images of N+-BDP signal in the root maturation zone of 4-day-old *pUBQ10::mCherry 1xPH(PLC)*[59] *Arabidopsis* seedlings (a), signal of PI(4,5)P2 reporter (b) and signal overlay (c). Scale bars = 50 μm. The signals obtained with N+-BDP and the expressed marker show a good superposition, suggesting that N+-BDP is specific for the plasma membrane.

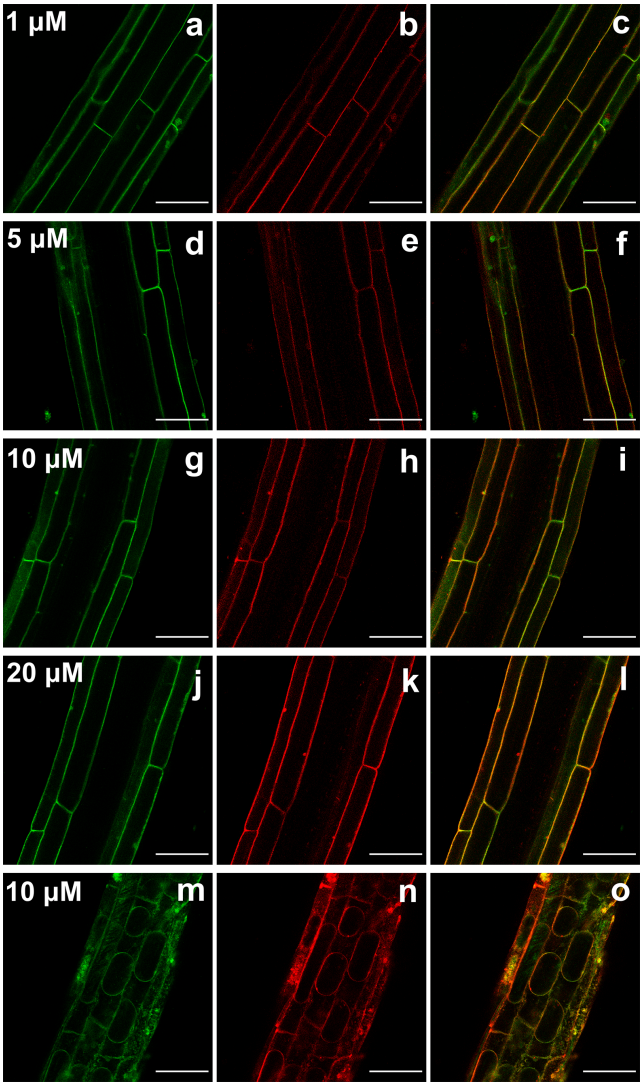

Figure 3.9: Influence of the N+-BDP concentration on its localization specificity. Confocal images of N+-BDP signal in the maturation zone of roots of 4-day-old *Arabidopsis* seedlings incubated at four different dye concentrations (a, d, g, j), corresponding N-(3-Triethylammoniumpropyl)-4-(6-(4-(Diethylamino) Phenyl) Hexatrienyl) Pyridinium Dibromide (FM4-64) membrane counterstain10 signal (b, e, h, k) and overlay (c, f, I, l). Confocal images of N+-BDP signal (m), FM4-64 signal (n) and signal overlay (o) in the maturation zone of Arabidopsis roots incubated at 10 μM N+-BDP, after hyperosmotic shock in 0.5M mannitol-supplemented 0.5x MS medium. Scale bars = 50 μm. The signals obtained with N+-BDP and FM4-64 show a good superposition at all used concentrations, even after plasmolysis, suggesting that the specificity of the N+-BDP probe is not affected by its concentration below 20 μM.

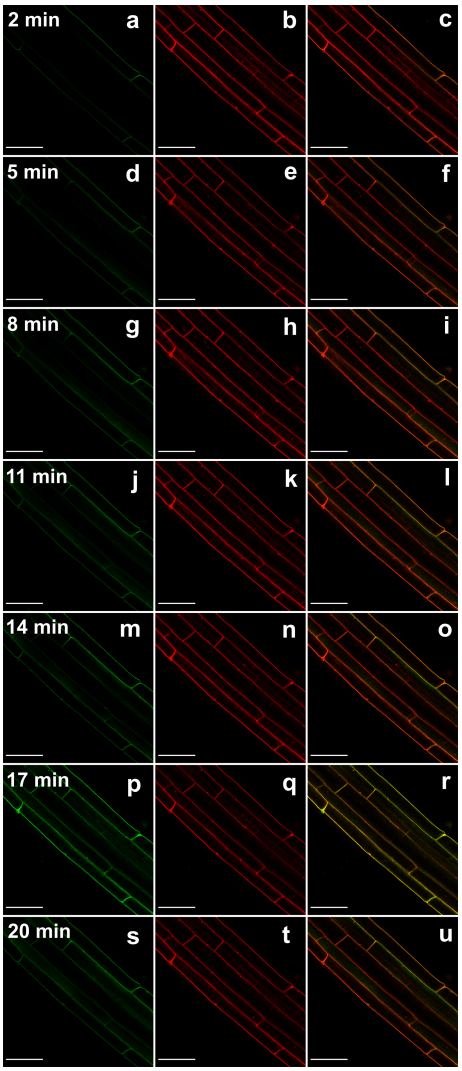

Figure 3.10: Influence of the incubation time on the specificity of N+-BDP localization. Confocal images of N+-BDP signal in the root maturation zone of 4-day-old *Arabidopsis* seedlings incubated with 10 μM N+-BDP for different durations (a, d, g, j, m, p, s), corresponding FM4-64 membrane counterstain signal[60] (b, e, h, k, n, q, t) and overlay (c, f, i, l, o, r, u) (scale bars = 50 μm). The signals of N+-BDP and FM4-64 show a good superposition at all incubation times, suggesting that the specificity of the N+-BDP probe is not affected by the incubation time below 20 min incubation. However, N+-BDP staining becomes complete as from around 14 min incubation.

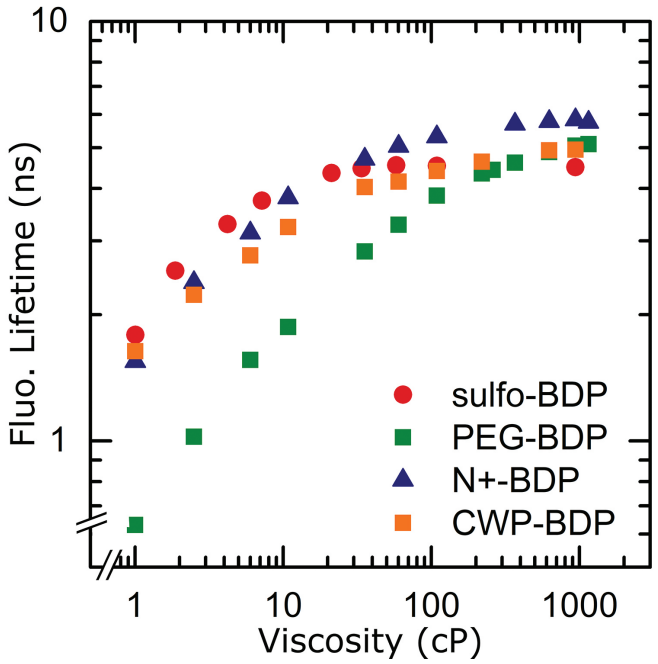

Figure 3.11: Rotor dye calibration in simple glycerol/water mixtures. Fluorescence lifetime evolution of sulfo-BDP, PEG-BDP, N+-BDP and CWP-BDP in glycerol/water mixtures of varied viscosities, upon excitation with a 475 nm laser line. The error bars representing the standard deviation over three measurements are smaller than the size of the data points. The four rotors retain their rigidochromic properties after functionalization.

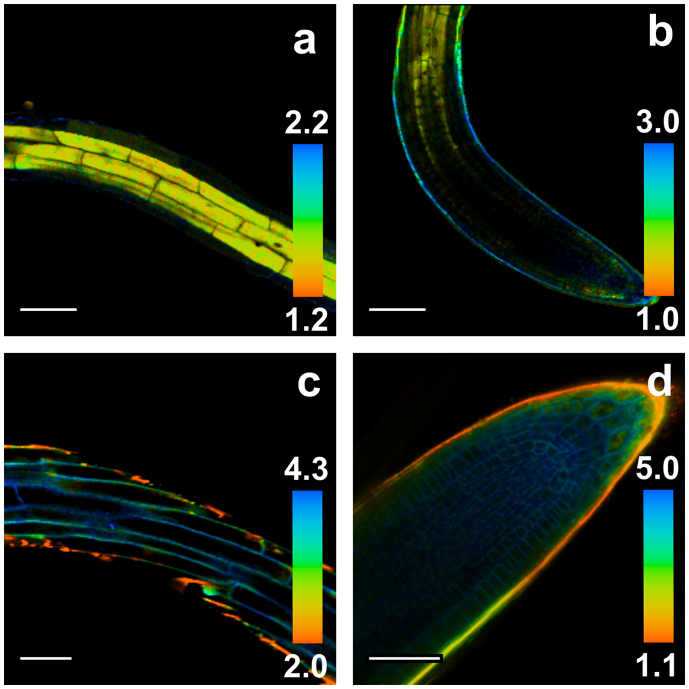

Figure 3.12: Rotor dyes in 4-day-old *Arabidopsis* seedlings. Fluorescence lifetime maps of roots 4-day-old *Arabidopsis* seedlings showing the vacuoles (sulfo-BDP, a-b, scale bar = 100 μm) and cytosol (PEG-BDP, c-d, scale bar = 50 μm). The internalization of sulfo-BDP and PEG-BDP into the root apex is limited as the dyes stick to the protective cuticle layer.

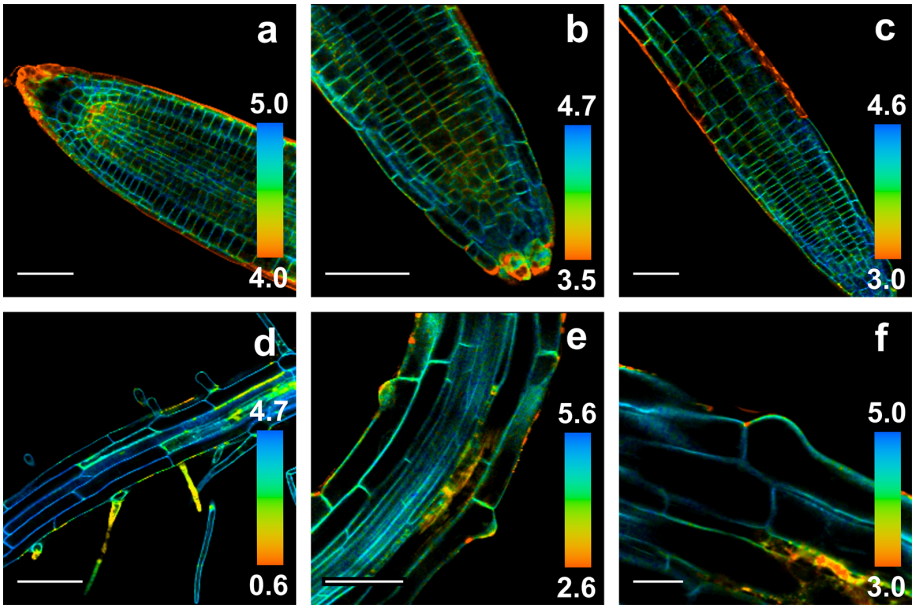

Figure 3.13: N+-BDP in 4-day-old *Arabidopsis* seedlings. Fluorescence lifetime fluidity maps of roots of 4-day-old *Arabidopsis* seedlings stained with N+-BDP (a-c,e, scale bar = 50 μm) (d, scale bar = 100 μm) (f, scale bar = 20 μm). Clear spatial variations in lifetime are visible according to cell function and developmental stage.

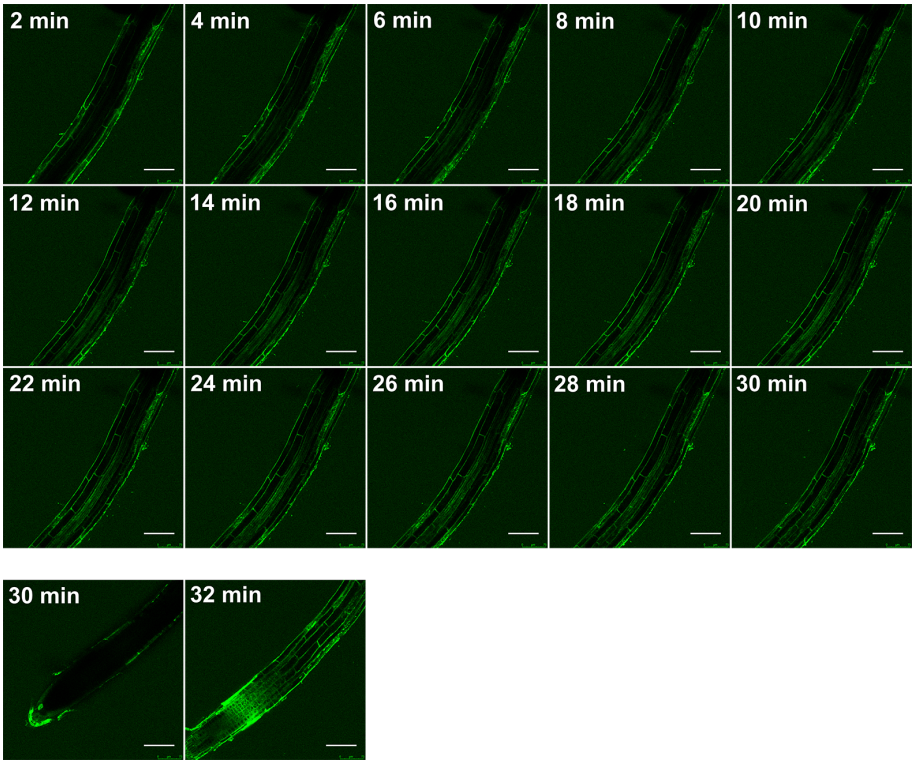

Figure 3.14: Staining kinetics in the root differentiation region with PEG-BDP. Confocal images of a root of 4-day-old *Arabidopsis* seedling taken at different incubation times in a solution of PEG-BDP in 0.5x MS medium (scale bar = 100 μm).

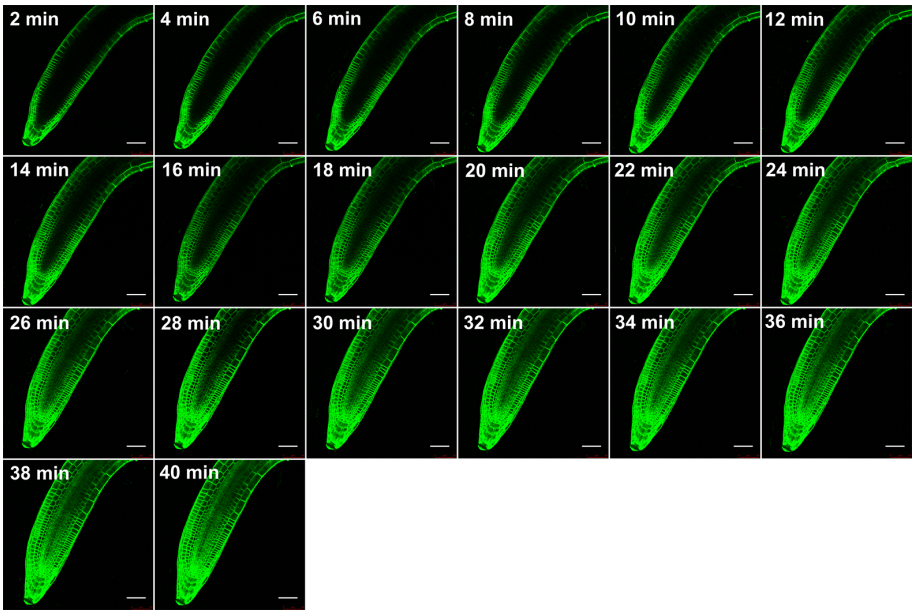

Figure 3.15: Staining kinetics in the root apex with N+-BDP. Confocal images of a root of 4-day-old *Arabidopsis* seedling apex taken at different incubation times in a solution of N+-BDP in 0.5x MS medium (scale bar = 50 μm).

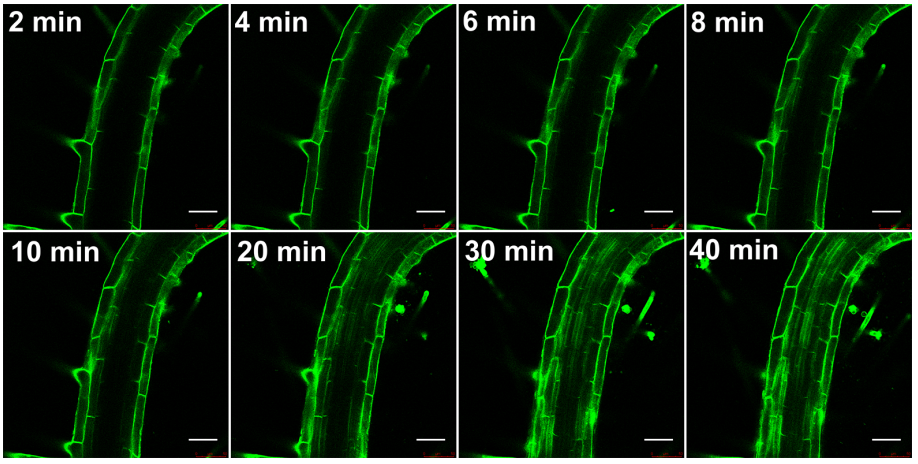

Figure 3.16: Staining kinetics in the root differentiation region with N+-BDP. Confocal images of a root of 4-day-old *Arabidopsis* seedling maturation region taken at different incubation times in a solution of N+-BDP in 0.5x MS medium (scale bar = 50 μm).

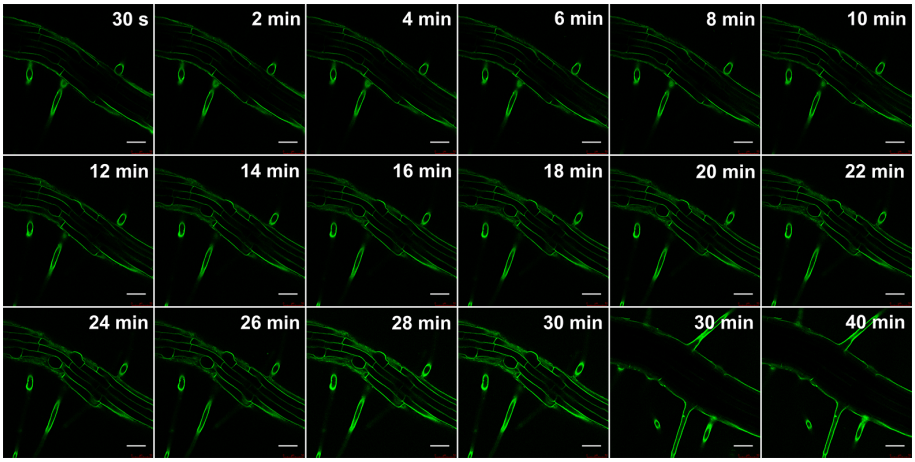

Figure 3.17: Staining kinetics in the root differentiation region with CWP-BDP. Confocal images of a root of 4-day-old *Arabidopsis* seedling taken at different incubation times in a solution of CWP-BDP in 0.5x MS medium (scale bar = 50 μm)

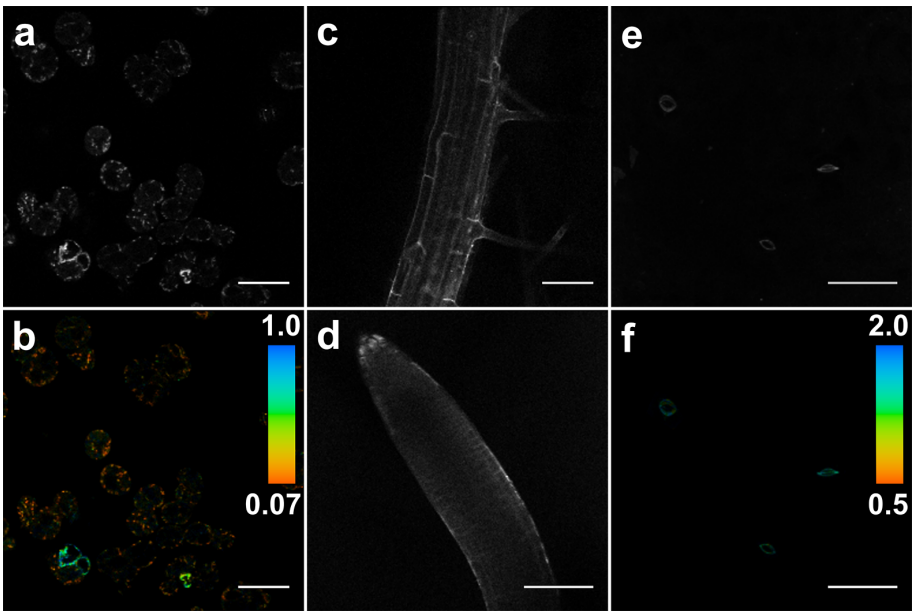

Figure 3.18: Autofluorescence control in the systems studied. Control images of autofluorescence intensity and lifetime within *Arabidopsis* suspension-cultured cells (scale bar = 100 μm) (a,b), a root of a 4-day-old *Arabidopsis* seedling (scale bar = 100 μm) (c,d), and *Arabidopsis* stomata guard cells (scale bar = 50 μm) (e,f).

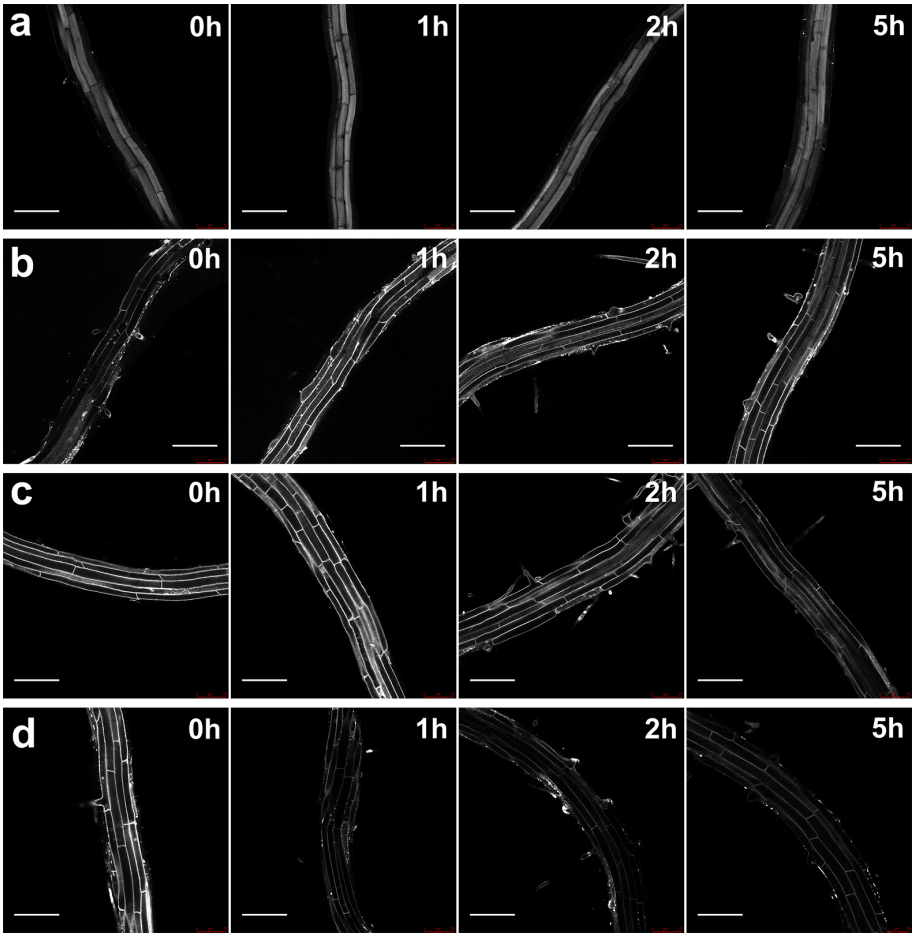

Figure 3.19: Staining persistence in the root differentiation region. Confocal images of roots of 4-day-old *Arabidopsis* seedlings immersed in 0.5x MS medium, taken at different times of incubation with sulfo-BDP (a), PEG-BDP (b), N+-BDP (c) and CWP-BDP (d) (scale bar = 100 μm).

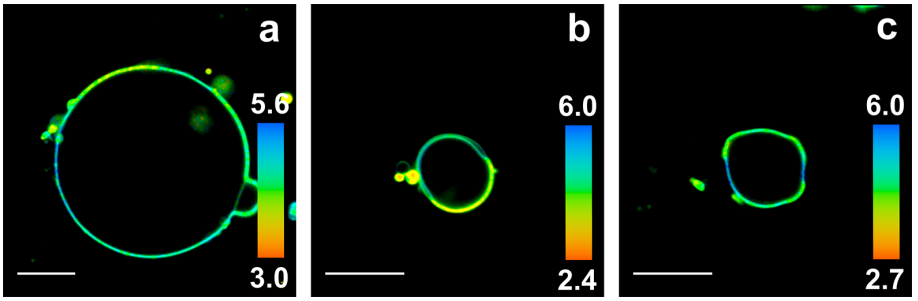

Figure 3.20: Rotor dyes in synthetic Giant Unilamellar Vesicles. FLIM images of demixed 1,2-dioleoyl-sn-glycero-3-phosphocholine (DOPC)/Sphingomyelin/cholesterol=0.24/0.56/0.20 (molar ratio) Giant Unilamellar Vesicles formed in 100 mM glucose, and stained with N+-BDP (scale bars = 10 μm). The liquid ordered (cholesterol/sphingomyelin-rich) and the liquid disordered (DOPC-rich) phases can be clearly differentiated on a fluorescence lifetime basis; the average fluorescence lifetime is higher in the liquid ordered phase where the probe rotation is more hindered.

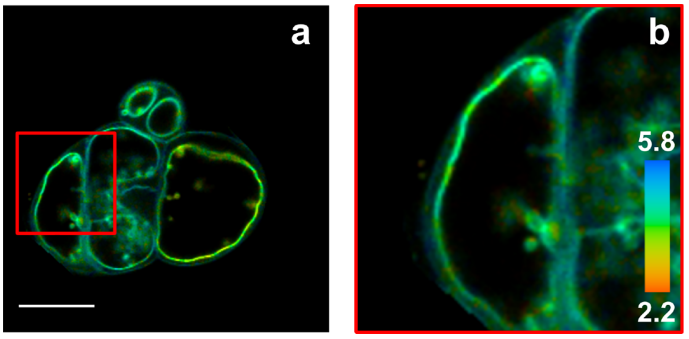

Figure 3.21: N+-BDP in *Arabidopsis* suspension-cultured cells. FLIM image of an *Arabidopsis* suspension-cultured cell stained with N+-BDP (a, scale bar = 20 μm) which exhibit distinct mechanical microdomains in the membrane (close-up view in b).

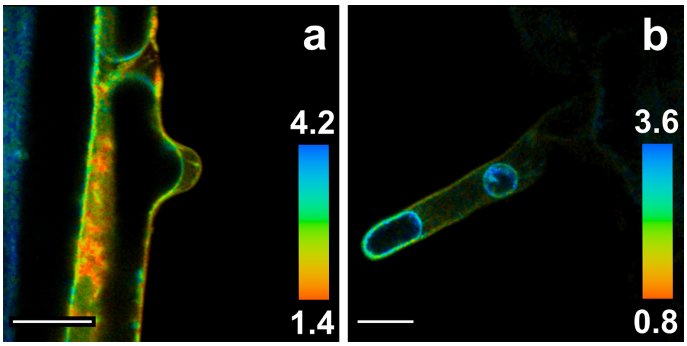

Figure 3.22: Plasmolysis of root hairs monitored by N+-BDP. Fluorescence lifetime maps of hairs of roots of 4-day-old *Arabidopsis* seedlings stained with N+-BDP and plasmolysed in 0.5M mannitol-supplemented 0.5x MS medium (scale bars = 20 μm). The fluorescence lifetimes within the membrane increase when the internal tension drops as the membrane detaches from the walls.

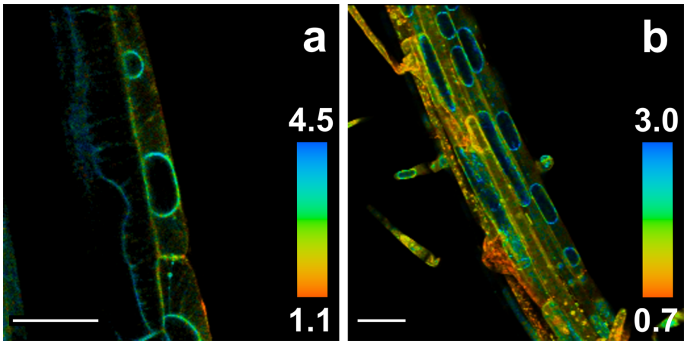

Figure 3.23: Plasmolysis of root epidermal cells monitored by N+-BDP. Fluorescence lifetime maps of roots epidermal cells of 4-day-old *Arabidopsis* seedlings stained with N+-BDP and plasmolysed in 0.5M mannitol-supplemented 0.5x MS medium (scale bars = 50 μm). The fluorescence lifetimes within the membrane increase when the internal tension drops as the membrane detaches from the walls.

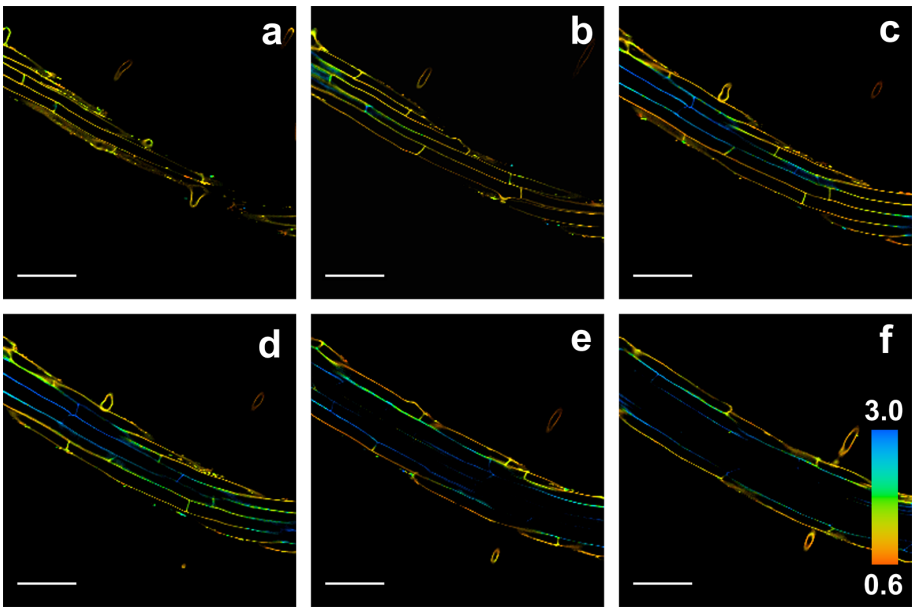

Figure 3.24: CWP-BDP in 4-day-old *Arabidopsis* seedlings. Fluorescence lifetime maps of a root of 4-day-old *Arabidopsis* seedling stained with CWP-BDP at different depths within the root, starting from the outside in (a to f) (scale bar = 100 μm). The probe permeates well in the epidermal layer, but diffuses more slowly in the core of the root.

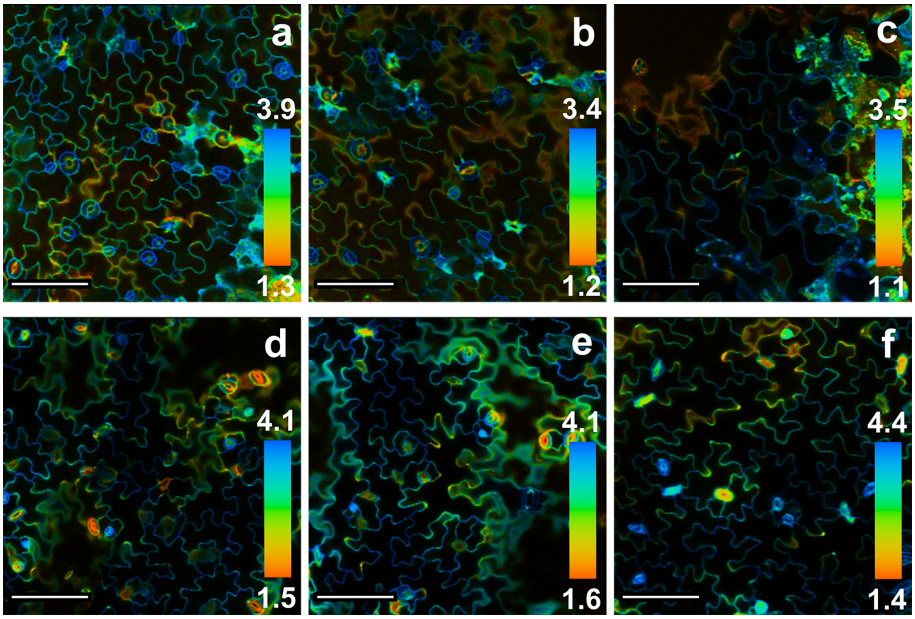

Figure 3.25: CWP-BDP in the cotyledon pavement cells of wild type and *qua2-1* mutant *Arabidopsis* seedlings. FLIM images of cotyledon pavement cells stained with CWP-BDP in *qua2-1* mutant *Arabidopsis* seedlings (a-c) versus wild type seedlings (d-f) (scale bars = 100 μm). The fluorescence lifetimes are lower in the cell walls of mutant seedlings compared to wild type seedlings, suggesting a higher wall porosity.

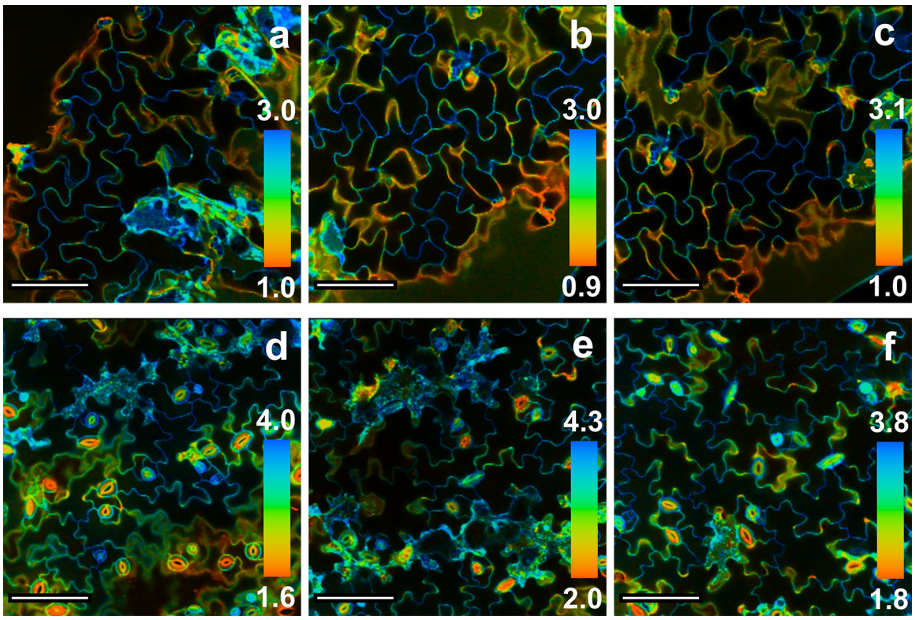

Figure 3.26: N+-BDP in the cotyledon pavement cells of wild type and *qua2-1* mutant *Arabidopsis* seedlings. FLIM images of cotyledon pavement cells stained with N+-BDP in *qua2-1* mutant *Arabidopsis* seedlings (a-c) versus wild type seedlings (d-f) (scale bars = 100 μm). The fluorescence lifetimes are lower in the cell membranes of mutant seedlings compared to wild type seedlings, suggesting a lower tension.

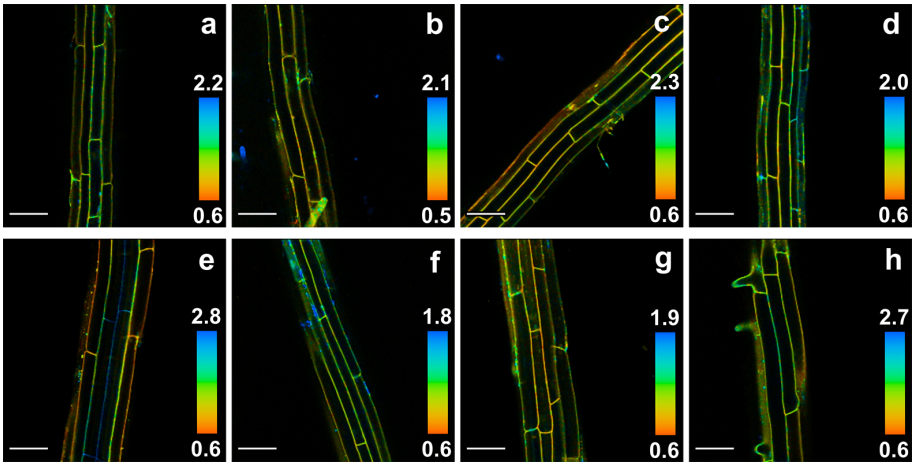

Figure 3.27: CWP-BDP in the root epidermal cells of wild type and *qua2-1* mutant *Arabidopsis* seedlings. Fluorescence lifetime maps of *qua2-1* mutant (a-d) and wild type (e-h) *Arabidopsis* epidermal root cells stained with CWP-BDP (scale bars = 100 μm). No significant difference can be highlighted when comparing the lifetime patterns within wild type and mutant root as the variation between different wild type epidermal root cells is already high.

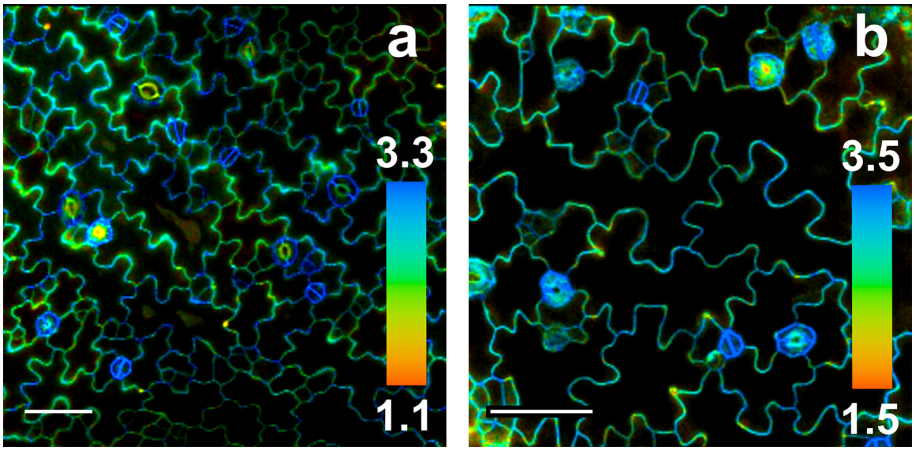

Figure 3.28: CWP-BDP in the cotyledon pavement and guard cells of *Arabidopsis* seedlings. FLIM images in the epidermal cell layer of a cotyledon, of a 4-day-old *Arabidopsis* seedling, stained with CWP-BDP (scale bar = 50 μm). Both stomata and pavement cells are visible, showing distinct lifetime patterns. The lifetimes are higher in the guard cells, reflecting the presence of dense pectinrich matter.

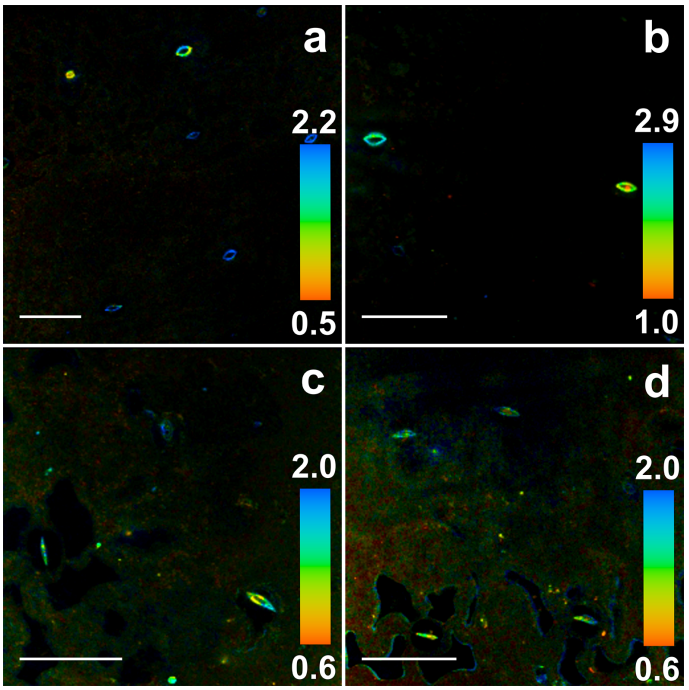

Figure 3.29: Closing of the cotyledon stomata of *Arabidopsis* seedlings monitored by CWP-BDP. FLIM images in the epidermal cell layer of a cotyledon of a 4-day-old *Arabidopsis* seedling stained with CWP-BDP, before (a-b) and after (c-d) abscisic acid (ABA) treatment (scale bar = 50 μm). The ABA treatment triggers the closure of stomatal cells[65], and a consequent decrease of fluorescence lifetime within the guard cells, likely due to a decrease in turgor.

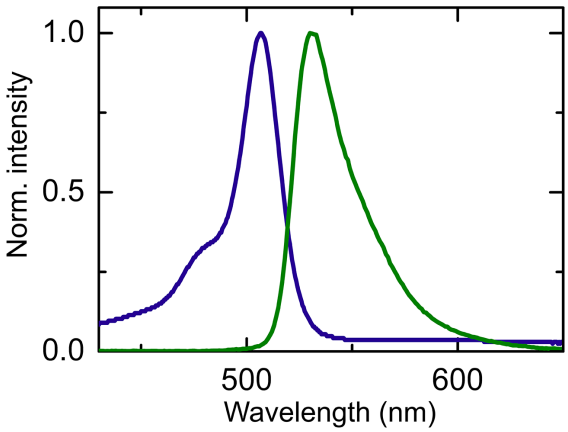

Figure 3.30: Absorption (blue) and fluorescence (green) spectra of sulfo-BDP in Milli-Q water, λ_{exc}=370nm

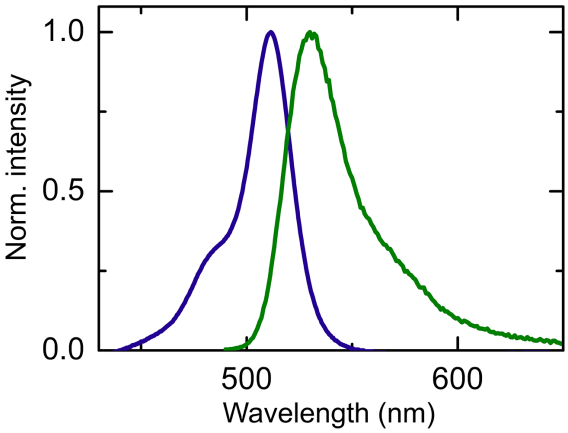

Figure 3.31: Absorption (blue) and fluorescence (green) spectra of PEG-BDP in Milli-Q water, λ_{exc}=370nm

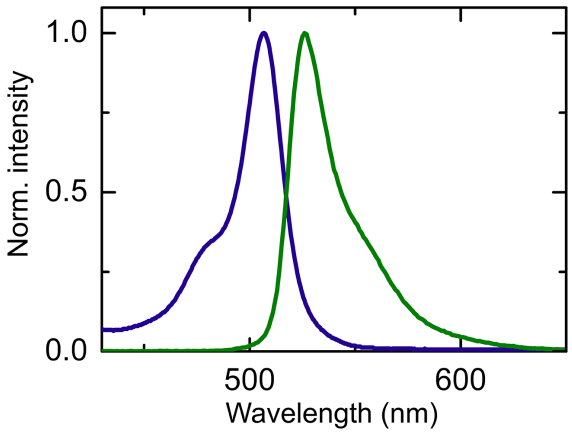

Figure 3.32: Absorption (blue) and fluorescence (green) spectra of N+-BDP in Milli-Q water, λ_{exc}=370nm

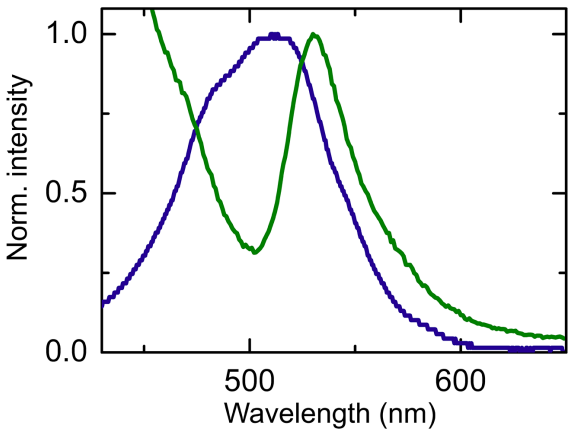

Figure 3.33: Absorption (blue) and fluorescence (green) spectra of CWP-BDP in Milli-Q water, λ_{exc}=370nm

References

[1] Puchkov, E. O. Intracellular Viscosity: Methods of Measurement and Role in Metabolism. *Biochemistry (Moscow) Supplement Series A: Membrane and Cell Biology*, 7:270–279, 2013.

[2] Uribe, S. Sampedro, J. G. Measuring Solution Viscosity and its Effect on Enzyme Activity. *Biol. Proced. Online*, 108–115, 2003.

[3] Gavish, B. Werber, M. M. Viscosity-dependent structural fluctuations in enzyme catalysis.. *Biochemistry*, 18:1269–1275, 1979.

[4] Carlson, J. G. Protoplasmic Viscosity Changes in Different Regions of the Grasshopper Neuroblast during Mitosis.. *Biological Bulletin*, 90:109–121, 1946.

[5] de Laat, S. W., van der Saag, P. T., Shinitzky, M. Microviscosity modulation during the cell cycle of neuroblastoma cells. *Proc. Natl. Acad. Sci.*, 74:4458–4461, 1977.

[6] Vasanji, A., Ghosh, P. K., Graham, L. M., Eppell, S. J. Fox, P. L. Polarization of Plasma Membrane Microviscosity during Endothelial Cell Migration. *Dev. Cell*, 6:29–41, 2004.

[7] de Laat, S. W., van Der Saag, P. T., Nelemans, S. A. Shinitzky, M. Microviscosity changes during differentiation of neuroblastoma cells. *Biomembranes*, 509:188–193, 1978.

[8] Binenbaum, Z., Klyman, E., Fishov, I. Division-associated changes in membrane viscosity of Escherichia coli. *Biochimie*, 81:921–929, 1999.

[9] Ranft, J. et al. Fluidization of tissues by cell division and apoptosis. *Proc. Natl. Acad. Sci.*, 107:20863–20868, 2010.

[10] Somssich, M., Khan, G. A. Persson, S. Cell Wall Heterogeneity in Root Development of Arabidopsis. *Front. Plant Sci.*, 7:1–11, 2016.

[11] Kirchhelle, C., Garcia-Gonzalez, D., Irani, N. G., Jérusalem, A. Moore, I. Two mechanisms regulate directional cell growth in Arabidopsis lateral roots. *eLife*, 8:e47988, 2019.

[12] Milani, P. et al. Matching Patterns of Gene Expression to Mechanical Stiffness at Cell Resolution through Quantitative Tandem Epifluorescence and Nanoindentation. *Plant Physiol.*, 165:1399–1408, 2014.

[13] Elsayad, K. et al. Mapping the subcellular mechanical properties of live cells in tissues with fluorescence emission–Brillouin imaging. *Science Signaling*, 9:rs5, 2016.

[14] Carisey, A., Stroud, M., Tsang, R. Ballestrem, C. Fluorescence recovery after photobleaching.. *Methods Mol. Biol.*, 769:387–402, 2011.

[15] Cole, N. B. et al. Diffusional mobility of Golgi proteins in membranes of living cells.. *Science*, 273:797–801, 1996.

[16] Nehls, S. et al. Dynamics and retention of misfolded proteins in native ER membranes. *Nat. Cell. Biol.*, 2:288–295, 2000.

[17] Wirtz, D. Particle-tracking microrheology of living cells: principles and applications. *Annu. Rev. Biophys.*, 38:301–326, 2009.

[18] Crocker, J. C. Hoffman, B. D. Multiple-particle tracking and two-point microrheology in cells. *Methods Cell Biol.*, 83:141–178, 2007.

[19] Haidekker, M. A. Theodorakis, E. A. Environment-sensitive behavior of fluorescent molecular rotors.. *J. Biol. Eng.*, 4:1–14, 2010.

[20] Vyšniauskas, A. et al. Exploring viscosity, polarity and temperature sensitivity of BODIPY-

based molecular rotors. *Phys. Chem. Chem. Phys.*, 19:25252–25259, 2017.

[21] Wang, D., Miyamoto, R., Shiraishi, Y. Hirai, T. BODIPY-Conjugated Thermoresponsive Copolymer as a Fluorescent Thermometer Based on Polymer Microviscosity. *Langmuir*, 25:13176–13182, 2009.

[22] Suhina, T. et al. Fluorescence Microscopy Visualization of Contacts Between Objects. *Angew. Chem. Int. Ed.*, 127:3759–3762, 2015.

[23] Alamiry, M. A. H., Bahaidarah, E., Harriman, A., Burab, T. Ziessel, R. Fluorescent molecular rotors under pressure: synergistic effects of an inert polymer. *RSC Advances*, 2:9851–9859, 2012.

[24] Haidekker, M. A. Theodorakis, E. A. Molecular rotors—fluorescent biosensors for viscosity and flow.. *Org. Biomol. Chem.*, 5:1669–1678, 2006.

[25] Kuimova, M. K., Yahioglu, G., Levitt, J. A. Suhling, K. Molecular Rotor Measures Viscosity of Live Cells via Fluorescence Lifetime Imaging. *J. Am. Chem. Soc.*, 130:6672–6673, 2008.

[26] López-Duarte, I., Vu, T. T., Izquierdo, M. A., Bull, J. A. Kuimova, M. K. A molecular rotor for measuring viscosity in plasma membranes of live cells. *Chem. Commun.*, 50:5282–5284, 2014.

[27] Raut, S. et al. A homodimeric BODIPY rotor as a fluorescent viscosity sensor for membrane-mimicking and cellular environments. *Phys. Chem. Chem. Phys.*, 16:27037–27042, 2014.

[28] MacDougall, A. J. The effect of peptide-pectin interactions on the gelation behaviour of a plant cell wall pectin. *Carbohydr. Res.*, 335:115–126, 2001.

[29] Echard, A. Burgess, D. The Changing Lipidome during Cell Division.. *Cell*, 156:394–395, 2014.

[30] Morris, C. E. Homann, U. Cell Surface Area Regulation and Membrane Tension. *Journal of Membrane Biology*, 179:79–102, 2001.

[31] Sheetz, M. P. Dai, J. Modulation of membrane dynamics and cell motility by membrane tension. *Trends Cell Biol.*, 6:85–89, 1996.

[32] Cosgrove, D. J. Growth of the plant cell wall.. *Nat. Rev. Mol. Cell. Biol.*, 6:850–861, 2005.

[33] Houston, K., Tucker, M. R., Chowdhury, J., Shirley, N. Little, A. The Plant Cell Wall: A Complex and Dynamic Structure As Revealed by the Responses of Genes under Stress Conditions.. *Front. Plant Sci.*, 7:1–18, 2016.

[34] Lingwood, D. Simons, K. Lipid rafts as a membrane-organizing principle. *Science*, 327:46–50, 2010.

[35] Silvius, J. R. Role of cholesterol in lipid raft formation:lessons from lipid model systems. *Biochimica et Biophysica Acta*, 1610:174–183, 2003.

[36] Brown, D. A. London, E. Structure and function of sphingolipid- and cholesterol-rich membrane rafts.. *J. Biol. Chem.*, 275:17221–17224, 2000.

[37] Colom, A. et al. A fluorescent membrane tension probe. *Nat. Chem.*, 10:1118–1125, 2018.

[38] Mongrand, S., Stanislas, T., Bayer, E. M. F., Lherminier, J. Simon-Plas, F. Membrane rafts in plant cells. *Trends in Plant Science*, 15:656–663, 2010.

[39] Rostovtsev, V. V., Green, L. G., Fokin, V. V. Sharpless, B. K. A Stepwise Huisgen Cycloaddition Process: Copper(I)-Catalyzed Regioselective "Ligation" of Azides and Terminal Alkynes.

Angew. Chem. Int. Ed., 41:2596–2599, 2002.

[40] Lampugnani, E. R., Khan, G. A., Somssich, M. Persson, S. Building a plant cell wall at a glance. *Journal of Cell Science*, 131:jcs207373, 2018.

[41] Braybrook, S. A. Jönsson, H. Shifting foundations: the mechanical cell wall and development. *Curr. Opin. Plant Biol.*, 29:115–120, 2016.

[42] Loutfy, R. O. Fluorescence probes for polymer free-volume. *Pure Appl. Chem.*, 58:1239–1248, 1986.

[43] Willats, W. G. et al. Modulation of the degree and pattern of methyl-esterification of pectic homogalacturonan in plant cell walls. Implications for pectin methyl esterase action, matrix properties, and cell adhesion. *J. Biol. Chem.*, 276:19404–19413, 2001.

[44] Barberon, M. Geldner, N. Radial Transport of Nutrients: The Plant Root as a Polarized Epithelium. *Plant Physiol.*, 166:528–537, 2014.

[45] Rondeau-Mouro, C., Defer, D., Leboeuf, E. Lahaye, M. Assessment of cell wall porosity in Arabidopsis thaliana by NMR spectroscopy. *International Journal of Biological Macromolecules*, 42:83—92, 2008.

[46] Leboeuf, E., Guillon, F., Thoiron, S. Lahaye, M. Biochemical and immunohistochemical analysis of pectic polysaccharides in the cell walls of Arabidopsis mutant QUASIMODO 1 suspension-cultured cells: implications for cell adhesion. *Journal of Experimental Botany*, 56:3171–3182, 2005.

[47] Nielsen, E. *Root Hairs*, 12:85–102, 2010.

[48] Ketelaar, T., Galway, M. E., Mulder, B. M. Emons, A. M. C. Rates of exocytosis and endocytosis in Arabidopsis root hairs and pollen tubes. *J. Microsc.*, 231:265–273, 2008.

[49] Palin, R. Geitmann, A. The role of pectin in plant morphogenesis. *Biosystems*, 109:397–402, 2012.

[50] Hetherington, A. M. Woodward, F. I. The role of stomata in sensing and driving environmental change. *Nature*, 424:901–908, 2003.

[51] Marom, Z., Shtein, I. Bar-On, B. Stomatal Opening: The Role of Cell-Wall Mechanical Anisotropy and Its Analytical Relations to the Bio-composite Characteristics. *Front. Plant Sci.*, 8:1–12, 2017.

[52] Franks, P.J. Farquhar, G. D. The Mechanical Diversity of Stomata and Its Significance in Gas-Exchange Control. *Plant Physiol.*, 143:78–87, 2007.

[53] Shtein, I. et al. Stomatal cell wall composition: Distinctive structural patterns associated with different phylogenetic groups. *Ann. Bot.*, 119:1021–1033, 2017.

[54] Peaucelle, A., Wightman, R. Höfte, H. The control of growth symmetry breaking in the Arabidopsis hypocotyl. *Curr Biol.*, 25:1746–1752, 2015.

[55] Braybrook, S. A. Peaucelle, A. Mechano-chemical aspects of organ formation in Arabidopsis thaliana: the relationship between auxin and pectin. *PLoS One*, 8:e57813, 2013.

[56] Peaucelle, A. et al. Pectin-induced changes in cell wall mechanics underlie organ initiation in Arabidopsis. *Curr. Biol.*, 21:1720–1726, 2011.

[57] Moscho, A., Orwar, O., Chiu, D. T., Modi, B. P. Zare, R. N. Rapid preparation of giant unilamellar vesicles. *Proc. Natl. Acad. Sci.*, 93:11443–11447, 1996.

[58] Lira, R. B., Steinkühler, J., Knorr, R. L., Dimova, R. Riske, K. A. Posing for a picture: vesicle immobilization in agarose gel. *Scientific Reports*, 6:1–12, 2016.

[59] Simon, M. L. A. et al. A multi-colour/multi-affinity marker set to visualize phosphoinositide dynamics in Arabidopsis. *The Plant Journal*, 77:322–337, 2013.

[60] Bolte, S. et al. FM-dyes as experimental probes for dissecting vesicle trafficking in living plant cells. *Journal of Microscopy*, 214:159–173, 2004.

[61] Scates, B.A. Polyethylene glycol-based homologated ligands for nicotinic acetylcholine receptors. *Bioorg. Med. Chem.*, 16:10295–10300, 2008.

[62] Segur, J. B. H.E., O. Viscosity of Glycerol and Its Aqueous Solutions. *Ind. Eng. Chem.*, 43:2117-2120, 1951.

[63] Alassimone, J., Naseer, S. Geldner, N. A developmental framework for endodermal differentiation and polarity. *Proc. Natl. Acad. Sci.*, 107:5214–5219, 2010.

[64] Terasaki, M. Reese, T. S. Characterization of endoplasmic reticulum by co-localization of BiP and dicarbocyanine dyes. *Journal of Cell Science*, 101:315-322, 1992.

[65] Eisele, J. F., Fäbler, F., Bürgel, P. F. Chaban, C. A Rapid and Simple Method for Microscopy-Based Stomata Analyses. *PLoS One*, 11:1-13, 2016.

Chapter 4

Chapter 4

On the accurate use of molecular rotors in biological experiments

4.1 Introduction

Molecular rotors are small fluorophores whose photophysical properties exhibit sensitivity towards hydrodynamic drag, confinement, polarity, and binding (e.g. via hydrogen bonding or electrostatic interactions). They have proven to be useful in the study of e.g. i) polymer dynamics in solution upon varying temperature [1] or pressure[2], ii) polymerization dynamics[3], iii) contact pressure between two surfaces[4] viscosity and flow of fluids under shear stress[5].

Molecular rotors undergo conformational changes upon excitation from the ground state to their excited state. BODIPY-based rotors are a category of molecular rotors which typically feature a boron dipyrromethene core, with a pendant phenyl ring that can rotate with respect to the base. In the ground state, they adopt a twisted conformation with a given angle - 55° as determined by Kee et al.[6], 57.7° as determined by Suhina et al.[7], 49° as determined by Alamiry et al.[8] - between the BODIPY core and the phenyl unit. This twisted conformation leaves the two parts of the molecule out-of-conjugation. Excited state decay in this state occurs by fluorescence emission from the BODIPY core. Upon photoexcitation, the BODIPY core has been shown to buckle slightly[7], and these two subunits to undergo an internal rotation with respect to each other. The two

units thereby reach a planar configuration with a 0° twist angle, creating a new extended π-conjugated system. In this conformation, decay of the excited state to the ground state occurs non-radiatively, and is therefore called 'dark state'. The access to this state requires a molecular motion around a rotational axis. The rate of this rotation depends on a variety of factors, which include, but is not limited to, the local viscosity as the rotation sets up a hydrodynamic flow in the surrounding medium. At high viscosities the rotation, which opens a non-radiative decay pathway, occurs much slower than fluorescence emission, hence the dark state is not accessed frequently and fluorescence emission is high. By contrast, at low viscosities, the characteristic time for rotation is much shorter than the fluorescence lifetime of the twisted state. As a result, the main part of the incoming energy is dissipated and not converted into fluorescence, hence the emission intensity is low. The sensitivity of the rotors' rotation rate to viscosity leads to a fluorescence emission intensity and fluorescence lifetime that is dependent on viscosity. As a result, these probes are referred to as 'rigidochromic' and find use as fluorescence sensors for local viscosity. However, other environmental parameters can influence the rotor rotation as well, such as temperature, probe confinement, polarity and binding (e.g. to biomolecules). This sensitivity makes quantitative experiments challenging, in particular in biological systems which are inhomogeneous and complex. In several previous studies the rotors were calibrated in a simple molecular solvent mixture, to convert fluorescence lifetime or intensity measurements in complex media to a 'microviscosity'[9, 10, 11]. Without knowledge of the other factors that could alter the probe's rotation rate in the real experiments, this conversion on the basis of calibrations in much simpler media is often only qualitative. The effective microviscosity that is measured is the viscosity of a simple fluid mixture in which the rotor would have the same rotation rate, but this does not always imply that the variations in rotation rate are hydrodynamic in origin. In the following sections we will discuss some of these complications, provide data to exemplify their significance, and elaborate what impact they could have on measurements in biological systems, such as the one presented in **Chapter 3**.

4.2 Environmental factors potentially controlling the rotation rate of the probe

4.2.1 Probe confinement

The BODIPY-based molecular rotors respond to changes in confinement and free volume available for rotation. The degree of confinement can change upon variations in crowding density, upon variations in crosslinking density when considering a polymer network, or upon binding to other solutes such as proteins in biological media. The rotation of part of the molecule in a confined space sets up a flow of the fluid that surrounds the rotor. If the confinement is strong, it will hinder this fluid flow and lead to a reduction in the probe rotation rate. This reduction in rotation rate is a direct result of the hydrodynamic coupling of the fluid to the boundaries of the confining network or space, and is enhanced with increased confinement. In view of this sensitivity, one of the first applications of molecular rotors as local mechanosensors was as free volume probes in polymeric materials[12].

Confinement in semidilute polymer solutions

In order to probe the effect of confinement, decoupled from changes in fluid viscosity, we studied the rotor function of PEG-BDP in semidilute polymer solutions. The fluorescence lifetime of PEG-BDP was measured as a function of ethylene glycol (EG), poly(ethylene glycol) (PEG) or poly(acrylic acid) (PAA) concentration in aqueous solution, using polymers of different chain lengths. By varying the polymer chain length we could tune the mesh size of the semidilute solutions and achieve systems with the same macroscopic viscosity but very different local free volumes for the rotor. The fluorescence decay traces of the PEG-BDP probe were recorded and fitted as illustrated in Figure 4.1 so as to determine the average fluorescence lifetime of the molecule in solution. Figure 4.2a illustrates the effect of these different confinements of the PEG-BDP probe in solution. The curves of lifetime versus polymer concentration, obtained for the different molecular weights of PEG and PAA superpose, showing that the rotor responds to changes in concentration rather than changes in macroscopic viscosity (Fig.4.2b). Indeed, two solutions obtained with two polymers of different chain length can

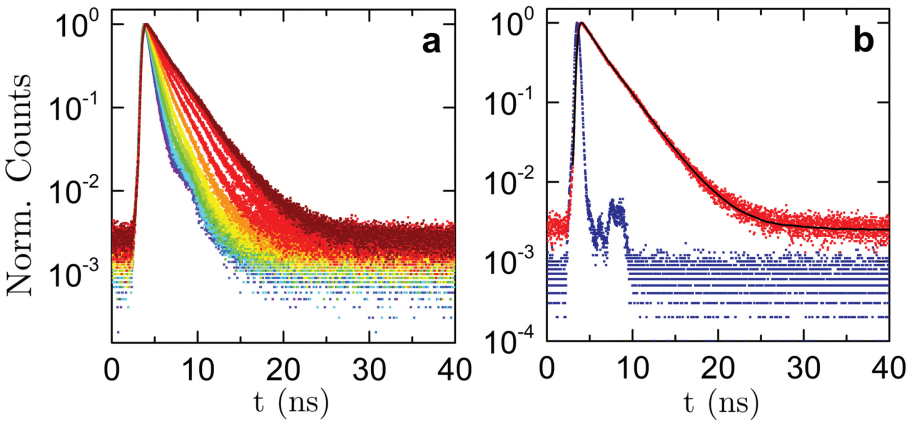

Figure 4.1: Fluorescence decay traces of PEG-BDP in PEG 1 kg mol^{-1} aqueous solutions with various concentrations ranging from 0 (purple) to 6 g cm^{-3} (brown) (a). Fluorescence decay trace obtained in a 6 g cm^{-3} PEG 1 kg mol^{-1} aqueous solution (red squares) with corresponding Instrument response function (blue squares) and bi-exponential fit curve (black line) used to determine the average fluorescence lifetime of the probe (b)

have the same chemical nature as well as the same polymer concentration but very different macroscopic viscosities, while still leading to lifetimes of the same magnitude. Even though ethylene glycol has a similar chemical composition as PEG, the curve obtained in ethylene glycol aqueous solutions does not superpose with the ones obtained in PEG solutions at concentrations above 0.1 g mL^{-1}. This can be seen as the result of a different nature of confinement in a solution of overlapping polymer chains compared to the one in a solution of low molecular weight solute. These results clearly illustrates why the use of molecular rotors as viscosity probes in fluids with mesoscopic structure, such as macromolecular solutions, must be performed with care.

Confinement in a dense polymeric network

Another example of a polymeric network in which the rotor senses changes in mesh size, rather than giving a quantitative measure for viscosity, are protein condensates. These have recently attracted attention due to their biological

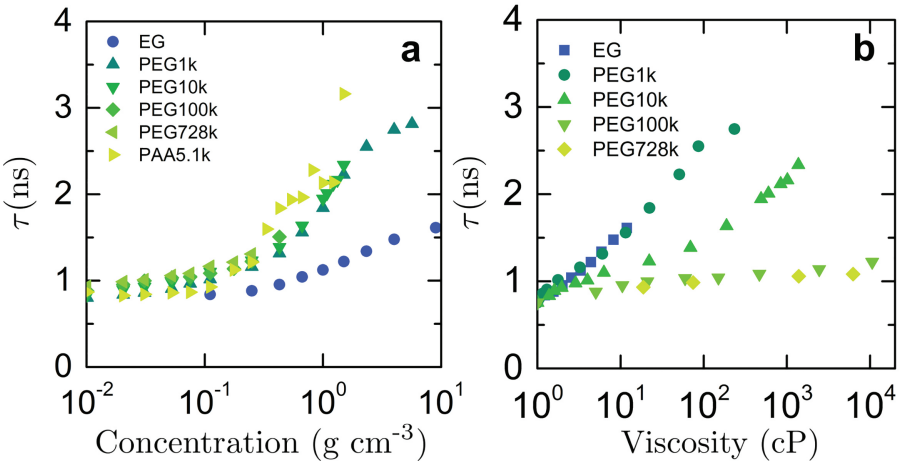

Figure 4.2: Evolution of the fluorescence lifetime of PEG-BDP in solutions of EG, PEG and PAA with various chain length, as a function of EG or polymer concentration (a), and as a function of viscosity as measured by DLS microrheology (b)

relevance[13, 14, 15]. To mimic biologically occurring protein condensates we prepared coacervates of anionic RNA and cationic polypeptide polylysine (PLL) [15, 16]. Upon addition to a phase separated system of RNA-PLL coacervate, in coexistence with a dilute phase of mostly buffer, the sulfo-BDP probe spontaneously partitions into the coacervate phase. The sulfo-BDP probe can be used to highlight variations in the network mesh size upon alteration of the salt concentration (Fig. 4.3). The mesh size of coacervates decreases with decreasing salt concentration as the polymer content in the coacervate phase increases[17, 18]. A consistent increase in lifetime was observed as the mesh size of the coacervates decreased, resulting in higher rotational constraint. Moreover, even inhomogeneities in the coacervate structure within a single droplet could be revealed using Fluorescence Lifetime Imaging, showing a looser network structure near the droplet interface, possibly related to a large interfacial width (Fig.4.3a-b).

Finally, in a more complex polymeric network such as the one constituting the plant cell wall, the CWP-BDP probe could highlight changes in network mesh size induced during cell elongation. The increase in mesh size induced by specialized proteins to allow for cell growth upon increase in turgor pressure was

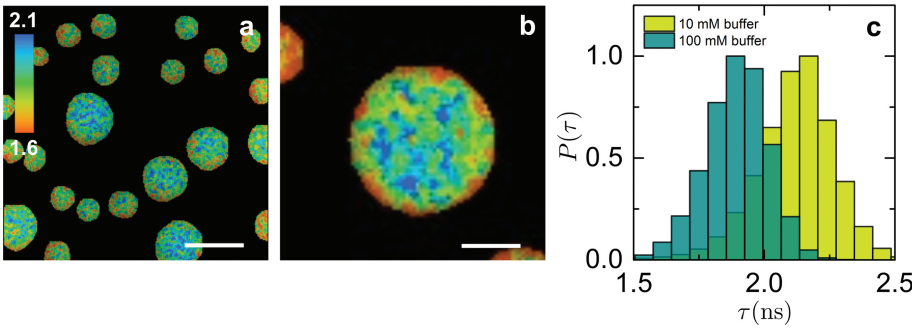

Figure 4.3: Fluorescence lifetime map obtained with sulfo-BDP in PLL/total RNA coacervates suspended in 100 mmol L^{-1} phosphate buffer (a, scale bar = 50 μm; b, scale bar = 15 μm) and corresponding lifetime distributions obtained for the same coacervates equilibrated in either 100 mmol L^{-1} phosphate buffer (N = 50) or 10 mmol L^{-1} phosphate buffer (N = 50) (b)

reflected by a spatial decrease in the rotor's fluorescence lifetime when going up the root (**Chapter 3**).

4.2.2 Solvent polarity

The BODIPY-based molecular rotors are sensitive to polarity; upon decreasing the polarity of the fluid, the fluorescence lifetime of the molecule increases. This increase in lifetime, in agreement with other studies mentioned previously[19, 9], can be explained by the partial charge transfer that occurs between the BODIPY core and the phenyl ring during the probe conformational change. This charge transfer induces an increase in dipole moment when going from the emissive locally excited 'bright state' to the non-emissive 'dark state'. A polar solvent stabilizes the dark state - i.e. increases the amount of energy required for the reorientation of solvent molecules which align with the fluorophore's dipole - and thus favours relaxation from that state, resulting in a lower fluorescence lifetime. This polarity-dependence is not reflected by a wavelength shift of the absorbance and emission spectra as the energy level of the locally excited state is relatively insensitive towards solvent polarity[20].

Graphically, the polarity dependence can be represented by an activation en-

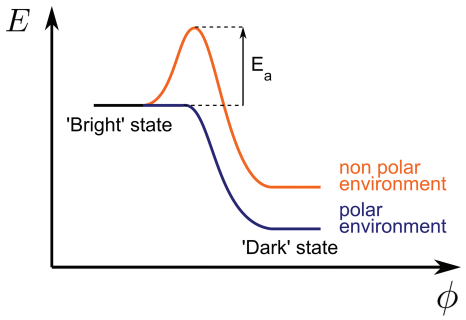

Figure 4.4: The photophysical model for BODIPY-based molecular rotors, established by Vyšniauskas et al.[9]. An energy barrier for conformational change rises as the solvent polarity decreases.

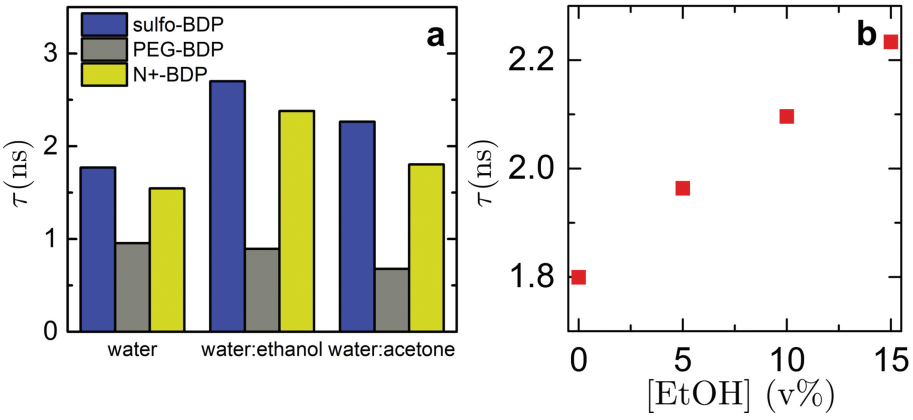

Figure 4.5: Evolution of the fluorescence lifetime of sulfo-BDP, PEG-BDP and N+-BDP in 50 v% ethanol- or 50 v% acetone-water solutions compared to pure water (a); Evolution of the fluorescence lifetime of sulfo-BDP in ethanol-water mixtures at various ethanol concentrations (b)

ergy barrier that the rotor needs to overcome to convert from the bright state to the dark state (Fig. 4.4). The amplitude of this energy barrier increases as the polarity decreases. The existence of such a barrier is supported by experiments which show an Arrhenius-like temperature dependence that becomes more pronounced in more apolar solvents[9]. In a biological system, e.g. in cells, the polar-

ity is likely to vary significantly when going from one cellular compartment to another. This makes it risky to compare, for instance, the fluorescence lifetime values obtained within the aqueous vacuolar compartment to the one obtained within the hydrophobic membrane bilayer if one wants to assess quantitatively variations in microviscosity. In addition, the BODIPY-based molecular rotors sensitivity to polarity seems to strongly depend on the nature of the substituents introduced on the phenyl ring. For example, an aliphatic tail in the para position of the phenyl ring[21] seems not to lead to significant polarity sensitivity at high viscosities; the lifetimes of this rotor in apolar castor oil show an excellent overlap with more polar methanol/glycerol mixtures at viscosities above 80 cP. However, at lower viscosities, a polarity-dependence arises; the fluorescence decay traces of the probe obtained in various organic solvents of comparable viscosities (methanol, chloroform, THF, toluene, propanediol, butanediol, pentanediol) deviate significantly. It is therefore important to consider both the relevant viscosity range, and the intrinsic polarity sensitivity of the chemical design, before neglecting polarity effects. Suhina et al.[7] showed that an ester-functionalized phenyl ring leads to little to no dependence on polarity. No significant correlation was found between the logarithm of the non-radiative decay constant and the solvent's orientational polarization function, the latter being a function of the relative permittivity of the solvent. They demonstrated the minor influence of polarity by highlighting a low Pearson correlation coefficient and a relatively high probability p=0.3 of those two variables to be uncorrelated. However for the same molecule this polarity dependence is debated. In another study carried out by Vyšniauskas et al.[9], they demonstrate that the same molecule has a non-negligible polarity dependence over a broad viscosity range, as the calibration curves obtained with solutions of similar viscosities but very different polarities – i.e. methanol/glycerol vs toluene/castor oil – are not superposable. Other functional groups, such as an aliphatic tail connected to the phenyl ring via an oxygen atom, a bromine atom[9], a hydrogen atom or a nitro group[19] have been shown to lead to polarity-dependence, with a dependence that attenuates at high viscosities. A few published studies employ BODIPY-rotor derivatives having different functional groups as viscosity sensors while neglecting the polarity dependence. They use methanol/glycerol calibration curves to give

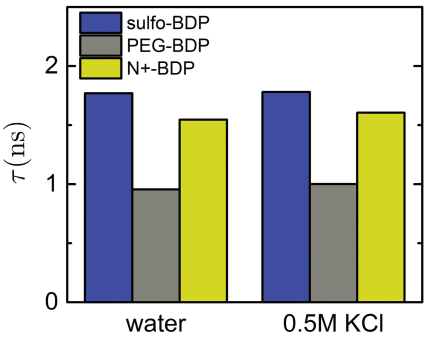

Figure 4.6: Evolution of the fluorescence lifetime of sulfo-BDP, PEG-BDP and N+-BDP in 0.5 M KCl solutions compared to pure water

an idea, or to directly translate measured fluorescent lifetimes into viscosities, even though the polarity as well as confinement in methanol/glycerol mixtures is often far from representative of the studied system[22, 23, 24]. The rotors we used as microviscosity probes in **Chapter 3** exhibit a non-negligible polarity dependence in organic solvent/water mixtures at low viscosities. Figure 4.5 shows the evolution of the probes' lifetimes in aqueous solutions of ethanol and acetone compared to pure water. Even though ethanol and acetone are slightly less viscous than water, the lifetime of the sulfo-BDP and N+-BDP probes tends to increase quite significantly when their content increases.

Polarity is an important parameter to consider when using BODIPY-based molecular rotors as free volume probes, even though the polarity dependence tends to become less critical as high viscosities. Those rotors have a relatively small change in dipole moment during conformational change compared to other rotor dyes - including the numerous ones that use Twisted Intramolecular Charge Transfer mechanism, where the charge transfer becomes significant and charge separation occurs over a much bigger distance -. This makes them globally less sensitive to polarity than their competitors[25, 26, 10]

4.2.3 Salt effect

In **Chapter 3**, the rotors were used in cellular compartments where the presence of high concentrations of electrolytes could potentially affect their fluorescence lifetime response. To confirm that this is not the case, we have performed experiments in salt solutions. Figure 4.6 shows that the presence of simple monovalent salts, in our case potassium chloride, does not seem to impact the non-radiative decay rate of the rotors. The fluorescence lifetimes of the rotors do not vary upon addition of potassium chloride.

4.2.4 Probe binding

One of the most interesting application for those BODIPY-based molecular rotors is the study of biological systems, as large scientific questions remain on the effects of local mechanics on biological processes. Being able to measure free volume in cells is a big step towards understanding fundamental biological processes. One aspect to consider is that these probes inherently have a hydrophobic and conjugated backbone and that cellular systems are rich in proteins and biopolymers, which often feature hydrophobic pockets that can bind to the probes and hinder the rotation. Binding events lead to variations in probe confinement, and variations in confinement can affect the hydrodynamic coupling between the probe and its environment (as discussed above) or lead to steric hindrance. Binding events can also lead to variations in polarity of the sensed environment; this can be the case if binding brings the probe into closer contact with some more or less polar components. These phenomena can alter the probe rotation rate and lead to a change in fluorescence lifetime even though the viscosity of the solvating medium itself does not change.

Figure 4.7 shows the evolution of the PEG-BDP probe lifetime in BSA and the evolution of the PEG-BDP and N+-BDP probes in lysozyme solutions of various concentrations. Even at low protein concentrations the fluorescence lifetime saturates in the BSA solutions, and does not show any dependence upon concentration. On the other hand, in the lysozyme solutions, both PEG-BDP and N+-BDP retain their rigidochromic properties. BODIPY dyes have been shown to interact non-specifically with BSA, resulting in a notable increase in their fluorescence intensity[27]. The rotor locates in the fluid surrounding the BSA proteins and

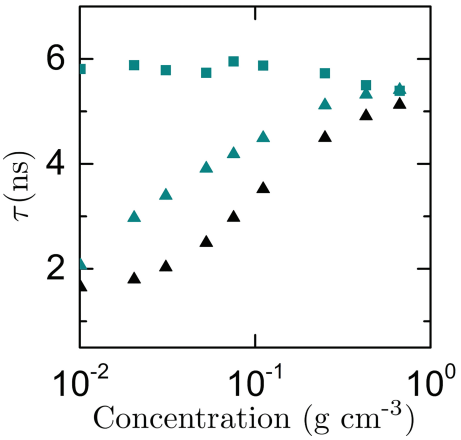

Figure 4.7: Evolution of the fluorescence lifetime of PEG-BDP in solutions of BSA (green squares) or Lysozyme (green triangles) as a function of protein concentration. Evolution of the fluorescence lifetime of N+-BDP in solutions of Lysozyme (black triangles) as a function of protein concentration

in one or several of their hydrophobic binding pockets. As the quantum yield of fluorescence increases when the lifetime increases, and probably because of preferential partitioning of the rotor within those pockets, the fluorescence component coming from the BSA binding pockets will dominate and result in a high average lifetime. This is one of the limitations of using such rotors as we cannot subtract one or the other contribution from the overall fluorescence decay. As a result, when interpreting FLIM images, a region of high lifetimes in cells can reflect a globally high confinement at the pixel size scale, or much more local confinement due to binding.

Figure 4.8 shows how binding to biopolymers such as RNA can affect the rotor response. A shift towards higher lifetimes in the fluorescence lifetime distribution of PR4-BDP, which features cationic amino acids having an electrostatic affinity to the anionic RNA, is observed in dilute RNA solution as compared to pure buffer solution. When using sulfo-BDP (anionic) in a PLL (polycation) solution no significant shift is observed as the probe does not bind strongly to the positively charged PLL chains (Fig. 4.8b). As binding occurs, the environment that is probed by the rotor changes.The difference between these two cases is

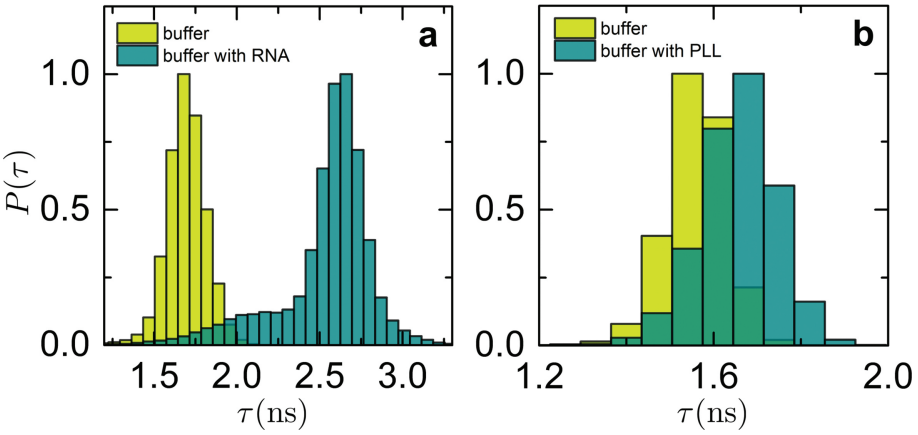

Figure 4.8: Evolution of the fluorescence lifetime distribution of PR4-BDP in total RNA solution compared to control phosphate buffer (a); Evolution of the fluorescence lifetime distribution of sulfo-BDP in PLL solution compared to control phosphate buffer (b)

probably due to the number of charges on the rotor; for the first example, the PR4-BDP carries four cationic charges, while the sulfo-BDP contains only two anionic groups. The binding affinity increases exponentially with the number of charges between the two oppositely charged molecules and is probably responsible for binding in the former and no-binding in the latter case.

This result highlights how much the choice of chemical composition of the rotor is critical as it will change the interaction with the environment and thus where and what we measure. This is one additional reason why calibration in methanol/glycerol mixtures is not appropriate to translate into viscosities the fluorescence lifetime data obtained in cellular membranes and in biological systems in general.

4.3 Implications for microviscosity mapping in biological medium

In **Chapter 3** we used BODIPY-based molecular rotors functionalized with different targeting functionalities to map microviscosity patterns in plant cells us-

ing FLIM. To interpret these patterns in a fair and transparent way it is important to consider what the rotor is actually sensing. The rotors respond to variations in confinement at a very local scale and therefore the term microviscosity might refer to different quantities depending on the probed length scale and the relative size ratio between the rotor and the surrounding components. In addition, cells are complex systems where polarity can vary a lot from one cellular compartment to another. A complete decoupling of the effects of confinement and polarity is impossible, therefore when interpreting the lifetime patterns one should take into account the nature of the system and compare systems with similar polarities. To achieve a quantitative measurement, calibration should be done in a medium that is most representative both for polarity and length scale. For example, to determine the vacuolar and cytosolic microviscosity, we can consider a calibration made in aqueous protein solutions at representative concentrations. To determine the membrane microviscosity, we can perform a systematic study of the rotor's response in synthetic membranes, i.e. in vesicles, when varying the tension applied on the membrane by varying the osmotic pressure mismatch between vesicle interior and the surrounding medium or mechanically, e.g. by micropipette aspiration. To have a reference in terms of cell wall microviscosity, we can think of implementing the probe in a synthetic polysaccharide network with controlled mesh sizes and polymer charge densities – to account for the spatial changes in pectin de-esterification –. This latter is most challenging, as the cell wall composition is highly complex and varies from cell-to-cell and from species to species.

Spatio-temporal increases in lifetime can reflect either an increased confinement, a decreased polarity, or an increased degree of binding. As a consequence using other analysis techniques in parallel, such as FRAP, Fluorescence Correlation Spectroscopy, or fluorescence anisotropy measurement, is needed to obtain more information on the system[28, 29]. Fluorescence anisotropy measurements can provide insight on probe binding. Using time-resolved fluorescence anisotropy one can assess the orientation and mobility of the dyes, as well as the processes that affect them. From the anisotropy decay of a dye's fluorescent emission, one can derive its rotational correlation time, which is related to viscosity, temperature, and molecular volume. A binding event increases the apparent volume

of the probe and as a result increases its rotational correlation time. Therefore at constant viscosity and temperature, this characteristic time is directly related to the degree of binding of the probe. The fluorescence lifetime τ and the rotational correlation time θ are related via the expression

$$\tau = a\theta^{\alpha} \tag{4.1}$$

where a and α are constants that can be determined on the basis of a calibration curve, measuring τ and θ as a function of viscosity. By performing lifetime and anisotropy measurements simultaneously and comparing the fluorescence lifetime and the rotational correlation time, we could in principle assess whether there is binding -in which case expression 4.1 would not hold anymore- or whether the dye diffuses freely[29, 30]. The absolute values of a and α might vary according to e.g. the degree of confinement or the polarity, but if the rotational correlation time and the fluorescence lifetime send back to the same viscosity magnitudes, we can then conclude that there is no significant binding. Furthermore, the shape of the anisotropy decay can also provide information on binding; if the anisotropy does not decay completely to zero after excitation, then the probe does not rotate in random directions but mainly along the rotation axis between the BODIPY core and the phenyl ring, which indicates some extent of binding or a tight interaction[30, 31]. Additionally, the relation 4.1 should not hold anymore if other environmental factors such as polarity affect the rotor response, but the fluorescence anisotropy should still be able to decay to zero.

To conclude, without a suitable calibration, FLIM maps are not quantitative. Yet, this does not mean they are without value. Within a single compartment, such as a membrane or a vacuole, these data provide insights into mechanical heterogeneity on a qualitative scale, e.g. reflecting relative changes in confinement or crowding densities, as well as providing information on the dynamics of cellular processes at a high resolution that cannot currently be achieved by other means.

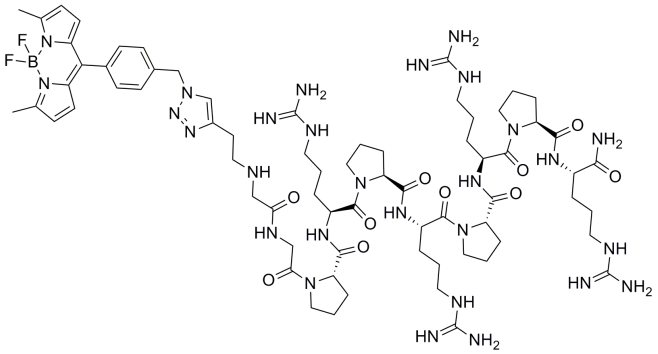

Figure 4.9: Chemical structure of the PR4-BDP probe (unprotonated version)

4.4 Materials and methods

Total RNA from yeast was purchased from Roche Diagnostics GmbH and PLL (Mn 66 kg mol^{-1}) was purchased from Alamanda Polymers. All other chemicals were purchased from Sigma-Aldrich, Polymer Source or Fischer Scientific and used as received unless indicated otherwise.

4.4.1 Synthesis of PR4-BDP

The peptide PRPRPRPR extended on the N-terminus with two G residues and 4-pentynoic acid in order to separate the cell wall binding peptide from the BODIPY rotor was purchased from pepscan (98%+ purity). The alkyne-peptide derivative was subjected to copper-catalysed alkyne-azide cycloaddition (CuAAC) conjugation to the azide-functionalized BODIPY rotor. For this, 2 (0.86 mg; 2.45 μmol) was mixed with the alkyne-peptide derivative (2 mg; 1.63 μmol) in DMF: water = 75:25 (400 μL). $CuSO_4$ (3.06 mg; 12.26 μmol) and sodium ascorbate (6.2 mg, 31.05 μmol) were added. The reaction was performed overnight at room temperature. The crude mixture was subjected to preparative RP-HPLC using a prep-LC-MS system (Alltima, C18, 5μ, 250mm x 22mm; gradient: 0–5 min @A, in 5–25 min to B, 25–30 min @B, in 30–35 min to A, 35–40 min @A [buffer A: 95% MilliQ, 5% MeCN, 0.1% TFA; buffer B: 95% MeCN, 5% MilliQ, 0.1% TFA], tR = 15.46 min). The purified fraction was freeze-dried to get PR4-BDP (0.42 mg,

16% yield).

4.4.2 Impact of probe confinement in polymer or protein solutions – solution preparation

Table 4.1: Specifications (Mn, PDI) of the different PEG used in the confinement study

Polymer	*Mn (g mol^{-1})*	*PDI*
PEG1k	1000	< 1.3[32]
PEG10k	10,000	< 1.3[32]
PEG100k	95,000	1.08
PEG728k	728,000	1.24

We studied the fluorescence lifetime response of PEG-BDP in aqueous solutions of ethylene glycol, poly(ethylene glycol) of various chain lengths (reported in Table 4.1), poly(acrylic acid) 5.1kg mol-1, Bovine Serum Albumin and Lysozyme from chicken egg white. The concentrations were varied between 0.01 g cm^{-3} and 10 g cm^{-3} until reaching the solute solubility limit. The viscosity of those solutions was determined by DLS microrheology.

4.4.3 DLS microrheology

PMMA-PEGMA particles with a hydrodynamic radius of 77 nm (PDI between 0.002 and 0.042) were synthesized by a standard emulsion polymerization. In a 250 mL round-bottom flask, methyl methacrylate (8.9 g) and PEG methacrylate (0.5 g) were mixed in MQ water (100 mL) containing a small amount of SDS (20 mg). The mixture was degassed by purging with nitrogen for 10 min. The flask was put under slight vacuum. The biphasic mixture was stirred at 75°C for 15min, and the stirring speed adjusted so as to avoid emulsification. A solution of potassium persulfate (100 mg) in MQ water (5 mL) was injected, and the reaction carried out for at least 24h. The obtained turbid suspension was filtered through glass wool and stored at 4°C in a plastic bottle.

The dynamic light-scattering experiments were carried out on a Malvern Nano-S, with a He-Ne laser (λ=632.8 nm), an avalanche photodetector at a detection angle of 173°. In all experiments the temperature was controlled at 20°C. The DLS particles were suspended in the samples of interest by diluting the stock 1000 times. The scattered intensity autocorrelation function was measured 3 times, for 1000 s to 1 h depending on the characteristic decorrelation time of each individual sample. The mean square displacement of the particles was determined from the scattered intensity autocorrelation functions, and the diffusion coefficient computed by using the slope of the mean square displacement vs time plot at time scales beyond the caging dynamics. The diffusion coefficient was directly translated into a viscosity using the Stokes-Einstein equation.

4.4.4 Fluorescence Lifetime measurements

The average fluorescence lifetime measurements in solution were performed as described in **Chapter 3**, using mono- or biexponential decay fits.

4.4.5 Coacervate preparation and fluorescence lifetime imaging

100 mmol L^{-1} and 10 mmol L^{-1} phosphate buffer (pH 7) was prepared by dissolving potassium phosphate monobasic and potassium phosphate dibasic trihydrate in MQ water. The pH was adjusted using a 1 M KOH solution. Stock solutions of 50 g L^{-1} of total RNA in 100 mmol L^{-1} buffer and 20 g L^{-1} PLL in MQ water were prepared. Coacervate samples were prepared (25 μL) in 200 μL eppendorf tubes by mixing 100 mmol L^{-1} phosphate buffer with the required volumes of RNA stock, sulfo-BDP stock and PLL stock to reach final concentrations of 1 wt% RNA, 20 μmol L^{-1} of sulfo-BDP and a charge ratio RNA:PLL of 1. PLL was added last. The solution was mixed by pipetting up and down 10 times. The coacervates formed were immediately transferred to plastic counting chambers (Bio Rad) for imaging.

A buffer exchange from 100 mmol L^{-1} to 10 mmol L^{-1} phosphate buffer was performed in order to reduce the mesh size of the polymer network within the coacervates. The coacervates were decanted and the supernatant exchanged with 10 mmol L^{-1} buffer. The samples were equilibrated for 10 min before imaging.

FLIM images of 256×256 pixels were recorded using a Leica TCS SP8 inverted scanning confocal microscope in the same conditions as reported in **Chapter 3** for sulfo-BDP. The imaging was performed with a 63× 1.2 NA water immersion objective.

4.4.6 Impact of binding – solution preparation

The lifetime distributions of PR4-BDP and sulfo-BDP were recorded using FLIM in a solution of 1 wt% total RNA or 1 wt% PLL in 100 mmol L^{-1} phosphate buffer. The dye concentration was set to 10 μM sulfo-BDP or 50 μM PR4-BDP (to compensate for a lower quantum yield in solution).

References

[1] Dongping Wang, Ryo Miyamoto, Yasuhiro Shiraishi, and Takayuki Hirai. Bodipy-conjugated thermoresponsive copolymer as a fluorescent thermometer based on polymer microviscosity. *Langmuir*, 25:13176–13182, 2009.

[2] M.A.H. Alamiry, Effat Bahaidarah, Anthony Harriman, Thomas Burab, and Raymond Ziessel. Fluorescent molecular rotors under pressure: synergistic effects of an inert polymer. *RSC Advances*, 2:9851–9859, 2012.

[3] M.A. Haidekker and E.A. Theodorakis. Molecular rotors—fluorescent biosensors for viscosity and flow. *Org. Biomol. Chem.*, 5:1669–1678, 2006.

[4] T. Suhina, B. Weber, C.E. Carpentier, K. Lorincz, P. Schall, D. Bonn, and A.M. Brouwer. Fluorescence microscopy visualization of contacts between objects. *Angew. Chem. Int. Ed.*, 127:3759–3762, 2015.

[5] Mark A. Haidekker and Emmanuel A. Theodorakis. Molecular rotors—fluorescent biosensors for viscosity and flow. *Org. Biomol. Chem.*, 5:1669–1678, 2007.

[6] Hooi Ling Kee, Christine Kirmaier, Lianhe Yu, Patchanita Thamyongkit, W. Justin Youngblood, Matthew E. Calder, Lavoisier Ramos, Bruce C. Noll, David F. Bocian, W. Robert Scheidt, Robert R. Birge, Jonathan S. Lindsey, and Dewey Holten. Structural control of the photodynamics of borondipyrrin complexes. *J. Phys. Chem. B*, 109:20433–20443, 2005.

[7] Tomislav Suhina, Saeed Amirjalayer, Sander Woutersen, Daniel Bonn, and Albert M. Brouwer. Ultrafast dynamics and solvent-dependent deactivation kinetics of bodipy molecular rotors. *Phys. Chem. Chem. Phys.*, 19:19998–20007, 2017.

[8] Mohammed A. H. Alamiry, Andrew C. Benniston, Graeme Copley, Kristopher J. Elliott, Anthony Harriman, Beverly Stewart, and Yong-Gang Zhi. A molecular rotor based on an unhindered boron dipyrromethene (bodipy) dye. *Chem. Mater.*, 20:4024–4032, 2008.

[9] Aurimas Vyšniauskas, Ismael López-Duarte, Nicolas Duchemin, T.T. Vu, Y. Wu, E.M. Budynina, Y.A. Volkova, E.P. Cabrera, D.E. Ramírez-Ornelas, and M.K. Kuimova. Exploring vis-

cosity, polarity and temperature sensitivity of bodipy-based molecular rotors. *Phys. Chem. Chem. Phys.*, 19:25252–25259, 2017.

[10] Michael R. Dent, Ismael López-Duarte, Callum J. Dickson, Phoom Chairatana, Harry L. Anderson, Ian R. Gould, Douglas Wylie, Aurimas Vyšniauskas, Nicholas J. Brooks, and Marina K. Kuimova. Imaging plasma membrane phase behaviour in live cells using a thiophene-based molecular rotor. *Chem. Commun.*, 52:13269–13272, 2016.

[11] Ismael López-Duarte, T.T. Vu, M.A. Izquierdo, J.A. Bull, and M.K. Kuimova. A molecular rotor for measuring viscosity in plasma membranes of live cells. *Chem. Commun.*, 50:5282–5284, 2014.

[12] R.O. Loutfy. Fluorescence probes for polymer free-volume. *Pure Appl. Chem.*, 58:1239–1248, 1986.

[13] William M. Aumiller, Fatma Pir Cakmak, Bradley W. Davis, and Christine D. Keating. Rna-based coacervates as a model for membraneless organelles: Formation, properties, and interfacial liposome assembly. *Langmuir*, 32:10042–10053, 2016.

[14] T-Y. Dora Tang, C. Rohaida Che Hak, Alexander J. Thompson, Marina K. Kuimova, D. S. Williams, Adam W. Perriman, and Stephen Mann. Fatty acid membrane assembly on coacervate microdroplets as a step towards a hybrid protocell model. *Nat. Chem.*, 6:527–533, 2014.

[15] Steven Boeynaems, Alex S. Holehouse, Venera Weinhardt, Denes Kovacs, Joris van Lindt, Carolyn Larabell, Ludo van den Bosch, Rhiju Das, Peter S. Tompa, Rohit V. Pappu, and Aaron D. Gitler. Spontaneous driving forces give rise to proteinrna condensates with coexisting phases and complex material properties. *Proc. Natl. Acad. Sci.*, 116:7889–7898, 2019.

[16] Yudan Yin, Lin Niu, Xiaocui Zhu, Meiping Zhao, Zexin Zhang, Stephen Mann, and Dehai Liang. Non-equilibrium behaviour in coacervate-based protocells under electric-field-induced excitation. *Nat. Commun.*, 7, 2016.

[17] Evan Spruijt, Frans A. M. Leermakers, Remco Fokkink, Ralf Schweins, Ad A. van Well, Martien A. Cohen Stuart, and Jasper van der Gucht. Structure and dynamics of polyelectrolyte complex coacervates studied by scattering of neutrons, x-rays, and light. *Macromolecules*, 46:4596–4605, 2013.

[18] Evan Spruijt, Adrie H. Westphal, Jan Willem Borst, Martien A. Cohen Stuart, and Jasper van der Gucht. Binodal compositions of polyelectrolyte complexes. *Macromolecules*, 43:6476–6484, 2010.

[19] Stepas Toliautas, Jelena Dodonova, Audrius Žvirblis, Ignas Čiplys, Artūras Polita, Andrius Devižis, Sigitas Tumkevičius, Juozas Šulskus, and Aurimas Vyšniauskas. Enhancing the viscosity-sensitive range of a bodipy molecular rotor by two orders of magnitude. *Chem. Eur. J*, 25:10342–10349, 2019.

[20] M.A. Haidekker and E.A. Theodorakis. Environment-sensitive behavior of fluorescent molecular rotors. *J. Biol. Eng.*, 4:1–14, 2010.

[21] Michael R. Dent, Ismael López-Duarte, Callum J. Dickson, Niall D. Geoghegan, Jonathan M. Cooper, Ian R. Gould, Rob Krams, James A. Bull, Nicholas J. Brooks, and Marina K. Kuimova. Imaging phase separation in model lipid membranes through the use of bodipy based molecular rotors. *Phys. Chem. Chem. Phys.*, 17:18393–18402, 2015.

[22] Aurimas Vyšniauskas, Ismael Lopez-Duarte, Alex J. Thompson, James A. Bull, and Marina K. Kuimova. Surface functionalisation with viscosity-sensitive bodipy molecular rotor. *Methods Appl. Fluoresc.*, 6:034001, 2018.

[23] Sangram Raut, J. Kimball, R. Fudala, H. Doan, B. Maliwal, N. Sabnis, A. Lacko, I. Gryczynski, S.V. Dzyuba, and Z. Gryczynski. A homodimeric bodipy rotor as a fluorescent viscosity sensor for membrane-mimicking and cellular environments. *Phys. Chem. Chem. Phys.*, 16:27037–27042, 2014.

[24] James A. Levitt, Marina K. Kuimova, Gokhan Yahioglu, Pei-Hua Chung, Klaus Suhling, and David Phillips. Membrane-bound molecular rotors measure viscosity in live cells via fluorescence lifetime imaging. *J. Phys. Chem. C*, 113:11634–11642, 2009.

[25] Mark A. Haidekker, Thomas P. Brady, Darcy Lichlyter, and Emmanuel A. Theodorakis. Effects of solvent polarity and solvent viscosity on the fluorescent properties of molecular rotors and related probes. *Bioorg. Chem.*, 33:415–425, 2005.

[26] Na Jiang, Jiangli Fana, Si Zhang, Tong Wua, Jingyun Wang, Pan Gao, Junle Quc, Fan Zhou, and Xiaojun Penga. Dual mode monitoring probe for mitochondrial viscosity in single cell. *Sensors and Actuators B*, 190:685–693, 2014.

[27] Laramie P. Jameson, Nicholas W. Smith, Onofrio Annunziata, and Sergei V. Dzyuba. Interaction of bodipy dyes with bovine serum albumin: a case study on the aggregation of a click-bodipy dye. *Phys. Chem. Chem. Phys.*, 18:14182–14185, 2016.

[28] Florly S. Ariola, Zaiguo Li, Christine Cornejo, Robert Bittman, and Ahmed A. Heikal. Membrane fluidity and lipid order in ternary giant unilamellar vesicles using a new bodipy-cholesterol derivative. *Biophys. J.*, 96:2696–2708, 2009.

[29] Marina K. Kuimova, Gokhan Yahioglu, J.A. Levitt, and Klaus Suhling. Molecular rotor measures viscosity of live cells via fluorescence lifetime imaging. *J. Am. Chem. Soc.*, 130:6672–6673, 2008.

[30] Klaus Suhling, Jan Siegel, Peter M. P. Lanigan, Sandrine Lévêque-Fort, Stephen E. D. Webb, David Phillips, Daniel M. Davis, and Paul M. W. French. Time-resolved fluorescence anisotropy imaging applied to live cells. *Opt. Lett.*, 29:584–586, 2004.

[31] James A. Dix and A. S. Verkman. Mapping of fluorescence anisotropy in living cells by ratio imaging. application to cytoplasmic viscosity. *Biophys. J.*, 57:231–240, 1990.

[32] Natalia Ziębacz, Stefan A. Wieczorek, Tomasz Kalwarczyk, Marcin Fiałkowskia, and Robert Hołyst. Crossover regime for the diffusion of nanoparticles in polyethylene glycol solutions: influence of the depletion layer. *Soft Matter*, 7:7181–7186, 2011.

Chapter 5

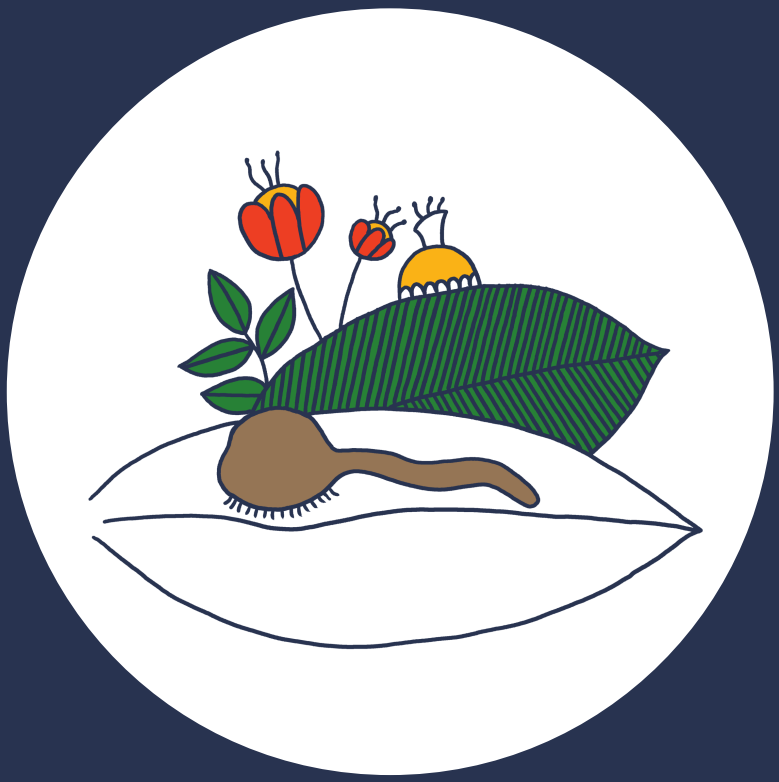

Chapter 5

Molecular sensors reveal the mechano-chemical response of P. infestans walls and membranes to mechanical and chemical stress

Phytophthora infestans, causal agent of late blight in potato and tomato, remains challenging to control. Unravelling its biomechanics of host invasion, and its response to mechanical and chemical stress, could provide new handles to combat this devastating pathogen. Here, we introduce two fluorescent molecular sensors that reveal the micromechanical response of the cell wall-plasma membrane continuum in *Phytophthora infestans* during invasive growth and upon chemical treatment. When visualized by live-cell imaging the two probes report changes in cell wall (CW) porosity, and in chemical polarity and lipid order in the plasma membrane (PM). During invasive growth, mechanical interactions between the pathogen and a surface reveal clear and localized changes in the structure of both CW and PM. Moreover, the probes can reveal the specificity of chemical treatment to either CW and/or PM, unravelling the mode-of-action of crop protection agents. This mechano-chemical imaging strategy resolves, non-invasively and with high spatiotemporal resolution, how the CW-PM continuum adapts and responds to abiotic stress, and provides information on the dynamics and locus of cellular stress responses for which, to date, no other methods are available.

This chapter was submitted as:
Lucile Michels, Jochem Bronkhorst, Michiel Kasteel, Djanick de Jong, Bauke Albada, Tijs Ketelaar, Francine Govers & Joris Sprakel *Molecular sensors reveal the mechano-chemical response of Phytophthora infestans walls and membranes to mechanical and chemical stress* (2021)

5.1 Introduction

Host infection by biotrophic filamentous plant pathogens invariably commences with host entry, a complex process in which the pathogen utilizes mechanical weaponry to breach the protective barrier posed by the plant surface, guided and aided by biochemical interactions between pathogen and host. Understanding the nature and mechanisms of host invasion is an important route to find new solutions to control plant pathogens and mitigate yield losses resulting from plant diseases. From this vantage point, obtaining a complete picture of the plant-microbe interactions during host entry requires study of the invasion process from the perspective of the host and that of the pathogen, and taking both mechanical and chemical interactions into account.

Among the most damaging plant pathogens, is the oomycete *Phytophthora infestans*, causal agent of late blight in potato and tomato, and responsible for large crop yield losses and economic damage[1, 2]. Despite tremendous progress in unravelling the biochemical host-pathogen interactions and continued efforts to breed resistant crops, *P. infestans* remains challenging to control, in part due to its large and rapid genetic adaptability[3]. While studies into the invasion strategies of this pathogen from a genetic, biochemical and cell biological perspective are abundant, very little is known about the strategies it exploits to gain mechanical entry into plants.

Various molecular-genetic and biochemical approaches as well as omics analyses are widely used to identify, on the one hand, *Phytophthora* genes encoding effectors and other proteins required for pathogenicity[4, 3, 5, 6, 7] and, on the other hand, plant genes implicated in immunity and susceptibility to late blight[8, 9, 10]. Additionnally, the molecular mechanisms underlying the manipulation of plant immunity by effectors are widely studied[11, 12, 13].

Studies on genetics, secreted effectors and cytoskeletal regulation are vital to elucidate essential components of the invasion machinery of *P. infestans*. Yet, connecting how these components work in synchrony during infection, and how they couple to the mechanical process necessary to breach the plant surface remains challenging.

In a recent study[14], we took a first step to unravel the mechanics of host entry by *Phytophthora* spp. By using a combination of surface deformation ima-

ging, molecular fracture sensors and modelling, we uncovered a mechanism, coined as 'naifu'-mechanism, that *Phytophthora* spp. use to enter their hosts. The discovery of this mechanism gives rise to a plethora of new questions on how *Phytophthora*, perceives and processes mechanical signals at the pathogen-host interface into intracellular mechano-biological responses.

Resolving this challenge requires new tools that provide access to local mechano-chemical properties at the surface of and inside the pathogens during mechanical invasion, ideally in live-cell imaging and with high spatio-temporal resolution. In a previous study[15], we introduced a toolbox of molecular mechanoprobes that can resolve complex micromechanical patterns in plant cells during a range of cellular processes. Yet, these approaches remain to be utilized for the study of pathogens during invasive growth.

In addition to the understanding of their invasion mechanics, the identification of novel chemical control agents for *Phytophthora* pathogens is an important strategy to combat late blight diseases more effectively[16, 17]. Suitable control agents typically act on specific parts of the pathogen anatomy. Usually, their effects are studied by monitoring alterations in colony propagation and cell morphology. However, this approach leaves the treatment's site- and mode-of-action unresolved. Moreover, screening the action of control agents quickly and at limited cost remains challenging and hinders deep screening of compounds. In that regard, mapping spatio-temporal variations in CW and PM properties using our molecular probes could reveal the outlines of the pathogen's mechano-chemical reaction to treatment relatively quickly and inexpensively, and provide a completely novel aspect to evaluate drug efficacy.

In this paper, we introduce a set of two synthetic molecular reporters that are capable of resolving the intracellular mechano-chemical response of the cell wall (CW) – plasma membrane (PM) continuum in *P. infestans* pathogens during hyphal and invasive growth. These reporters also reveal the CW and PM response to various chemical treatments known to inhibit invasion. The first molecular reporter is a cell-wall binding molecular rotor[15] that reports on spatial and temporal changes in CW porosity and composition. The second is a solvatochromic PM probe that reveals changes in membrane polarity and molecular order. Using a combination of both probes we show how invasive growth generates a loc-

alized sub-cellular response at the pathogen-host contact point as a gateway for mechanical signal internalization, and how chemical treatment elicits specific responses in the wall-PM continuum. These new tools can contribute to bridging the gap between the genetic, biochemical, cell biological and mechanical aspects of host entry by these devastating pathogens.

5.2 Materials and Methods

Synthesis of fluorescent molecular reporters

The CW probe CWP-BDP dye was synthetized as reported in Michels et al.[15], and the PM reporter, NR12S, was synthesized following the protocol reported by Kucherak et al.[18]. A comprehensive overview of all experimental details, including synthesis and chemical characterization of the probes are provided in **Chapter 2**. Absorbance and emission spectra of the probes are given in Figure 5.6.

P. infestans growth and spore generation

P. infestans wild-type strain 88069 (*P. infestans*-wt), was maintained on rye sucrose agar (RSA) medium[19] supplemented with Vancomycin (20 μg mL^{-1}), Ampicillin (100 μg mL^{-1}), and Amphotericin A (10 μg mL^{-1}). Cultures were grown for 10 days at 18°C in the dark, and maintained by regularly transferring a 5x5 mm mycelial plug to new plates.

Zoosporogenesis was initiated by adding sterile tap water (4°C) (10 mL for 100-mm-diameter plates, 5 mL for 60-mm-diameter plates) to a 10 to 14-day-old culture, followed by incubation at 4°C for 3h. After cooling, the zoospore suspension was collected and zoospores were encysted through manual physical stimulation (i.e. shaking for 1 min). The cysts were diluted 5x with milli-Q water, to reach a concentration of c. 1 10^5 spores mL^{-1} for experimental use.

For imaging optimization experiments with NR12S, *P. infestans*-wt mycelium was exposed to a relatively low concentration of β-sitosterol. This was done by placing two mycelium plugs (about 2 mm diameter) from a 7 day old *P. infestans* culture grown on Plich medium[20] lacking sterols on opposite sites of a disk (1 cm diameter, 0.5 cm thickness) of synthetic agar medium supplemented with 0.2

μg mL^{-1} β-sitosterol (from a stock of 2 g L^{-1} β-sitosterol in DMSO) and allowing hyphae to grow into the disk.The final percentage DMSO in the medium was 0.1% (v/v). Disks were incubated at 18°C in the dark for three days before use in microscopy experiments.

Imaging procedures

Artificial substrate preparation

All reactive PDMS polymers were purchased from Gelest Inc. and used as received. For observation of invasive growth, artificial substrates that mimic the hydrophobicity and stiffness of plant leaves were used. Previous work has shown that these substrates elicit a similar invasion response as real host surfaces[14]. Stiff PDMS elastomer surfaces were prepared from a commercial 2-component polydimethyl siloxane rubber (Sylgard 184, Dow Corning) in a 10:1 base: cross-linker ratio. The two components were mixed by vortexing for 3 to 4 min. Bubbles and dust were removed from the viscous mixture by centrifugation at 1000g for 10 min. #1 18x18 mm glass coverslips were cleaned before spincoating with the elastomer precursor mixture; coverslips were rinsed sequentially with isopropyl-alcohol (IPA), Milli-Q deionized water, and IPA, and subsequently dried in a nitrogen stream, followed by heating to 60°C for 5 min. Coverslips were pre-treated using an O_2/N_2 plasma for 1 min and then spincoated with 130 μL of mixture, at 500 rpm for 30s, followed by 2000 rpm for 2 min, to reach a 33 μm layer thickness (as determined by confocal microscopy). The Young's modulus, representing the elastic constant for uniaxial tensile deformations, of these substrates was measured on a home-built indentation set-up, as described previously[21], and determined to be 1.5 MPa. The samples were placed inside a vacuum chamber for at least 30 min to remove air bubbles, beforecuring at 50°C overnight.

For observations in non-invasive hyphae, solvent-free PDMS elastomer surfaces were prepared following the procedure reported by Cai et al.[22]. For preparation of the precursor, the following components were used; Backbone: vinylmethylsiloxane–dimethylsiloxane copolymer, trimethylsiloxy terminated, c. 300 vinyl groups per molecule, Mw $\simeq$ 50 000 g mol^{-1} (VDT-5035). Side chain: monohydride-terminated poly(dimethylsiloxane), Mw $\simeq$ 4750 g mol^{-1} (MCR-H21).

Crosslinking chain: hydride-terminated polydimethysiloxane, Mw $\simeq$ 17 200 g mol^{-1} (DMS-H25). The PDMS linear polymers were mixed at a VDT-5035: MCR-H21: DMS-H25 = 1:13.3:1.72 mass ratio to achieve a 1:140:5 backbone: side chains: crosslinks number ratio, and a final Young's modulus of 15 kPa. The three components were mixed by vortexing for 3 min. Bubbles were removed by sonicating the sample for 10s. The Karstedt's catalyst was added to the precursor mixture at a concentration of 5 μL g^{-1} from a 2% platinum solution in xylene. The solution was again thoroughly mixed and sonicated for 10s. Plasma cleaned #1 coverslips were then spincoated with 130 μL of mixture, at 500 rpm for 30s, followed by 2000 rpm for 2 min. The samples were eventually cured at 70°C for 48 h.

Cell incubation and fluorescence imaging

For imaging experiments, a 80 μL droplet of a spore suspension ($\simeq$105 cysts per mL) was deposited onto the elastomer surface, followed by placement inside bespoke 3D printed sample chambers (Fig. 5.7) to minimize water evaporation. For staining, a portion of the aqueous phase of the droplet, 50 μL, was replaced three times with a solution of either CWP-BDP or NR12S, dissolved at 10 μmol L^{-1} in water. The staining was performed for 15 min (CWP-BDP) or 7 min (NR12S), after which any unbound dye was removed by replacing 50 μL of the droplet three times with water.

To image PM polarity in *P. infestans* mycelium using NR12S, 80 μL of NR12S staining solution at 10 μmol L^{-1} in water were deposited onto the mycelium grown on a solid agar pad. Staining was performed for 7 min and the dye solution was subsequently removed. The agar pad was placed upside down on a coverslip for imaging.

Two-dimensional Fluorescence Lifetime Imaging (FLIM) experiments of samples stained with CWP-BDP were performed on a Leica TCS SP8 inverted confocal microscope coupled to a Becker&Hickl TCSPC lifetime module (SPC830). Samples were excited with a 514-nm pulsed laser source (pulse duration <1 ps) with a repetition rate of 40 MHz, and fluorescence emission was captured through a 63× water immersion objective (numerical aperture = 1.2). A line scanning speed of 400 Hz was used and the emission was collected, using a spectral window extending from 518 nm to 600 nm, onto a Leica HyD SMD hybrid photode-

tector. Acquisition time was fixed at 120 s for each 256 × 256 pixel image. FLIM images were processed using the SPCImage 7.1 software to fit the fluorescence decay curves in each pixel with a two-component exponential decay.

Three-dimensional FLIM imaging, using FastFlim, for CWP-BDP, as well as 2D- and 3D- ratiometric imaging with NR12S were performed on a Leica TCS SP8 Two-photon inverted confocal microscope. Samples were excited with a Chameleon Ti:Sapphire pulsed laser source (pulse duration = 140 fs), at either 810 nm (CWP-BDP) or 830 nm (NR12S), with a repetition rate of 80 MHz. Fluorescence was captured through a 40× water immersion objective (numerical aperture = 1.2). A line scanning speed of 400 Hz was used and the emission was collected in a Leica 4 Tune detection unit equipped with Leica HyD SMD hybrid photodetectors. The emission of CWP-BDP was collected in a single photodetector, using a spectral window extending from 500 nm to 600 nm. The emission of NR12S was collected in two separate channels, using spectral windows extending from 500 nm to 585 nm, and from 585 nm to 700 nm respectively. The acquisition time was fixed at 15 s for each 256 × 256 pixel image. For three-dimensional image stacks, the z-step was set to 0.5 μm.

FLIM images obtained with CWP-BDP imaging were processed using the SP8 Falcon software that determines lifetimes based on the average arrival time of photons. Ratiometric images obtained with NR12S were constructed from the recorded intensity images using a custom Matlab routine that divides the photon count in each pixel of the 500-585 nm (so-called 'blue') channel image, by the photon count in the corresponding pixel of the 585-700 nm (so-called 'red') channel image. Resulting images are reported in a false-color scale that represents the mean CWP-BDP fluorescence lifetime (in nanoseconds), or the NR12S intensity ratio for each pixel.

Control images for the evaluation of autofluorescence intensities and fluorescence lifetimes were recorded on unstained specimens with the same imaging conditions and the highest laser intensity used, i.e. less than 10 μW (single-photon microscope) or 5 mW (multiphoton microscope) at the sample level. The autofluorescence levels in the CW and PM were too low to perturb our results (Fig. 5.8).

Giant Unilamellar Vesicle (GUV) preparation

Stock solutions of sphingomyelin (SM) and 1,2-dioleoyl-sn-glycero-3-phosphocholine (DOPC) in chloroform were purchased from Avanti Polar Lipids and used as is. Cholesterol was purchased from VWR. Giant Unilamellar Vesicles (GUV) were formulated via agarose gel swelling using the method of Horger et al.[23]. Two types of vesicles were formulated, with the following lipid molar ratios; DOPC: SM = 1:1 and DOPC: SM: Chol = 1:1:0.7. To do so, two lipid solutions in chloroform were prepared; for the cholesterol-free solution, DOPC (1.2 mmol L^{-1}, 57 mg of 25 g L^{-1} stock solution in chloroform) and SM (1.2 mmol L^{-1}, 137 mg of 10 g L^{-1} stock solution in chloroform) were mixed in chloroform (370 μl). For the cholesterol-supplied solution, DOPC (1.0 mmol L^{-1}, 48 mg of 25 g L^{-1} stock solution in chloroform), SM (1.0 mmol L^{-1}, 117 mg of 10 g L^{-1} stock solution in chloroform), and cholesterol (0.7 mmol L^{-1}, 42 mg of 10 g L^{-1} stock solution in chloroform) were mixed in chloroform (361 μL).

In parallel, Type IX-A ultralow melting agarose (gel point, Tg $\leq$ 20 °C; melting point, Tm $\leq$ 62 °C; electroendosmosis, EEO $\leq$ 0.12) films were formed on glass slides. For that purpose, a 1% (w/w) solution of agarose in deionized water was prepared, of which 400 μL were spread on the glass surface equilibrated at 40°C on a heating plate. The agarose coated slide was then left to dry at 40°C for 2h, until formation of a dry agarose film.

To generate a lipid film on and inside the films of agarose, 30 μL of the lipid solution of interest were spread on the agarose using the procedure described in detail by Horger et al.[23]. The sample was dried for 20 min under vacuum to remove residual chloroform, and subsequently immersed in a 0.1 mol L^{-1} glucose aqueous solution to allow for agarose gel and simultaneous vesicle swelling. The dish remained undisturbed at room temperature for 3h to yield the giant vesicles suspension. The vesicles were then immobilized in a 0.5% (w/v) agarose gel for imaging, as reported previously[24].

Hypo-osmotic treatment

We subjected cysts to osmotic shock by adding poly(ethylene glycol) (PEG) 2000 g L^{-1} as a calibrated osmolyte[25, 26, 14]. The osmolyte was added to cysts at a 90 mmol L^{-1} concentration to achieve an osmotic pressure in the medium of

0.6 MPa. The cyst-osmolyte mixtures were applied to PDMS substrates, left to incubate for 3h upon which 50 μL of the droplet was exchanged three times with water. Staining with CWP-BDP or NR12S was performed right before applying the osmotic shock, as described above but using a 10 μmol L^{-1} dye solution in 90 mmol L^{-1} PEG2000. Analysis of the effect of the osmotic shock was performed by looking at the cyst exclusively.

Chemical treatments

Treatment with cell wall and plasma membrane-targeting control agents

To investigate the effect of chemical stress on the CW and PM properties, cells were treated with two different compounds reported to act on the structural properties of either the PM or the CW. Each treatment was started 1h after application of the encysted zoospores on the substrate, and performed during 1h before staining and imaging. During imaging, cells were kept in the same treatment conditions to avoid additional stress.

To perturb the CW composition and structure, valifenalate solubilized in a 0.25 mmol L^{-1} stock solution in DMSO was added to the germlings to a final concentration of 125 nmol L^{-1} valifenalate (DMSO content<0.05% (v/v)). To induce variations in PM composition and lipid order, fluopicolide solubilized in a 0.26 mmol L^{-1} stock solution in DMSO was added to the germlings to a final concentration of 25 nmol L^{-1} fluopicolide (DMSO content<0.05% (v/v)).

Treatment with cytoskeletal depolymerizing drugs

To perturb the organized actin cytoskeleton of the pathogens, LatB solubilized in a 0.1 mmol L^{-1} stock solution in DMSO was added to the germlings to a final concentration of 1 μmol L^{-1} LatB and 1% (v/v) DMSO. To disrupt the microtubule network, oryzalin solubilized in a 0.1 mmol L^{-1} stock solution in DMSO was added to the germlings to a final concentration of 0.1 μmol L^{-1} oryzalin and 1% (v/v) DMSO.

As a control, cells were also treated with 1% (v/v) DMSO only. Analysis of the effects of the chemical treatments was performed by looking at the hyphal tip exclusively.

Growth and invasivity assays

We verified the invasion efficiency under each treatment, following the procedure adopted previously[14]. The invasion efficiency is defined as the percentage of germinated cysts, counting only those whose germ tube exceeds c. 10 μm in length, that have successfully fractured the artificial surface 2h post application (hpa).

Statistical analysis

All the described imaging experiments, were repeated at least two times on different cell batches and different days (Table 5.1). For each repeat, at least ten cells were imaged. Fluorescence lifetime and intensity ratio distributions were extracted from the corresponding images, and summed over the different repeats. All distributions are built from at least 4000 data points. To ascertain the noise threshold for changes in lifetime or intensity ratio that can be detected with statistical significance, we perform measurements in homogeneous control media strictly deprived of spatial inhomogeneities (Fig. 5.9-5.10). We find a noise threshold, determined as the full-width at half-maximum (FWHM) of the observed distributions in homogeneous media to be 0.45 ns for the lifetime measurements on CWP-BDP and ratio = 0.02 for the ratiometric imaging of N12RS. We only consider an observed response significant if its change is either 1x larger than 1x the noise floor, for CWP-BDP, and or 3x larger than the noise floor for NR12S. The distribution widths we report in this paper on biological specimens are always well above those reported in homogeneous media; these thus do not represent measurement error but rather reflect real spatial inhomogeneities in the CW or PM properties of the organism.

5.3 Results

Molecular rotor CWP-BDP maps cell wall mesh sizes in *P. infestans*

While the method from Bronkhorst et al.[14] allowed visualization of stresses applied by the pathogen to the substrate, our method provides a way to visualize the response to these stresses in the CW and PM of the pathogen. In order to

investigate CW and PM structural modifications during non-invasive and invasive hyphal growth of *P. infestans*, we implemented the wall-targeting fluorescent molecular rotor CWP-BDP, and the PM chemical polarity probe NR12S in encysted zoospores, 1.5 hpa.

CWP-BDP is a phenyl-substituted borondipyrromethene (Ph-BODIPY) molecular rotor, substituted on the phenyl ring by a peptide mimicking the pectin binding domain of extensins, a family of glycoproteins that are highly abundant in plant CWs[27]. As such, it has been designed to target and bind specifically to the wall of plant cells. The molecular rotor, whose mode-of-action is described in detail elsewhere[15], offers a mechano-optical coupling that allows qualitative measurements of local CW mesh sizes, using a fluorescence lifetime read-out (Fig. 5.1a-c). Although the CWs of *Phytophthora* spp. have a different composition than plant CWs and contain mainly polymers of D-glucose[28, 29], we observe that also in *P. infestans* CWP-BDP binds to the CW, presumably through electrostatic interactions with other anionic carbohydrates (Fig. 5.1d,e).

Solvatochromic probe NR12S reveals membrane chemical polarity and order *P. infestans*

NR12S is a solvatochromic Nile Red-based probe developed by Kucherak et al.[18] (Fig. 5.2a). In its design, the Nile Red unit is decorated with a long alkyl tail and a zwitterionic group, which allows for specific staining of the PM and restricts flip-flopping of the dye from the outer to the inner leaflet, thereby reducing subsequent incorporation in intracellular membranes. This probe exhibits a shift in the wavelength of maximum emission in response to changes in the local chemical polarity of its surroundings. The read-out for this probe consists of ratiometric imaging, in which the total emission of the dye is split into two channels. Changes in membrane chemical composition and lipid phase both impact the chemical polarity of the probe microenvironment, triggering a change in the intensity ratio between the blue and red channels (Fig. 5.2b,c). Kucherak et al.[18] used these properties to image variations in PM lipid order and cholesterol content in mammalian cells. Here we extend the use of this probe to walled cells.

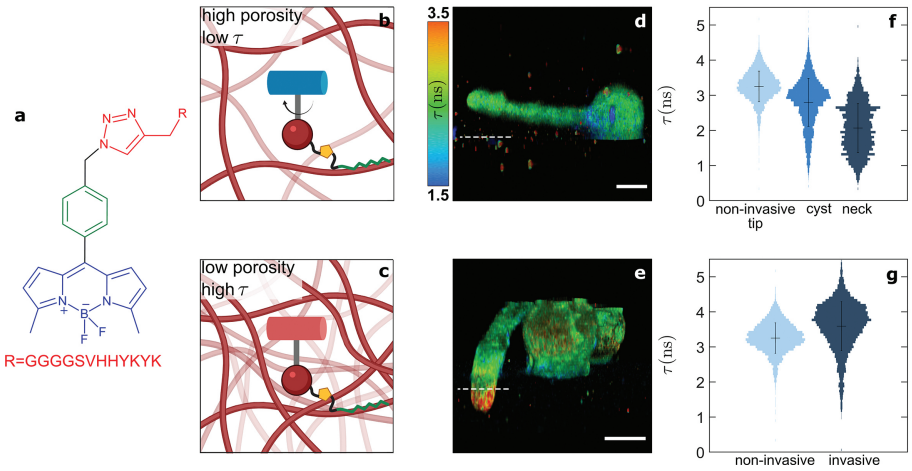

Figure 5.1: Mapping of spatial variations in the cell wall mesh size of *Phytophthora infestans* germlings using the molecular rotor CWP-BDP. (a) Chemical structure of CWP-BDP. (b,c) Schematic illustrations showing the molecular mechanism by which CWP-BDP reports mesh sizes. 3D fluorescence lifetime mesh size map of *Phytophthora infestans* germlings (d) upon growth at the PDMS substrate surface and (e) upon invasion. Scale bars = 5 μm. The colorscale translates the fluorescence lifetime values expressed in ns. The white dashed line is used to indicate substrate surface location (f) Fluorescence lifetime probability distributions obtained in different regions of the germlings (N = 30 cells). (g) Fluorescence lifetime probability distributions obtained in the tip of germ tubes before and after invasion (N = 30 cells).

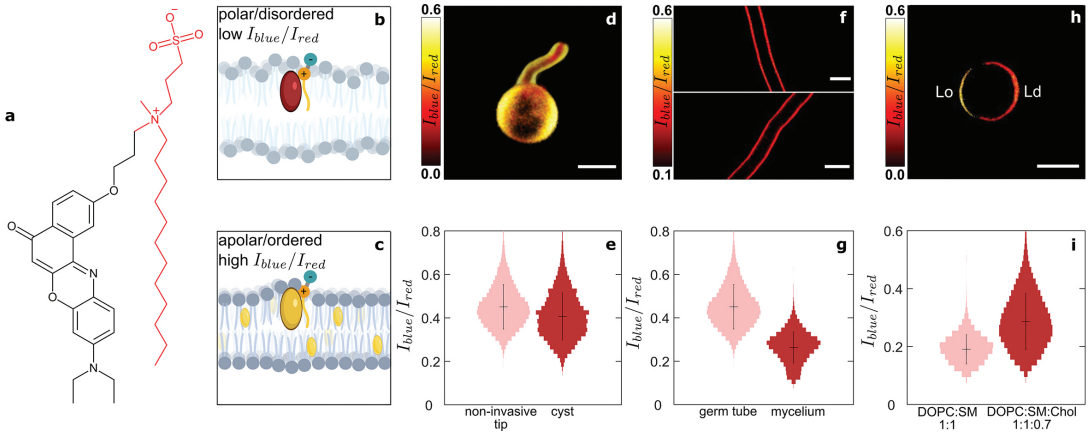

Figure 5.2: Mapping of spatial variations in the plasma membrane chemical polarity of *Phytophthora infestans* germlings using the solvatochromic probe NR12S. (a) Chemical structure of NR12S. (b,c) Schematic illustrations showing the mechanism by which NR12S reports changes in chemical polarity and lipid phase. (d) 3D intensity ratio chemical polarity map of *Phytophthora infestans* germlings upon growth at the PDMS substrate surface. Scale bar = 5 μm. The colorscale translates the intensity ratio values. (e) Intensity ratio probability distributions obtained in different regions of the germlings (N = 30 cells) (f) Intensity ratio chemical polarity map of *Phytophthora infestans* mycelium. Scale bars = 10 μm. (g) Fluorescence lifetime probability distributions obtained in the young germ tubes tip (N = 30 cells) versus mycelial cells grown on agar (3 mycelia, N = 30 images). (h) Intensity ratio chemical polarity map of DOPC:SM:Cholesterol = 1:1:0.7 (molar ratio) synthetic vesicles exhibiting phase separation between a cholesterol-rich ordered (Lo), and a cholesterol-poor disordered (Ld) phases. Scale bar = 5 μm. (i) Intensity ratio probability distributions obtained in DOPC:SM = 1:1 (molar ratio) (N = 20 vesicles) versus DOPC:SM:Cholesterol = 1:1:0.7 (molar ratio) (N = 20 vesicles) synthetic vesicles.

Mechano-chemical response of walls and membranes to mechanical stress

Using FLIM, we built three-dimensional reconstructions of the CW of *P. infestans* cells during non-invasive and invasive growth on an artificial host-mimicking substrate based on a PDMS elastomer[14] (Fig. 5.1d,e, Fig. 5.11-5.13). The FLIM mesh size images provide quantitative information, which we extract as lifetime probability distributions (Fig. 5.1f,g). For example, in non-invasive cells, variations in lifetime emerge when comparing the cyst to the germ tube neck and tip. The lifetime diminishes locally to 2.0 ± 1.9 ns in the neck, while increasing slightly in the tip of the germ tube to 3.2 ± 0.9 ns (Fig. 5.1d,f). These differences reflect a relative increase in wall mesh size in the neck, and concomitant reduction in mesh size in the germ tube tip. By contrast, upon invasion, the fluorescence lifetime recorded within the tip of the germ tube in contact with the substrate rises strongly and abruptly to 3.7 ± 1.2 ns (Fig. 5.1e,g). The lifetime distribution keeps a comparable width but exhibits a small shoulder centered on the non-invasive case value of 3.2 ns. To test whether this increase of lifetime is caused by compression of the CW between the PDMS substrate and the cytoplasm, we applied a hypo-osmotic shock to the cells; a similar increase in lifetime was observed in the wall of cysts (Fig. 5.3a-c, Fig. 5.14). These images reveal the compression of the CW upon substrate invasion, as the mechanical stress at the pathogen-substrate contact squeezes water from the carbohydrate network, increasing its density at the invasion site. This approach thus enables direct visualization of the locus of mechanical interactions between pathogen and substrate.

To unravel how growth and invasion affect the properties of the PM that lies underneath the CW, we compare the response of the probe NR12S between non-invasive versus invasive cysts. We measure the emission intensity in two channels in cells stained with the NR12S probe and represent the results as intensity ratio images from which we derive probability distributions (Fig. 5.2d,e). In cells growing non-invasively, the intensity ratio remains constant throughout the cell, around 0.4. This suggests that the PM composition and hydration level are relatively constant along the germ tube at early stages of growth. The invasive part of cells could not be imaged with NR12S due to the low dye penetration and emission intensity underneath the PDMS surface. Hypo-osmotic shock only

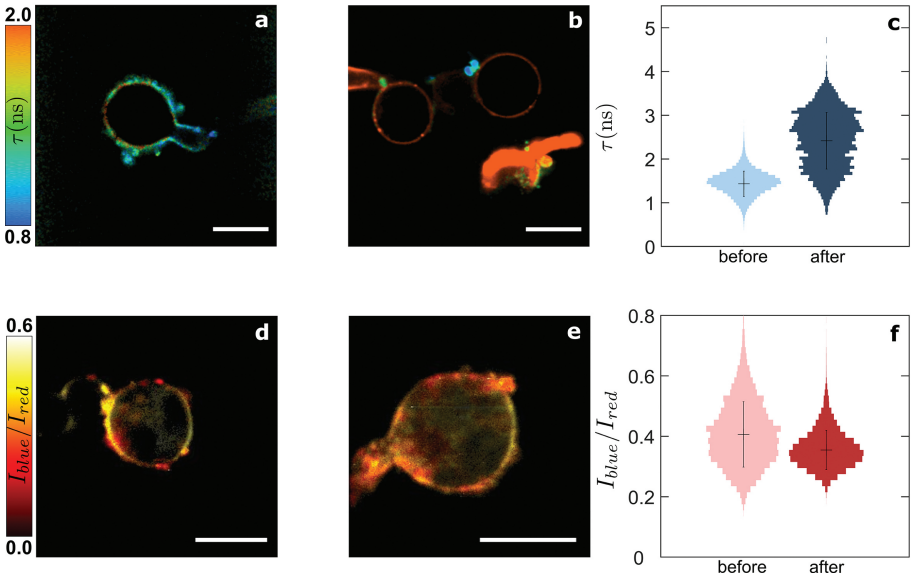

Figure 5.3: Effects of hypo-osmotic treatment on the cell wall and plasma membrane mechano-chemical properties of *Phytophthora infestans* germlings. Fluorescence lifetime cell wall mesh size map of germlings growing (a) in a 90 mmol L^{-1} PEG2000g mol^{-1} aqueous solution for 3h, (b) in a 90 mmol L^{-1} PEG2000g mol^{-1} aqueous solution for 3h followed by transfer to water. (c) Corresponding fluorescence lifetime probability distributions in (a-b) (N = 20 cells). Intensity ratio plasma membrane chemical polarity map of germlings growing (d) in a 90 mmol L^{-1} PEG2000g mol^{-1} aqueous solution for 3h, (e) in a 90 mmol L^{-1} PEG2000g mol^{-1} aqueous solution for 3h followed by transfer to water. (f) Corresponding intensity ratio probability distributions in (d-e) (N = 20 cells). Scale bars = 10 μm.

results in small changes in the ratiometric measurements of the PM (Fig. 5.3d, f). This implies that the PM polarity and lipid order is only weakly sensitive to the compressive forces that push the PM against the cell wall. This observation implies that upon invasive growth, as the hyphal tip is mechanically stressed by the substrate, compressive forces would not substantially alter the properties of the membranes.

In mature *P. infestans* mycelium, the intensity ratio is decreased to 0.22 ± 0.15 (Fig. 5.2f,g), in comparison to the ratio of 0.42 ± 0.21 measured in the tip of young germ tubes. This observation suggests a significant change in PM composition and lipid order as the cells grow and maturate, and confirms the probe responsiveness to changes in membrane chemical polarity. We validated this hypothesis by implementing NR12S in synthetic giant-unilamelar vesicles made of DOPC, SM, and cholesterol (1:1:0.7 molar ratio). This lipid composition can lead to phase separation between an ordered (Lo) phase rich in SM and cholesterol, and a liquid-like (Ld) phase, enriched in DOPC (Fig. 5.2h). GUVs made of only DOPC and SM show a single phase, and a narrow intensity ratio distribution centered around 0.17 ± 0.11. In the cholesterol-supplemented GUVs, phase separation and the global increase in lipid order is reflected by an upward shift of the ratio distribution mean value and width to 0.26 ± 0.22 (Fig. 5.2i). These results confirm the responsiveness of NR12S to changes in lipid phase. The difference in PM properties in the mycelium as compared to the cyst life stage thus hints at a reduced lipid order and packing density in mycelial membranes. We speculate that these differences are due to changes in PM composition, e.g. lipid composition and/or protein content, as both life stages utilize distinct metabolic pathways in which lipids, and hence the PM, play different roles[30, 31, 32, 33].

Revealing the mode-of-action of chemical control agents

Using the CWP-BDP CW and the NR12S PM probes, we investigated the effects of different chemical stresses on *P. infestans* germinated cysts during substrate contamination and invasion process. In particular, we looked at the effect of adding active ingredients from fungicides (i.e. valifenalate, fluopicolide) (Fig. 5.4).

We selected the PM targeting compound fluopicolide and the cellulose syn-

thase inhibitor valifenalate[34] to verify their specifity of action to either membranes or walls. Fluopicolide dislocates spectrin-like proteins in *Phytophthora* from the membrane to the cytoplasm [35, 36]. Upon treatment with 25 nmol L^{-1} fluopicolide, NR12S reports a significant drop in the NR12S intensity ratio within the PM, going from 0.42 ± 0.21 to 0.23 ± 0.09 (Fig. 5.4e,f,h, Fig. 5.15). This change could reflect either a loss in PM tensegrity by spectrin-like protein expulsion and potential cytoskeletal de-adhesion from the membrane, or result from the intercalation of the rather polar fluopicolide molecule into the PM. To discriminate between these two hypotheses, we perform experiments in synthetic vesicles which lack spectrins and other PM proteins, by submitting GUVs to the same concentration of fluopicolide (Fig. 5.4i-k, Fig. 5.16). No change in intensity ratio was reported in synthetic vesicles, which confirms that the increase in polarity within the PM is due to an alteration of the membrane structure and not by fluopicolide entry into the PM. By contrast, the same fluopicolide treatment results in only minor changes in the CW, as confirmed by CWP-BDP fluorescence lifetime imaging (Fig. 5.4a,b,d, Fig. 5.15), likely due to the presence of DMSO (Fig. 5.4d, Fig. 5.17). This suggests that there is no direct link between the correct localization of spectrin-like proteins in the PM and wall mechanics and biosynthesis. We note that while NR12S displays a significant shift in intensity ratio upon treatment with this low fluopicolide concentration, this dose does not lead to a significant inhibition of pathogen invasion. In the absence of fluopicolide the invasivity is 71.3% (N=138 cells), versus 63% (N=84 cells) with fluopicolide. Even though the treatment has a limited effect on the invasivity of cells that remain viable, we do note that this dose leads to a substantial fraction of non viable cells, i.e. cells that do not germinate and become highly autofluorescent upon laser exposure. At higher fluopicolide doses, we observe a decrease in the amount of germination, but no substantial reduction in invasivity of the remaining germinated cells. This indicates that NR12S is sensitive enough to report changes in the physico-chemical properties of the viable cells well before invasivity is hampered.

Valifenalate is used to target and weaken the CW of oomycetes[37, 38]. We observe that valifenalate distinctly changes the pathogen wall properties; imaging with CWP-BDP reveals an increase in fluorescence lifetime from 3.2 ± 0.9

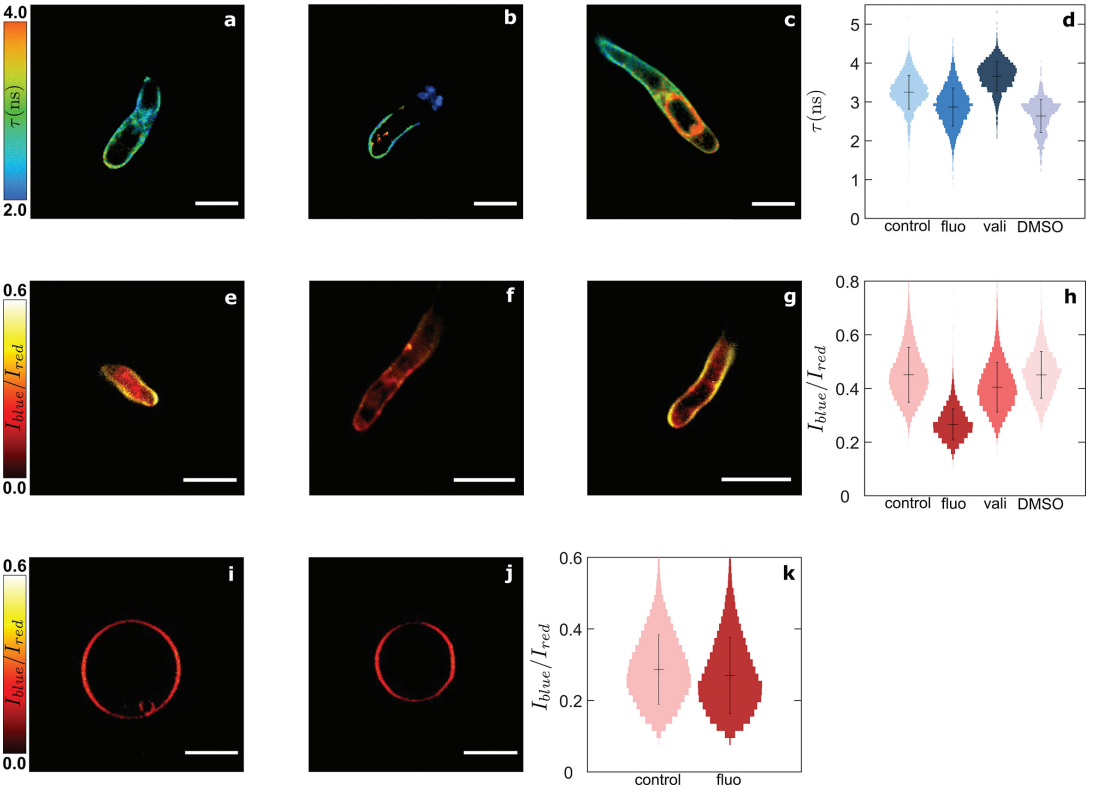

Figure 5.4: Effects of treatments with control agents on the cell wall and plasma membrane mechano-chemical properties of *Phytophthora infestans* germlings. Fluorescence lifetime cell wall mesh size map of germlings growing in (a) water for 1h, (b) in water for 1h followed by treatment with 25 nmol L^{-1} fluopicolide (fluo) for 1h and (c) in water for 1h followed by treatment with 125 nmol L^{-1} valifenalate (vali) for 1h. (d) Fluorescence lifetime probability distributions in (a-c) (N = 30 cells). Intensity ratio plasma membrane chemical polarity map of germlings growing (e) in water for 1h (f) in water for 1h followed by treatment with 25 nmol L^{-1} fluopicolide (fluo) for 1h and (g) in water for 1h followed by treatment with 125 nmol L^{-1} valifenalate (vali) for 1h. (h) Intensity ratio probability distributions in (e-g) (N = 30 cells). Intensity ratio chemical polarity map of DOPC:SM:Cholesterol = 1:1:0.7 (molar ratio) synthetic vesicles in (i) absence and (j) presence of 25 nmol L^{-1} fluopicolide (fluo). (k) Fluorescence lifetime probability distributions in (i-j) (N = 30 cells). Scale bars = 10 μm.

ns in non-treated germlings to 3.6 ± 0.8 ns in germlings treated with 125 nmol L^{-1} valifenalate, and the emergence of distinct spatial variations along the germ tube, marking the transition between the wall portions synthesized before and during treatment (Fig. 5.4a,c,d, Fig. 5.18). Staining of an unknown structure inside the cells led to an intracellular fluorescent signal that was excluded from the analysis. This structure could result from the accumulation of CW precursors in the cytoplasm. After treatment, cellulose synthase inhibition results in a denser CW, which not only changes the probe lifetime but also weakly reduces the staining efficiency due to a lower permeability. We previously reported a similar trend in the evolution of the wall mesh size during polarized growth of Arabidopsis root hairs[15]. During root hair growth and maturation, the CW starts from a dense network of flexible carbohydrates, malleable enough to yield under turgor to enable tip growth. At later stages, the wall is reinforced by a network of stiff cellulose fibers which exhibit a much larger mesh size. In other words, a loss of the cellulose network results in a decrease in porosity and an increase in fluorescence lifetime of the probe. Even though the chemical composition of the CW in oomycetes is less known than the Arabidopsis root hair CW, our observations are consistent with this picture where valifenalate treatment inhibits cellulose synthesis, resulting in less porous and more malleable CWs. By comparison, the intensity ratio of NR12S is not affected, showing no influence of valifenalate on PM properties (Fig. 5.4e,g,h, Fig. 5.18). Also for this compound, the effects on CW and PM are decoupled and the chemical acts specifically on a singular target in the CW-PM continuum. When investigating invasion efficiency under treatment with 125 nmol L^{-1} valifenalate, we only notice a slight reduction in the invasivity from 71.3% (N=138 cells) to 59.2% (N=103 cells), while leading to a large amount of non-viable autofluorescent cells. This confirms the sensitivity of CWP-BDP to changes in CW properties even before large effects on invasivity can be detected.

Changes in wall and membranes in response to cytoskeletal disruption

The cell cytoskeleton is known to play a leading role in establishing and maintaining the polarity required for hyphal growth and thereby in the invasion fitness of *Phytophthora* pathogens[39, 40, 41, 42, 43, 44, 14]. To examine how the CW-PM continuum of *P. infestans* responds to perturbations in cytoskeletal or-

ganization, we studied the consequences of treatment with the actin depolymerising drug LatB[44] and treatment with the microtubule inhibitor oryzalin[45, 41, 46]. Treatment with LatB at 1 μmol L^{-1} affects the morphology of the cells, which exhibit the tip swelling behavior characteristic for the loss of polarization. However, very minor fluorescence lifetime changes are visible within the CW (Fig. 5.5a,b,g, Fig. 5.19). A shift in intensity ratio from 0.42 ± 0.21 to 0.36 ± 0.17 is visible within the PM (Fig. 5.5d,e,i, Fig. 5.19). Large doses of LatB strongly disrupt the actin cytoskeleton involved in the transport of CW precursors to the growing tip[44, 47, 48]. Even though one could have expected that 1 μmol L^{-1} of LatB would affect CW synthesis, our images reveal an intact CW for all cells studied under this treatment. Hence we conclude that LatB treatment does not substantially affect the CW. The same treatment results in an increase in the PM polarity, possibly reflecting a reduction of membrane stability due to the lack of tension applied by the disrupted cytoskeleton. This LatB dose applied being highly cytotoxic, we observe that the majority of cells treated for the invasivity assay - right before application on the substrate - show lysis, and the few remaining viable cells are incapable of substrate penetration. Treatment with the microtubule inhibitor oryzalin at 0.1 μmol L^{-1}, leads to a reduction of fluorescence lifetime of CWP-BDP to 2.5 ± 0.9 ns in the hyphal tip (Fig. 5.5a,c,h, Fig. 5.20), while the intensity ratio of NR12S decreases to 0.34 ± 0.18 (Fig. 5.5d,f,j, Fig. 5.20). While the exact function of microtubules in the lifestage of germinated cysts, both during invasive and non-invasive growth, is yet unresolved, our results show that disruption of the microtubule network leads to changes in both the CW porosity and PM tensegrity. This could point towards a role for microtubules in regulating the structure and tension in both organs. At this low dose of oryzalin, the invasivity of the cells remains at 68.1% (N=201 cells). Also here, the combination of our molecular probes enables connecting action on other cellular components to their effects on the cell exterior formed by the CW and PM, even when invasivity is not affected.

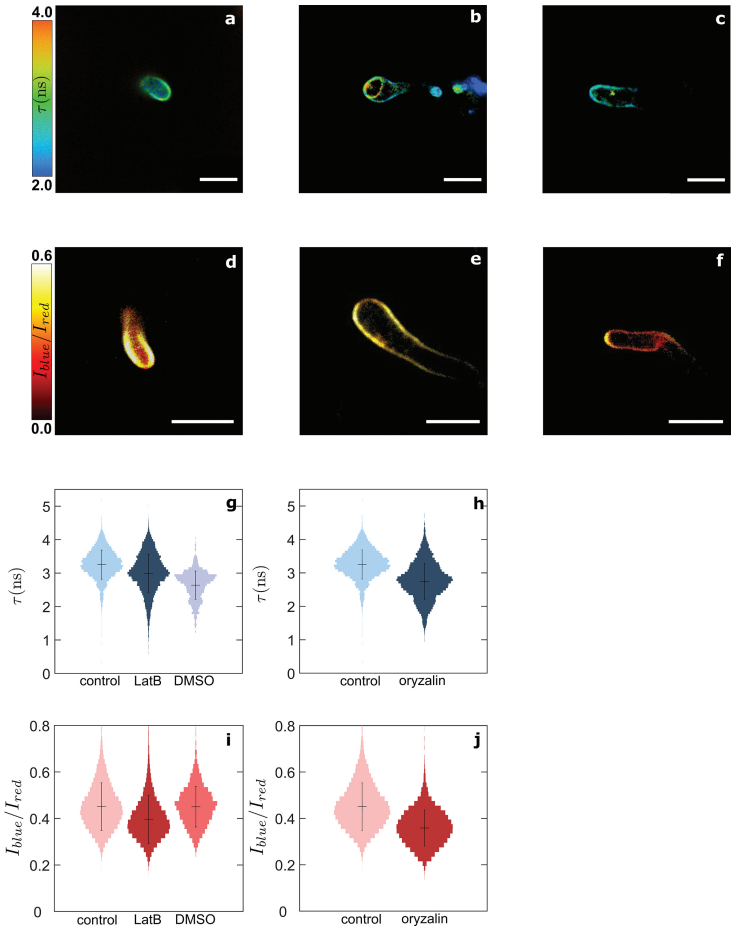

Figure 5.5: Effects of treatments with cytoskeletal depolymerizing drugs on the cell wall and plasma membrane mechano-chemical properties of *Phytophthora infestans* germlings. Fluorescence lifetime cell wall mesh size map of germlings growing (a) in water for 1h, (b) in water for 1h followed by treatment with 1 μmol L^{-1} latrunculin B for 1h, (c) in water for 1h followed by treatment with 0.1 μmol L^{-1} oryzalin for 1h. Intensity ratio plasma membrane chemical polarity map of germlings growing (d) in water for 1h, (e) in water for 1h followed by treatment with 1 μmol L^{-1} latrunculin B for 1h, (f) in water for 1h followed by treatment with 0.1 μmol L^{-1} oryzalin for 1h. (g, h) Fluorescence lifetime probability distributions in (a-c) (N = 30 cells). (i, j) Intensity ratio chemical polarity probability distributions in (d-f) (N = 30 cells). Scale bars = 10 μm.

5.4 Discussion

The CW and PM of cells form a continuum that plays a major role in the mechano-chemical response of cells. The CW being the stiffest part of the cell, and the direct connection between the cell and its immediate surroundings, it is where the perception and transduction of mechanical cues begins. While the molecular mediators of mechano-perception in *Phytophthora* are still unknown, other walled microorganisms – yet, not showing invasive growth - such as yeasts exhibit various CW-localized mechano-receptors[49, 50, 51]. In the case of species that grow invasively, such as *Phytophthora*, mechano-perception becomes central to the understanding of cell function. Physical perturbations of the CW are internalized into the cells through the PM. In response to mechanical force, the PM can deform and change composition, for example through recruitment of proteins, or opening of mechanosensitive ion channels by increased lateral tension[52, 53]. Structural modifications of these two entities reflect part of the mechano-chemical response of cells to external stress.

The oomycete CW and PM undergo structural and chemical modifications during development. After zoospore encystment, a CW is formed around the cyst and the cell is able to generate turgor pressure. During germination of the cyst, the CW progressively extends and thickens [54]. Subsequent germ tube growth requires local modification of the CW to reduce its yield limit at the tip, such that turgor action leads to polarized tip growth[42, 55]. Meanwhile, very little is known about modulations of the PM properties, to allow for e.g. recruitment of stretch-activated ion channels involved in tip growth[56, 57], or active vesicle secretion of effector proteins[58]. This dynamic adaptation of the cells can be triggered by external stimuli, such as mechanical and chemical interactions with the host plant. To date, the development of treatments to inhibit *P. infestans* growth and combat the late blight has relied partly on chemicals able to prevent its structural adaptation, or that induce structural modifications as a side effect[43, 59].

Resolving these modifications with spatio-temporal resolution could help understanding the mechanics of growth and invasion, as well as the mode of action of chemical control agents. In agriculture, chemical control is still crucial to combat oomycete plant pathogens. In this study, we implemented the CW target-

ing molecular rotor CWP-BDP and the PM ratiometric probe NR12S in *P. infestans*, but this method is readily applicable to other oomycetes. In parallel, we also tried to implement other fluorescent molecular rotors reported previously[15], analog to CWP-BDP but used to target the PM, the cytoplasm and the vacuole respectively; the PM probe could stain the plasma membrane successfully but its dynamic response range to changes in membrane tension was not suitable to clearly highlight variations in membrane structural properties. Meanwhile, the cytoplasm and vacuole dyes did not penetrate the cells at all, highlighting the lower permeability of oomycete cells in comparison to plant root cells.

With our combination of fluorescent reporters, we are able to map variations in CW mesh size and PM chemical polarity, respectively, during growth and invasion. Upon treatment with active compounds found in oomycide mixtures, or with cytoskeletal depolymerizing drugs, clear changes in CW and PM structural properties are visible and give a real-time indication on the effect of the chemical stress. To achieve a quantitative measurement, systematic calibrations of the two probes are needed. These are not trivial steps as they need to be conducted in a medium that is simultaneously representative of the chemical composition for the compartment of interest, regarding both polarity and length scales, and quantitatively tuneable. For example, to have a reference in terms of CW mesh size, we could imagine implementing CWP-BDP in a synthetic polysaccharide network with controlled mesh sizes and polymer charge densities. In parallel, to determine the PM chemical polarity and lipid phase, we envision systematic studies of the NR12S response in vesicles reconstituted from cell extracts and systematically introducing sterols in the preparation protocol as a way to tune the lipid order. These calibrations can be challenging, as the CW and PM compositions are highly complex and vary from species to species, cell to cell and location to location. Yet, even without calibration to enable quantitative data, the probes already provide valuable qualitative insights into mechano-chemical heterogeneities, reflecting relative changes in probe confinement and local chemical polarity, respectively, as well as providing information on the dynamics of cellular processes at a high resolution that cannot currently be achieved by other means. These probes could be valuable in combination with genetic modification techniques, such as CRISPR-CAS and silencing, as it could help to decipher the

role of different biochemical pathways and proteins in determining CW and PM structural properties.

Unravelling the complex mechano-chemical interactions between pathogens and host would ultimately require implementation of this method on real plant hosts rather than on artificial surfaces, to take into account the complex mechano-biological responses of both parties. Chemical engineering of the probes to provide even more precise, and organism specific, targeting, and using designs with two complementary emission wavelengths would allow simultaneous mapping of both pathogen and plant properties, and help understand their mechanical interactions. To do so, several promising strategies to achieve selective binding arise; for instance, the use of metabollic labelling, previously employed to incorporate alkyne or azide groups in the pectin network of Arabidopsis seedling roots CW, allowing for a subsequent click-reaction to fluorescent dyes[60, 61, 62], or the use of genetic labelling by means of SNAP-tags, previously implemented in animal cells to label e.g. PM proteins[63, 64]. Such approaches could prove valuable for a more systemic perspective on the complex mechanobiology and mechanochemistry of host invasion.

5.5 Supporting Information

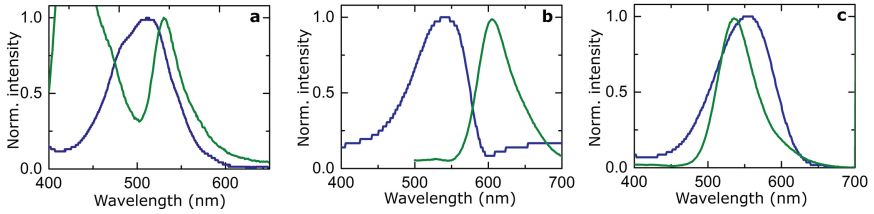

Figure 5.6: Spectroscopic characterization of CWP-BDP and NR12S. Absorbance (blue) and fluorescence emission (green) spectra of (a) CWP-BDP in chloroform, (b) NR12S in chloroform, (c) NR12S in methanol.

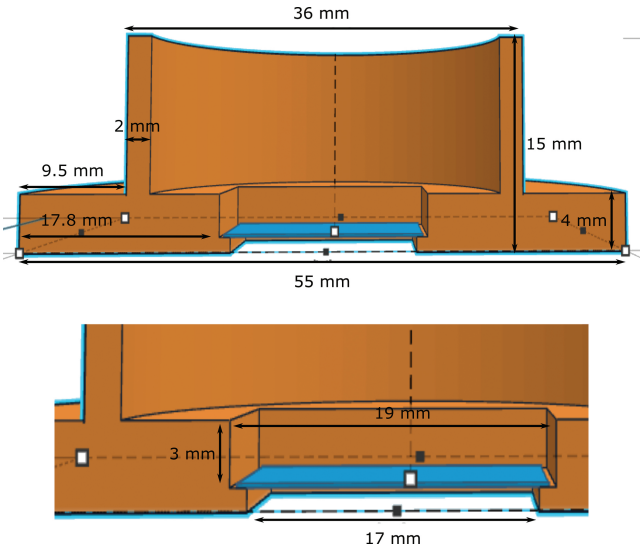

Figure 5.7: Schematic of the 3D-printed observation chambers used for all cell imaging experiments.

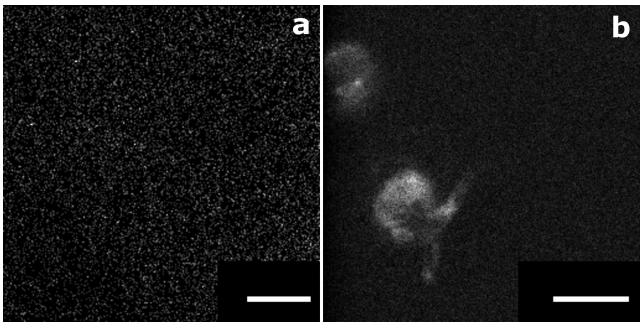

Figure 5.8: Autofluorescence signal of the *Phytophthora infestans* germlings. (a) Autofluorescence obtained by single-photon excition on the TCS SP8, with a laser intensity ten times higher than the maximum laser intensity used for CWP-BDP excitation. Only noise was imaged. Scale bar = 50 μm. (b) Autofluorescence obtained by two-photon excitation on the TCS SP8 multiphoton, with the maximum laser intensity used for CWP-BDP and NR12S excitation. The autofluorescence signal is low and only visible inside the cell, not within the cell wall and plasma membrane. Scale bar = 10 μm.

Table 5.1: Number of samples and observations

Experiments	Figures	Sample numbers
Growth of germinated cysts	Figure 5.1d,e Figure 5.2d Figure 5.4a,e Figure 5.5a,d Figure 5.11-5.13	Non-invasive: N=30 cells from 3 cell batches for each probe; invasive: N=30 cells from 3 cell batches for CWP-BDP
DMSO	Figure 5.17	N=30 cells from 2 cell batches for each probe
Giant synthetic vesicles	Figure 5.2h Figure 5.4i,j Figure 5.16	DOPC:SM=1:1 (molar ratio): N=20 vesicles from 3 vesicle batches for NR12S; DOPC:SM:cholesterol=1:1:0.7 (molar ratio): N=20 vesicles from 3 vesicle batches for NR12S; vesicles supplemented with fluopicolide: N=20 vesicles from 2 vesicle batches for each vesicle type (cholesterol-free and cholesterol-rich), for NR12S
Mycelium	Figure 5.2f	Supplemented with 0.2 μg ml^{-1} β-sitosterol: N=3 mycelia for NR12S
Hypo-osmotic shock	Figure 5.3a,b,d,e Figure 5.14	N=20 cells from 2 cell batches for each probe
Fluopicolide	Figure 5.4b,f Figure 5.15	N=30 cells from 3 cell batches
Valifenalate	Figure 5.4c,g Figure 5.18	N=30 cells from 3 cell batches for each probe
Latrunculin B	Figure 5.5b,e Figure 5.19	N=30 cells from 2 cell batches for each probe
Oryzalin	Figure 5.5c,f Figure 5.20	N=30 cells from 2 cell batches for each probe
Autofluorescence control	Figure 5.8	2 cell batches for both single-photon and two-photon excitation set-ups

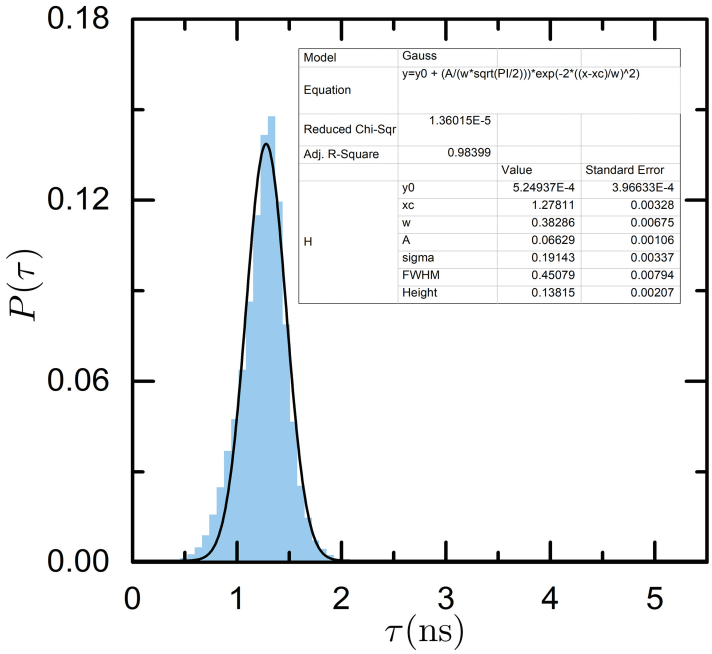

Figure 5.9: Fluorescence lifetime distribution of CWP-BDP in water. The fluorescence lifetime distribution obtained in a homogeneous aqueous solution is fitted with a Gaussian to determine the noise threshold of the probe.

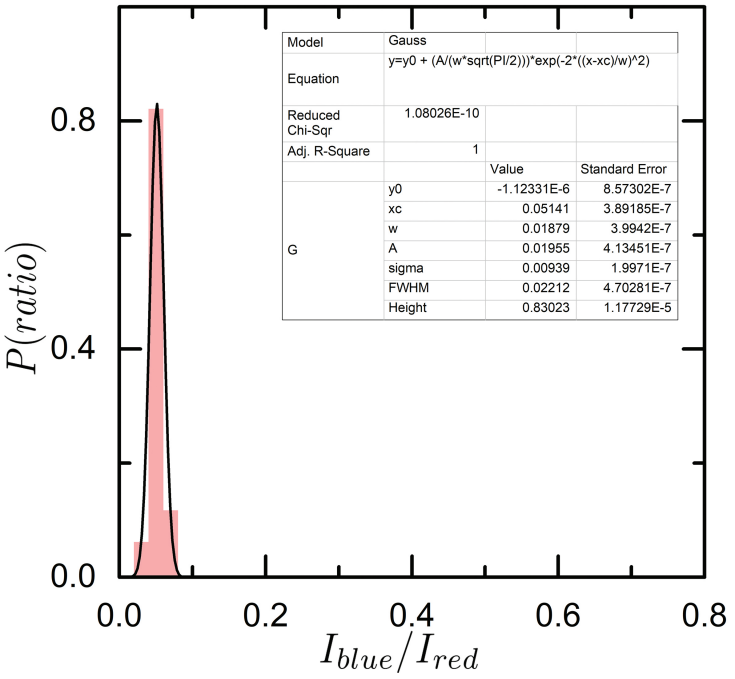

Figure 5.10: Intensity ratio distribution of NR12S in chloroform. The intensity ratio distribution obtained in a homogeneous solution in chloroform is fitted with a Gaussian to determine the noise threshold of the probe. The same experiment performed in methanol or dimethylsulfoxide does not allow to plot a ratio distribution given the very low photon count obtained in the blue channel.

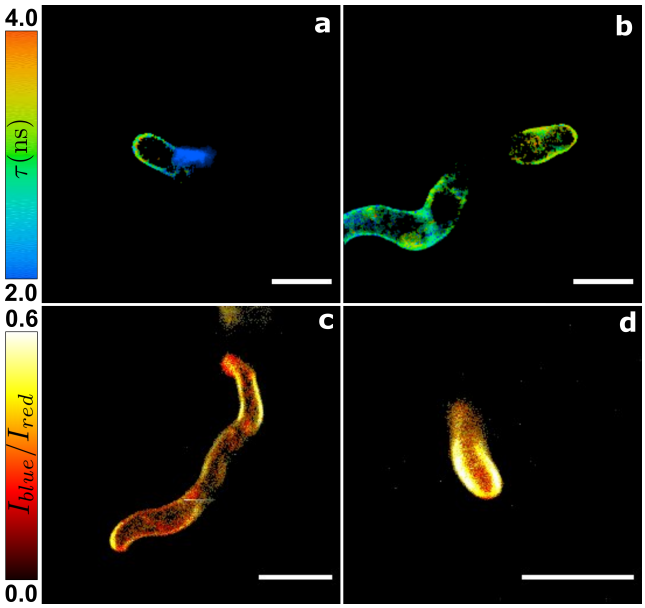

Figure 5.11: Mapping of spatial variations in the cell wall mesh size and plasma membrane chemical polarity of *Phytophthora infestans* germlings. (a, b) Fluorescence lifetime mesh size map of control germlings growing in water 1h post application. (c, d) Intensity ratio chemical polarity map of control germlings growing in water 1h post application. Scale bars = 10 μm.

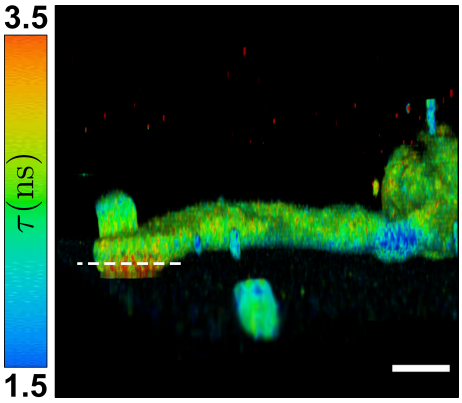

Figure 5.12: 3D-mapping of spatial variations in the cell wall mesh size of *Phytophthora infestans* germlings. 3D fluorescence lifetime mesh size map of *Phytophthora infestans* germlings upon interaction with the host surface. Scale bar = 5 μm.

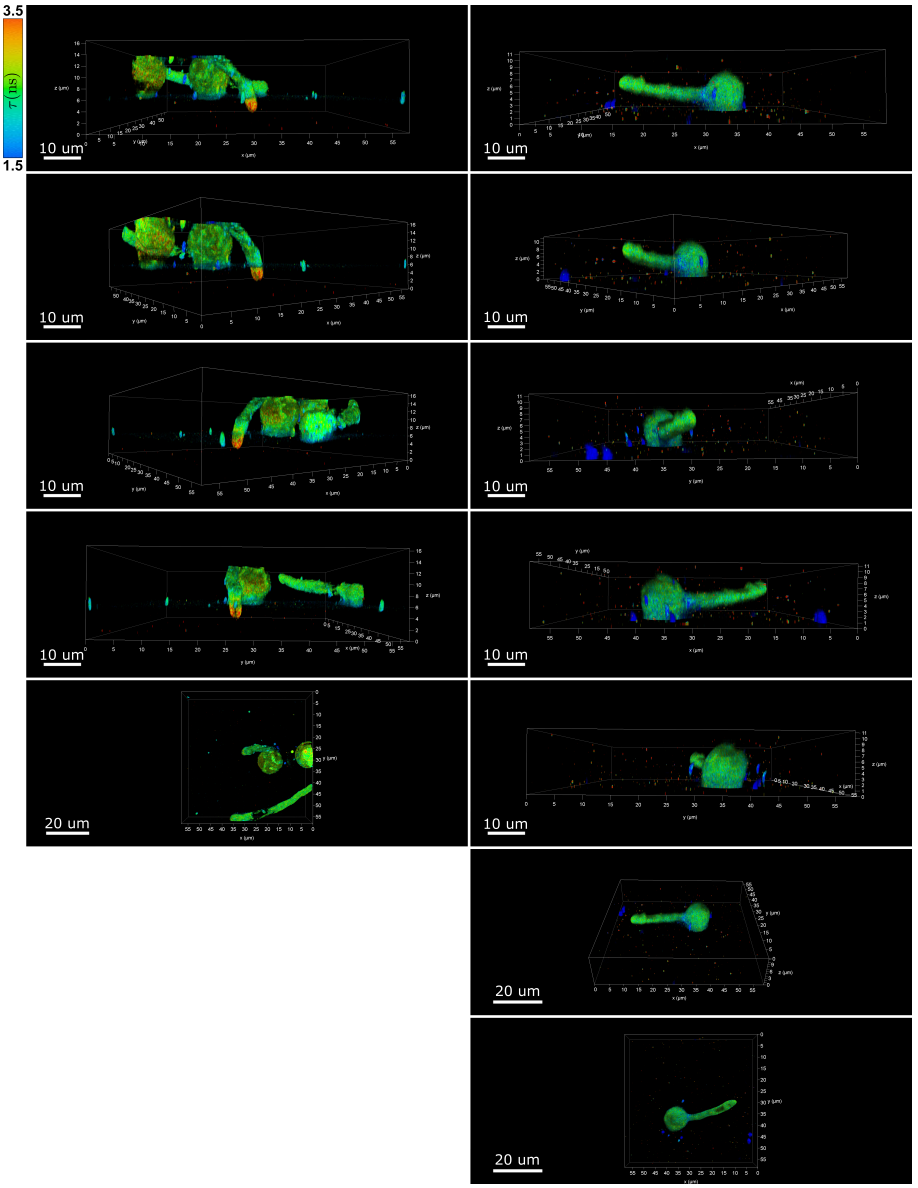

Figure 5.13: 3D-mapping of spatial variations in the cell wall mesh size of *Phytophthora infestans* germlings. Rotation views of the 3D fluorescence lifetime mesh size maps of *Phytophthora infestans* germlings represented in Fig. 5.1.

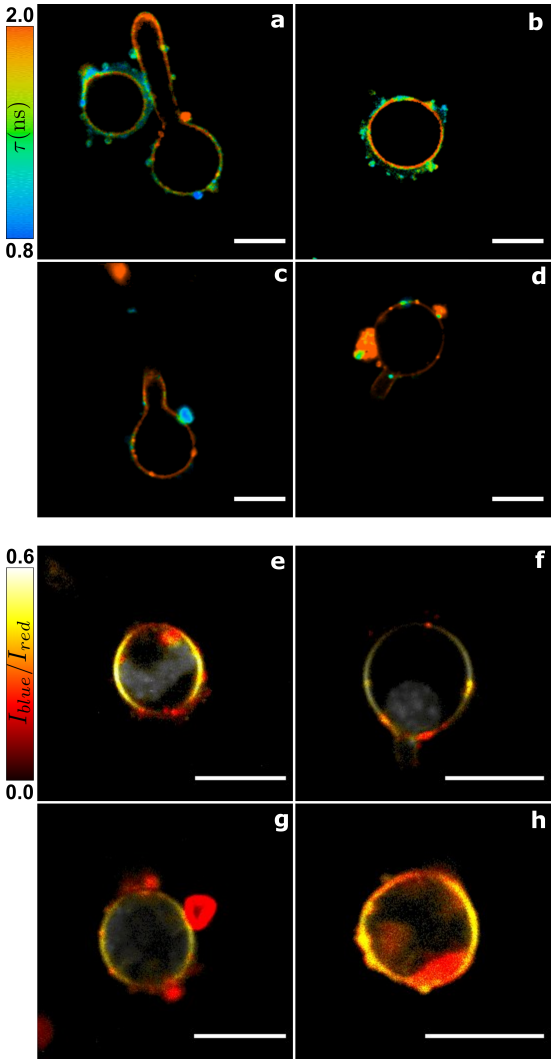

Figure 5.14: Hypo-osmotic treatment on *Phytophthora infestans* germlings, and effect on their cell wall and plasma membrane mechano-chemical properties. (a, b) Fluorescence lifetime mesh size map of germlings growing in a 90 mmol L^{-1} PEG2000g mol^{-1} aqueous solution. (c, d) Fluorescence lifetime mesh size map of germlings after transfer from the 90 mmol L^{-1} PEG2000g mol^{-1} aqueous solution to water. (e, f) Intensity ratio chemical polarity map of germlings growing in a 90 mmol L^{-1} PEG2000g mol^{-1} aqueous solution. (g, h) Intensity ratio chemical polarity map of germlings after transfer from the 90 mmol L^{-1} PEG2000g mol^{-1} aqueous solution to water. Scale bars = 10 μm.

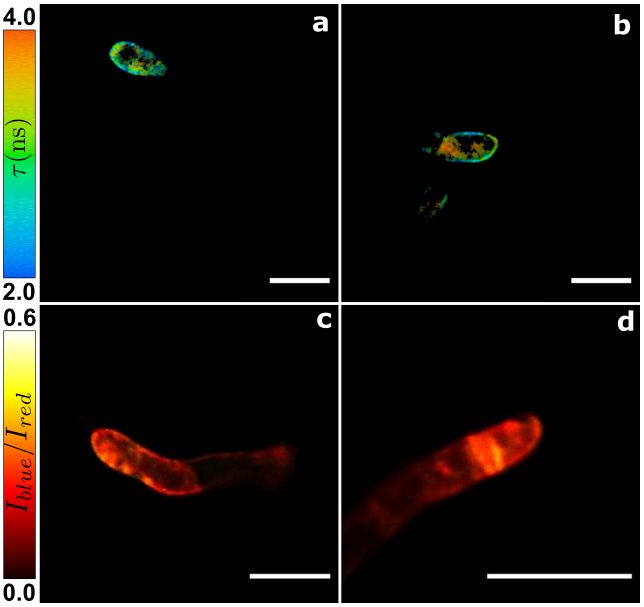

Figure 5.15: Mapping of spatial variations induced by treatment with 25 nmol L^{-1} fluopicolide in the cell wall mesh size and plasma membrane chemical polarity of *Phytophthora infestans* germlings. (a, b) Fluorescence lifetime mesh size map of germlings growing in water 1h post application, and treated with 25 nmol L^{-1} fluopicolide for 1h. (c, d) Intensity ratio chemical polarity map of germlings growing in water 1h post application, and treated with 25 nmol L^{-1} fluopicolide for 1h. Scale bars = 10 μm.

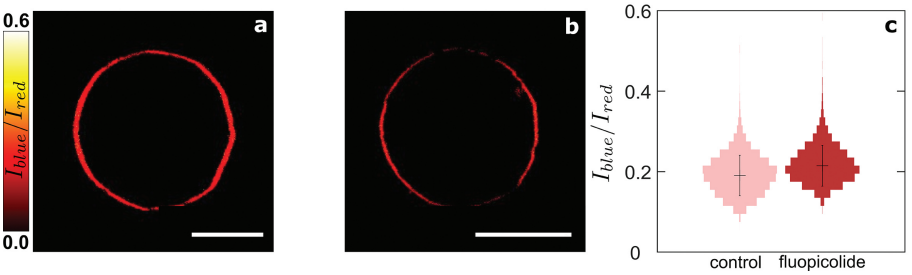

Figure 5.16: Mapping of spatial variations in plasma membrane chemical polarity in DOPC:SM synthetic vesicles. (a) Intensity ratio chemical polarity map of 1,2-dioleoyl-sn-glycero-3-phosphocholine (DOPC):sphingomyelin (SM) = 1:1 (molar ratio) synthetic vesicles. (b) Intensity ratio chemical polarity map of the same vesicles incubated with 25 nmol L^{-1} fluopicolide. (c) Corresponding intensity ratio probability distributions. Scale bars = 10 μm.

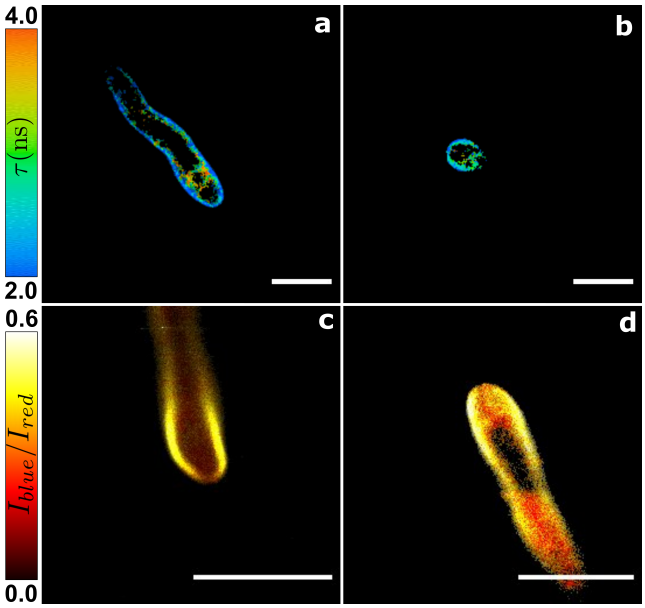

Figure 5.17: Mapping of spatial variations induced by treatment with 1% (v/v) DMSO in the cell wall mesh size and plasma membrane chemical polarity of *Phytophthora infestans* germlings. (a, b) Fluorescence lifetime mesh size map of germlings growing in water 1h post application, and treated with 1% (v/v) DMSO for 1h. (c, d) Intensity ratio chemical polarity map of germlings growing in water 1h post application, and treated with 1% (v/v) DMSO for 1h. Scale bars = 10 μm.

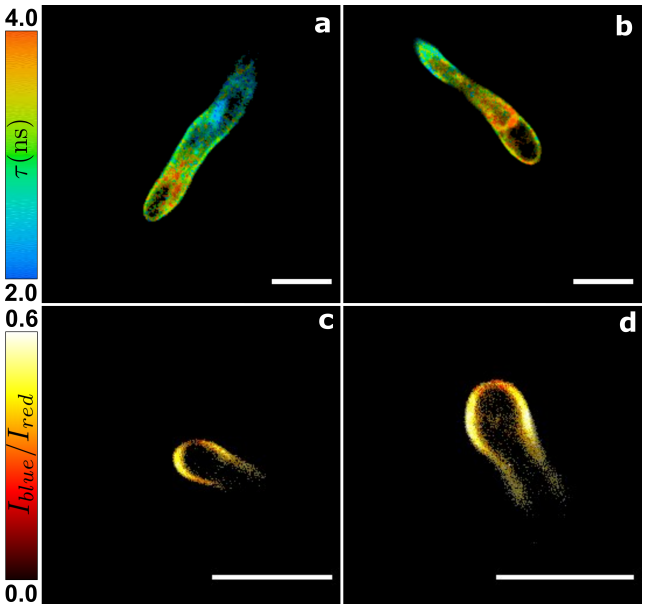

Figure 5.18: Mapping of spatial variations induced by treatment with 125 nmol L^{-1} valifenalate in the cell wall mesh size and plasma membrane chemical polarity of *Phytophthora infestans* germlings. (a, b) Fluorescence lifetime mesh size map of germlings growing in water 1h post application, and treated with 125 nmol L^{-1} valifenalate for 1h. (c, d) Intensity ratio chemical polarity map of germlings growing in water 1h post application, and treated with 125 nmol L^{-1} valifenalate for 1h. Scale bars = 10 μm.

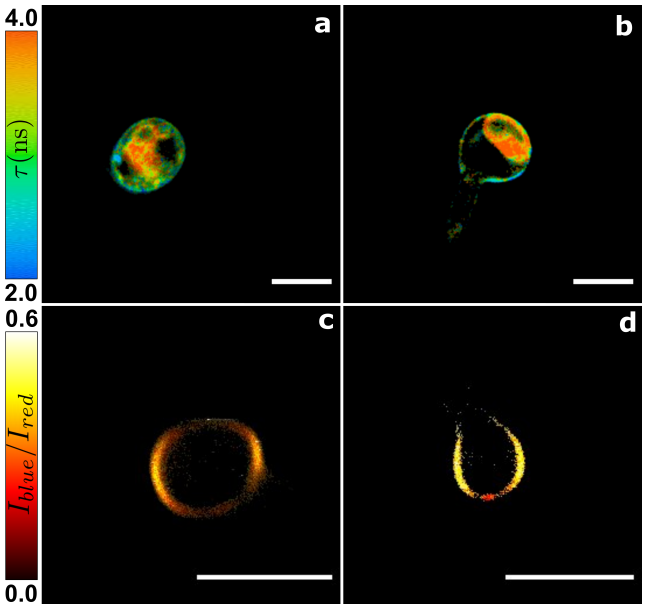

Figure 5.19: Mapping of spatial variations induced by treatment with 1 μmol L^{-1} latrunculin B in the cell wall mesh size and plasma membrane chemical polarity of *Phytophthora infestans* germlings. (a, b) Fluorescence lifetime mesh size map of germlings growing in water 1h post application, and treated with 1 μmol L^{-1} latrunculin B for 1h. (c, d) Intensity ratio chemical polarity map of germlings growing in water 1h post application, and treated with 1 μmol L^{-1} latrunculin B for 1h. Scale bars = 10 μm.

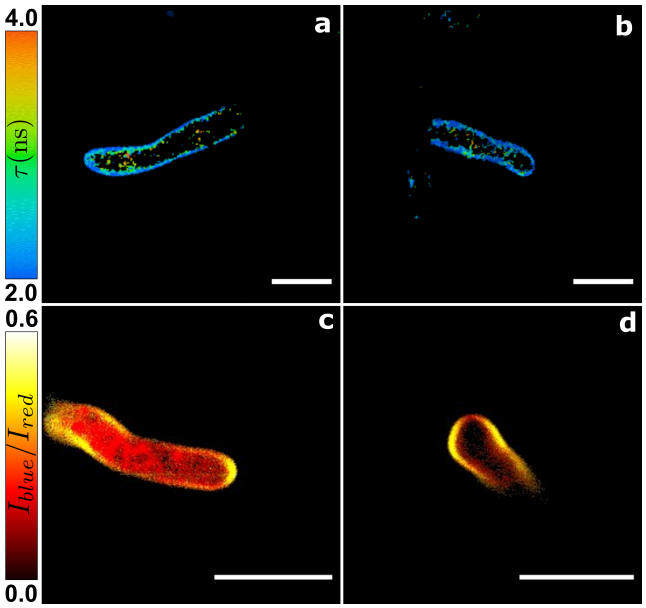

Figure 5.20: Mapping of spatial variations induced by treatment with 0.1 μmol L^{-1} oryzalin in the cell wall mesh size and plasma membrane chemical polarity of *Phytophthora infestans* germlings. (a, b) Fluorescence lifetime mesh size map of germlings growing in water 1h post application, and treated with 0.1 μmol L^{-1} oryzalin for 1h. (c, d) Intensity ratio chemical polarity map of germlings growing in water 1h post application, and treated with 0.1 μmol L^{-1} oryzalin for 1h. Scale bars = 10 μm.

References

[1] A. J. Haverkort, P. C. Struik, R. G. F. Visser, and E. Jacobsen. Applied biotechnology to combat late blight in potato caused by phytophthora infestans. *Potato Res.*, 52:249–264, 2009.

[2] Sophien Kamoun, Oliver Furzer, Jonathan D G Jones, Howard S. Judelson, Gul Shad Ali, Ronaldo J. D. Dalio, Sanjoy Guha Roy, Leonardo Schena, Antonios Zambounis, Franck Panabières, David Cahill, Michelina Ruocco, Andreia Figueiredo, Xiao-Ren Chen, Jon Hulvey, Remco Stam, Kurt Lamour, Mark Gijzen, Brett M. Tyler, Niklaus J. Grünwald, M. Shahid Mukhtar, Daniel F. A. Tomé, Mahmut Tör, Guido van den Ackerveken, John McDowell, Fouad Daayf, William E. Fry, Hannele Lindqvist-Kreuze, Harold J. G. Meijer, Benjamin Petre, Jean Ristaino, Kentaro Yoshida, Paul R. J. Birch, and Francine Govers. The top 10 oomycete pathogens in molecular plant pathology. *Mol. Plant Pathol.*, 16(4):413–434, 2015.

[3] Brian J. Haas, Sophien Kamoun, Michael C. Zody, Rays H. Y. Jiang, and Robert E. Handsaker. Genome sequence analysis of the irish potato famine pathogen p infestans. *Nature*, 461:393–398, 2009.

[4] Howard S. Judelson, Audrey M. V. Ah-Fong, George Aux, Anna O. Avrova, Catherine Bruce, Cahid Cakir, Luis da Cunha, Laura Grenville-Briggs, Maita Latijnhouwers, Wilco Ligterink, Harold J. G. Meijer, Samuel Roberts, Carrie S. Thurber, Stephen C. Whisson, Paul R. J. Birch, Francine Govers, Sophien Kamoun, Pieter van West, and John Windass. Gene expression profiling during asexual development of the late blight pathogen phytophthora infestans reveals a highly dynamic transcriptome. *Mol. Plant. Microbe Interact.*, 21(4):433–447, 2008.

[5] Svante Resjö, Maja Brus, Ashfaq Ali, Harold J G Meijer, Marianne Sandin, Francine Govers, Fredrik Levander, Laura Grenville-Briggs, and Erik Andreasson. Proteomic analysis of p infestans reveals the importance of cell wall proteins in pathogenicity. *Mol. Cell. Proteomics*, 16(11):1958–1971, 2017.

[6] Yan Wang and Yuanchao Wang. Phytophthora sojae effectors orchestrate warfare with host immunity. *Current Opinion in Microbiology*, 46:7–13, 2018.

[7] Jamie McGowan and David A. Fitzpatrick. Recent advances in oomycete genomics. *Advances in Genetics*, 105:175–228, 2020.

[8] Vivianne G. A. A. Vleeshouwers, Sylvain Raffaele, Jack H. Vossen, Nicolas Champouret, Ricardo Oliva, Maria E. Segretin, Hendrik Rietman, Liliana M. Cano, Anoma Lokossou, Geert Kessel, Mathieu A. Pel, and Sophien Kamoun. Understanding and exploiting late blight resistance in the age of effectors. *Annu. Rev. Phytopathol.*, 49:507–531, 2011.

[9] Kaile Sun, Anne-Marie A. Wolters, Jack H. Vossen, Maarten E. Rouwet, Annelies E. H. M. Loonen, Evert Jacobsen, Richard G. F. Visser, and Yuling Bai. Silencing of six susceptibility genes results in potato late blight resistance. *Transgenic Res.*, 25(5):731–742, 2016.

[10] Kamil Witek, Florian Jupe, Agnieszka I. Witek, David Baker, Matthew D. Clark, and Jonathan D. G. Jones. Accelerated cloning of a potato late blight-resistance gene using renseq and smrt sequencing. *Nat. Biotechnology*, 34(6):656–660, 2016.

[11] Yu Du, Mohamed H. Mpina, Paul R. J. Birch, Klaas Bouwmeester, and Francine Govers. P infestans rxlr effector avr1 interacts with exocyst component sec5 to manipulate plant immunity. *Plant Physiol.*, 169(3):1975–90, 2015.

[12] Petra C. Boevink, Paul R. J. Birch, Dionne Turnbull, and Stephen C. Whisson. Devastating intimacy: the cell biology of plant–phytophthora interactions. *New Phytologist*, 228(2):445–458, 2020.

[13] Benjamin Petre, Mauricio P. Contreras, Tolga O. Bozkurt, Martin H. Schattat, Jan Sklenar, Sebastian Schornack, Ahmed Abd-El-Haliem, Roger Castells-Graells, Rosa Lozano-Durán, Yasin F. Dagdas, Frank L. H. Menke, Alexandra M. E. Jones, Jack H. Vossen, Silke Robatzek, Sophien Kamoun, and Joe Win. Host-interactor screens of phytophthora infestans rxlr proteins reveal vesicle trafficking as a major effector-targeted process. *Plant Cell.*, 33(5):1447–1471, 2021.

[14] Jochem Bronkhorst, Michiel Kasteel, Stijn van Veen, Jess M. Clough, Kiki Kots, Jesse Buijs, Jasper van der Gucht, Tijs Ketelaar, Francine Govers, and Joris Sprakel. A slicing mechanism facilitates host entry by plant pathogenic phytophthora. *Nature Microbiology*, 2021.

[15] Lucile Michels, Vera Gorelova, Yosapol Harnvanichvech, Jan Willem Borst, Bauke Albada, Dolf Weijers, and Joris Sprakel. Complete microviscosity maps of living plant cells and tissues with a toolbox of targeting mechanoprobes. *Proc. Natl. Acad. Sci.*, 117(30):18110–18118, 2020.

[16] Niklaus J. Grünwald, Anne K. Sturbaum, Gaspar Romero Montes, Edith Garay Serrano, Hector Lozoya-Saldaña, and William E. Fry. Selection for fungicide resistance within a growing season in field populations of phytophthora infestans at the center of origin. *Phytopathology*, 96(12):1397–1403, 2007.

[17] Wen-qiao Wang, Peng Zhang, Run-jie Meng, Jian-jiang Zhao, Qi-liang Huang, Xiu-ying Han, Zhi-qiang Ma, and Xiao-feng Zhang. Fungitoxicity and synergism of mixtures of fluopicolide and pyraclostrobin against phytophthora infestans. *Crop Protection*, 57:48–56, 2014.

[18] Oleksandr A. Kucherak, Sule Oncul, Zeinab Darwich, Dmytro A. Yushchenko, Youri Arntz, Pascal Didier, Yves Mély, and Andrey S. Klymchenko. Switchable nile red-based probe for cholesterol and lipid order at the outer leaflet of biomembranes. *J. Am. Chem. Soc.*, 132(13):4907–4916, 2010.

[19] C. E. Caten and J. L. Jinks. Spontaneous variability of single isolates of phytophthora infestans. *Canadian Journal of Botany*, 46(4):329–347, 1968.

[20] Theo van der Lee, Ijfke De Witte, André Drenth, Carlos Alfonso, and Francine Govers. Aflp linkage map of the oomycete phytophthora infestans. *Fungal Genetics and Biology*, 21(3):278–291, 1997.

[21] J N M Boots, R Fokkink, J van der Gucht, and T E Kodger. Development of a multi-position indentation setup: Mapping soft and patternable heterogeneously crosslinked polymer networks. *Rev. Sci. Instrum.*, 90(1):015108, 2019.

[22] Li-Heng Cai, Thomas E. Kodger, Rodrigo E. Guerra, Adrian F. Pegoraro, Michael Rubinstein, and David A. Weitz. Soft poly(dimethylsiloxane) elastomers from architecture-driven entanglement free design. *Adv. Mater.*, 27:5132–5140, 2015.

[23] Kim S Horger, Daniel J Estes, Ricardo Capone, and Michael Mayer. Films of agarose enable rapid formation of giant liposomes in solutions of physiologic ionic strength. *J. Am. Chem. Soc.*, 131(5):1810–1819, 2009.

[24] Rafael B. Lira, Jan Steinkühler, Roland L. Knorr, Rumiana Dimova, and Karin A. Riske. Posing for a picture: vesicle immobilization in agarose gel. *Scientific Reports*, 6(25254), 2016.

[25] N P Money. Osmotic pressure of aqueous polyethylene glycols : Relationship between molecular weight and vapor pressure deficit. *Plant Physiol.*, 91(2):766–769, 1989.

[26] R. J. Howard, M. A. Ferrari, D. H. Roach, and N. P. Money. Penetration of hard substrates by a fungus employing enormous turgor pressures. *Proc. Natl. Acad. Sci.*, 88(24):11281–11284, 1991.

[27] A J MacDougall, G M Brett, V J Morris, N M Rigby, M J Ridout, and S G Ring. The effect of peptide-pectin interactions on the gelation behaviour of a plant cell wall pectin. *Carbohydr. Res.*, 335:115–126, 2001.

[28] Harold J. G. Meijer, Peter J. I. van de Vondervoort, Qing Yuan Yin, Chris G. de Koster, Frans M. Klis, Francine Govers, and Piet W. J. de Groot. Identification of cell wall-associated proteins from phytophthora ramorum. *Molecular Plant-Microbe Interactions*, 19(12):1348–1358, 2006.

[29] Jennifer Mach. Cellulose synthesis in phytophthora infestans pathogenesis, chemistry of hyphal walls of phytophthora. *The Plant Cell*, 20(3):500, 2008.

[30] B. R. Grant, W. Greenaway, and F. R. Whatley. Metabolic changes during development of phytophthora palmivora examined by gas chromatography/mass spectrometry. *Journal of General Microbiology*, 134:1901–1911, 1988.

[31] Alon Savidor, Ryan S. Donahoo, Oscar Hurtado-Gonzales, Miriam L. Land, Manesh B. Shah, Kurt H. Lamour, and W. Hayes McDonald. Cross-species global proteomics reveals conserved and unique processes in phytophthora sojae and phytophthora ramorum. *Molecular Cellular Proteomics*, 7(8):1501–1516, 2008.

[32] Zhili Pang, Vaibhav Srivastava, Xili Liu, and Vincent Bulone. Quantitative proteomics links metabolic pathways to specific developmental stages of the plant-pathogenic oomycete phytophthora capsici. *Molecular Plant Pathology*, 18(3):378–390, 2017.

[33] Sander Y. A. Rodenburg, Michael F. Seidl, Dick de Ridder, and Francine Govers. Genome-wide characterization of phytophthora infestansmetabolism: a systems biology approach. *Molecular Plant Pathology*, 19(6):1403–1413, 2018.

[34] Fungicide Resistance Action Committee, 2021.

[35] Valérie Toquin, Franççois Barja, Catherine Sirven, and Roland Bffa. Fluopicolide, a new anti-oomycetes fungicide with a new mode of action inducing perturbation of a spectrin-like protein. *Modern Crop Protection Compounds*, pages 675–682, 2007.

[36] Valérie Toquin, François Barja, Catherine Sirven, Stéphanie Gamet, Lucile Mauprivez, Philippe Peret, Marie-Pascale Latorse, Jean-Luc Zundel, Frédéric Schmitt, Marc-Henri Lebrun, and Roland Beffa. Novel tools to identify the mode of action of fungicides as exemplified with fluopicolide. *Recent Developments in Management of Plant Diseases*, pages 19–36, 2009.

[37] E. Marsilii, S. O. Cacciola, A. Salamone, G. Scarito, F. Raudino, A. Pane, and G. M. di San Lio. Efficacy of valifenalate against phytophthora spp. of ornamental plants. *Protezione delle Colture*, 2:108–109, 2009.

[38] A. Salamone, F. Raudino, S. O. Cacciola, and G. M. di San Lio. Efficacy of the fungicide valifenalate against crown rot of rose caused by phytophthora citrophthora. *Modern fungicides and*

antifungal compounds VII. Proceedings of the 17th International Reinhardsbrunn Symposium., pages 55–60, 2013.

[39] I. Brent Heath and Susan G. W. Kaminskyj. The organization of tip-growth-related organelles and microtubules revealed by quantitative analysis of freeze-substituted oomycete hyphae. *J. Cell Sci.*, 93(1):41–52, 1989.

[40] Eugen Temperli, Urs-Peter Roos, and Hans R. Hohl. Germ tube growth and the microtubule cytoskeleton in p infestans: Effects of antagonists of hyphal growth, microtubule inhibitors, and ionophores. *Mycological Research*, 95(5):611–617, 1991.

[41] G J Hyde and A R Hardham. Microtubules regulate the generation of polarity in zoospores of phytophthora cinnamomi. *Eur. J. Cell. Biol.*, 62(1):75–85, 1993.

[42] A. Geitmann and A. M. Emons. The cytoskeleton in plant and fungal cell tip growth. *J. Microsc.*, 198:218–245, 2000.

[43] M. Blum, M. Boehler, E. Randall, V. Young, M. Csukai, S. Kraus, F. Moulin, G. Scalliet, and A. O. Avrola. Mandipropamid targets the cellulose synthase-like picesa3 to inhibit cell wall biosynthesis in the oomycete plant pathogen, phytophthora infestans. *Mol. Plant Pathol.*, 11(2):227–243, 2010.

[44] Tijs Ketelaar, Harold J G Meijer, Marjolein Spiekerman, Rob Weide, and Francine Govers. Effects of latrunculin b on the actin cytoskeleton and hyphal growth in phytophthora infestans. *Fungal Genet. Biol.*, 49(12):1014–1022, 2012.

[45] L. C. Morejohn, T. E. Bureau, J. Molè-Bajer, A. S. Bajer, and D. E. Fosket. Oryzalin, a dinitroaniline herbicide, binds to plant tubulin and inhibits microtubule polymerization in vitro. *Planta*, 172:252–264, 1987.

[46] V. Dostál and L. Libusová. Microtubule drugs: action, selectivity, and resistance across the kingdoms of life. *Protoplasma*, 251(5):991–1005, 2014.

[47] H.J.G. Meijer, C. Hua, K. Kots, T. Ketelaar, and F. Govers. Actin dynamics in p infestans; rapidly reorganizing cables and immobile long-lived plaques. *Cellular Microbiology*, 16(6):948 – 961, 2014.

[48] Kiki Kots, Harold J. G. Meijer, Klaas Bouwmeester, Francine Govers, and Tijs Ketelaar. Filamentous actin accumulates during plant cell penetration and cell wall plug formation in phytophthora infestans. *Cell. Mol. Life Sci.*, 74(5):909–920, 2017.

[49] C. Kock, Y. F. Dufrêne, and J.J. Heinisch. Up against the wall: is yeast cell wall integrity ensured by mechanosensing in plasma membrane microdomains? *Appl. Environ. Microbiol.*, 81(3), 2015.

[50] Tarek Elhasi and Anders Blomberg. Integrins in disguise - mechanosensors in saccharomyces cerevisiae as functional integrin analogues. *Microb. Cell.*, 6(8):335–355, 2019.

[51] Ramakanth Neeli-Venkata, Ruben Celador, Yolanda Sanchez, and Nicolas Minc. Detection of surface forces by cell wall mechanosensor. *BioRxiv*, 2020.

[52] Naomi Nakayama, Richard S Smith, Therese Mandel, Sarah Robinson, Seisuke Kimura, Arezki Boudaoud, and Cris Kuhlemeier. Mechanical regulation of auxin-mediated growth. *Curr. Biol.*, 22(16):1468–1476, 2012.

[53] Olivier Hamant and Elizabeth S. Haswell. Life behind the wall: sensing mechanical cues in

plants. *BMC Biology volume*, 15(59), 2017.

[54] Laura J Grenville-Briggs, Victoria L Anderson, Johanna Fugelstad, Anna O Avrova, Jamel Bouzenzana, Alison Williams, Stephan Wawra, Stephen C Whisson, Paul R J Birch, Vincent Bulone, and Pieter van West. Cellulose synthesis in phytophthora infestans is required for normal appressorium formation and successful infection of potato. *The Plant Cell*, 20(3):720–738, 2008.

[55] Rabah Zerzoura, Jens Kroeger, and Anja Geitmann. Polar growth in pollen tubes is associated with spatially confined dynamic changes in cell mechanical properties. *Developmental Biology*, 334(2):437–446, 2009.

[56] A. Garrill, R. R. Lew, and I. B. Heath. Stretch-activated ca2+ and ca2+-activated k+ channels in the hyphal tip plasma membrane of the oomycete saprolegnia ferax. *J. Cell. Sci.*, 101(3):721–730, 1992.

[57] A Garrill, S L Jackson, R R Lew, and I B Heath. Ion channel activity and tip growth: tip-localized stretch-activated channels generate an essential ca2+ gradient in the oomycete saprolegnia ferax. *Eur. J. Cell. Biol.*, 60(2):358–365, 1993.

[58] Stephan Wawra, Rodrigo Belmonte, Lars Löbach, Marcia Saraiva, Ariane Willems, and Pieter van West. Secretion, delivery and function of oomycete effector proteins. *Current Opinion in Microbiology*, 15(6):685–691, 2012.

[59] Ulrich Gisi and Helge Sierotzki. *Oomycete Fungicides: Phenylamides, Quinone Outside Inhibitors, and Carboxylic Acid Amides.* Fungicide Resistance in Plant Pathogens. Springer, Tokyo, 2015.

[60] Charles T. Anderson, Ian S. Wallace, and Chris R. Somerville. Metabolic click-labeling with a fucose analog reveals pectin delivery, architecture, and dynamics in arabidopsis cell walls. *Proc. Nat. Ac. Sci.*, 109(4):1329–1334, 2012.

[61] Marie Dumont, Arnaud Lehner, Boris Vauzeilles, Julien Malassis, Alan Marchant, Kevin Smyth, Bruno Linclau, Aurélie Baron, Jordi Mas Pons, Charles T. Anderson, Damien Schapman, Ludovic Galas, Jean-Claude Mollet, and Patrice Lerouge. Plant cell wall imaging by metabolic click-mediated labellingof rhamnogalacturonan ii using azido 3-deoxy-d-manno-oct-2-ulosonic acid. *The Plant Journal*, 85:437–447, 2016.

[62] Yuntao Zhu, Jie Wu, and Xing Chen. Metabolic labeling and imaging of n-linked glycans in arabidopsis thaliana. *Angew. Chem. Int. Ed.*, 55(32), 2016.

[63] Xiaoli Sun, Aihua Zhang, Brenda Baker, Luo Sun, Angela Howard, John Buswell, Damien Maurel, Anastasiya Masharina, Kai Johnsson, Christopher J. Noren, Ming-Qun Xu, and Ivan R. Corrêa Jr. Development of snap-tag fluorogenic probes for wash-free fluorescence imaging. *ChemBioChem*, 12(14):2217–2226, 2011.

[64] Peter J. Bosch, Ivan R. Corrêa Jr., Michael H. Sonntag, Jenny Ibach, Luc Brunsveld, Johannes S. Kanger, and Vinod Subramaniam. Evaluation of fluorophores to label snap-tag fused proteins for multicolor single-molecule tracking microscopy in live cells. *Biophysical Journal*, 107(4):803–814, 2014.

Chapter 6

General Discussion

In this thesis, we have presented a toolbox of fluorescent molecular reporters that can be used to obtain spatial information about a property of interest (e.g. microviscosity, wall porosity, chemical polarity) in living cells. In particular, the mechano-sensitive probes, which report on the local microviscosity, give access to features previously impossible to determine inside multicellular tissues and with sub-cellular resolution. Since the notion of a microviscosity is not well-defined in literature, we worked on establishing more accurately what these probes measure in different cases, and on providing a more objective view on the advantages and disadvantages of using them. While we primarily developed these tools for plant cells, they has proven to be applicable to a wider range of cell types, including plant pathogens, such as fungal cells (e.g. *Magnaporthe*), oomycetes (e.g. *Phytophtora*), and yeasts (e.g. *Schizosaccharomyces*).

The molecular rotors were particularly useful to highlight spatio-temporal fluctuations in the mechanical and structural properties of the membrane and wall of cells during fundamental cellular processes (such as elongation and aging of *Arabidopsis thaliana* root hairs, host invasion by *Phytophthora infestans* or turgor generation in *Magnaporthe oryzae*). Yet, without a proper calibration, the microviscosity assessment using Fluorescence Lifetime Imaging Microscopy (FLIM) imaging has remained semi-quantitative. A calibration in a model system, representative of the system of interest in terms of chemical polarity and nature of probe confinement, is still needed. Such a calibration would allow for an absolute quantification of the imaging signal and thereby allow for accurate comparisons between different systems and cell types. In addition, the imaging of microviscosity patterns using the rotor toolbox relies on advanced imaging equipment, such

as FLIM, and without access to a costly and not widely accessible fast-FLIM instrumentation, suffers from poor temporal resolution, making it challenging to probe fast cellular processes. To make our toolbox more widely accessible and improve on its temporal resolution, a ratiometric probe that can be detected using simple fluorescence imaging tools would present an important step forward.

While the work on molecular reporters described in this thesis has allowed a significant step forward, many more steps are needed for these types of probes to be used to their full potential. In that regard, the project described in this thesis has opened a plethora of challenges for future research. In this last Chapter, we discuss the outcomes of this project in the light of these unresolved challenges, e.g. probe calibration, developing a ratiometric equivalent to the lifetime-based probes, implementing the toolbox in other biological systems, and we suggest approaches, on the basis of preliminary results, to resolve these challenges in future research.

5.6 Calibration of the plasma membrane-targeting molecular rotor

When incorporated in the plasma membrane, molecular rotors sense local differences in the lipid packing. When the membrane packing density is high, the free volume available for the rotation to occur is limited, and relaxation of the molecule to the ground state by photon emission is energetically favored. On the other hand, when the membrane dilates and the spacing between lipid tails increases, rotation becomes less hindered, resulting in an increase in the proportion of excited state relaxation by rotation and a non-radiative decay. As a result, membrane-bound rotors sense differences in membrane phase (e.g. gel vs liquid), which are linked to changes in lipid composition (e.g. saturated vs unsaturated lipids, lipids closer or further from their phase transition), but also changes in membrane tension. The membrane rotor thus offers the possibility to map variations in the lipid packing density, and for a given lipid composition, spatio-temporal variations in tension during cellular processes. For this reason the membrane rotor raised an appreciable interest in the biology community, and along with it, the ambition to quantify tension and compression forces from

the fluorescence lifetime readout.

Since many of the cells we aimed to study, including plant, fungal and oomycete cells, are surrounded by a stiff cell wall, it is not easy to perform a calibration of the membrane probe in-situ. As a consequence, we have searched for a model system in which we can apply and measure accurately a tension along the membrane, while simultaneously recording the lifetime response of the rotor. In this context, synthetic lipid bilayers are often used as biological membrane mimicks. In particular, giant and large unilamellar vesicles have been used as elementary building blocks for artificial cells[1, 2, 3, 4, 5, 6]. Giant unilamellar vesicles (GUV) have sizes comparable to cell dimensions and allow for microscopy observation. Therefore, spatial variations in fluorescence lifetime within the membrane can be assessed. However, they do not allow to gather a lot of statistics, as each vesicle needs to be imaged individually. On the contrary, performing spectroscopy on large unilamellar vesicles (LUV) in suspension can provide more statistics, but the outcome of the measurement is averaged over an ensemble of vesicles, without providing information about inter- and intravesicle heterogeneity. We decided to try both approaches in parallel, as complementary methods to calibrate the N+-BDP probe.

5.6.1 Implementation in LUV

LUV made of 1,2-dioleoyl-sn-glycero-3-phosphocholine (DOPC) were formed by lipid film hydration in 1 Osm PBS buffer supplemented with sucrose, followed by extrusion through a 100 nm pore filter. This method resulted in the formation of 273 ± 4 nm diameter vesicles, as measured by Dynamic Light Scattering (DLS). To subject these vesicles to a well-defined tension, we used osmotic shock, by varying the osmolarity of the suspending medium[7]. The vesicles were suspended in buffer with an osmolarity varying between 1 Osm and 300 mOsm, by changing the concentration of dissolved sucrose. For each osmotic differential between vesicle interior (1 Osm) and medium (1 Osm-300 mOsm), fluorescence lifetime measurements were performed, and transient fluorescence intensity decays fitted to determine an average fluorescence lifetime. Surprisingly, we find that for all osmotic pressure differences the curves superpose almost perfectly (Figure 5.21). For all osmotic stresses, a lifetime of 5.4 ns (χ^2 = 1.088) was meas-

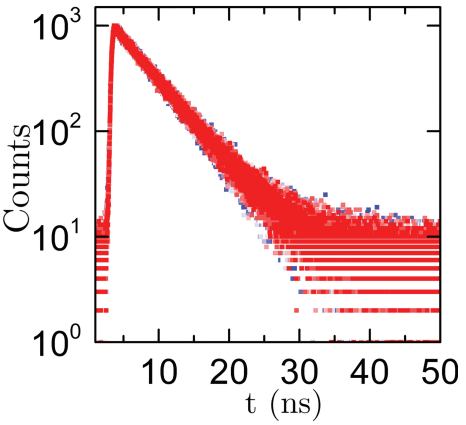

Figure 5.21: Fluorescence decays of N+-BDP in DOPC LUV upon application of an osmotic differential δ_{osm} between the inside and the outside of the vesicle (δ_{osm} = osm_{in}-osm_{out}). δ_{osm} varies from 0 (red) to 700 mOsm (blue).

ured. This indicates that any osmotically-induced change in lipid spacing was too small to be detected by the probe, either due to a lack of sensitivity in the probe itself, or due to either vesicle leaking or lipid exchange that lead to tension relaxation.

5.6.2 Implementation in GUV

A wide diversity of techniques has been employed to form giant lipid vesicles. Popular formation techniques include dehydration-rehydration methods[8, 9], microfluidics-based methods[2, 10, 11], electroformation[12, 13, 14] or gel-assisted lipid swelling[15, 16]. These techniques all have distinct advantages and limitations. The lipid film rehydration and the gel-assisted lipid swelling methods are gentle and compatible with a wide range of lipids, but both lead to heterogeneous vesicle populations, with a low degree of unilamellarity. On the contrary, electroformation enables modulation of the lipid hydration process to form relatively monodisperse vesicles, with narrow lipid composition. Yet, charged lipids compromise vesicle formation, and vesicles are not unilamellar per se. Microfluidics-based methods are the most suitable to keep inter-vesicle repeatability, as they

provide an excellent control over the size, composition and (uni)lamellarity of the vesicles. Nevertheless, this technique remains a lot more technically challenging to set up[17, 18]. On the basis of these considerations we decided to formulate giant vesicles using the electroformation technique[12, 13].

We prepared giant unilamellar vesicles of DOPC: 1,2-dioleoyl-sn-glycero-3-phosphoethanolamine (DOPE): 1,2-dioleoyl-sn-glycero-3-phospho-L-serine (DOPS): Cholesterol: N+-BDP = 55:22:11:11:1 or DOPC: 1,2-dioleoyl-sn-glycero-3-phospho-(1'-rac-glycerol) (DOPG): DOPE-cap-biotin: N+-BDP = 48,5:48,5:2:1. The first lipid composition is often used in literature as a mimic of the natural inner leaflet composition of lipid headgroups in mammalian cells, and was employed to follow the protocol described in reference[19] to apply a tension on GUV membrane. The second lipid composition was used in a view of future work on membrane interactions with antimicrobial peptides[20, 21]. The vesicles were formed in a sucrose solution and diluted in a glucose-supplemented buffer, before being immobilized on an avidin-coated glass slide through binding of the biotin-capped lipids. The density difference between the sucrose and the glucose solutions leads the vesicles to sink to the bottom of the imaging chamber, and allows for vesicle immobilization and subsequent imaging. Once a vesicle is immobilized, a tension can be applied and the probe response subsequently measured using FLIM imaging. Two options to apply a tension exist, either by using an osmotic shock[22], or by changing the adhesive interactions between vesicle and substrate, which in turn induces a lateral dilatation[23]. From the three-dimensional shape of the adhered vesicle on the substrate, the tensile force can be calculated using purely geometrical considerations[23].

We first tried to tune the degree of adhesion of the DOPC: DOPE: DOPS: Cholesterol: N+-BDP GUV on the substrate by adding various concentrations of a divalent cation (Mg^{2+}) in the medium. As reported in the literature, magnesium ions can act as bridges between the negatively charged phospholipids within the GUV and the negatively charged surface of the passivated glass and promote adhesion[19]. Figure 5.22 compares GUV profiles, and the corresponding fluorescence lifetime images and distributions, for GUV having different adhesion areas. In the first comparison set (Fig. 5.22a-c) the lifetime distribution for a bigger adhesion area is shifted towards a lower average lifetime, but in the second

set (Fig. 5.22a,d,e) the distributions superpose almost perfectly. These data reveal that the compositional heterogeneity, and number of lamella, between different GUVs is too large to make any valid conclusions about membrane tension and the corresponding response of the probe.

Therefore we decided to work in parallel on a simpler lipid composition (DOPC: DOPG: DOPE-cap-biotin: N+-BDP = 48,5:48,5:2:1). Since this composition lacks the cation-chelating DOPS lipids, we used a different approach to tune adhesion strength that is more suitable for the DOPC and DOPG phospholipids. We varied the avidin coating density of the glass surface; in one case the substrate was coated with 1 μM avidin, and the remaining bare glass passivated with Bovine Serum Albumin (BSA), while in a second case, the glass was only passivated with BSA. The profile of the vesicles and the fluorescence lifetime of the probe was simultaneously imaged in both cases. Figure 5.23 and 5.24 show the lifetime distribution histograms obtained for DOPC: DOPG: DOPE: N+-BDP = 48,5:48,5:2:1 and for DOPC: DOPE: DOPS: Cholesterol: N+-BDP = 55:22:11:11:1 respectively. This time, for the DOPC: DOPG composition, the average lifetime in the membrane was very slightly lowered upon membrane stretching (Fig. 5.23d,e). With such a small shift, and given the noticeable increase in adhesion area needed to trigger this shift, it appears that the probe either lacks sensitivity to membrane tension in this geometry, or that tension is relaxed by lipid exchanges with a reservoir in its surroundings. Moreover, since electroformation is known to lead to some degree of compositional heterogeneity, it is challenging to unambiguously interpret the observed shift in fluorescence lifetime. For the DOPC: DOPE: DOPS: cholesterol composition, changing the GUV adhesion area did not result in measurable changes in rotor response (Fig. 5.24c). For both compositions, no significant spatial variations throughout the vesicles were observed, even considering the difference between the lateral tension (membrane under tension) and the apical tension (membrane under compression) linked to the density difference between the intra- and extravesicular medium.

In an attempt to increase the adhesion area to promote change in probe response in the membrane of the DOPC: DOPG: DOPE-cap-biotin: N+-BDP = 48,5:48,5:2:1 GUV, we increased the density difference between the GUV inner

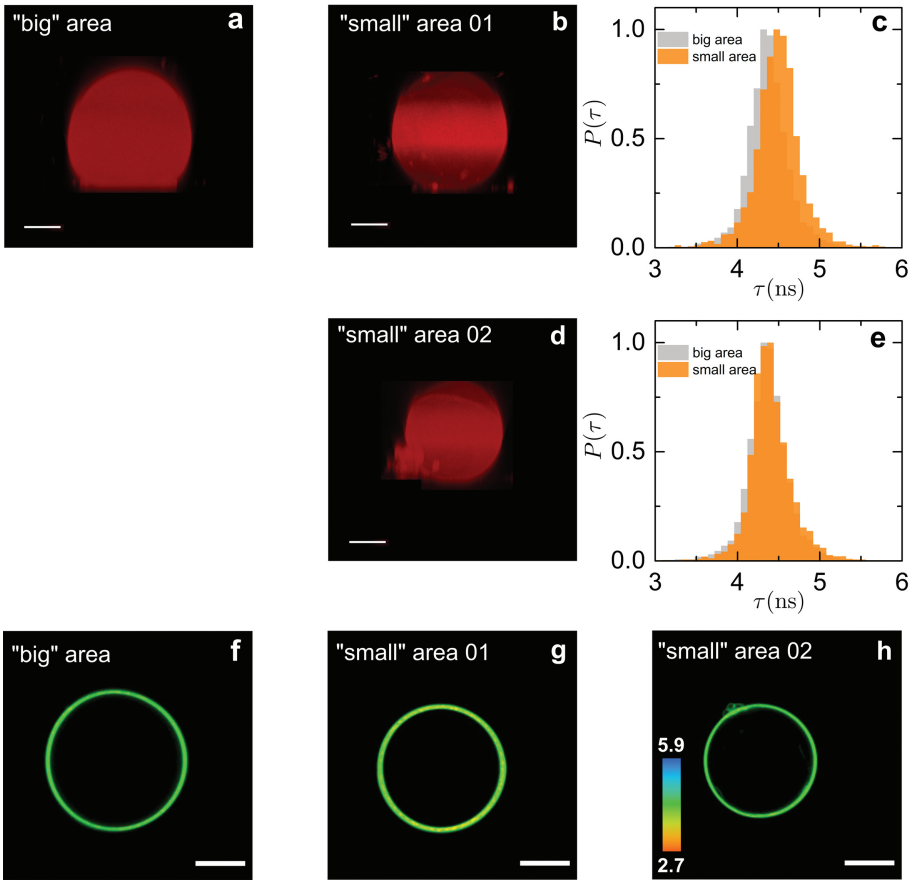

Figure 5.22: Profiles of DOPC:DOPE:DOPS:Cholesterol:N+-BDP = 55:22:11:11:1 GUV submitted to different concentrations of Mg^{2+} in the suspending medium: 5 mM (a) and 1 mM (b,d). Fluorescence lifetime distributions (c,e) and images (f-h) associated to the three GUV profiles. Scale bars = 20 μm.

solution and the outer suspending solution by varying the concentration of glucose in the surrounding medium. By doing so, an osmotic imbalance was simultaneously applied, as the glucose concentration was lowered with all other concentrations kept fixed. This change in density combined to the effect of vesicle dilatation triggers a change in adhesion area on the substrate, and a significant change in membrane shape and tension. Still, no variations in fluorescence life-

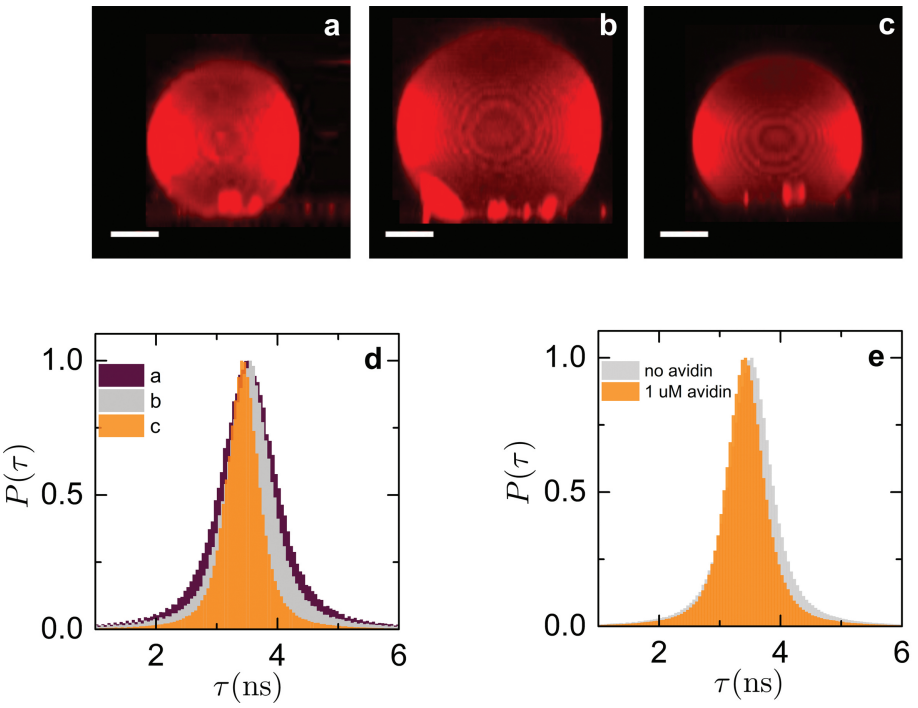

Figure 5.23: Profiles of DOPC:DOPG:DOPE-cap-biotin:N+-BDP=48,5:48,5:2:1 GUV adhered to a glass substrate passivated with 100 μM BSA (a,b). Profile of a GUV from the same formation batch, adhered to a glass substrate coated with 1 μM avidin and subsequently passivated with 100 μM BSA (c). Scale bars = 10 μm. Corresponding individual fluorescence lifetime distributions (d). Averaged fluorescence lifetime distributions, obtained by summing individual distributions for 6 vesicles per condition (e).

time were observed (Fig. 5.25).

This total absence of lifetime response could confirm the rotor's sensitivity range incompatibility in the experiment configuration, but could also be due to lipid rearrangements occurring within the membrane, combined with lipid exchanges going on between the membrane and smaller lipid structures floating around. These exchanges would prevent a significant change in lipid spacing, and consequently, changes in fluorescence lifetime.

A rigorous evaluation of these findings requires future experimental efforts in which lipid exchange, and tension relaxation, is limited. This would require –

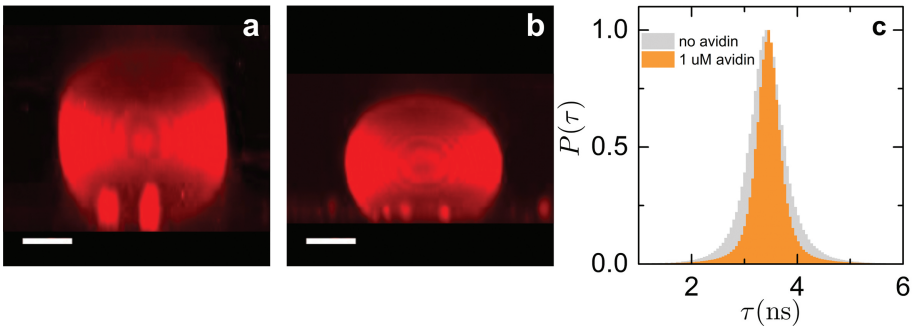

Figure 5.24: Profile of a DOPC:DOPE:DOPS:Cholesterol:N+-BDP = 55:22:11:11:1 GUV adhered to a glass substrate passivated with 100 μM BSA (a). Profile of a GUV from the same formation batch, adhered to a glass substrate coated with 1 μM avidin and subsequently passivated with 100 μM BSA (b). Scale bars = 5 μm. Corresponding individual fluorescence lifetime distributions (c).

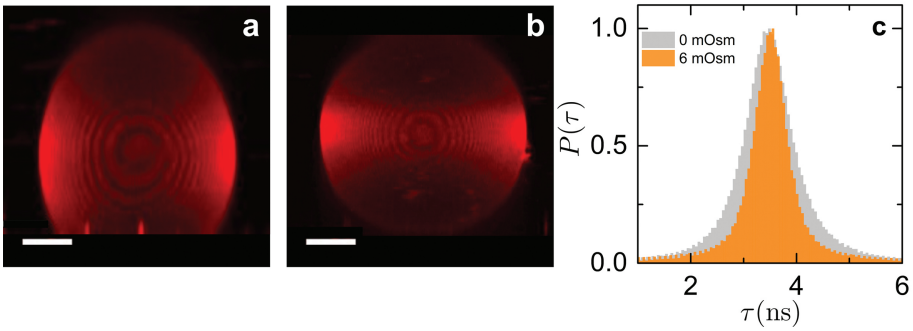

Figure 5.25: Profiles of DOPC:DOPG:DOPE:N+-BDP=48,5:48,5:2:1 GUV submitted to different osmolarity and density differentials by varying the concentration of glucose in the suspending medium; δ_{osm} = 6 mOsm (a), δ_{osm} = 0 mOsm (b). Corresponding fluorescence lifetime distributions (c). Scale bars = 10 μm.

without having to make purely unilamellar vesicles and removing lipid clusters in suspension (e.g. by using microfluidics as GUV formation method) – inducing smaller variations in membrane tension, by applying small osmotic gradients, and without inducing strong changes in vesicle shape and adhesion area. To do so, an option would be to keep mainly sucrose inside and outside the vesicles, but

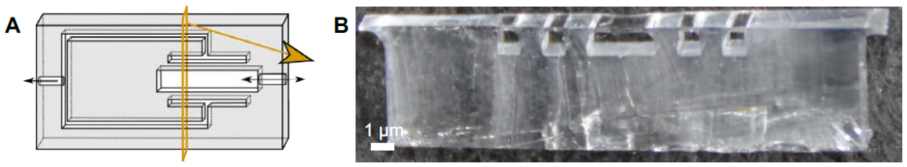

Figure 5.26: Schematic and cross-sectional view of the PDMS stretching device, reprinted from reference [19].

supplement the suspending medium with a constant, small amount of glucose - high enough to allow for fast vesicle decantation and easy glass immobilization, but low enough to prevent vesicle flattening on the surface -, and vary the sucrose concentration outside. The changes in vesicle adhesion and shape would then be smaller and would not induce gradients of tension inside the vesicles' membrane (i.e. by vesicle squeezing under its own weight). Nevertheless, the best option to be able to incriminate or discriminate the effect on fluorescence lifetime of membrane tension, lipid composition, and lipid exchanges, remains the use of more sophisticated microfluidics experiments to both formulate and manipulate the GUV.

5.6.3 Implementation in supported lipid bilayers

To reduce lipid rearrangements and exchanges, but also to have a better overview of the membrane and to assess higher degrees of membrane stretching, we also explored working on two dimensional membranes through the use of solid supported lipid bilayers. As a solid and stretchable substrate, we used a flexible PDMS film adapted in a device developed by Kliesch et al.[19]. A schematic of the device is shown on Figure 5.26. The stretchable polydimethylsiloxane (PDMS) sheet has a thickness of about 180 μm, and is attached to two adjacent channels. The air pressure in those two channels can be reduced by syringe aspiration, leading to film extension, and a simultaneous dilatation of the attached lipid bilayers. Lipid bilayer dilatation using this method has proven to enhance substantially LUV fusion efficiency, due to an increased lipid spacing[19]. We wanted to see whether this increase in lipid spacing was reflected by a lowering in fluorescence lifetime.

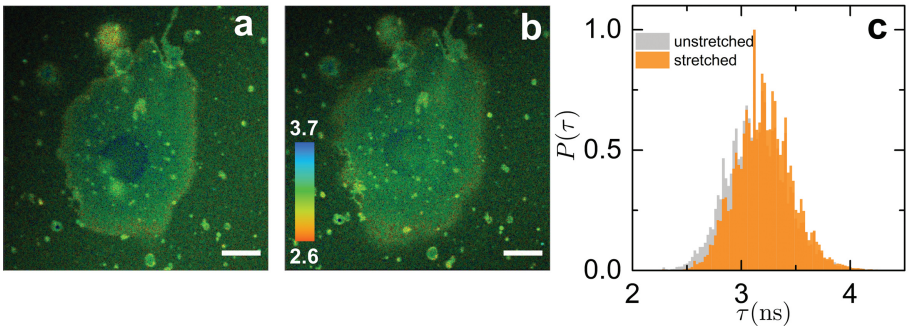

Figure 5.27: Fluorescence Lifetime images in an unstretched (a) vs stretched (b) DOPC:DOPG:DOPE:N+-BDP=48,5:48,5:2:1 lipid bilayer. Scale bars = 20 μm. Corresponding fluorescence lifetime distributions (c).

The supported lipid bilayers were formed by fusing the previously used DOPC: DOPG: DOPE: N+-BDP = 48,5:48,5:2:1 GUV, decreasing the suspending medium glucose concentration (i.e. increasing the density imbalance) enough to provoke GUV adhesion and lysis under their own weight. The resulting bilayers were stretched and the fluorescence lifetime of the N+-BDP probe measured simultaneously for different stretching degrees. Figure 5.27 shows the fluorescence lifetime map within a supported bilayer, before and after stretching. No difference in lifetime was observed despite the significant change in bilayer area. The very slight shift of the average lifetime towards higher lifetimes upon stretching does not reflect an increase in lipid spacing, since one would expect the opposite trend. Several hypotheses could explain this finding; 1) the change in lipid spacing could be out of the sensitivity range of the probe. The lipid packing stays too dense to allow for non-radiative relaxation of the probe. 2) The fusion of small lipid structures floating around the bilayer prevents a build-up in membrane tension by allowing stress relaxation. 3) The initial GUV were not unilamellar. In other similar studies[19, 12, 13] GUV were formed by electroformation and assumed to be unilamellar, but unilamellarity assessments were not performed to confirm this assumption. If the GUV are multilamellar, then exchanges of lipids between the different layers could lead to a relatively constant lipid spacing.

To overcome these drawbacks in performing a rotor calibration using GUV, it would be preferable to use vesicles formed using microfluidics (e.g. Octanol-assisted Liposome Assembly (OLA) method[10]), to make sure they are unilamellar, and to have a constant vesicle composition and diameter. The unilamellarity can easily be checked for all vesicles using e.g. an α-hemolysin[24] or a dithionite assay[25]. This remains a challenge for future work.

5.7 Development of a ratiometric membrane probe

The current toolbox of molecular rotors requires signal detection using sophisticated Time-correlated Single Photon Counting (TCSPC) or FastFLIM instrumentation, which is not available in every laboratory. To increase the accessibility of our method in mapping mechanical gradients, we have explored the option of developing a ratiometric mechanoprobe composed of a microviscosity-sensitive unit (i.e. the previously used molecular rotor), covalently bound to a reference unit (i.e. a fluorescent dye whose quantum yield does not vary with microviscosity or chemical polarity). Measuring the ratio of the rotor dye emission to the reference dye emission intensity on a standard 2-channel fluorescence microscope or spectrometer gives a measurement for the local microviscosity, while simultaneously correcting for variations in local probe concentration.

We decided to synthesize a ratiometric probe made of a Förster Resonance Energy Transfer (FRET) pair to target cell plasma membrane[26]; coumarin was used as a FRET donor, and the BODIPY rotor as a FRET acceptor. The two dyes are linked via a single covalent bond to fix and minimize the distance between the two probes, thereby minimizing uncertainty in measurements due to conformational flexibility. A single bond limits changes in distance and orientation between the two units, and makes sure FRET transfer mainly occurs between the covalently linked dyes, and not between separate molecules that are in close proximity. By contrast to conventional FRET studies, where changes in the donor-acceptor distances are used to make a specific measurement, here the probe is predominantly sensitive to microviscosity changes; on the one hand the amount of FRET transfer -between the coumarin unit and the BODIPY rotor unit- and the quantum yield of the coumarin unit are assumed to be constant, while on

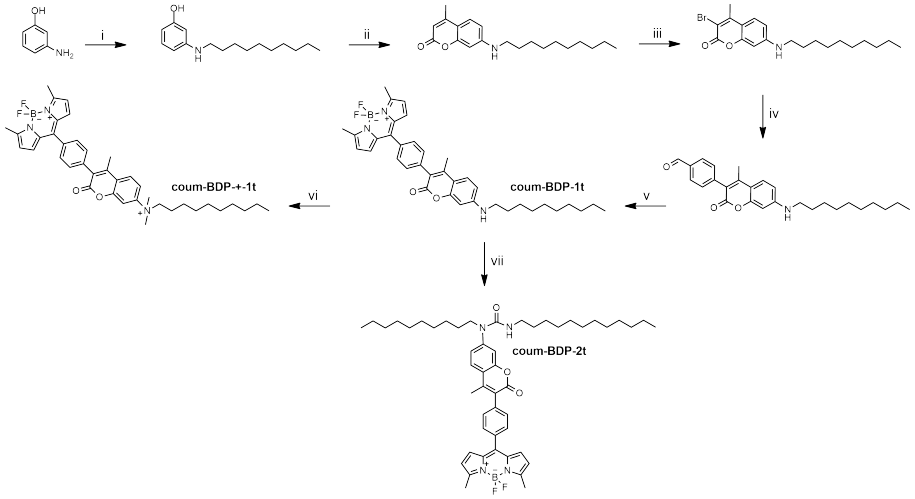

Figure 5.28: Synthesis paths of the three versions of the ratiometric probe; coum-BDP-1t, coum-BDP-+-1t, and coum-BDP-2t. i) iododecane/K_2CO_3, DMF, 60 °C, 3h, 52%; ii) $CH_3COCH_2COOEt/ZnCl_2$, ethanol, reflux, 24h, 37%; iii) NBS, DMF, RT, 22h, 94%; iv) 4-Formylphenylboronic acid/$Pd(PPh_3)_4/K_2CO_3$/dimethoxymethane, reflux, 16h, 79%; v) 2-methylpyrrole/TFA, DCM, RT, 3h, then DDQ, DCM, RT, 1h, then BF_3-Et_2O, Et_3N, DCM, RT, 16h, 10%; vi) CH_3I, DMF, 40°C, 48h, then $NaHCO_3$, DMF, 40°C, 5h, 57%; vii) dodecylamine/K_3PO_4, THF, RT, 16h, 13%.

the other hand the quantum yield of the BODIPY rotor unit varies as its rotation rate varies, in response to the local microviscosity. With the aim of targeting the plasma membrane in plant cells specifically, the coumarin unit was functionalized with one, or two, aliphatic tail(s), with or without a positive charge. This results in three different designs, whose synthetic routes are adapted from Lin et al.[27] and Yang et al.[26], and illustrated in Figure 5.28.

The spectroscopic response of the three probes was studied in mixtures of castor oil and chloroform to span a wide range of solvent viscosities (Fig. 5.29). We find a good correlation between the fluorescence lifetime of the BODIPY rotor unit and the intensity ratio of the BODIPY unit emission over the coumarin emission (Fig. 5.29e), suggesting the useability of the ratiometric probes in microviscosity sensing. Moreover, we note that coum-BDP-1t has the highest sensitivity to changes in viscosity.

However, when incubating *Arabidopsis* seedling roots with these probes, only

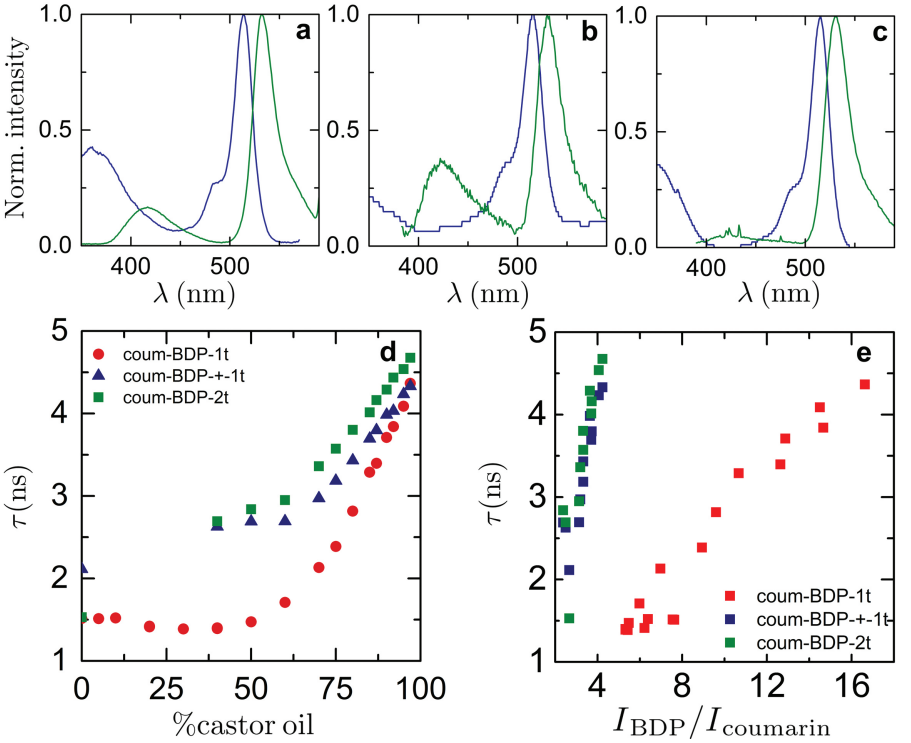

Figure 5.29: Absorbance and fluorescence emission spectra of the three ratiometric dyes in chloroform, coum-BDP-1t (a), coum-BDP-+-1t (b) and coum-BDP-2t (c). Fluorescence lifetime calibration in simple castor oil/chloroform mixtures (d). Evolution of the dye fluorescence lifetime as a function of the corresponding acceptor over donor intensity ratio (e).

very weak to no staining is observed. Coum-BDP-1t seems to localize in the plasma membrane (Fig. 5.30c), but its fluorescence signal is only slightly higher than the cell autofluorescence. Also in other *Arabidopsis* cell types, such as cells from suspension culture or embryonic tissues, the staining does not improve. The dyes reach little to no internalization in suspension cells, while they appear to be completely internalized in embryos (Fig. 5.30). A slightly better staining is obtained with coum-BDP-+-1t in suspension cells, but the probe fluorescence intensity is not much higher than the autofluorescence level (Fig. 5.30e). In all cases, high laser powers were required to obtain a reasonable signal, which in

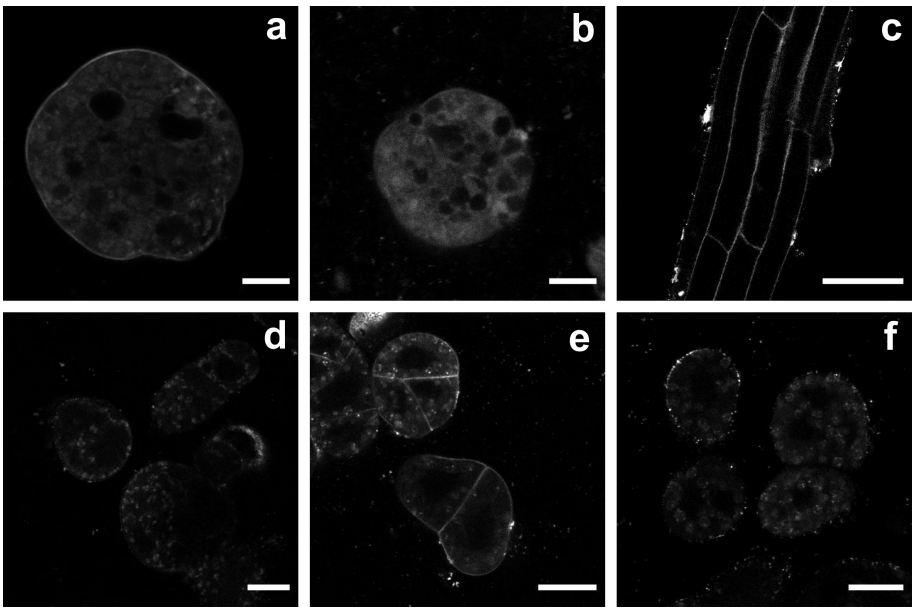

Figure 5.30: Intensity images of the three ratiometric dyes in *Arabidopsis thaliana* living cells: coum-BDP-1t (a) and coum-BDP-2t (b) in embryos (scale bars = 10 μm), coum-BDP-1t in the root of a 4-day-old seedling (c, scale bar = 50 μm), coum-BDP-1t (d), coum-BDP-+-1t (e) and coum-BDP-2t (f) in suspension cells (scale bars = 20 μm).

turn triggers strong autofluorescence due to the 405nm excitation wavelength. Even at very high laser powers, the recorded fluorescence intensity per pixel was insufficient to allow for an accurate intensity ratio determination.

In addition to having a low staining capability, we uncovered these dual probes to be extremely sensitive to chemical polarity. Figure 5.31 shows the fluorescence emission spectrum of coum-BDP-1t in various solvents of similar viscosities but different polarities. Both a shift in spectrum and a significant variation in the peak intensity ratio can be observed, indicating the high sensitivity of coum-BDP-1t to changes in chemical polarity. While this indicates that these probes may make interesting polarity reporters, this strongly hampers their use as mechanoprobes.

We concluded that these ratiometric probes are not suitable for microviscosity imaging in live cells; microviscosity imaging in the plasma membrane of cells

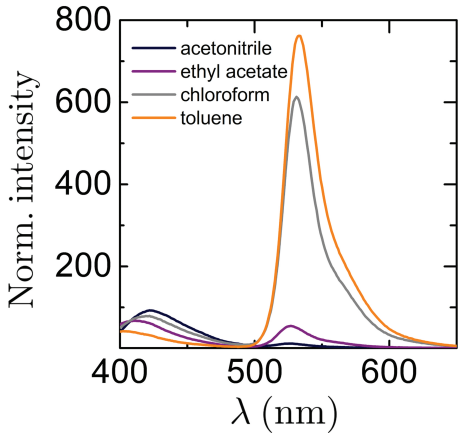

Figure 5.31: Fluorescence emission of coum-BDP-1t in four solvents of different polarity.

requires a probe i) with reasonable quantum yield and excitable in the visible region of the light spectrum, to minimize autofluorescence and cell phototoxicity, ii) whose fluorescent properties do not depend on chemical polarity, iii) smaller in size, to facilitate crossing of the cell wall, and with greater affinity for the plasma membrane. The design of ratiometric mechanoprobes that obey these requirements remains an unresolved challenge.

5.8 Implementation in other biological systems

Chapters 3 to **5** illustrate the successful use of the rotor dyes in *Arabidopsis thaliana* seedlings, and in *Phytophthora infestans*. Staining trials with the rotors were however not limited to these systems. Attempts to stain *Arabidopsis thaliana* embryos were performed with N+-BDP and CWP-BDP respectively, but did not result in a very specific staining of the plasma membrane nor of the cell wall (Fig. 5.32). Membrane dyes (such as DiI, and N+-BDP), tend to diffuse inside the cell rapidly and stain the whole embryo without plasma membrane specificity. CWP-BDP also tends to diffuse intracellularly and does not outline the very young cell walls inside the embryo's globule. The poor CWP-BDP staining is likely to be due to a different embryo cell wall composition as opposed to different tissues,

since CWP-BDP binds to deesterified pectins preferentially. Staining of *Magnaporthe oryzae* with N+-BDP has allowed to study evolution in plasma membrane mechanical properties during appressorium development and maturation; this work is currently being conducted by Dr. Lauren Ryder and Prof. Nick Talbot at the Sainsbury Laboratory (Norwich, UK). A manuscript is in preparation. Stainings of *Saccharomyces* cerevisiae (budding yeast) and *Schizosaccharomyces* pombe (fission yeast) plasma membrane and cytoplasm were achieved successfully with N+-BDP and PEG-BDP respectively. These two probes are currently being used to study the effect of a change in cytoplasm density in yeast cells on cytoskeleton dynamics[28]. The cytosol probe sulfo-BDP, with its two negatively charged sulfonate groups, could not cross the wall barrier. An attempt was made to implement the plasma membrane dye N+-BDP in shPAB human muscle cells (aging model myoblasts) in the hope to get insight into muscle cell senescence and muscle aging in late onset muscular disorders and normal aging[29]. Unfortunately, the fast dynamics and high permeability of the membrane in these cells did not allow for a specific staining, and the dye was immediately internalized (Fig. 5.33).

These results suggest that the rotor dyes are applicable to a wide range of non-animal cells, with a staining efficiency and specificity that varies significantly for different cell sizes and types. Exploring routes for high-fidelity targeting thus remains a challenge for each new cell type or biological question.

5.9 Conclusion

Many interesting molecular mechanoprobes are now available from the material science community, with new probes emerging every year and exhibiting functionalities that are different from the probes explored here. These probes could become valuable assets to resolve mechanical patterns and answer mechanobiological questions. Yet, many challenges remain to allow for their practical use. Most of these probes are designed for use in synthetic and apolar materials; thus a major challenge is to make the probes water-soluble, biocompatible, and able to target defined cellular structures or compartments of interest (e.g. by making them small enough to enable rapid diffusion-based transport through the cel-

lular barriers, or tuning their selective binding ability). However, several promising strategies to achieve selective binding arise; for instance, the use of metabolic labelling, previously employed to incorporate alkyne or azide groups in the pectin network of *Arabidopsis* seedling roots cell wall, allowing for a subsequent click-reaction to fluorescent dyes[30, 31, 32], or the use of genetic labelling by means of SNAP-tags, previously implemented in animal cells to label e.g. plasma membrane proteins[33, 34]. Another open and pressing question is how to make the imaging with mechanoprobes fully quantitative. Ideally one would want to measure the amplitude of actual forces inside plant cells, as well as the orientation of these forces. A few molecular probes that directly measure tensions have been reported (e.g. based on synthetic conjugated polymers[35], on DNA constructs[36, 37], or on small mechanophores such as spiropyrans[38] or benzocyclobutene[39]), but none of them has been designed for implementation in plants yet. Furthermore, to allow for absolute quantification, an accurate calibration of the probe is needed, taking into account the structural and physicochemical properties of cells. Resolving these challenges undoubtedly requires a cross-disciplinary approach, involving -among others- chemistry (synthesis), biology (probe design and application) and modelling (development of mechanical models to compare what the probe measures and what is expected).

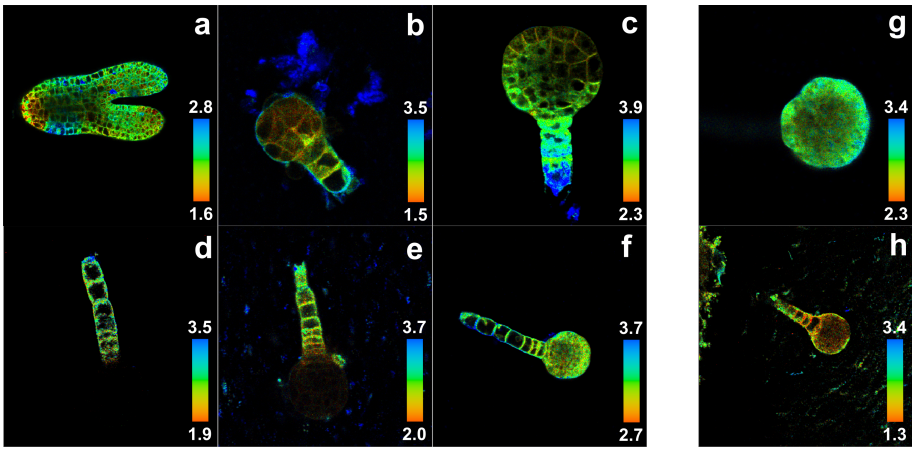

Figure 5.32: Fluorescence lifetime images of *Arabidopsis* embryos incubated with N+-BDP (a-f) or CWP-BDP (g,h), taken and supplied by Vera Gorelova.

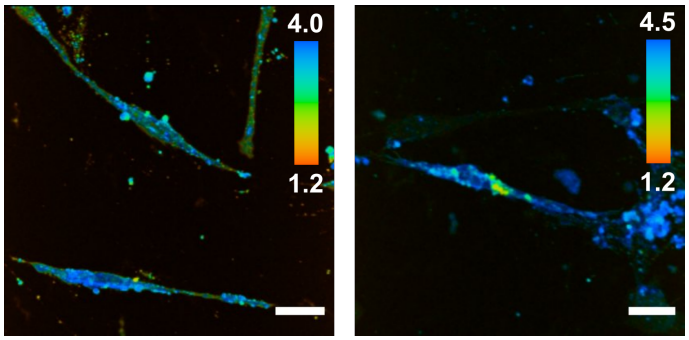

Figure 5.33: Fluorescence lifetime images of shPAB human muscle cells incubated with N+-BDP. Scale bars = 30 μm.

References

[1] Andrew Pohorille and David Deamer. Artificial cells: prospects for biotechnology. *Trends Biotechnol.*, 20(3):123–128, 2002.

[2] Sandro Matosevic. Synthesizing artificial cells from giant unilamellar vesicles: state-of-the art in the development of microfluidic technology. *Bioessays*, 34(11):992–1001, 2012.

[3] Bastiaan C. Buddingh' and Jan C. M. van Hest. Artificial cells: Synthetic compartments with life-like functionality and adaptivity. *Acc. Chem. Res.*, 50(4):769–777, 2017.

[4] Siddharth Deshpande, Willem Kasper Spoelstra, Marleen van Doorn, Jacob Kerssemakers, and Cees Dekker. Mechanical division of cell-sized liposomes. *ACS Nano.*, 12(3):2560–2568, 2018.

[5] Siddharth Deshpande, Frank Brandenburg, Anson Lau, Mart G. F. Last, Willem Kasper Spoelstra, Louis Reese, Sreekar Wunnava, Marileen Dogterom, and Cees Dekker. Spatiotemporal control of coacervate formation within liposomes. *Nat. Commun.*, 10, 2019.

[6] Yuval Mulla, Anders Aufderhorst-Roberts, and Gijsje H Koenderink. Shaping up synthetic cells. *Phys. Biol.*, 15(4), 2018.

[7] Margrethe A. Boyd and Neha P. Kamat. Visualizing tension and growth in model membranes using optical dyes. *Biophysical Journal*, 115(7):1307–1315, 2018.

[8] Christopher Kirby and Gregory Gregoriadis. Dehydration-rehydration vesicles: A simple method for high yield drug entrapment in liposomes. *Nat. Biotechnol.*, 2:979–984, 1984.

[9] Philippe Girard, Jacques Pécréaux, Guillaume Lenoir, Pierre Falson, Jean-Louis Rigaud, and Patricia Bassereau. A new method for the reconstitution of membrane proteins into giant unilamellar vesicles. *Biophysical Journal*, 87(1):419–429, 2004.

[10] Siddharth Deshpande, Yaron Caspi, Anna E. C. Meijering, and Cees Dekker. Octanol-assisted liposome assembly on chip. *Nat. Commun.*, 7, 2016.

[11] Sadao Ota, Satoko Yoshizawa, and Shoji Takeuchi. Microfluidic formation of monodisperse, cell-sized, and unilamellar vesicles. *Angew. Chem. Int. Ed.*, 48:6533 –6537, 2009.

[12] Agata Witkowska, Lukasz Jablonski, and Reinhard Jahn. A convenient protocol for generating giant unilamellar vesicles containing snare proteins using electroformation. *Scientific Reports*, 8, 2018.

[13] Valerio Pereno, Dario Carugo, Luca Bau, Erdinc Sezgin, Jorge Bernardino de la Serna, Christian Eggeling, and Eleanor Stride. Electroformation of giant unilamellar vesicles on stainless steel electrodes. *ACS Omega*, 2(3):994–1002, 2017.

[14] L.-Ruth Montes, Alicia Alonso, Felix M. Goñi, and Luis A. Bagatolli. Giant unilamellar vesicles electroformed from native membranes and organic lipid mixtures under physiological conditions. *Biophysical Journal*, 93(10):3548–3554, 2007.

[15] Andreas Weinberger, Feng-Ching Tsai, Gijsje H Koenderink, Thais F Schmidt, Rosângela Itri, Wolfgang Meier, Tatiana Schmatko, André Schröder, and Carlos Marques. Gel-assisted formation of giant unilamellar vesicles. *Biophysical Journal*, 105(1):154–164, 2013.

[16] Kim S Horger, Daniel J Estes, Ricardo Capone, and Michael Mayer. Films of agarose enable rapid formation of giant liposomes in solutions of physiologic ionic strength. *J. Am. Chem. Soc.*, 131(5):1810–1819, 2009.

[17] Peter Walde, Katia Cosentino, Helen Engel, and Pasquale Stano. Giant vesicles: Preparations and applications. *ChemBioChem*, 11(7):848–865, 2010.

[18] Ida Louise Jørgensen, Gerdi Christine Kemmer, and Thomas Günther Pomorski. Membrane protein reconstitution into giant unilamellar vesicles: a review on current techniques. *Eur. Biophys. J.*, 46(2):103–119, 2017.

[19] Torben-Tobias Kliesch, Jörn Dietz, Laura Turco, Partho Halder, Elena Polo, Marco Tarantola, Reinhard Jahn, and Andreas Janshoff. Membrane tension increases fusion efficiency of model membranes in the presence of snares. *Scientific Reports*, 7(1), 2017.

[20] Md Moniruzzaman, Md Zahidul Islam, Sabrina Sharmin, Hideo Dohra, and Masahito Yamazaki. Entry of a six-residue antimicrobial peptide derived from lactoferricin b into single vesicles and escherichia coli cells without damaging their membranes. *Biochemistry*, 56(33):4419–4431, 2017.

[21] Moynul Hasan and Masahito Yamazaki. *Elementary Processes and Mechanisms of Interactions of Antimicrobial Peptides with Membranes-Single Giant Unilamellar Vesicle Studies-*, volume 1117 of *Antimicrobial Peptides. Advances in Experimental Medicine and Biology*. Springer, Singapore, 2019.

[22] Sayed Ul Alam Shibly, Chiranjib Ghatak, Mohammad Abu Sayem Karal, Md Moniruzzaman, and MasahitoYamazaki. Experimental estimation of membrane tension induced by osmotic pressure. *Biophysical Journal*, 111(10):2190–2201, 2016.

[23] Martin Gleisner, Benjamin Kroppen, Christian Fricke, Nelli Teske, Torben-Tobias Kliesch, Andreas Janshoff, Michael Meinecke, and Claudia Steinem. Epsin n-terminal homology domain (enth) activity as a function of membrane tension. *J. Biol. Chem.*, 291(38):19953–19961, 2016.

[24] Laura R. Arriaga, Sujit S. Datta, Shin-Hyun Kim, Esther Amstad, Thomas E. Kodger, Francisco Monroy, and David A. Weitz. Ultrathin shell double emulsion templated giant unilamellar lipid vesicles with controlled microdomain formation. *Small*, 10(5):950–956, 2014.

[25] Michael Schaich, Jehangir Cama, Kareem Al Nahas, Diana Sobota, Hannah Sleath, Kevin Jahnke, Siddharth Deshpande, Cees Dekker, and Ulrich F. Keyser. An integrated microfluidic platform for quantifying drug permeation across biomimetic vesicle membranes. *Mol. Pharmaceutics*, 16(6):2494–2501, 2019.

[26] Zhigang Yang, Yanxia He, Jae-Hong Lee, Nayoung Park, Myungkoo Suh, Weon-Sik Chae, Jianfang Cao, Xiaojun Peng, Hyosung Jung, Chulhun Kang, and Jong Seung Kim. A self-calibrating bipartite viscosity sensor for mitochondria. *J. Am. Chem. Soc.*, 135(24):9181–9185, 2013.

[27] Qiuning Lin, Qi Huang, Chunyan Li, Chunyan Bao, Zhenzhen Liu, Fuyou Li, and Linyong Zhu. Anticancer drug release from mesoporous silica based nano-photocage regulated by either one- or two-photon process. *J. Am. Chem. Soc.*, 132(31):10645–10647, 2010.

[28] A. T. Molines, J. Lemière, C.H. Edrington, C-T. Hsu, I.E. Steinmark, K. Suhling, G. Goshima, L.J. Holt, G. J. Brouhard, and F. Chang. Physical properties of the cytoplasm modulate the rates of microtubule growth and shrinkage. *bioRxiv*, 2020.

[29] Cyriel Sebastiaan Olie, Erik van der Wal, Cikes Domagoj, Loes Maton, Jessica C. de Greef, I.-

Hsuan Lin, Yi-Fan Chen, Elsayad Kareem, Josef M. Penninger, Benedikt M. Kessler, and Vered Raz. Cytoskeletal disorganization underlies pabpn1-mediated myogenic disability. *Scientific Reports*, 10, 2020.

[30] Charles T. Anderson, Ian S. Wallace, and Chris R. Somerville. Metabolic click-labeling with a fucose analog reveals pectin delivery, architecture, and dynamics in arabidopsis cell walls. *Proc. Nat. Ac. Sci.*, 109(4):1329–1334, 2012.

[31] Yuntao Zhu, Jie Wu, and Xing Chen. Metabolic labeling and imaging of n-linked glycans in arabidopsis thaliana. *Angew. Chem. Int. Ed.*, 55(32), 2016.

[32] Marie Dumont, Arnaud Lehner, Boris Vauzeilles, Julien Malassis, Alan Marchant, Kevin Smyth, Bruno Linclau, Aurélie Baron, Jordi Mas Pons, Charles T. Anderson, Damien Schapman, Ludovic Galas, Jean-Claude Mollet, and Patrice Lerouge. Plant cell wall imaging by metabolic click-mediated labellingof rhamnogalacturonan ii using azido 3-deoxy-d-manno-oct-2-ulosonic acid. *The Plant Journal*, 85:437–447, 2016.

[33] Xiaoli Sun, Aihua Zhang, Brenda Baker, Luo Sun, Angela Howard, John Buswell, Damien Maurel, Anastasiya Masharina, Kai Johnsson, Christopher J. Noren, Ming-Qun Xu, and Ivan R. Corrêa Jr. Development of snap-tag fluorogenic probes for wash-free fluorescence imaging. *ChemBioChem*, 12(14):2217–2226, 2011.

[34] Peter J. Bosch, Ivan R. Corrêa Jr., Michael H. Sonntag, Jenny Ibach, Luc Brunsveld, Johannes S. Kanger, and Vinod Subramaniam. Evaluation of fluorophores to label snap-tag fused proteins for multicolor single-molecule tracking microscopy in live cells. *Biophysical Journal*, 107(4):803–814, 2014.

[35] Ties van de Laar, Hent Schuurman, Pieter van der Scheer, Jan Maarten van Doorn, Jasper van der Gucht, and Joris Sprakel. Light from within: Sensing weak strains and femtonewton forces in single molecules. *Chem*, 4(2):269–284, 2018.

[36] Hari Shroff, Björn M. Reinhard, Merek Siu, Harish Agarwal, Andrew Spakowitz, and Jan Liphardt. Biocompatible force sensor with optical readout and dimensions of 6 nm3. *Nano Lett.*, 5(7):1509–1514, 2005.

[37] Brandon L Blakely, Christoph E Dumelin, Britta Trappmann, Lynn M McGregor, Colin K Choi, Peter C Anthony, Van K Duesterberg, Brendon M Baker, Steven M Block, David R Liu, and Christopher S Chen. A dna-based molecular probe for optically reporting cellular traction forces. *Nature Methods*, 11:1229–1232, 2014.

[38] Rafal Klajn. Spiropyran-based dynamic materials. *Chem. Soc. Rev.*, 43:148–184, 2014.

[39] Cameron L. Brown and Stephen L. Craig. Molecular engineering of mechanophore activity for stress-responsive polymeric materials. *Chem Sci.*, 6(4):2158–2165, 2015.

Summary

Biological processes in cells result from a complex interplay between gene expression, molecular interactions, and mechanical forces. Yet, no generalized frameworks exist to explain how chemical, genetic and mechanical influences on living systems are intertwined. This is the central goal of the emerging field of mechanobiology, which aims at understanding how mechanical signals are transduced in cells, and converted into biochemical signals that interact with the genetic machinery of the organism to regulate complex biological function. Most of the efforts in this field have been focused on the animal kingdom, while the study of mechanobiological processes in plants or other walled systems (e.g. fungi and oomycetes) has received much less attention. This is in part due to a lack of methods to probe mechano-chemical effects in these species with sufficient resolution. In this thesis, we harnessed the mechanochemistry of fluorescent molecular rotors to enable the study walled cell mechanobiology, as a stepping stone to better understand how walled cells and their tissues cope with mechanical stress. We developed new molecular mechanoprobes to target and stain various compartments of walled cells and tissues (i.e. cell wall, plasma membrane, cytoplasm, vacuole). Their implementation in plant and oomycete cells, combined with quantitative imaging, allowed us to unveil and visualize mechanical patterns, in-vivo and with subcellular resolution.

In **Chapter 2** we provide a technical overview of the various synthesis routes used in this thesis to design and make BODIPY-based molecular rotors that are functionalized to target and report microviscosity patterns in the different cellular compartments studied.

In **Chapter 3** we implement a set of BODIPY-based molecular rotors in Arabidopsis seedlings. We use Fluorescence Lifetime Imaging to image spatial variations in the rotors' fluorescence lifetime, in order to construct so-called 'microviscosity' maps. This approach opens up new ways to understand the role of mechanics in the regulation of biological processes. In particular, it could provide valuable insights on the role of mechanical stress in cell polarisation and differentiation, and on the adaptation of local mechanics during important stages in the life cycle of the cell.

We critically reflect and refine the notion of 'microviscosity' in **Chapter 4**, by discussing the potential factors controlling the molecular rotation rate, and subsequently, the fluorescence lifetime of BODIPY-based molecular rotors in cells. We conclude that fluorescence lifetime mapping with these rotors gives information on the relative confinements and crowding density within cells, but that direct translation of lifetime into absolute microviscosity values requires cautious

calibration.

In **Chapter 5**, we show that our dye toolbox is not restricted to use in plants, but can be readily adapted for micromechanical mapping in other walled organisms, such as oomycetes. Using the cell-wall targeting molecular rotor in combination with a plasma membrane chemical polarity probe, we are able to visualize effects of mechanical and chemical stress on the mechano-chemical properties of *Phytophthora infestans* cell wall and plasma membrane during invasion. The generated insight can be used to understand the mechanisms of plant-pathogen mechanical interaction, as well as the mode of action of fungicides developed to inhibit growth and host invasion.

The work in this thesis highlights how a physico-chemical approach, utilizing mechano-chemistry tools, can help shed light on the complex biological processes occurring in walled cells. Through direct visualization of mechanical patterns at the microscopic scale, we can gain understanding of a wide variety of processes. In the **General Discussion**, we put our work in a broader context, provide routes to develop the work further, and suggest approaches, on the basis of preliminary results, to perform a probe calibration and develop a ratiometric equivalent to the lifetime-based probes.

List of Publications

THIS DISSERTATION:

- L. Michels, V. Gorelova, Y. Harnvanichvech, J. W. Borst, B. Albada, D. Weijers and J. Sprakel: **Complete microviscosity maps of living plant cells and tissues with a toolbox of targeting mechanoprobes** *PNAS*, 117(30), 18110-18118 (2020) (Chapter 3)
- L. Michels, J. Bronkhorst, M. Kasteel, D. de Jong, B. Albada, T. Ketelaar, F. Govers and J. Sprakel: **Molecular sensors reveal the mechano-chemical response of *Phytophthora infestans* walls and membranes to mechanical and chemical stress** (Chapter 5) Manuscript in preparation

Acknowledgments

Four years and a half ago, I arrived in the Netherlands to do my end-of-study internship in the laboratory of Physical Chemistry and Soft Matter. And here we are now!

I want to start with a big thank you to my supervisor. Joris, I find it difficult to find right and not-too-cheesy words to express the gratitude I have towards you. Thank you for your communicative enthusiasm, your ideas, your presence and your infallible support. You taught me a lot and you brought me all the confidence. For all of this, thank you.

Thank you to all my colleagues and friends from PCC. Thank you for the relaxed, fun and supportive atmosphere. With you all around, I felt at home and coming to work every day could not have been more fulfilling. Pieter, thank you for introducing me to the lab and putting me on the right track! Ping, Jochem, Djanick, but also Vera , Dolf, Jan Willem, from BIC, Arjen (BIP), Bauke (ORC), Michiel (CLB & PHP), Tijs (CLB) and Francine (PHP), I really enjoyed collaborating with you all on our exciting mechanobiology projects. Thank you for your precious help! Jasper, thanks again for your help on writing the Matlab routines! Martijn, stay as you are, and thank you very much for being at my side, on stage, during the defense. My dear office mates Ilse, Inge, Sophie, Chuanbao, and of course my lab companions Diane and Jessica, it was a pleasure to work in your company, in such a peaceful and considerate atmosphere.

Mara, Leonie, and Marioes, thank you very much for your help on ordering material, taking care of the administrative sides of my PhD, and promoting the good mood in the corona times!

A special thank you to my (ex) students, Daisy, Martijn, Annemarie and Maarten, for their commitment and contribution to my research. I keep fond memories of our work together. It has been a very special and enjoyable experience to be able to guide and share with you along these months.

I also want to thank my friends and everyone I met during these past years, who have made of the whole dutch experience such an enriching and exciting one. Apart from the people I already mentioned above, I want to thank particularly Flo (my second paranymph, merci!), Renan, Ping, Qimeng, Stijn, Cindy, Marion, Chloé, Marine, Léa, Deena and Teresa. Taking dutch classes with a priest, biking all around the country, going for big walks in the forest, discovering the Wageningse food-, sport-, and nightlife, and even attending a survival run competition; that was a lot of fun!

Lodi, j'ai beaucoup de chance de t'avoir rencontré, merci d'être à mes côtés. Je suis contente de célébrer ce moment avec toi!

Papa et Maman, Thomas et Clémence, vous êtes formidables et vous me manquez beaucoup. Papa et Maman, je ne pourrai jamais vous remercier assez d'avoir toujours fait de votre mieux pour nous, et de m'avoir toujours encouragée et accompagnée dans mes choix et mes expériences. Merci !

Thank you!!

Lucile

Overview of completed training activities

Discipline specific activities

MechanoChemBio conference, Germany (MPI, 2017)*
RPK-A module: Polymer chemistry course, The Netherlands (PTN, 2018)
Dutch Soft Matter Meeting, The Netherlands (2019)*
MechanoChemBio conference, Canada (MPI, 2019)*
CHAINS, The Netherlands (NWO, 2019)*
Future Leaders in Mechanobiology seminar, United States (CEMB, 2021)*
Dutch Biophysics, The Netherlands (NWO, 2021)*
*poster or oral presentation

General courses

Essentials of Scientific Writing and Presenting, The Netherlands (WGS, 2017)
Presenting with Impact, The Netherlands (WGS, 2018)
Scientific Artwork, The Netherlands (WGS, 2018)
Scientific Writing, The Netherlands (WGS, 2019)
Career Perspectives, The Netherlands (WGS, 2020)

Optionals

Preparation of research proposal (2017)
Group meetings & colloquia (PCC, 2017-2021)
Journal Club (PCC, 2019)

The research described in this thesis was financially supported
by the Netherlands Organisation for Scientific Research (NWO)
through VIDI programme 'Light from Within' (project number: 723.016.001)

Printed by Proefschriftmaken.nl in 80 copies